

RICE UNIVERSITY

**Two-photon photoassociative spectroscopy of
strontium-86**

by

James Allen Aman

A THESIS SUBMITTED
IN PARTIAL FULFILLMENT OF THE
REQUIREMENTS FOR THE DEGREE

Doctor of Philosophy

APPROVED, THESIS COMMITTEE:

Thomas C. Killian, Chair
Professor of Physics and Astronomy

Randall G. Hulet
Fayez Sarofim Professor of Physics and
Astronomy

Kevin F. Kelly
Associate Professor of Electrical and
Computer Engineering

Houston, Texas

August, 2019

ABSTRACT

Two-photon photoassociative spectroscopy of strontium-86

by

James Allen Aman

This dissertation describes two-photon photoassociation to the least-bound vibrational level of the $X^1\Sigma_g^+$ electronic ground state of the $^{86}\text{Sr}_2$ dimer, which represents the first observation of this naturally occurring halo molecule. We measure the binding energy of this state to be $E_b = 83.00(7)(20)$ kHz. Using the precise determination of the halo state binding energy and the universal theory for a very weakly-bound state on a potential that asymptotes to a van der Waals form, we determine *s*-wave scattering lengths for all strontium isotopes. Our results are consistent with, but substantially more accurate than the previously determined values found from spectroscopic determination of long-range coefficients using other strontium isotopes.

With a radial expectation value of $\langle r \rangle \approx 21$ nm the halo state extends well into the classically forbidden region, which results in a large sensitivity of the dimer binding energy to light near-resonant with a bound-bound transition on the metastable $^1S_0 - ^3P_1$ potential. This suggests that ^{86}Sr may be a promising candidate for manipulating atomic interactions via optical coupling of the molecular bound states and probing naturally occurring Efimov states.

Furthermore, we observe novel multi-photon spectral loss features due to strong coupling and small detuning of the photoassociation lasers. Numerical simulations of a simple three-level model undergoing a simultaneous two-frequency drive, shows

that solutions of the time-dependent Schrödinger equation accurately reproduce these additional loss features. A Floquet analysis of this model, yields analytic formulas for predicting the AC Stark shift of the halo molecule.

Additionally, we report on the current state and recent modifications of our ultracold neutral strontium apparatus with a particular emphasis on the installation of a 532 nm optical lattice. Characterization of this laser system and applications are discussed for further investigation of the strontium-86 halo molecule and additional photoassociation experiments.

Contents

Abstract	ii
List of Illustrations	viii
List of Tables	xii
1 Introduction	1
1.1 Halo molecules	4
1.2 Properties of strontium	7
1.3 Thesis Outline	10
2 The Neutral apparatus	12
2.1 Experimental procedure	13
2.1.1 Characteristic performance	17
2.2 Vacuum system and atom source	19
2.3 Laser systems	28
2.3.1 Wideband cooling stage: 461 nm	28
2.3.1.1 Overview	28
2.3.1.2 922 nm master	31
2.3.1.3 Zeeman subsystem	35
2.3.1.4 MOT subsystem	37
2.3.2 Narrowband cooling stage: 689 nm	44
2.3.2.1 Overview	44
2.3.2.2 689 nm Master	47
2.3.2.3 Neutral red system	48
2.3.3 Optical dipole trap: 1064 nm	54

2.3.3.1	Modeling the potential	56
2.3.3.2	Trap frequency calibration	61
2.3.4	Optical toolbox	66
2.3.4.1	Absorption imaging system	66
2.3.4.2	Highly tunable 689 nm spectroscopy system	70
2.3.4.3	Spin-manipulation laser with dynamic polarization control	76
2.4	Apparatus interface	80
2.4.1	Software	80
2.4.2	Hardware control and measurement systems	81
2.4.3	Ancillary laboratory systems	84
2.4.3.1	Trim coils	84
2.4.3.2	Zero crossing AC line trigger	86
2.4.3.3	Pneumatic actuated mirror mounts	89
3	Photoassociation in ultracold gases	91
3.1	Introduction	91
3.2	Theory of trapped boson gases	93
3.2.1	Extracting data from column densities	94
3.3	Atomic collisions	98
3.3.1	Single channel scattering near threshold	100
3.4	Modeling of photoassociation lineshapes	106
4	High-intensity photoassociation spectroscopy of a halo molecule	113
4.1	Probing the ground state potential	113
4.2	Experimental setup	114
4.3	Modeling the photoassociative loss	122

4.4	Frequency dependence of the binding energy	128
4.5	Multi-photon loss processes	135
5	Binding energy of the $^{86}\text{Sr}_2$ halo molecule	139
5.1	Photoassociation in shallow traps	140
5.1.1	Effects of truncation on collision energy	143
5.1.2	Fitting the thermally averaged spectra	150
5.2	Determination of energy shifts	153
5.2.1	AC Stark shift due to excitation lasers	155
5.2.2	Density-dependent frequency shift	159
5.2.3	AC Stark Shift due to Trapping Lasers	160
5.3	Discussion of the halo binding energy	162
6	Installation of a 532 nm lattice	172
6.1	Background	173
6.2	Kapitza-Dirac scattering	177
6.3	Setup and alignment	179
6.4	Measurement and results	190
7	Conclusion	195
Bibliography		199
Appendices		228
A	Two-particle momentum probability distribution	229
A.1	Standard form	229
A.2	Truncated form	230
B	Concise derivation of effective volumes	237

C Doppler-free spectroscopy	240
C.1 Common setup	240
C.2 Addition of Zeeman shift	242
D Repair of 922 Lynx master	243
E Recent changes to the vacuum system	247
E.1 Nozzle redesign - nuiNozzle 2018	247
E.2 Opening vacuum - data and setup	249

Illustrations

1.1	The photoassociation process	2
1.2	$^{86}\text{Sr}_2$ halo radial wavefunction	6
1.3	Partial energy level diagram of strontium	8
2.1	Neutral apparatus vacuum system	20
2.2	Source assembly - side view	21
2.3	Source assembly - rear view	21
2.4	2D collimator assembly	22
2.5	Cryo tower assembly	22
2.6	Typical fluorescence of Zeeman beam looking down 2D collimator	25
2.7	Atom oven and nozzle construction	27
2.8	461 nm light generation system	29
2.9	922 nm master optical schematic	32
2.10	922 nm doubling cavity length stabilization feedback diagram	33
2.11	922 nm frequency stabilization block diagram	34
2.12	Zeeman subsystem optical schematic	36
2.13	MOT subsystem optical schematic	38
2.14	461 nm MOT schematic	40
2.15	461 nm saturated absorption setup	42
2.16	689 nm light generation system	45
2.17	689 nm master system	49
2.18	Neutral 689 nm trapping and cooling setup	50

2.19	1064 nm optical dipole trap schematic	55
2.20	Two-level avoided crossing	57
2.21	Modeling an optical dipole potential	60
2.22	Example center-of-mass oscillations	62
2.23	Absorption imaging and blow away pulser optical schematic	67
2.24	Timing diagram of PixelFly doubleshutter mode	68
2.25	Comparison of background subtraction methods	71
2.26	Optical schematic: 689 spectroscopy laser	72
2.27	Infinite sample and holding timing diagram	73
2.28	Characterization of the OPLL performance	77
2.29	Spin polarization of strontium-87	79
2.30	Zeroing residual magnetic fields	85
2.31	Circuit diagram of the zero crossing AC line trigger	87
2.32	Comparison of PulseBlaster timing jitter	88
2.33	Pneumatic actuators diagram	90
3.1	Schematic of the photoassociation process	92
3.2	Ballistic expansion of particles	95
3.3	Examples of scattering state solutions	99
3.4	^{86}Sr radial scattering wavefunction near $E = 0$	102
3.5	Effects of mass-scaling on strontium scattering wavefunctions	103
4.1	$^{86}\text{Sr}_2$ halo molecule excitation scheme	115
4.2	Accessible halo resonance PAS processes	117
4.3	Schematic of PAS light generation	119
4.4	Histogram of PAS beam intensity variation	121
4.5	Atom-loss spectra due to halo molecule spectroscopy	123
4.6	Halo state resonances and susceptibilities, χ_{689}	129

4.7	Comparison of a three-level model to experimental halo PAS	131
4.8	Analytic approximation of the susceptibility	133
4.9	Observation of higher order Raman processes	136
4.10	Multi-photon Raman processes	138
5.1	Surface plot of the trapping volume in single-beam trap	144
5.2	Two-particle Maxwell-Boltzmann distribution	146
5.3	Relative collision energy distributions for various truncations	149
5.4	Comparison of lineshape fits at various ϵ_{\max}	151
5.5	Atom-loss spectra with varying 689 nm intensity	157
5.6	Fit of 689 nm AC Stark shift	158
5.7	Atom-loss spectra with varying 1064 nm intensity	161
5.8	Measurement of halo state susceptibility, χ_{1064}	163
5.9	Determination of 86 <i>s</i> -wave scattering length	165
5.10	Comparison of C_6 coefficient estimates	167
5.11	Estimation of scattering lengths via mass scaling	171
6.1	1D band structure as a function of lattice depth	174
6.2	Tunneling rate, J , and interaction energy, U , for strontium in a 532 nm optical lattice	177
6.3	Evolution of plane wave population using Kapitza-Dirac diffraction .	179
6.4	Oscillation period between $n = 0 \rightarrow n = 2$ band at $q = 0$	180
6.5	Lattice optical schematic	182
6.6	Lattice Arm A profile	183
6.7	Lattice Arm B profile	183
6.8	Lattice Arm C profile	184
6.9	Lattice depth calibration	184
6.10	Center-of-mass amplitude suppression when overlapping traps	185

6.11	Observation of breathing mode oscillation	188
6.12	Superfluid to Mott insulator transition	192
6.13	Characterization of heating in the optical lattice	194
A.1	2D Surface plot of the relative collision likelihood	235
A.2	Behavior of $\hat{\mathcal{G}}_E(\epsilon_{\max}, \epsilon)$ vs. collision energy	236
A.3	Behavior of $\hat{\mathcal{G}}_E(\epsilon_{\max}, \epsilon)$ vs. ϵ_{\max}	236
D.1	Damaged 922 master PZT	245
D.2	Removing the circuit board of the 922 master	245
D.3	Newly installed 922 master PZT	246
E.1	nuiNozzle Neutral strontium oven	248

Tables

2.1	Sample trapping performance of ^{84}Sr	17
2.2	Sample trapping performance of ^{86}Sr	18
2.3	Sample trapping performance of ^{88}Sr	18
2.4	Sample trapping performance of ^{87}Sr	18
2.5	461 nm system AOM details	30
2.6	689 nm system AOM details	46
2.7	Arbitrary waveform generation details	82
5.1	Comparison of fitted resonance energies	154
5.2	Experimental parameters for evaluating the $^{86}\text{Sr}_2$ halo binding energy	156
5.3	Comparison of C_6 values from literature	169
5.4	Comparison of calculated s -wave scattering lengths	170
6.1	Inventory of 532 nm lattice optics	181

Chapter 1

Introduction

A guiding principle in the study of physics is that of limiting behavior. When approaching any new problem or system, a great deal of insight may be achieved by first considering the most extreme examples. For the field of ultracold atomic physics, this extreme has been the pursuit of near zero-energy atomic and molecular gases, which has proven to be an incredibly fruitful endeavor. Specifically, the development of ultracold and quantum degenerate neutral gases has allowed us to consider the quantum nature of matter, and its interaction with external fields, in the few-body and many-body regimes [9, 13, 13, 31, 35, 66, 105, 140, 167, 194].

Rapid advancement in the ability to laser cool and trap atoms [125, 125, 153] has led to a number of notable achievements in recent years, including the creation of novel macroscopic states of quantum matter such as Bose-Einstein condensates (BEC) and degenerate Fermi gases [2, 25, 47, 50, 117, 123, 132, 179, 209], the observation of the BEC-BCS crossover and quantum phase transitions [22, 34, 72, 74, 95, 158, 173, 207, 210], as well as the formation of macroscopic ensembles of ro-vibrational ground state molecules [94, 110, 147, 159, 162, 177].

Each of these successes has been enabled by taking advantage of the precision control and manipulability that is accessible in ultracold atomic gases. In particular, the use of external fields to dynamically influence the evolution and occupation of quantum states within an atomic gas has become an invaluable addition to the atomic physicist's toolbox [35]. An example of such a process is photoassociation, whereby

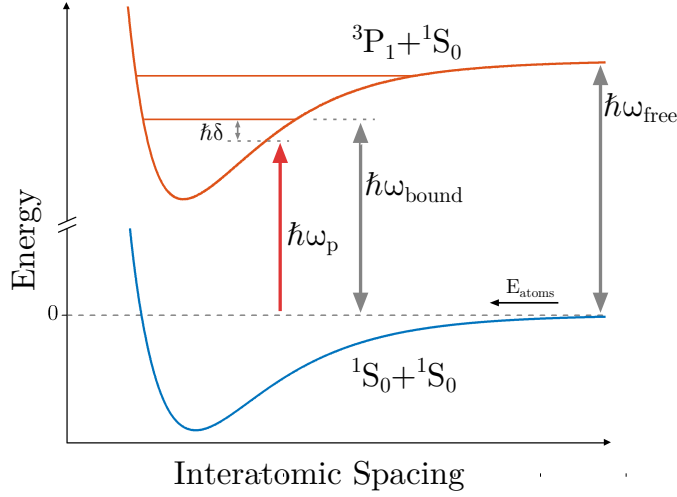


Figure 1.1 : The photoassociation process

Two atoms colliding with energy, E_{atom} , on a ground state potential in the presence of a photoassociation light field of frequency, ω_p . This process will associate the two free atoms when the photoassociation light energy matches the energy difference between the incoming state and excited molecular state, $\hbar\omega_p = \hbar\omega_{\text{free}} - \hbar\omega_{\text{bound}}$.

one or more resonant or near-resonant light fields is used to couple internal states of a gas of interacting atoms. By absorbing one or more photons from the light field(s), the initially free atoms may then associate and form bound molecular states, leading to occupation of a new quantum state [27, 94, 105].

For neutral atoms, interactions between particles occur primarily at interparticle separations $< 100 a_0$, where a_0 is the Bohr radius [35]. These interactions give rise to the potential well that supports bound states, as shown in Fig. 1.1. This figure outlines a typical example of photoassociation using a single light field, known as one-photon photoassociation. In this example, absorption of one photon will promote the internal energy of one atom of the colliding pair up to an excited potential.

Thus, when the laser frequency is appropriately tuned to a bound state energy, this absorption results in the creation of an excited weakly-bound molecular state. The formation of this molecule is followed by spontaneous or stimulated decay, typically resulting in loss of both atoms from the trap. Detection of atom loss is commonly observed as evidence of photoassociation and thus spectroscopy may be used to search for bound-state resonances. The process of photoassociative spectroscopy (PAS) typically involves scanning the photoassociation (PA) laser frequency to the red of the free-atom asymptote. This yields a series of molecular resonance energies progressively further from the free-atom excited state, which correspond to increasingly more deeply bound molecular states and consequently molecules with shorter bond lengths. This reduction of the spatial extent of the deeply-bound molecular wavefunctions is important as it impacts the likelihood of association of the initial free-atom state to the final molecular state via overlap of the wavefunctions. Thus, photoassociation of free atoms favors the creation of weakly-bound molecular states due to the long-range nature of the initial scattering wavefunctions which preferentially overlap with weakly-bound molecular states having large spatial extent. Moreover, molecular states with small binding energies exhibit similar characteristics of the constituent free atoms, while more deeply bound molecules exhibit structure and properties reflective of the properties of the short-range atomic potential [94].

Using photoassociative spectroscopy in ultracold gases, the binding energy of molecular states may be directly measured. These measurements reveal details about the short-range interaction potential between atoms and may be used to determine parameters such as the interparticle scattering length that characterizes the free-atom scattering behavior.

By adding an additional light field, two-photon photoassociation may be used to

populate excited molecular states of the ground state potential. This technique has proven to be an incredibly precise way to discern information about the collisional properties of ultracold atomic gases [1, 118].

However, the direct coupling of free atoms to the most deeply bound molecular states is not an efficient process and generally requires the use of additional photoassociative steps. These may include STIRAP or preferential decay from excited-molecular states as has been recently demonstrated [38, 39, 162, 177]. Ro-vibrational ground state molecules are interesting as their use has been proposed for precision measurements of variations of the proton-electron mass ratio [108, 206] and the fine structure constant [7].

1.1 Halo molecules

For some atomic species, external magnetic fields may be used to create weakly-bound molecular states through the use of magnetic Feshbach resonances [35, 105]. These scattering resonances are the result of coupling between free scattering states (called open channels) and bound states (closed channels) where the scattering and bound states lie on two separate atomic interaction potentials with differential magnetic moments. When the closed channel is swept through the threshold energy of the open channel, a weakly-bound molecular state known as a Feshbach molecule is formed [46, 74, 81, 159, 181]. Additionally, if these Feshbach molecules are created with the closed channel just below threshold they behave as exotic long-range molecules known as halo molecules [105]. These molecules feature wavefunctions that extend far into the classically forbidden region. Such states may be characterized by the large positive value of the free atom scattering length a that is related to the binding

energy of the halo molecule by

$$E_b = -\frac{\hbar^2}{2\mu a^2} \quad (1.1)$$

where μ is the reduced mass of the atom pair.

This concept of a spatially extended, few-particle, halo system is well-known and has been applied in various fields such as nuclear and molecular physics, with the most well known examples being the deuteron and ${}^4\text{He}_2$ molecules [105, 114, 170]. In atomic physics, halo molecules exist as the least-bound state in the extreme case of a scattering resonance, of which Feshbach resonances are a particular type. Halo molecules are interesting quantum states due to their spatially extended wavefunctions which reach well past the classical turning point, $r_{\text{classical}} \cong \left(\frac{2\mu a^2 C_6}{\hbar^2}\right)^{1/6}$. Fig. 1.2 shows the radial component of the ${}^{86}\text{Sr}_2$ halo wavefunction with a farthest extent $> 1000 a_0$. Such halo systems are notable for their universality, whereby molecular properties such as size and binding energy can be parameterized by a single quantity, the *s*-wave scattering length a , independent of other details of the atom-pair interaction [23, 105]. Additionally, Efimov trimers may also exist in systems near a scattering resonance, influencing dimer and atomic scattering properties and introducing additional universal phenomena [24, 144].

In this work, we probe the naturally occurring halo state which exists in the absence of tuning with a magnetic Feshbach resonance. This extremely weakly-bound molecular state depends strongly on the long-range portion of the strontium interaction potential between atoms that determines atom-atom scattering properties.

There are important differences between halo molecules associated with magnetic Feshbach resonances and the naturally occurring halo molecule in ${}^{86}\text{Sr}$. With magnetic Feshbach resonances, the relevant scattering and bound molecular states lie on different molecular potentials and the halo state results from mixing of different

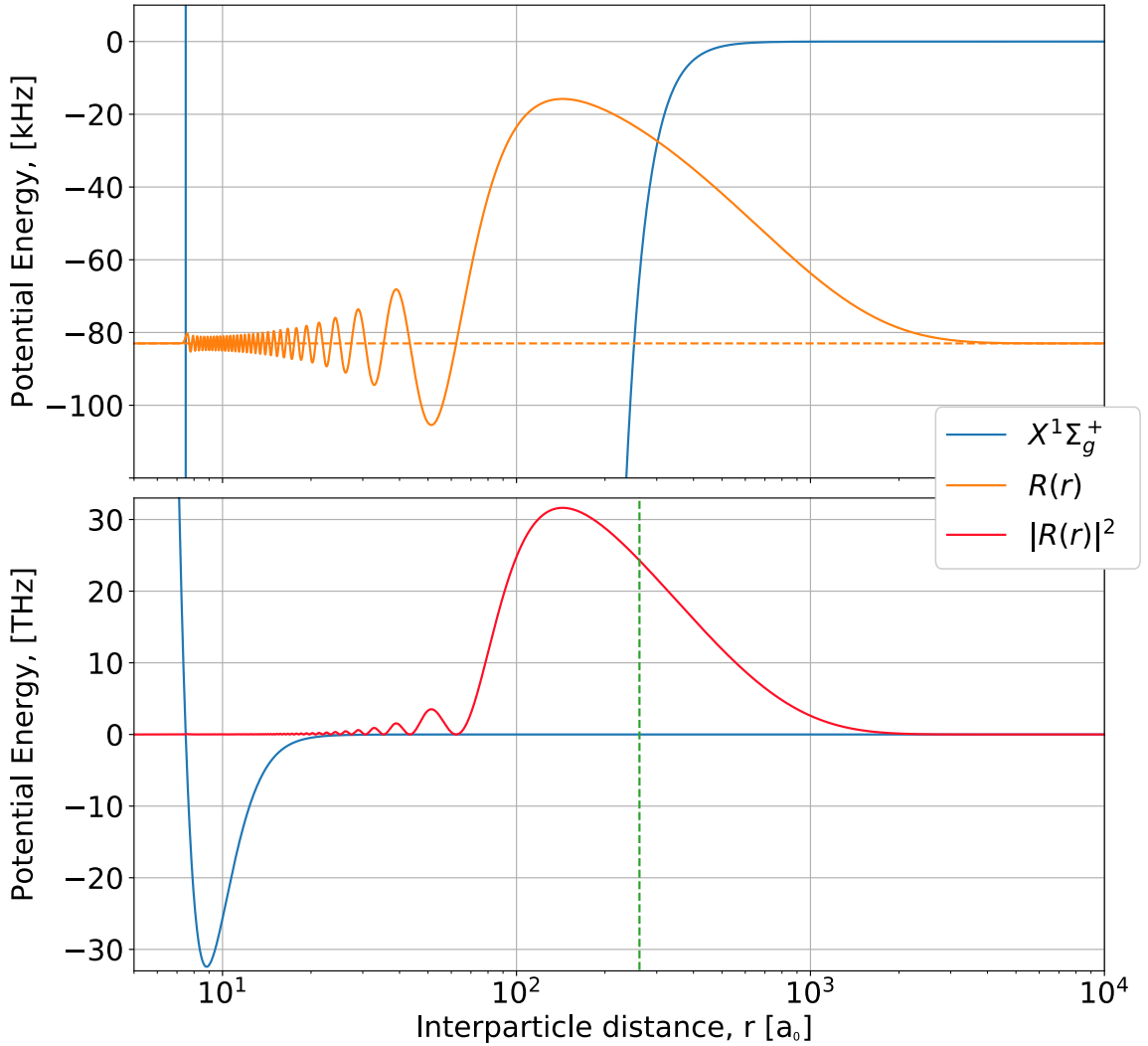


Figure 1.2 : $^{86}\text{Sr}_2$ halo radial wavefunction

The extent of the strontium-86 halo radial wavefunction, $R(r)$, is shown compared to ground state potential. The complete bound state wavefunction is given by $\psi(\mathbf{r}) = Y_{0,0}(\theta, \phi) \frac{R(r)}{r}$, where $Y_{l,m}(\theta, \phi)$ is the spherical harmonic. The radial Schrödinger equation is solved for $R(r)$ using the Johnson renormalized Numerov method [65, 93] with the $X^1\Sigma_g^+$ potential from Ref. [175]. The vertical dashed line is placed at the classical turning point $r_{\text{classical}} \approx 260 a_0$. Note, the difference in energy scales between the top and bottom plots. The wavefunction normalization applied to each plot is arbitrary and only for illustrative purposes.

states. Measuring the properties of these engineered states may then be challenging. Several techniques have been demonstrated to measure molecular binding energies such as single-photon magnetic-dipole transitions and RF or microwave spectroscopy [35, 36, 189]. Typically, this is done by first forming molecules through magneto-association and then driving bound-free or bound-bound transitions converting the halo molecule into a different state and observing this loss. Other methods of measuring the binding energy include spectroscopy with an oscillating magnetic field [189], a modulated optically controlled Feshbach resonance [42], and Ramsey-type measurements of atom-molecule oscillation frequencies [43]. These are powerful techniques for manipulating quantum gases of alkali metals and other open-shell atoms in systems where magnetic Feshbach resonances are readily accessible. Strontium, however, due to its closed-shell electronic structure, lacks magnetic Feshbach resonances in the electronic ground state.

1.2 Properties of strontium

Strontium is an alkaline-earth element with four naturally occurring isotopes, three bosonic and one fermionic. The two valence electrons in its outer shell may align their spin anti-parallel or parallel, giving rise to a singlet and triplet series, respectively, of states. Thus, two laser cooling phases are required to cool strontium to $\approx 1 \mu\text{K}$. The first using the strong dipole-allowed $^1S_0 \rightarrow ^1P_1$ transition at 461 nm and the second using the narrow intercombination line $^1S_0 \rightarrow ^3P_1$ transition at 689 nm [41, 90, 100, 113, 130, 139, 142]. These laser cooling transitions, as well as required repumping transitions, are shown in Fig. 1.3.

The isotopic differences in strontium have important implications for their use in certain experiments. In particular, the bosonic isotopes of strontium ^{88}Sr , ^{86}Sr ,

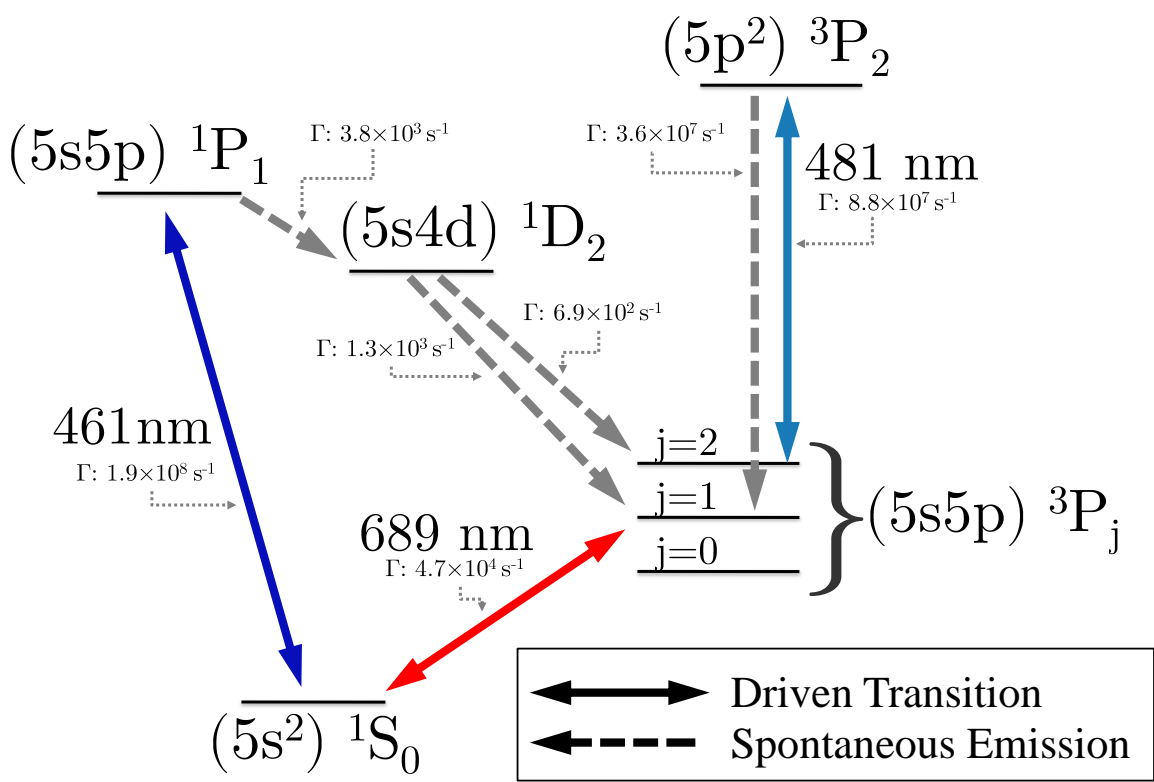


Figure 1.3 : Partial energy level diagram of strontium

Shown are the relevant transitions and decay rates utilized to perform laser cooling and spectroscopy.

and ^{84}Sr have no nuclear spin, $\mathbf{I} = 0$. This lack of hyperfine structure results in a single ground state potential, which greatly simplifies the treatment of collisions and scattering for these atoms. Conversely, the fermionic isotope ^{87}Sr has a large nuclear spin, $\mathbf{I} = 9/2$, which when combined with the lack of electronic angular momentum in the ground state, results in a high degree of symmetry that must be considered when considering the behavior of these atoms during collisions. This $SU(N)$ symmetry of ^{87}Sr has led it to become a popular candidate for proposals exploring exotic phases of quantum magnetism [10, 32, 33].

In addition to the differences in quantum statistics and shifts of transition frequencies between isotopes, the homonuclear s -wave scattering lengths range from -2 a_0 for ^{88}Sr to $\sim 800\text{ a}_0$ for ^{86}Sr . Importantly for this work, we use the isotope with the largest homonuclear scattering length, strontium-86, to measure the binding energy of the least-bound state of the ground state potential via two-photon photoassociation performed near the narrow intercombination line $^1S_0 \rightarrow ^3P_1$ transition. A considerable number of studies have previously reported photoassociation near this transition due to the availability of laser sources near 689 nm and the reduced off-resonant scattering rate that may be achieved when detuning from resonance. The most abundant isotope, ^{88}Sr , has been studied extensively in the context of narrow-line photoassociation, including one-photon PAS in a lattice [122, 205], excitation of coherent Rabi oscillations between atomic and molecular condensates [201], and the observation of optical Feshbach resonances [12, 202]. Two-photon PAS experiments were also performed in ^{88}Sr using this transition to measure the least-bound state of the $X^1\Sigma_g^+$ potential [118]. Additionally, related techniques have produced more deeply bound vibrationally excited molecules in the electronic ground state using ^{88}Sr [120, 121, 161, 162] and ^{84}Sr [177] trapped in optical lattices. Finally,

one-photon photoassociation spectroscopy has been used to probe the excited state molecular binding energies in bulk trapped gases near the intercombination transition in ^{86}Sr [21, 163] and ^{84}Sr [163, 177].

1.3 Thesis Outline

This thesis will describe our work probing the weakly-bound halo state of strontium-86. Chapter 2 will outline our standard laser cooling and trapping procedures for producing samples of ultracold strontium at $\approx 1\,\mu\text{K}$ in an optical dipole trap. Additionally, the experimental apparatus and systems for trapping will be discussed. Chapter 3 will develop the theoretical underpinnings of the photoassociation process that has a rate dependent on the spatial and thermal distribution of the atoms as well as the dynamical coupling provided by the applied PAS light fields. Furthermore, this chapter explores atomic collisions and the importance of short-range interactions in determining the long-range behavior of scattering states. In chapters 4 and 5, we present our findings from experiments probing the $^{86}\text{Sr}_2$ halo molecule. The first experiments are performed in a high-intensity regime where we observed non-linear scaling of loss features and AC Stark shifts on the order of the binding energy of the halo molecule. Following this, we performed a complimentary set of experiments, being careful to stay in a weakly perturbing regime, where we precisely determined the binding energy of the halo molecule accounting for several different possible shifts of the resonance energy. This binding energy is then used to estimate improved scattering lengths for all isotopes of strontium. Chapter 6 describes the installation and characterization of a 532 nm lattice laser system. This system will be indispensable for our future work investigating quantum magnetism with fermionic strontium-87 as well as for studies of the properties of halo molecules and future work. Further

discussion of our proposed work will be given in chapter 7, along with concluding remarks.

Chapter 2

The Neutral apparatus

The Neutral apparatus has been one of the pioneering experiments for the trapping, cooling, and creation of quantum degenerate gases of neutral strontium [21, 50, 116, 118, 127, 129, 131, 132, 142, 143, 190, 201, 202]. As such, there is a plethora of previous theses and publications that explain how to achieve these goals [113, 139, 163]. In particular, we refer the reader to the PhD theses of previous Killian lab students: Francisco Camargo [29], Brian DeSalvo [49], Mi Yan [199], Pascal Mickelson [128], Natali Martinez de Escobar [117], and Sarah Nagel [141]. Additionally, the PhD work of Simon Stellmer [176] and review of strontium quantum degenerate gases are also highly recommended reading [178].

Building upon this previous work, this chapter will forego an extensive review of the laser cooling techniques for strontium. Instead, we will focus on the systems and processes that are crucial to the operation of the experiment with an emphasis on technical findings and recent changes.

We will begin with a brief overview of our trapping procedure in order to contextualize the remaining sections focusing on the hardware including the vacuum system, various laser systems, and experimental control software, hardware, and electronics.

2.1 Experimental procedure

Experiments begin by cooling and trapping atomic strontium utilizing well-established atomic physics techniques [14, 50, 84, 90, 100, 113, 116, 125, 132, 139, 179, 186].

Fig. 1.3 shows the simplified energy level diagram employed in our cooling process.

The majority of cooling is done using 461 nm light acting on the strong $5s^2 {}^1S_0 \rightarrow 5s5p {}^1P_1$ transition. The excited state lifetime of 5 ns ($\Gamma = 1.9 \times 10^8 \text{ s}^{-1}$) and large energy separation between the states results in a hefty saturation intensity of 40.5 mW/cm² for this transition. Therefore laser powers on the order of 100 mW are necessary to produce large optical forces and rapid cooling rates. Subsequent laser cooling on the narrow 689 nm intercombination line along the $5s^2 {}^1S_0 \rightarrow 5s5p {}^3P_1$ transition allows us to reach temperatures on the order of 1 – 2 μK using only optical forces. The 3P_1 state has a long lifetime of 21 μs ($\Gamma = 4.7 \times 10^4 \text{ s}^{-1}$). Following the two laser cooling stages, we perform forced evaporation to obtain bulk samples in an optical dipole trap containing on the order of 10^6 atoms at temperatures $< 1 \mu\text{K}$ and densities between $10^{12} - 10^{15} \text{ cm}^{-3}$ depending upon the isotope.

The laser cooling procedure is generally consistent for trapping all isotopes of strontium with the major difference being timescales and laser frequencies. The trapping protocol for the bosonic isotopes of strontium is nearly identical while fermionic ${}^{87}\text{Sr}$ presents a greater challenge due to its high nuclear spin, $\mathbf{I} = 9/2$. For a thorough and detailed discussion of the relevant physics of trapping ${}^{87}\text{Sr}$, we refer the interested reader to the fermion portion of section 2.7.3 in the PhD thesis of Simon Stellmer [176] and section 2.2.1 of Pascal Mickelson’s PhD thesis [128].

The trapping process begins with heating solid strontium in an oven to approximately 400 °C. The resulting strontium vapor escapes through collimating tubes to produce a partially collimated beam with a mean velocity of $\sim 450 \text{ m/s}$ [119]. To aid

in collimation, the atoms undergo a stage of transverse two dimensional optical molasses, this stage is known as 2D collimation. We typically observe a $7\times$ improvement in trapped atom number with the 2D collimator versus without.

Upon entering the magnetic field of the Zeeman slower, the highest velocity atoms begin to scatter photons from the Zeeman beam, which is red detuned from the $^1S_0 \rightarrow ^1P_1$ transition by $\sim 16\times$ the natural linewidth. Large detunings help to eliminate unwanted photon scattering from the Zeeman beam once atoms have been sufficiently cooled and are accumulating in the MOT fields of the science chamber. After reducing the atoms velocity down to ~ 30 m/s, the atoms exit the Zeeman slower, pass through a minimum in the magnetic field*, and begin scattering photons in a 461 nm magneto-optical trap (MOT) also using the $^1S_0 \rightarrow ^1P_1$ transition. Typically the MOT operates at a detuning of approximately $\frac{-3\Gamma}{2} \approx -45$ MHz. In practice, the optimal trapping frequency is slightly different for each isotope. We therefore optimize the laser detuning to trap the largest number of atoms using a tunable saturated absorption spectroscopy setup, described in Sec. 2.3.1.4.

The broad dipole allowed $^1S_0 \rightarrow ^1P_1$ transition used for the first MOT stage is not completely closed as shown in Fig. 1.3. This slow leak results in population of the 3P_1 and 3P_2 states. While atoms that fall to the 3P_1 state will eventually decay to the ground state, the leak to the 3P_2 state results in a build up of magnetically trappable low-field seeking m_j states that are trapped by the anti-Helmholtz field of

*While the functioning of a Zeeman slower only relies on the magnitude of the B-field, the anti-Helmholtz MOT field and the decaying field outside of the Zeeman slower may lead to a local maximum or zero near the interface of the Zeeman and science chamber dependent on the orientation of the Zeeman B-field. The configuration in use on the Neutral apparatus produces a zero at this interface, which gives $2\times$ more trapped atoms compared to the other possible configuration.

the MOT and are dark to the 461 nm light. This allows us to take advantage of the long lifetime of the metastable 3P_2 state and accumulate a large number of atoms which can then be repumped back down to the 1S_0 ground state. The lifetime of the magnetic trap is typically limited by background pressure ($\sim 15 - 25$ s) and therefore the maximum number of atoms that can be held by the magnetic trap is much greater than in the MOT. On average, an atom will fall into the 3P_2 state after scattering $\approx 5 \times 10^4$ photons from the $^1S_0 \rightarrow ^1P_1$ transition [44]. Although, only 2 out of the 5 magnetic sub-levels are trappable.

Repumping from the 3P_2 state is achieved via a 481 nm transition along the $5s5p\,^3P_2 \rightarrow 5p^2\,^3P_2$ transition for approximately 50 ms. During the repumping exposure we continue to illuminate the cloud with 461 nm light but reduce the light intensity by an order of magnitude. We refer to this stage as the "cold" blue MOT and find that reduction of the intensity, while maintaining consistent laser detuning, significantly increases the transfer efficiency into the red MOT stage[†]. At the conclusion of the 461 nm MOT and repumping phase, we typically have samples of a few million atoms at ≈ 1 mK.

Once the atoms have been returned to the ground state, we begin a second MOT stage using the intercombination transition $^1S_0 \rightarrow ^3P_1$ to cool below 1 mK. Operation of this narrow-line MOT is quite different compared to typical dipole allowed MOTs due to the long lifetime of the excited state. We replicate the behavior of a broad transition MOT by frequency modulating the 689 nm light using voltage controlled RF sources coupled to the light via an acousto-optic modulator (AOM) during the initial

[†]We have explored ramping the laser intensity closer to atomic resonance as we expected reduced intensity at farther red-detuning to result in a weakened trapping force. However, we did not find any improvement with the added complexity of varying the blue laser frequency during this stage.

stages of cooling. Additionally, the overall laser detuning, amplitude of modulation, and laser intensity begin at large values in order to trap the initially hotter atoms from the blue MOT stage. As cooling with the 689 nm light becomes increasingly effective, we dynamically vary these three parameters along with the magnetic field gradient in order to efficiently cool and compress the entire sample. Ultimately, the red MOT is reduced to single frequency operation near resonance at extremely low laser intensity to achieve final temperatures between 1 - 2 μK after 400 ms of cooling.

During the last 50 - 100 ms of the 689 MOT (typically during single frequency operation) we illuminate the 689 nm MOT with the high-intensity 1064 nm optical dipole trap (ODT). The red MOT then continues to cool atoms into the typically 10 μK deep ODT with transfer efficiencies as high as 75%. After loading into the ODT, we subsequently extinguish the red MOT and allow a period (\sim 10 - 100 ms) of free evaporation for the sample to equilibrate in the trap before beginning forced evaporative cooling to produce the final sample of ultracold or quantum degenerate gas.

The end of the evaporation sequence typically marks the beginning of the experimental phase and the divergence of the protocol into the specific procedures necessary. These may include ramping or pulsing on lattice beams, exciting a collective mode, probing the gas with PAS lasers, shelving, etc. Following the completion of the experimental phase, we measure the cloud characteristics via absorption imaging along the $^1S_0 \rightarrow ^1P_1$ transition. Typically absorption imaging is performed after a time-of-flight to measure both the atom number and temperature at the time of release. However, this is not strictly necessary and certain experiments may result in low atomic densities which are not amenable to a time-of-flight diagnostic due to their low optical depth.

Date	Load Time [s]	Magnetic trap		BB Red MOT		SF Red MOT		ODT	
		Num. ($\times 10^6$)	Num. ($\times 10^6$)	Temp. [μK]	Num. ($\times 10^6$)	Temp. [μK]	Num. ($\times 10^6$)	Temp. [μK]	Num. ($\times 10^6$)
1/18/16	5	–	–	–	3.5	1.7	2	1.4	
	15	–	–	–	6	1.7	4.3	1.4	
8/11/16	5	–	–	–	3.2	2.1	1.4	2.1	
	15	–	–	–	7.6	2.1	3.3	1.9	
3/15/18	5	–	2.2	4.5	2.2	1.8	1.6	1.5	
	15	–	4	4.2	3.8	1.8	2.6	1.5	
5/23/18	5	5.8	3.1	5.8	2.6	2.2	1.3	1.6	
	15	13.3	5.5	8	4.5	2.3	2.3	1.6	
8/3/18	5	–	3.3	5.1	2.8	1.7	–	–	
	15	–	5.8	5.2	5.2	1.9	–	–	

Table 2.1 : Sample trapping performance of ^{84}Sr

2.1.1 Characteristic performance

Tables 2.1 - 2.4 outline sample trapping performance at various stages of the cooling procedure for each isotope. Each column of the tables show the number of atoms and measured temperatures from time-of-flight (not applicable for the magnetic trap). The abbreviated column labels refer to the broadband (BB) and single frequency (SF) red MOTs and ODT is the optical dipole trap. Unless otherwise specified, the ODT configuration used for each of these characterizations is the independent arm ODT[‡] discussed in Sec. 2.3.3. Note, that while we have recently demonstrated the ability to dual trap 84 and 87, full characterization and optimization of this process is currently the subject of investigation.

[‡]This may also be called the crossed beam trap in some documentation

Date	Load Time [s]	Magnetic trap ($\times 10^6$)	BB Red MOT		SF Red MOT		ODT	
			Num. ($\times 10^6$)	Temp. [μK]	Num. ($\times 10^6$)	Temp. [μK]	Num. ($\times 10^6$)	Temp. [μK]
11/29/16	1	–	–	–	9.5	2	7.4	1.7
	3	–	–	–	23	2.5	15	2
1/20/17	1	–	–	–	5	1.7	4	1.6
	3	–	–	–	9.1	2	7.7	1.7
3/30/17	1	–	–	–	6.6	2	5	1.7
	3	–	–	–	12.8	2.7	9	1.9
11/15/18	1	7.9	9.7	4.7	7.3	3.4	6.1	3.5
	3	24	21.5	5.1	14.4	3.5	11.4	3.7

Table 2.2 : Sample trapping performance of ^{86}Sr

Date	Load Time [s]	Magnetic trap ($\times 10^6$)	BB Red MOT		SF Red MOT		ODT	
			Num. ($\times 10^6$)	Temp. [μK]	Num. ($\times 10^6$)	Temp. [μK]	Num. ($\times 10^6$)	Temp. [μK]
6/14/17	0.5	–	–	–	3.2	1.6	–	–
	1.5	–	–	–	5	1.6	–	–
2/1/18	0.5	–	–	–	10	2.1	5	1.4
	1.5	–	–	–	19	2.2	6.5	1.4
2/12/18	0.5	25	–	–	–	–	–	–
	1.5	54.1	–	–	–	–	–	–

Table 2.3 : Sample trapping performance of ^{88}Sr

Date	Load Time [s]	Magnetic trap ($\times 10^6$)	BB Red MOT		SF Red MOT		ODT	
			Num. ($\times 10^6$)	Temp. [μK]	Num. ($\times 10^6$)	Temp. [μK]	Num. ($\times 10^6$)	Temp. [μK]
8/15/17	5	–	–	–	0.7	3	0.22	1.7
	15	–	–	–	1.6	2.6	0.5	1.7
9/8/17	5	–	–	–	1	1.8	0.6	1.6
	15	–	–	–	1.8	1.6	1	1.4
	40	–	–	–	1.8	1.6	1.5	1.4
5/1/18	5	8	5.5	8.4	1.8	1.1	1.5	1.1
	15	17	10	11	2.6	1.2	2.2	1.2
12/13/18	5	15	10.3	8.1	2.65	2.3	1.8	2
	15	31	18.7	8.5	4	2.2	2.6	2.1
2/26/19	5	13	8.5	9.9	1.7	1.9	1.25	1.6
	15	21	12	12	2.5	2	–	–

Table 2.4 : Sample trapping performance of ^{87}Sr

2.2 Vacuum system and atom source

Overview

The Neutral apparatus is built around a custom stainless steel chamber positioned above the table to facilitate optical access. Typical pressures are in the ultrahigh vacuum regime, $< 1 \times 10^{-10}$ torr. Details on the original construction can be found in Refs. [117, 128]. The master's of Francisco Camargo [28] outlines the construction of the similar Rydberg apparatus. This more recent apparatus has benefited from the many lessons learned during the early life of the Neutral experiment.

Figure 2.1 shows a complete overview of the assemblies that form the Neutral vacuum system. Figures 2.2 - 2.5 show various views of the atom source, 2D collimator, and cryo tower assemblies. Note the red markers and green arrows denote the positions of heater bands and thermo-couples respectively. For more information please see App. E.

From right to left, the system starts with an oven source based around a custom nozzle design that uses a rod heater to vaporize elemental strontium. Next, there is a 6-way tee used for the optical molasses step that we refer to as the 2D collimator. From here atoms pass through a narrow differential pumping tube and into the entry port of the Zeeman slower where a majority of the laser cooling takes places as atoms traverse the one dimensional cooling stage. Following the Zeeman slower, atoms enter the science chamber where a plethora of lasers are used to manipulate and probe their behavior. Chief among these laser systems are the MOT beams and high-intensity far off-resonant optical dipole traps used for the final stage of confinement. Lastly, the body of the science chamber is supported by the cryo tower which houses a titanium sublimation cartridge (model: Varian 916-0061 series) and is the entry point for the

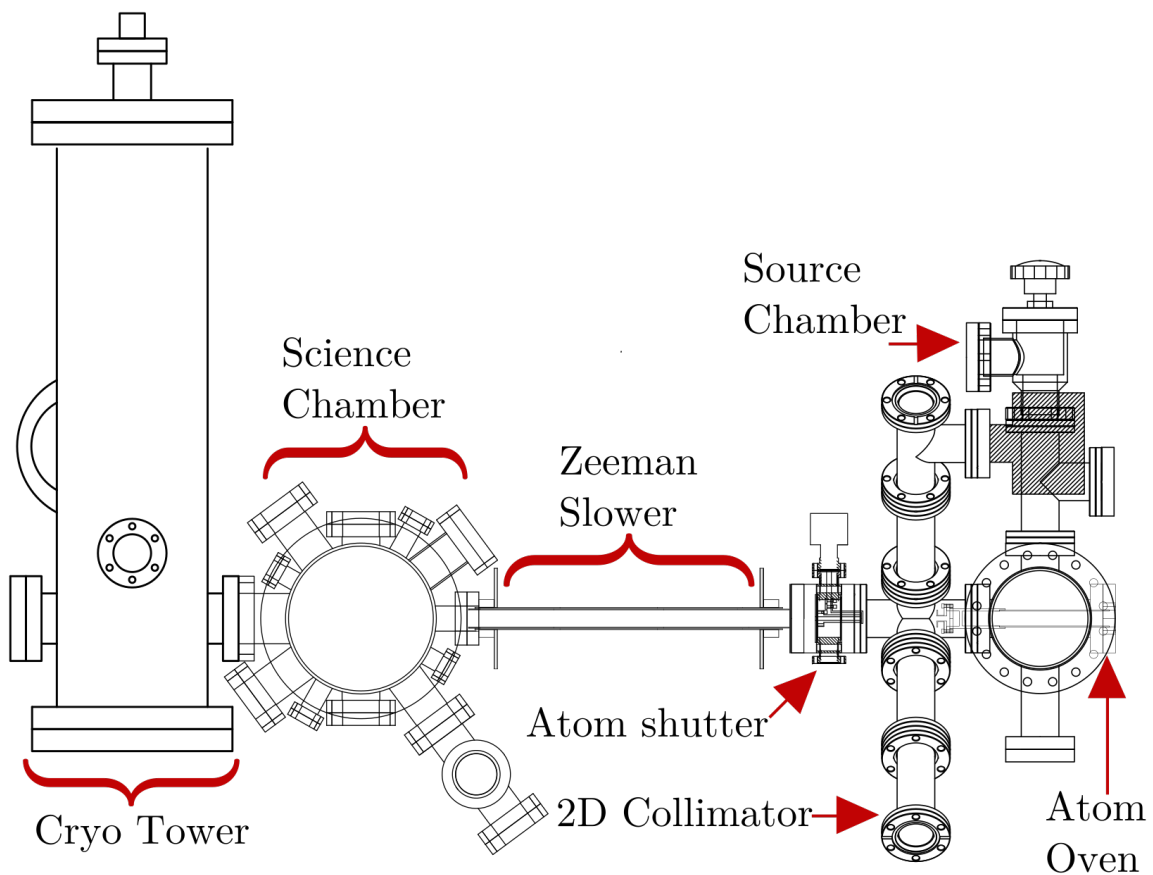


Figure 2.1 : Neutral apparatus vacuum system

Some components are rotated to provide easier identification.

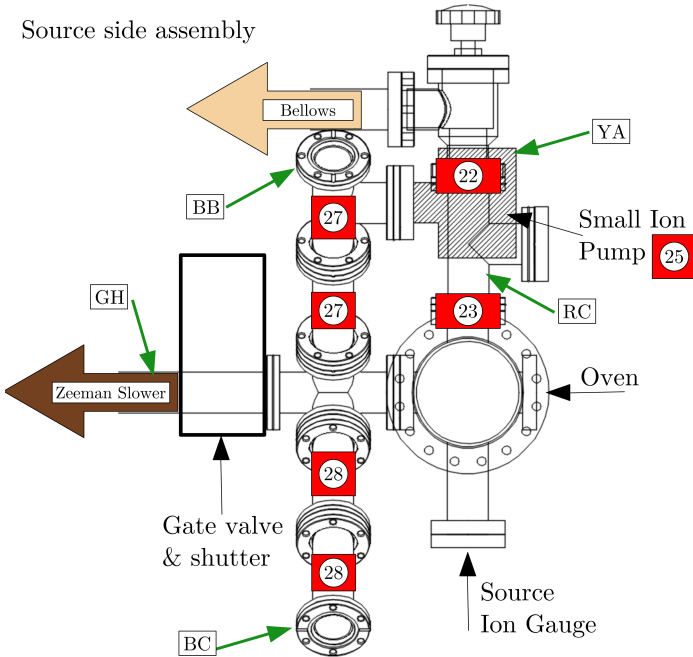


Figure 2.2 : Source assembly - side view

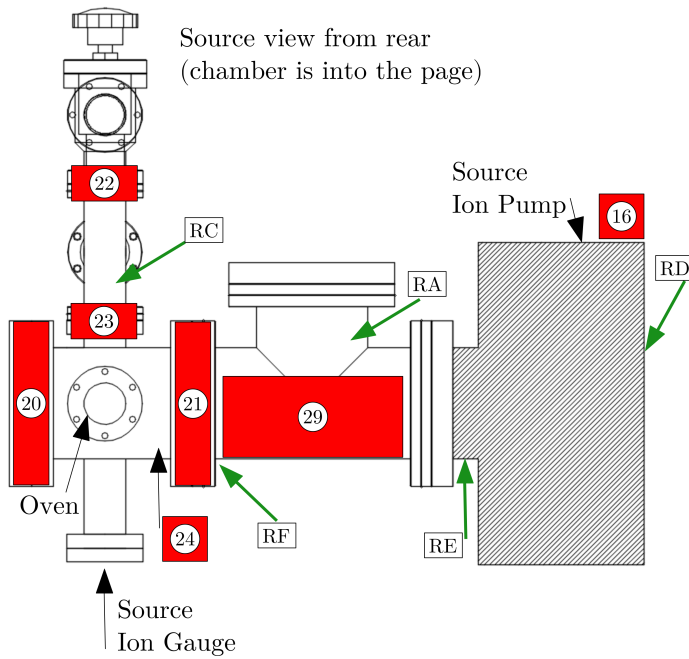


Figure 2.3 : Source assembly - rear view

2D Collimator view from rear
(source is out of page and chamber is into page)

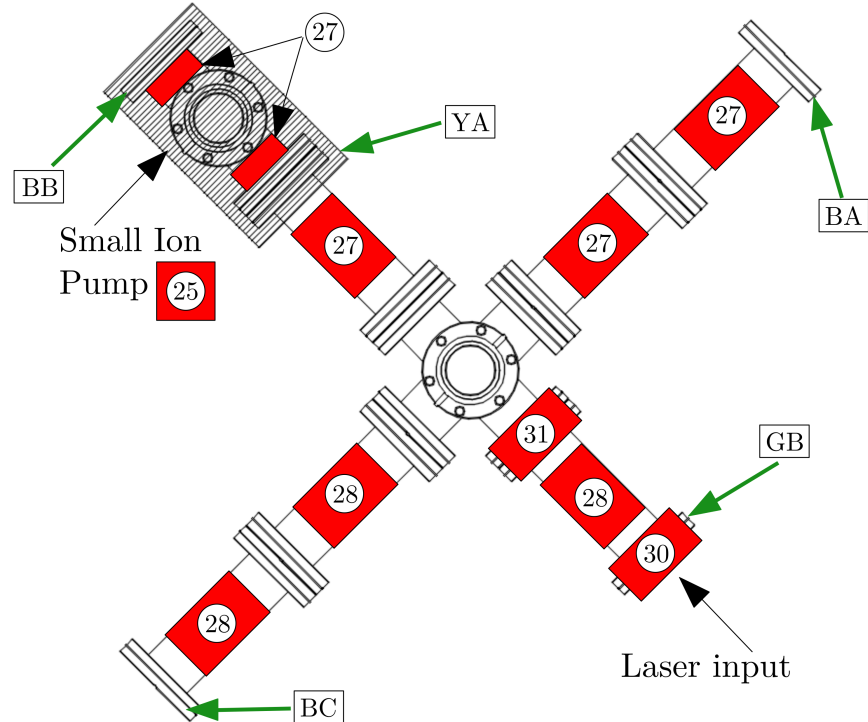


Figure 2.4 : 2D collimator assembly

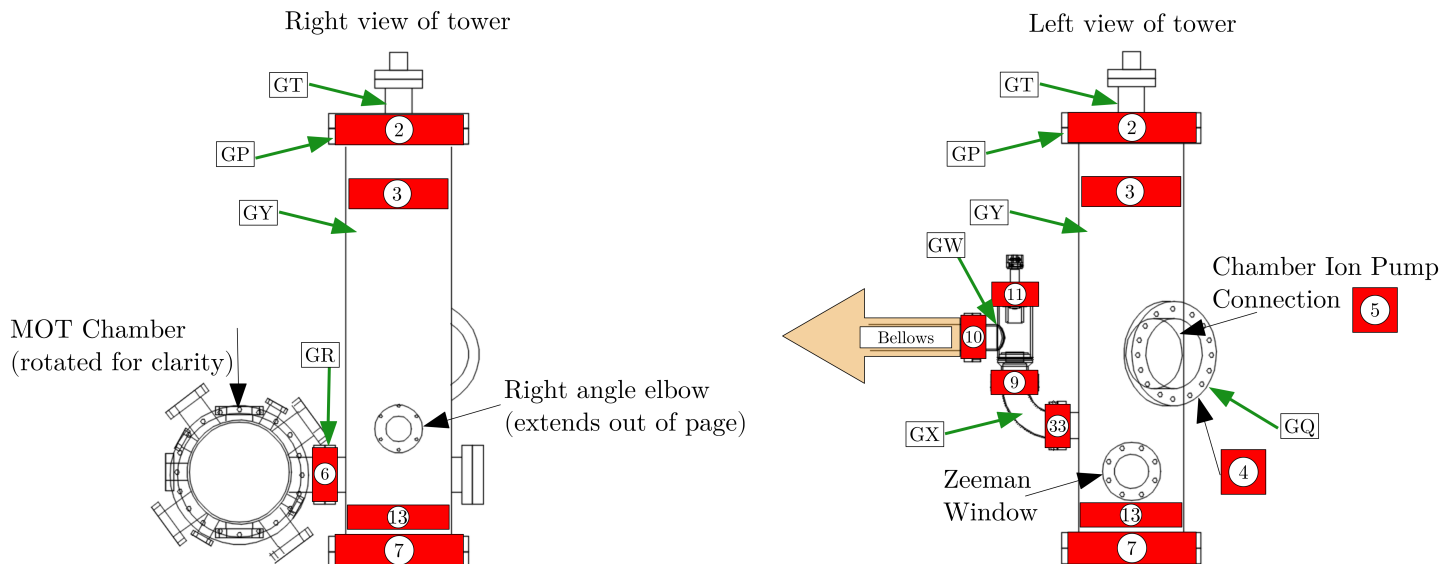


Figure 2.5 : Cryo tower assembly

Zeeman laser. It is worth explicitly noting that this Zeeman window is necessarily directly opposite the atomic source and therefore is subject to a flux of hot atomic strontium which will eventually coat the vacuum side. A brief note on a possible solution to this problem is explored at the end of this section.

While the source and science chamber have remained largely unchanged since the publication of Natali de Escobar's thesis, several key improvements and events have occurred over the last few years*. The original drawings of these components can be found in App. A.10 of [117] along with detailed information on the window coatings.

Recent changes

Addition of platform: While exploring routes to produce quantum degenerate gases of strontium, it was determined that different geometries of traps were necessary to achieve efficient forced evaporation. The task of redesigning the optical dipole traps was undertaken by Ying Huang and is detailed in her master's thesis [86]. As part of this project, a raised platform was designed and built around the chamber to facilitate beam shaping and launching of the ODT laser. Details of the platform are available in the main apparatus CAD drawing.

The raised platform has become the primary method for directing lasers into the chamber including the 1064 nm bulk optical dipole trap and the 532 nm optical lattice, both of which are outlined below. During installation of the free space optical lattice we observed heating and hypothesized that relative movement of the platform and

*As of April 2019, the most up to date CAD drawing for the Neutral apparatus is located at KillianDrobo:\Neutral\Laboratory Systems\Vacuum Chamber\Neutral Chamber\2017.12.26_strontiumvacuum35_latticetable.dwg. Additionally, please consult the README file located in this folder for further information.

chamber may be a cause. Supporting struts were then added beneath the chamber in an attempt to secure it to the platform around 2016. However, the extreme sensitivity of cold atoms and occasional observation of shot to shot fluctuations persisted.

We observed increased stability with the addition of a partial cover over the platform optics for the optical dipole and lattice traps. Initially meant as an optical safety measure for enclosing the high power beams, the cover led to a marked decrease in shot to shot fluctuations of the cloud position after a time of flight. With further testing we were able to attribute the increased stability to a mitigation of air currents caused by close proximity of the platform optics to the ventilation system meant to reduce dust accumulation inside the experimental enclosure.

Running out of strontium: In the winter of 2017 the neutral apparatus had been under vacuum for \sim 8 years when abruptly we were no longer able to trap a significant number of atoms [†]. After extensive testing, we hypothesized that we had run out of elemental strontium within the atomic source. This led us to break vacuum, reload strontium, and perform a light bakeout procedure to reestablish the requisite ultrahigh vacuum for experiments. Details of this bakeout procedure can be found in App. E. Through this process we confirmed our hypothesis that lack of strontium was the cause of the issue. Figure 2.6 shows the atom beam fluorescence after refilling the oven. This image was taken while using the Zeeman laser to cause photon scattering and looking down the 2D collimator. Prior to this event the Neutral apparatus enjoyed lifetimes of approximately 25 s as measured by background lifetimes measurements within the IR optical dipole trap. Approximately a year after restoring vacuum we

[†]It is was expected any trapping loss due to low strontium would be gradual and we were not able to determine the cause of the sudden behavior.

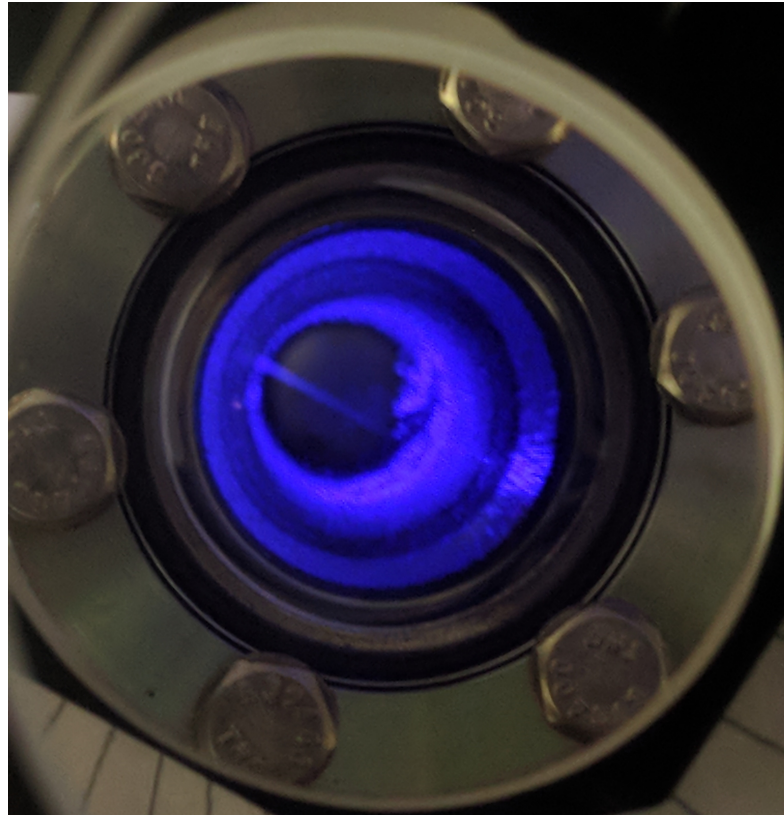


Figure 2.6 : Typical fluorescence of Zeeman beam looking down 2D collimator
This view is found using a 2 in mirror aligned along the path of the first pass of the 2D collimator and looking down the collimator tube. While looking at this angle, we are able to see the Zeeman beam move across the atom column when moving the last turning mirror. Reduction in this fluorescence signal from that shown was the primary indicator of lack of strontium in the source.

have measured lifetimes on the order of 15 s.

Finally, after removing the atom oven to replace strontium, we placed a temporary viewport to facilitate alignment of the Zeeman beam through the length of the vacuum system. While aligning we observed an unexpected partial occlusion of the Zeeman beam and upon further investigation learned that the differential pumping tube is noticeably not parallel to the atom trajectory. We were not able to determine the severity of the misalignment since the tube is not easily accessible and replacement is problematic as the tube is attached to a copper gasket held between flanges connecting the atom source chamber and the 6-way tee of the 2D collimator. The main readily measurable symptom is the occlusion of the Zeeman beam, which with an input power of ~ 120 mW before expansion optics and entering the chamber, only measures ~ 60 mW of transmitted power through the length of the vacuum system. However, full repair of the tube would necessitate a drastic and practically infeasible deconstruction of the vacuum system.

Clarifications from Natali de Escobar's thesis

HV version 1 & 2: As a point of clarification, Natali de Escobar's thesis [117] presents two versions of the HV chamber in figures A.42 - A.47 while referencing that the original construction proceeded with version 1. However, version 2 (the cryo tower) was installed around 2011 and is currently in use. Version 2 is shown in Fig. 2.5 and details are available in the apparatus CAD drawing.

Collimating array in nozzle: Natali de Escobar's thesis refers to the installation of an improved nozzle design incorporating an array of collimating tubes constructed from $2\ \mu\text{m}$ hypodermic needles. Modeling and construction of this design was

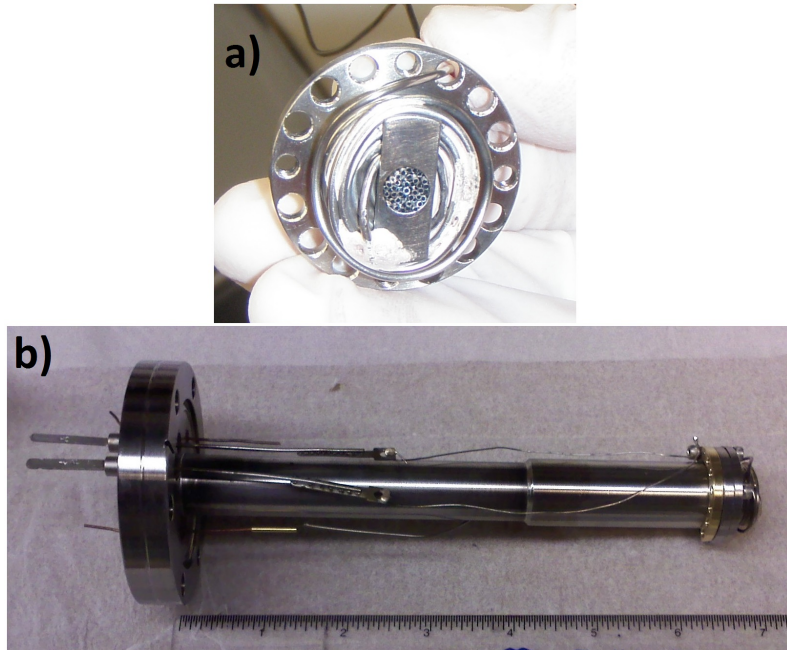


Figure 2.7 : Atom oven and nozzle construction

- a) The nozzle through which vaporized strontium enters the experiment. Here we see the array of collimating tubes behind which solid strontium is packed.
- b) The complete oven construction which houses the cartridge heater and the nozzle at the tip.

done by Anton Mazurenko, [119], with the goal of improving the angular discrimination of the oven assembly to produce a better collimated beam of atoms. Figure 2.7 shows the improved nozzle design [‡]. The original assembly of this oven also incorporated a heat shield that would insert over the construction shown in Fig. 2.7b but this shield is not currently installed on the source oven.

[‡]For reference, this nozzle design is labeled "new nozzle summer 2010" in the apparatus CAD file to distinguish it from the other nozzle drawings also present.

2.3 Laser systems

The heart of any atomic physics experiment is the laser systems which form the basis for laser cooling and various probes. Our lab has transitioned to primarily using diode laser system and relies heavily upon the use of injection locked master - slave setups. Below we will outline the specifics of our light generation setups.

2.3.1 Wideband cooling stage: 461 nm

2.3.1.1 Overview

As discussed in the experimental overview, the majority of our laser cooling is done using 461 nm light. We generate and control these photons by amplifying and frequency doubling 922 nm light from a master ECDL diode laser. Fig. 2.8 shows an overview of how we generate and use the 461 nm light. We will explore each of these sections in detail below, with emphasis on the MOT subsystem since it is the basis for many different components of the overall 461 generation.

In conjunction with the block diagram, Table 2.5 shows the details of the frequency shifts and AOM details. The position of these AOMs is represented by the numbered grey squares, while the labeled red squares define the system frequencies at various points along the system. The primary frequency relations for trapping and imaging are schematically represented in the lower portion of Fig. 2.8 and are determined via Eq. 2.1. Table 2.5 defines the shift variables used in these equations.

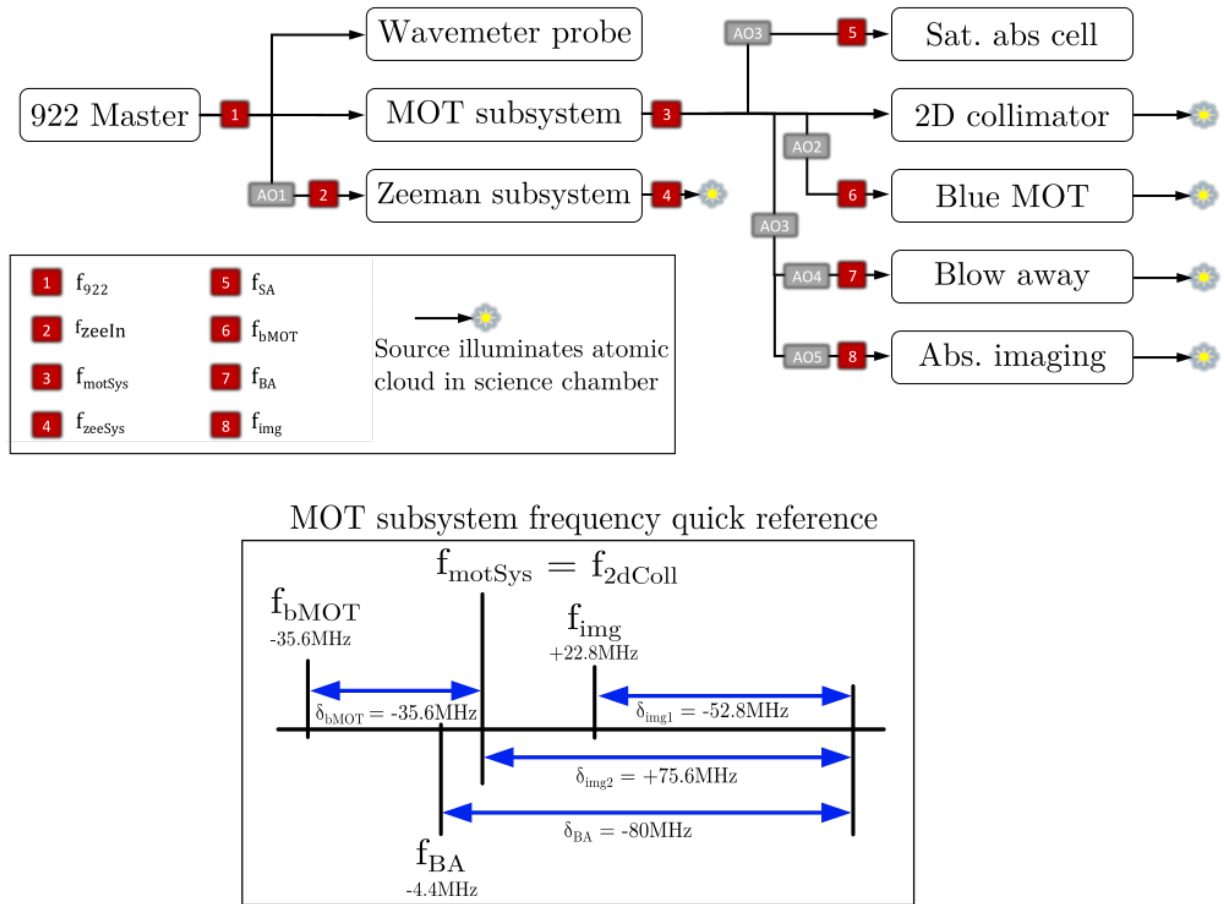


Figure 2.8 : 461 nm light generation system

Top - Block schematic showing the relations of the various systems, AOMs, and frequencies used to lock the system for 461 nm trapping and spectroscopy. Sat. abs. refers to the saturated absorption cell and abs. imaging refers to the absorption imaging system. See Table 2.5 for information on the AOMs. Bottom - Relative frequencies of the MOT subsystem at various stages of the 461 system. Frequencies are quoted with respect to f_{motSys} which in turn is controlled via the tunable saturated absorption cell to address different isotopes.

Label	Ind.	System	Shift variable	Nominal Freq. [MHz]	Freq. Source	Freq. control	AOM Model
Zeeman	AO1	922 master	δ_{zeeman}	-252.4	Mini Circuits ZOS-300	Static voltage	Crystal Tech. 3200-1113
Blue MOT	AO2	MOT	δ_{bMOT}	-35.5	Mini Circuits ZOS-50	Static voltage	IntraAction AOM-402A1
Image 2	AO3	Abs. imaging & Blow away	δ_{img2}	+75.6	Mini Circuits ZOS-75+	Static voltage	IntraAction ATM-1001A1
Image 1	AO4	Abs. imaging	δ_{img1}	-52.8	Mini Circuits ZOS-150	Static voltage	IntraAction AOM-602A1
Blow away pulser	AO5	Blow away	δ_{BA}	-80	IntraAction ME-801T7	Internal synth.	IntraAction ATM-802DA1
Sat. abs. shifter	AO6	Sat. abs	δ_{SA}	+317.3	Mini Circuits ZOS-400+	Static voltage	Crystal Tech. 3200-141

Table 2.5 : 461 nm system AOM details

The second column labels the AOMs as in Fig.2.8. The sign of the nominal frequency indicates the AOM order used.

$$\begin{aligned}
f_{\text{motSys}} &= 2f_{922} & f_{\text{zeeSys}} &= 2(f_{922} + \delta_{\text{zeeman}}) \\
f_{\text{2dColl}} &= f_{\text{motSys}} & f_{\text{bMOT}} &= f_{\text{motSys}} + \delta_{\text{bMOT}} \\
f_{\text{img}} &= f_{\text{motSys}} + \delta_{\text{img2}} + \delta_{\text{img1}} & f_{\text{SA}} &= f_{\text{motSys}} + \delta_{\text{SA}} \\
f_{\text{BA}} &= f_{\text{motSys}} + \delta_{\text{img2}} + \delta_{\text{BA}}
\end{aligned} \tag{2.1}$$

Overall frequency control, f_{922} , is determined via the magnetically tunable saturated absorption cell. The use of magnetic tunability to control the 461 nm light frequency is well documented in section 2.2.1 of Natali de Escobar's thesis [117] and section 2.1.1 of Pascal Mickelson's thesis [128]. A more recent undergraduate project also explored optimizations of this scheme for the Rydberg apparatus [126].

2.3.1.2 922 nm master

The master 922 laser is derived from a Sacher Lynx 922 nm IR diode laser in a Littrow ECDL configuration. Fig. 2.9*, shows a simplified optical schematic of the master setup.

Starting at the master output, the beam is shaped and sent through two optical isolators before it is coupled into an optical fiber. The fiber output immediately goes through an AOM which detunes the diffracted order by approximately 250 MHz. The diffracted and zeroth order are then separated with the unshifted beam sent towards the MOT generation subsystem and the shifted light towards the Zeeman subsystem. We find it necessary to include dual isolators in front of the master laser and have

*This figure, and related optical schematics throughout this thesis, were created using the ComponentLibrary software, which is licensed under the Creative Commons Attribution-NonCommercial 3.0 Unported License [61].

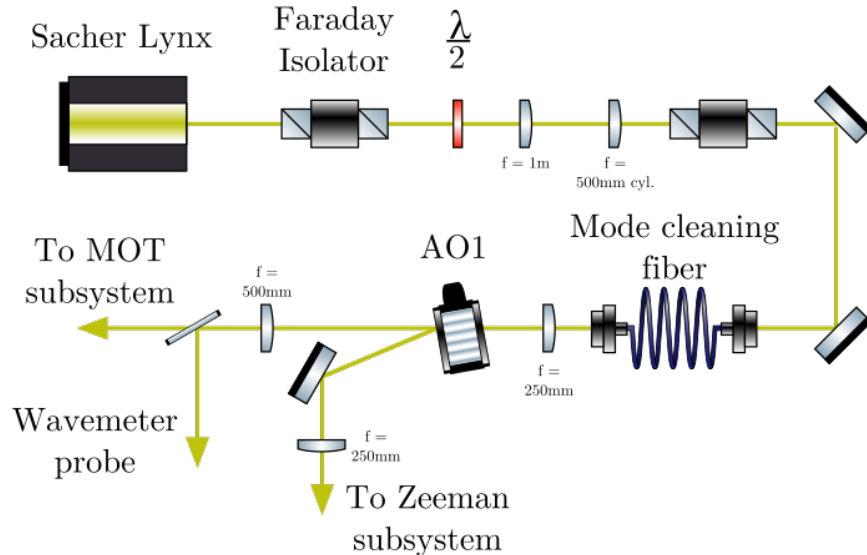


Figure 2.9 : 922 nm master optical schematic

found that inadequate alignment of these isolators can lead to significant instability in the frequency of the master, which in turn may lead the doubling cavities to be unable to maintain a lock.

Fig. 2.10 shows a simplified schematic of the negative feedback path for stabilizing the length of the doubling cavities. Light out of the 922 master has sidebands added via a high bandwidth AC coupled current modulation directly to the laser diode [†]. The doubling cavities of the MOT and Zeeman subsystems are length stabilized via these sidebands using the Pound-Drever-Hall (PDH) technique [51]. Currently, the reference oscillator RF source is a PTS 160 from Programmed Test Sources with an output power of 12 dbm and frequency of 39.55 MHz. This RF is sent to a 3-way

[†]This direct coupling means the RF must be turned on prior to enabling the DC current. Conversely, the DC current should be disabled before turning off the RF source. Failure to follow this order may result in destruction of the laser diode.

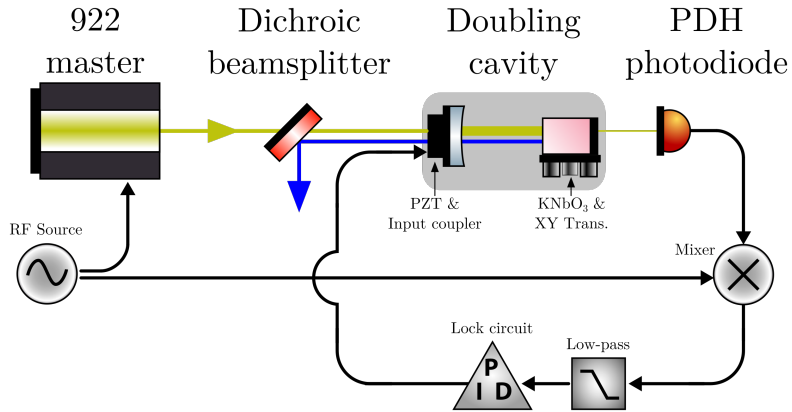


Figure 2.10 : 922 nm doubling cavity length stabilization feedback diagram

power splitter which sends roughly a third of the power ($\sim 4 \text{ dbm}$) to each of the MOT and Zeeman PDH mixers for demodulation. The remaining third is attenuated by 3 db before coupling directly to the laser diode.

Once 461 nm light is available, we stabilize the frequency of the 922 nm master using light from the MOT subsystem to interrogate a strontium heat pipe via frequency modulated Doppler-free saturated absorption from which an error signal of the $^1S_0 \rightarrow ^1P_1$ transition is derived. As shown in Fig. 2.11, this error signal is sent into a homemade integrator circuit with a fast feedback path controlling the 922 nm diode current and a super low-bandwidth[‡] path controlling for long term frequency drifts via the ECDL's internal PZT. We found that addition of this super low-bandwidth lock has significantly improved the continuous lock time of the 461 system. When enabled, the experiment may stay locked for upwards of 24 hours at a time. Additional details on the original construction of the 922 nm system can be found in App. A.8 of

[‡]This super low-bandwidth lock is based on an Arduino PID controller with a long time constant and was built by Josh Hill. We refer the interested reader to Josh's forthcoming thesis for details of this general purpose slow lock.

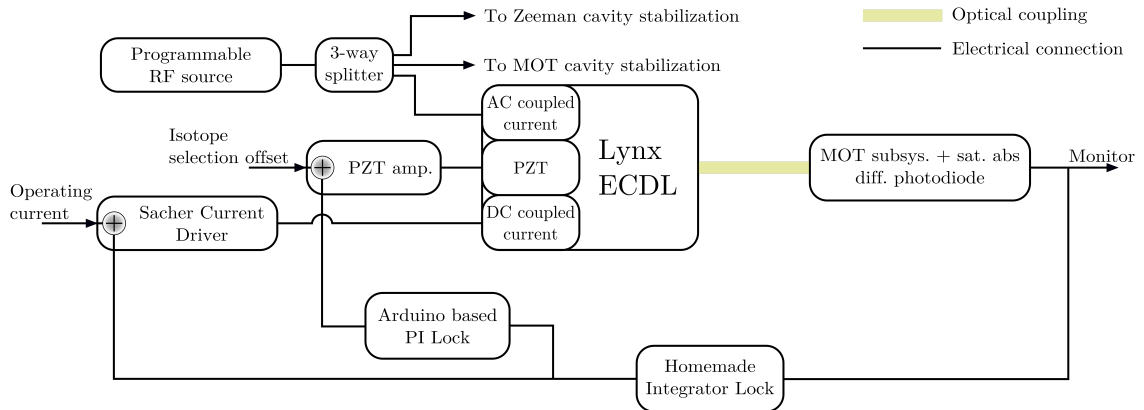


Figure 2.11 : 922 nm frequency stabilization block diagram

Multiple feedback paths allow for controlling the 922 master across disparate timescales. Note that the generation of the error signal used in the feedback is optically connected to the 922 master via the MOT subsystem and saturated absorption cell discussed in Sec. 2.3.1.4.

Natali de Escobar's thesis [117].

Historical notes and tips for usage

PZT driver and replacement: The PZT driver provided by Sacher has become problematic over the last few years. When varying the voltage we would occasionally hear a "clicking" noise from the Lynx laser as if the voltage was abruptly changing. We began using a Thorlabs analog PZT driver (model: MDT694A) and no longer observe this behavior[§].

[§]We attempted to use the newer Thorlabs MDT694B which incorporates a digital potentiometer instead of the analog pot of the "A" model. However, we found the resolution of the digitization caused the laser frequency to jump and we were unable to maintain the frequency lock.

In early 2017, we found that the Lynx PZT was no longer responding to applied voltage. We believe this was caused by the afore mentioned "clicking" issue and was the motivation for changing PZT drivers. Details and pictures of the PZT replacement are available in App. D.

Sacher temperature setpoint: Care must be taken when attempting to change the set temperature of the laser diode as the internal potentiometer does not maintain full contact such that when attempting to turn it ever so slightly, the set point temperature may jump from ~ 16 °C to 11 °C . Worse yet, we have observed that after changing the temperature there is a settling time during which the temperature setpoint may change while not be monitored. For these reasons we generally avoid touching this control as the present setpoint of 16.1 °C is adequate and no major improvements have been found when changing this temperature.

Daily alignment: The input coupler for the 922 cleanup fiber is not a reliable mount and tends to drift significantly from day-to-day. Therefore, we find it necessary to regularly peak up the alignment into this fiber and typically achieve a coupling efficiency of $\sim 51\%$ through the 922 mode cleaning fiber.

2.3.1.3 Zeeman subsystem

The Zeeman subsystem is a dedicated TA + doubling cavity for 461 nm light exclusively used for the one-dimensional Zeeman cooling stage. The original construction details are available in App A.8 of Natali de Escobar's thesis [117]. Figure 2.12 shows a simplified optical schematic of this system. Light from the 922 master (~ 20 mW) is shaped and coupled into a tapered amplifier to produce nearly 300 mW of 922 nm light. After being shaped further and passed through dual isolators, the light is then

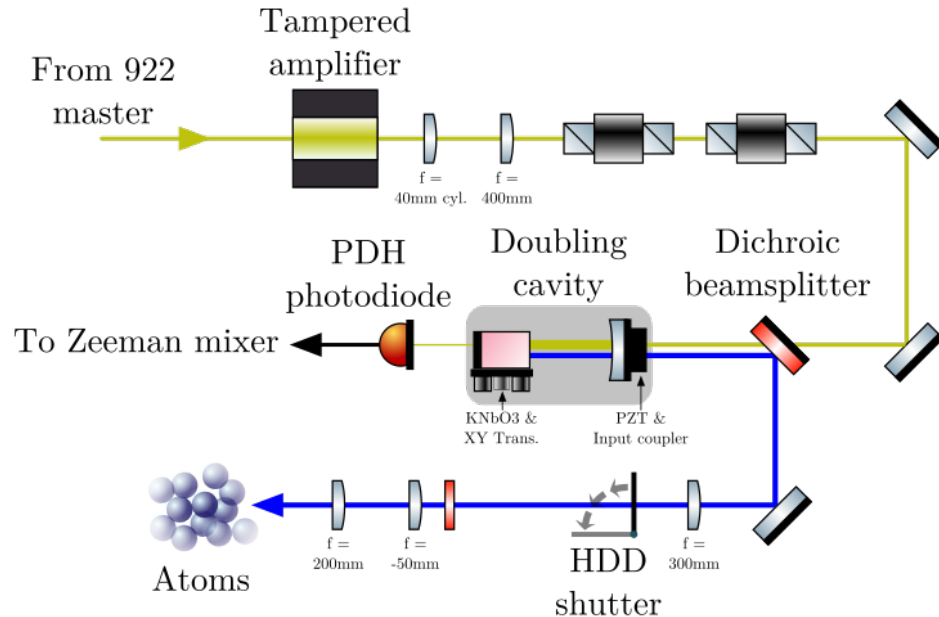


Figure 2.12 : Zeeman subsystem optical schematic

coupled into the homemade doubling cavity where a potassium niobate crystal is held within an optical resonance cavity to produce the 461 nm light. For approximately 300 mW into the cavity we are able to produce \sim 125 mW of 461 nm light. This light is sent through a final beam expander and into the chamber where we have designed the system to focus the Zeeman beam just at the tip of the atom nozzle to maximize the spatial and temporal interaction between hot atoms and the Zeeman beam.

Historical notes and tips for usage

Mode instability: Doubling cavities at short wavelengths are known to be mercurial [166] so stabilizing them can be difficult. We find that this cavity tends to become stable with \sim 300 mW of input power but increasing the power results in an initial cavity lock producing more 461 nm light but which quickly mode releases into

a lower power mode. While we have seen cavity output powers of up to 150+ mW, these are not stable modes. Additionally, the locking circuit contains an auto re-lock feature that can occasionally result in locking to a lower power mode, usually around ~ 80 mW. We have found that power cycling the TA current driver is the least intrusive and quickest method to reattain the 125 mW output. If cycling does not work, then the TA current output may need to be adjusted or the cavity alignment tweaked.

2.3.1.4 MOT subsystem

The MOT path generates light used for a multitude of processes as shown in Fig. 2.8. Here we detail the systems required for laser cooling and trapping, leaving the details of the blow away pulser and absorption imaging to be discussed in Sec. 2.3.4. Furthermore, we begin our discussion with a focus on the light generation of the MOT subsystem and next we will explore the child setups derived from this subsystem.

Fig. 2.13 shows a simplified optical schematic of the MOT subsystem which is modeled after the Zeeman setup described previously. Light from the 922 nm is shaped, amplified, and coupled into the doubling cavity where the same feedback mechanism shown in Fig. 2.10 is used to stabilize the cavity length. Since the MOT system is situated close to the experimental chamber, a "black-house" wall and shroud were constructed to minimize stray reflections (not shown in figure). This enclosure was placed around the MOT subsystem to mitigate stray 461 nm light which can significantly hinder the achievement of quantum degenerate strontium gases[¶]. Part of this enclosure is a fast (~ 2 ms) shutter (model: Uniblitz CS45) used to block the

[¶]Even stray reflected light off the glossy ceiling of the experimental enclosure has been found to cause atom heating!

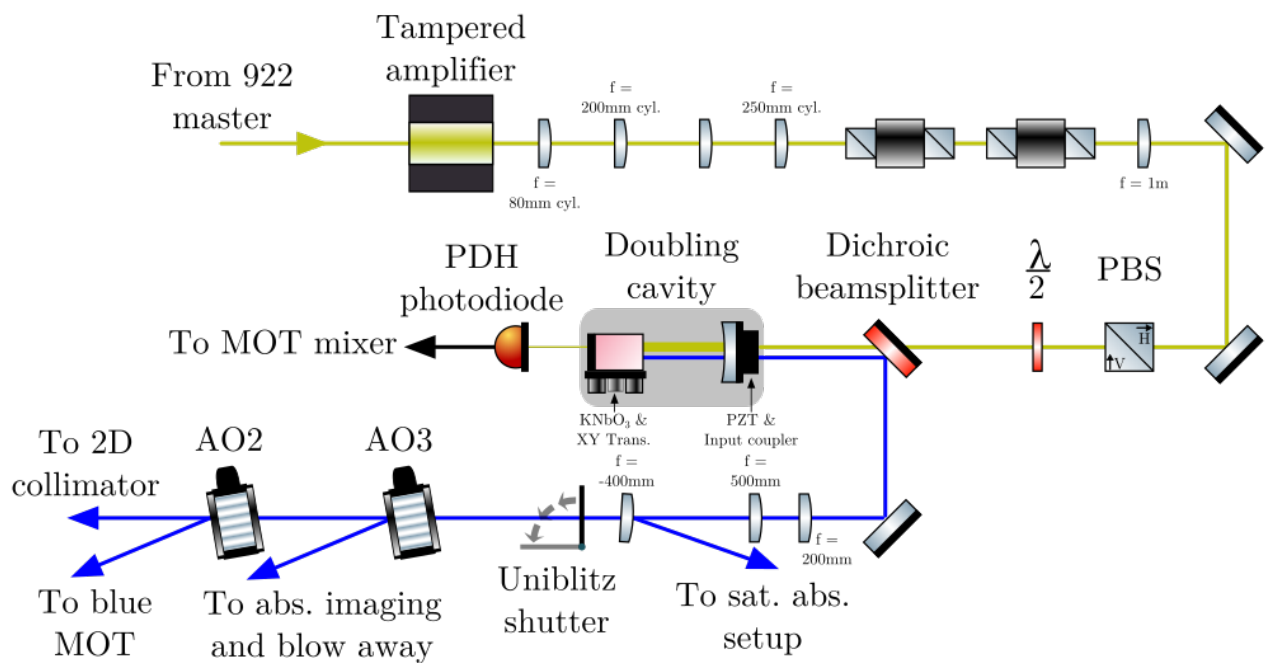


Figure 2.13 : MOT subsystem optical schematic

Note the sharing of power between the 2D collimator and blue MOT paths. While the blue MOT is power stabilized as shown in Fig. 2.14 the 2D collimator utilizes the remaining laser power.

461 nm light during the red MOT and evaporation stages. Additional hard drive (HDD) shutters are also placed along the MOT path behind the black-house shutter as leakage light through the blue MOT AOM (AO2) was seen to cause additional heating when utilizing the blow away pulser.

One concern we face with this MOT setup is the coupling of power between the various paths. Typically we do not operate the imaging & blow away pulser while trapping so all available power from the doubling cavity is available for these processes. However, the 2D collimator and 461 nm MOT operate concurrently during the first stages of trapping, thus the available laser power must be split between these two systems.

461 nm MOT

Fig. 2.14 gives an overview of the 461 nm MOT optics^{||}. Separation of the laser beams is performed on the table level where custom dichroics are used to combine the 461 and 689 MOT paths. Following the dichroics, the MOT beams are directed up to the platform layer via periscopes and subsequently pass through dual wavelength waveplates which retard 461 nm light by three-quarters of a period and 689 nm by one-quarter. This setup allows us to maintain well defined polarization along the MOT paths.

Saturated absorption

The saturated absorption cell is used to interrogate the $^1S_0 \rightarrow ^1P_1$ transition to lock the frequency of the 922 master. App. C outlines a brief derivation for determining

^{||}The MOT arms are labeled as they are organized on the table, where Arm B is closest to the "computer side" of the table.

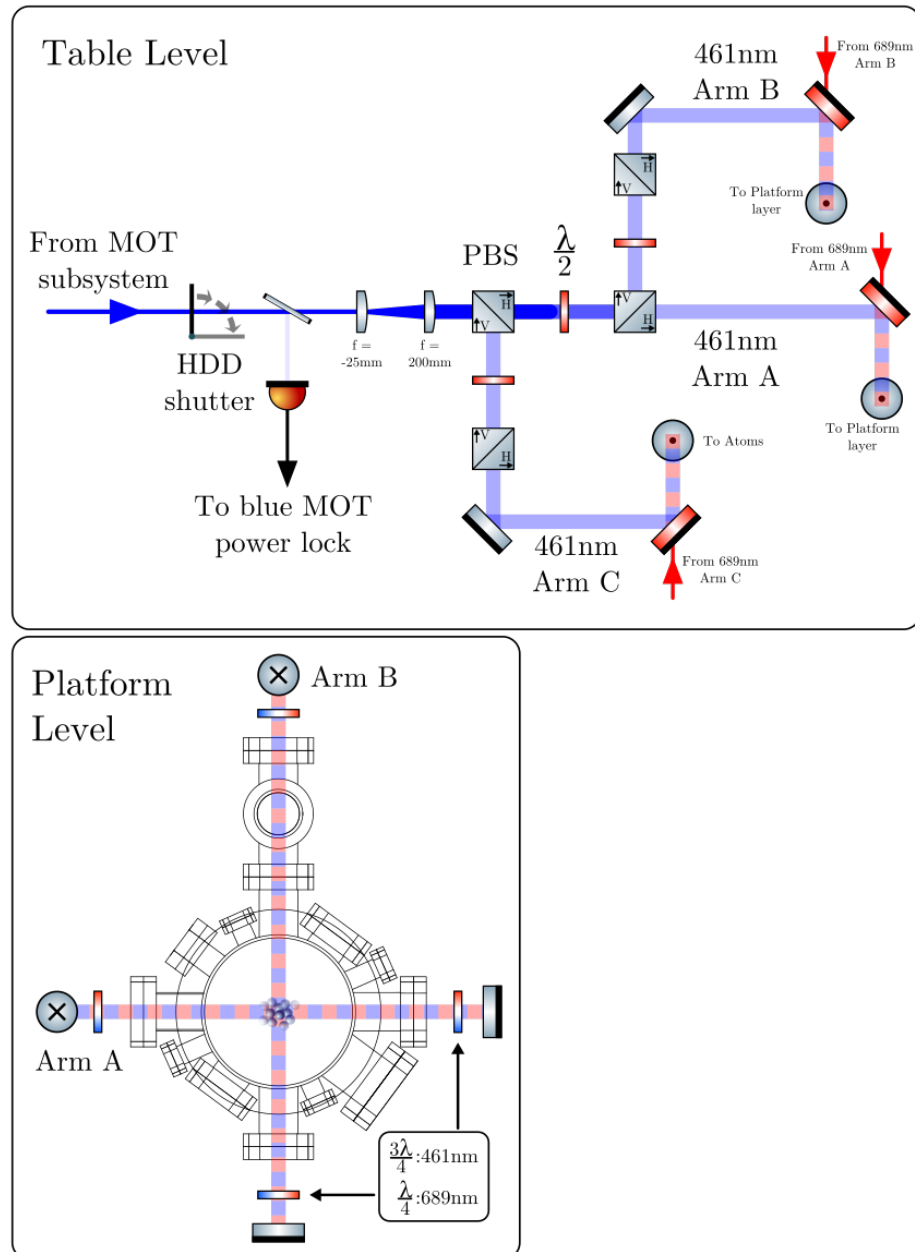


Figure 2.14 : 461 nm MOT schematic

Typical MOT setup with an additional HDD shutter to mitigate light leakage from AO2. Transparency of the laser beams represents the intensity. Note the 461 nm and 689 nm light follow the same path through the science chamber. Custom waveplates acting on both wavelengths are used to provide the appropriate polarization.

the lock point when a constant offset is added to the laser frequency, as is the case here. As outlined in the derivation, by utilizing the Zeeman tunability of magnetic sublevels, we can shift the resonance frequency of the atoms in the heat pipe. Thus, by interrogating and locking to the transition frequency of the most abundant isotope, ^{88}Sr , we can shift its resonance to cover the isotope shifts of the other strontium isotopes. This provides a simple method for trapping various isotopes and mixtures of strontium.

A detailed walkthrough of the construction and relevant physics of a blue saturated absorption cell can be found in the undergraduate report of Michael Viray [126]. Additionally, the original construction of the Neutral cell is covered in section 2.2.1 of Natali de Escobar's thesis. Fig. 2.15 shows the optical setup used to generate the error signal and reference traces of Doppler bowl and frequency lock error signal. This error signal is generated by frequency modulating the magnetic field of the cell and performing Doppler-free saturated absorption.

Historical notes and tips for usage

Daily alignment of MOT TA: The simplified optical schematic of the MOT subsystem in Fig. 2.13, does not reflect the approximately two meter lever arm which is present between the Zeeman split AOM and the input to the MOT TA due to the relative positions of the cavities. We have found this requires us to peak up the alignment of the 922 master beam into the MOT TA on a daily basis and is hypothesized to be the cause of large long time power variations ($\sim 15\%$) on the output power of the MOT cavity which we observe throughout the course of the day. Typically with an input power of $\sim 300 \text{ mW}$ of 922 nm light we get between 100 - 115 mW out on a daily basis.

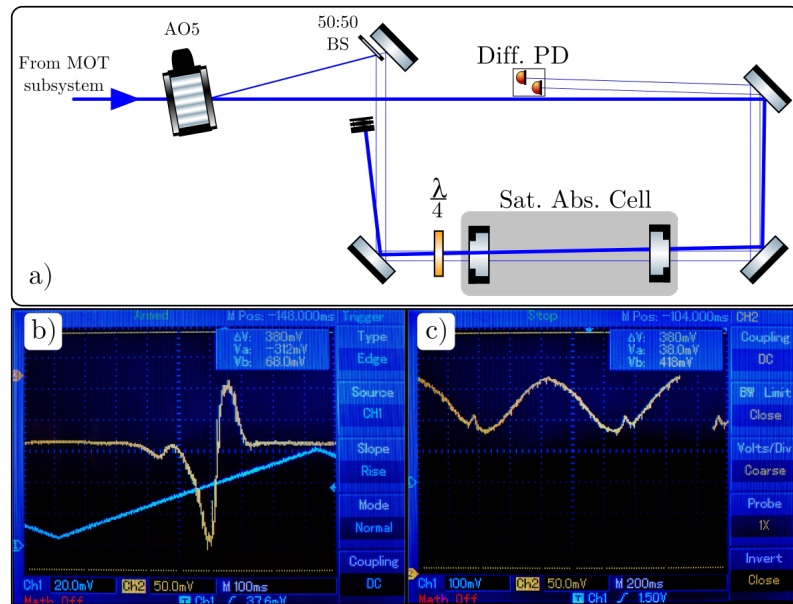


Figure 2.15 : 461 nm saturated absorption setup

a) Optical setup for frequency locking the 922 nm master. b) Example error signal. The cause of the asymmetry is unknown but occurs around approximately $\pm 1.7\text{A}$ drive. The offset seen here can be nulled by balancing the amplification applied to the differential photodiode inputs. c) Example of the Doppler bowl where the Lamb dip can be seen. Note that the Lamb dip interacts with a specific velocity class determined by δ_{SA} .

Note on changing isotopes: While the basic setup of the saturated absorption cell has not changed over the many years, we have recently moved away from the original current source based on a home built high-current FET amplifier to a Bi-polar current source (BOP) (model: Kepco BOP-20-10DL). This change allows for more expansive coverage of the $^1S_0 \rightarrow ^1P_1$ isotopes shifts. The previous current source limited our dual trapping capability to 87+88, and required an AOM to be tweaked and the saturated absorption cell to be realigned for trapping 84 and 86. Using the BOP, we can now easily shift the transition frequency over ~ 200 MHz which allows us to span the range between 84 and 87 within a single experimental cycle. Given the geometry of our solenoid, large currents are required to apply such large Zeeman shifts. We have observed that these large currents increase the heat load on the cell, which can lead to a reduction in the error signal. We mitigate this additional heating by varying the heater current to maintain approximately 50% absorption of the pump beam. As we expect, the timescale for these effects are minutes, so short term variations (i.e. when doing spectroscopy) do not cause significant heating when the duty cycle is kept low.

Due to the heating from the Zeeman coil, we chose to balance the currents needed to trap 84 and 87 by "centering" the pump-probe beams frequency such that the magnitude of the currents needed for both isotopes is similar, but with 84 requiring a (+) current and 87 a (-) current. However, trapping of 88 still requires the realignment of the saturated absorption cell pump-probe beams as this shift is just beyond the capabilities of the current drive. Care should be taken when adjusting this alignment as the paths are highly coupled as can be seen in Fig. 2.15a.

2.3.2 Narrowband cooling stage: 689 nm

2.3.2.1 Overview

Arguably the most important transition for strontium is the $^1S_0 \rightarrow ^3P_1$ intercombination line transition at 689 nm. In addition to cooling and trapping, most experiments performed in our lab utilize this transition as the primary spectroscopic probe owing to the long lifetime of the excited states. This allows for high precision measurements and large detunings using conventional techniques. This section describes the generation and trapping setups in use on the Neutral apparatus. The primary spectroscopy probe system and spin manipulation setup are outlined in section 2.3.4.

Recently, the 689 nm generation system has seen significant growth and undergone a complete restructuring. For notes on the original Neutral setup refer to App A.3 & A.4 in Natali de Escobar's thesis. Most notably, the master laser system is now shared between multiple laboratories including the Rydberg apparatus, the Dunning lab, and the Neutral apparatus. This setup has required a modular approach to the master 689 nm system to ensure independence of the various lab activities.

Fig. 2.16 shows a block diagram outlining the relationships between the master laser setup and various Neutral systems which utilize this stable light source. In conjunction with the block diagram, Table 2.6 details the frequency shifts and AOMs in use. The block diagram denotes the position of AOMs by the grey squares and the red squares denote system frequencies determined by the various shifts. Lastly, the frequency axis beneath the block diagram illustrates the relative frequencies at various points of the complete red system specified with respect to the $^{88}\text{Sr} \ ^1S_0 \rightarrow ^3P_1$ transition and shown along with the isotope shifts of the same transition.

The versatility of the 689 nm transition is apparent from Fig. 2.16 but comes at

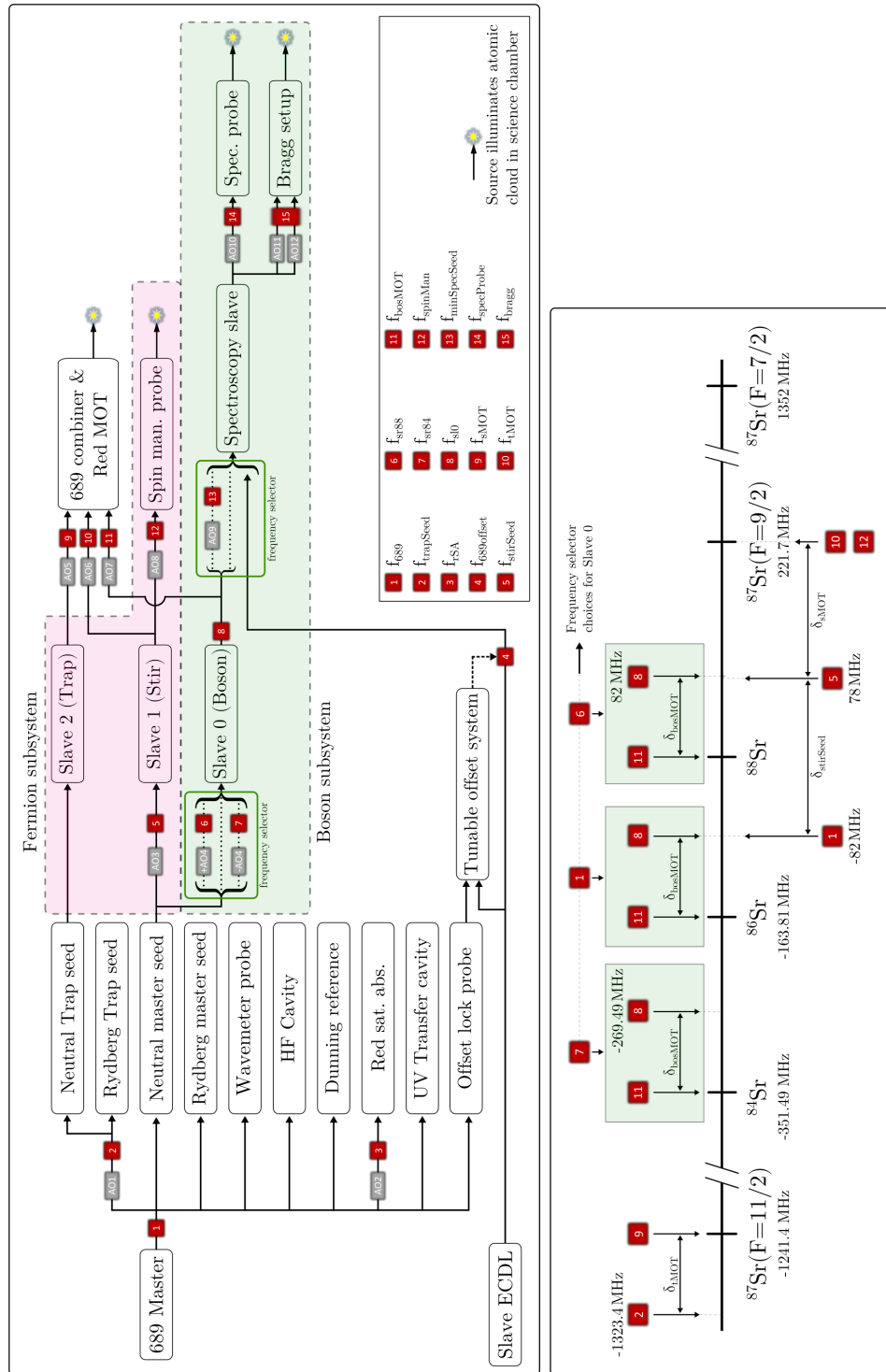


Figure 2.16 : 689 nm light generation system

Top - Block diagram showing various systems, AOMs, and the frequencies of red system. Table 2.6 gives further details on the AOMs. Bottom - Relevant isotopic shifts and system frequencies given relative to ^{88}Sr intercombination transition.

Label	Ind.	Shift variable	Nominal Freq. [MHz]	Freq. Source	AOM Model
Trap Seed	AO1	$\delta_{trapSeed}$	-1241.44	Novasource G6	Brimrose TEF-1300-200-550
Red Sat. Abs.	AO2	δ_{rSA}	+164±0.5	Novatech 409B (Dithered)	IntraAction ATM-1643DA1
Stir Seed	AO3	$\delta_{stirSeed}$	+160	Novatech 409B	IntraAction ATM-1602DA1
Boson isotope Selector	AO4	δ_{isoSel}	+164 or -187.49	Novatech 409B	IntraAction ATM-2001A2
Trap MOT	AO5	δ_{tMOT}	+82	Trap VCO / Novatech 409B	IntraAction ATM-852DA2
Stir MOT	AO6	δ_{sMOT}	+143.7	Stir VCO / Novatech 409B	IntraAction ATM-1402DA1
Boson MOT	AO7	δ_{bosMOT}	-82	Boson VCO / Novatech 409B	Isomet 1205C-2
Spin man. probe	AO8	$\delta_{spinProbe}$	-144±2	Novatech 409B	IntraAction ATM-1402DA1
Spec. slave seed	AO9	$\delta_{specSeed}$	-40	Novatech 409B	IntraAction AOM-402A1
Spec. probe	AO10	$\delta_{specProbe}$	-82±20	Novatech 409B	IntraAction ATM-902DA1
Bragg #1	AO11	δ_{bragg1}	90±20	Novatech 409B	Crystal Tech. 3110-125
Bragg #2	AO12	δ_{bragg2}		Novatech 409B	Crystal Tech. 3110-125

Table 2.6 : 689 nm system AOM details

Ind. labels the AOMs as shown in Fig. 2.16. The sign of the nominal freq. indicates the AOM order. The MOT AOMs are shown with two freq. sources which are used during the broadband red MOT and single frequency red MOT respectively.

the cost of increased complexity. Unlike the blue system, where the overall system frequency was determined by varying the master laser frequency, the red master is locked at a fixed frequency relative to the ^{88}Sr $^1S_0 \rightarrow ^3P_1$ transition. Nearly all frequency shifts are accomplished using AOMs driven with digital synthesizers such that each subsequent system derived from the master laser inherits the frequency stability and narrow linewidth of the master.

Fig. 2.16 also highlights the boson and fermion subsystems. These setups allow the Neutral apparatus to simultaneously trap and cool mixtures of a single bosonic isotope and fermionic strontium-87. The isotope selector AOM (A04) determines which bosonic isotope this system can trap. We denote the different frequencies available to injection lock slave 0 through the "frequency selector" box in the top part of the above figure. From each choice of input frequency, the output of slave 0 is also shown relative to other laser trapping frequencies and the isotope shifts of the $^1S_0 \rightarrow ^3P_1$ transitions.

2.3.2.2 689 nm Master

Our master 689 nm source is a Toptica DL-pro. This is a Littrow configuration ECDL which outputs ~ 30 mW of usable 689 nm light past its internal optical isolator. Fig. 2.17a shows how this power is distributed amongst the various subsystems and directed towards each laboratory. From the figure we see that the gigahertz AOM (AO1 is the first optic the light passes through since this AOM has a diffraction efficiency around $\sim 20\%$. The ~ 6 mW of shifted light is then split between the Neutral and Rydberg experiments where it is used to injection lock a dedicated slave diode used for the trapping MOT light needed for strontium-87.

Following the GHz AOM, a series of waveplates and PBS cubes are used to ap-

portion light to various fiber paths and laboratories. A beam sampler along the path directs light into a mode-cleaning fiber that outputs to the high-finesse cavity system and the remaining power ($\sim 2 \text{ mW}$) is sent to a long heat pipe in order to interrogate the intercombination line transition.

The moderate finesse cavity is used to narrow the laser linewidth using the Pound-Drever-Hall (PDH) technique. The cavity length is varied with a PZT to lock the laser frequency to the atomic transition via saturated absorption, as illustrated in Fig. 2.17b. The atomic error signal is generated using standard frequency modulated Doppler-free saturated absorption where frequency modulation is performed via fast switching ($\sim 11 \text{ kHz}$) of the RF drive frequency applied to AO2. The narrowing cavity is discussed in detail in Natali de Escobar's thesis and has remained unchanged since her publication**.

2.3.2.3 Neutral red system

The Neutral 689 nm system is composed of four slave diodes, which may be designated into the Boson and Fermion subsystems as illustrated in Fig. 2.18. Light from the 689 master system is transported to the Neutral apparatus via the master seed and trap seed fibers. These fiber outputs provide approximately 3 mW and 1 mW for the master and trap respectively. This light is used to seed slaves 0-2, with spectroscopy slave (or slave 3) injection locked from the slave 0 output. Each of the three MOT systems integrates an independent AOM which is used to provide dynamic intensity control and frequency offset & dithering during the 689 nm trapping and cooling stage. The gross detuning of these AOM's is fixed and specified in Table 2.6.

**As of April 2019, a ultra-low expansion cavity system is being implemented and tested to replace our homemade HF cavity.

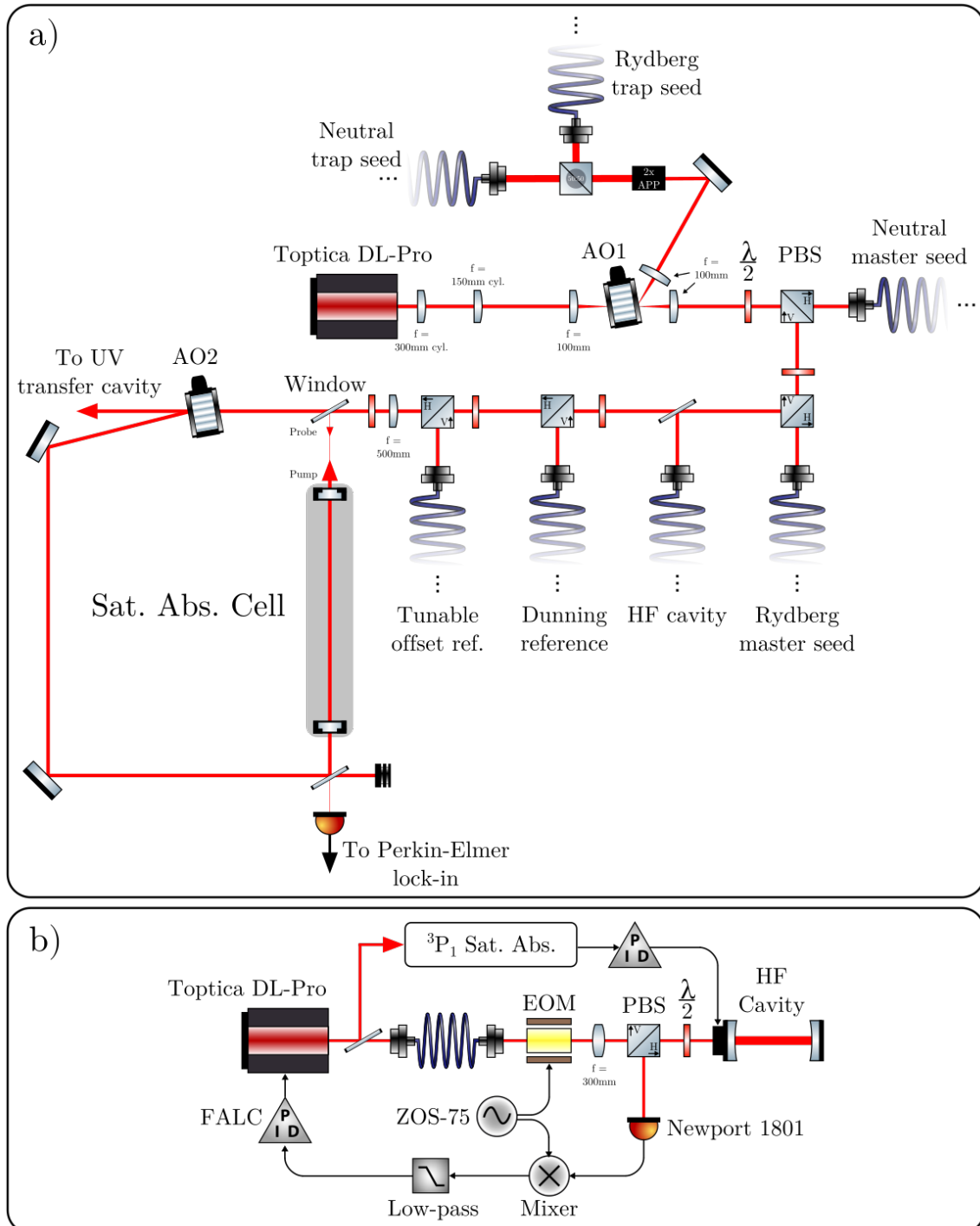


Figure 2.17 : 689 nm master system

- a) A simplified optical schematic showing the distribution of light as outlined in Fig. 2.16. b) Frequency stabilization scheme for the 689 nm master.

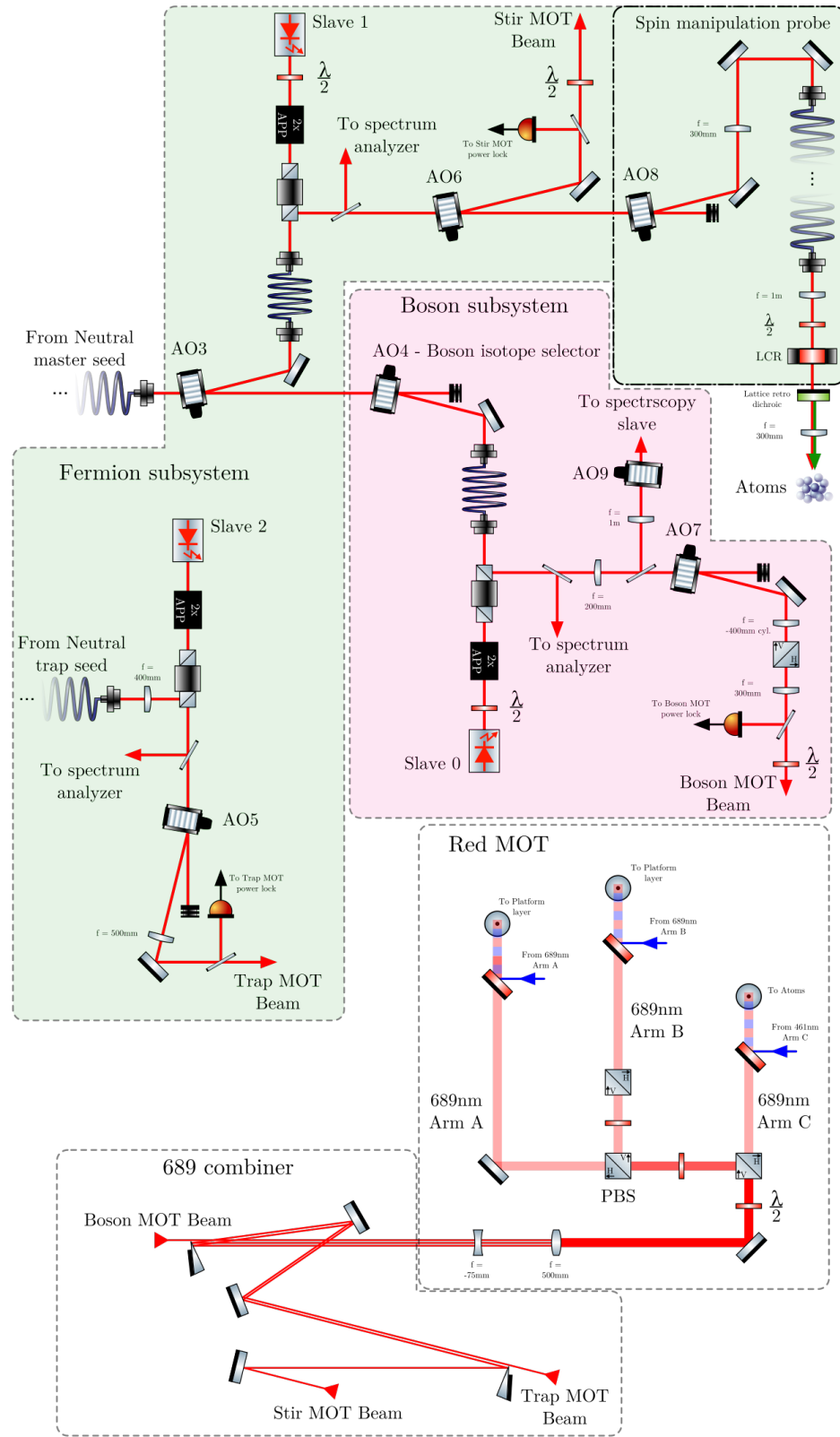


Figure 2.18 : Neutral 689 nm trapping and cooling setup

Fermion subsystem: Fig. 2.18 highlights the Fermion subsystem in green and is dedicated to the ^{87}Sr isotope. This allows the seed laser frequencies to remain fixed as shown on the frequency axis given in Fig. 2.16.

As discussed in Sec. 2.1, trapping strontium-87 requires us to address two hyperfine transitions, which we label the trap, operating along $^1S_0(F = 9/2) \rightarrow ^3P_1(F' = 11/2)$, and the stir, operating along $^1S_0(F = 9/2) \rightarrow ^3P_1(F' = 9/2)$. Due to the change in spin between the singlet and triplet series, there is a mismatch in the Zeeman shifts of the 1S_0 and 3P_1 states, which results in anti-trapped edge states causing atoms to be expelled from the MOT laser acting on the trapping transition. The complication can be overcome by adding an additional stir laser to randomize the m_F populations in the 1S_0 ground state.

We generate these trapping and cooling photons using independent laser diodes, slave 1 and 2 for the stir and trap respectively, seeded with appropriately shifted light from the master laser. Light from slave 2 is used exclusively for the trap MOT while slave 1 is used for the stir MOT and spin manipulation probe, both of which operate along the ($F = 9/2 \rightarrow F' = 9/2$) transition.

Boson subsystem: Fig. 2.18 highlights the Boson subsystem in red. This setup enables the Neutral apparatus to individually trap each of the three bosonic isotopes of strontium. Additionally, this setup incorporates a spectroscopy probe that also features several choices for the input seed frequency. This system is detailed in Sec. 2.3.4.

Changing the bosonic isotope of interest is accomplished via switching the RF drive to the boson isotope selector AOM (AO4) and realigning through the mode-cleaning fiber to injection lock slave 0. This process has proven to be a fast and robust means for switching between various isotopes without the need for dedicated

diode systems for each isotope. Accounting for the boson MOT AOM (AO7) frequency, Table 2.6 gives the necessary drive frequencies for trapping strontium-88 and strontium-84. Strontium-86 is attainable by removing the drive frequency from the AOM such that slave 0 follows the 689 master frequency. Therefore, relative to the $^{88}\text{Sr } ^1S_0 \rightarrow ^3P_1$ transition, the input frequencies for slave 0 are [$^{84}\text{Sr} \rightarrow -269.49\text{ MHz}$, $^{86}\text{Sr} \rightarrow -82\text{ MHz}$, $^{88}\text{Sr} \rightarrow +82\text{ MHz}$]. These details are represented schematically on the frequency axis of Fig. 2.16.

689 combiner & MOT: Finally, Fig. 2.18 also illustrates the 689 combiner & red MOT paths. The 689 combiner is a series of D-type mirrors for combining the boson, stir, and trap MOT beams such that these three light sources co-propagate onto the atoms. We find that long path lengths ensure acceptable alignment along the entire path length with the only major drawback that the individual arm powers are not independently controllable for each of the three MOT beams.

As outlined in Fig. 2.14 and Sec. 2.3.1.4, the red MOT and blue MOT share the same path through the science chamber by utilizing beam combining dichroics and custom dual-wavelength waveplates.

Historical notes and tips for usage

Fiber usage for injection locking: Optical fibers provide several key advantages when used to injection lock slaves. The foremost being a cleaner TEM_{00} output mode that can be easily mode-matched to the slave. Additionally, fibers provide a quick and effective means for ensuring optimal alignment of the injection locking light by coupling the rejected light from the slave diode "backwards" through the fiber. Although rejected light is typically minimized when setting up a slave diode,

by temporarily placing a waveplate before the isolator you can scramble the input polarization and increase the rejected power to facilitate alignment through the fiber. This process generally results in a quite robust alignment of the fiber output and the laser diode and is much faster than the free space method of coupling over a long distance. This alignment advantage along with improved mode matching has allowed us to injection lock a slave diode with as little as $300\ \mu\text{W}$ while producing up to $\sim 30\ \text{mW}$ of output power.

2.3.3 Optical dipole trap: 1064 nm

The ground state of strontium is a spin-less $J = 0$ state. Therefore, magnetic traps, which are common to alkali experiments, cannot be used for trapping the strontium ground state. Instead, we utilize optical dipole traps (ODTs), which rely on the AC stark shift for trapping atoms.

The isotopes of strontium display a wide range of thermalization behavior due to their variation in scattering lengths. These differences in thermalization make it difficult to use a single ODT geometry for efficient trapping and evaporation of strontium. For this reason, the Neutral apparatus underwent a significant redesign of our ODT system as outlined in Ying Huang's thesis [86].

The experiments presented in chapter 4 of this thesis have relied on the trap configuration we call the independent arm ODT, while the following chapter utilizes a single-beam trapping potential. Fig. 2.19 shows a simplified optical layout of the independent arm configuration as this has been our primary configuration for recent experiments. This trap is composed of two 1064 nm beams, labeled the loading and sheet traps, which are controlled by independent AOMs. At the atoms, the approximate spot size of the loading trap is $300 \mu\text{m} \times 60 \mu\text{m}$ and the sheet trap is $400 \mu\text{m} \times 40 \mu\text{m}$. Both beams have the short axis parallel to gravity to produce an oblate spheroid trapping volume that is useful for maintaining low density strontium-86 gases where reduction of three-body recombination is important.

As shown in the figure, the two AOMs for the ODT are placed sequentially to better utilize the available 18 W from the IPG. We typically load into a $10 \mu\text{K}$ deep trap from the red MOT which requires $\sim 4 \text{ W}$ in the loading trap and $\sim 3 \text{ W}$ in the sheet trap. Once transferred into the ODT, we perform forced evaporation following a power law trajectory [149], where the timescale for evaporation is isotope dependent.

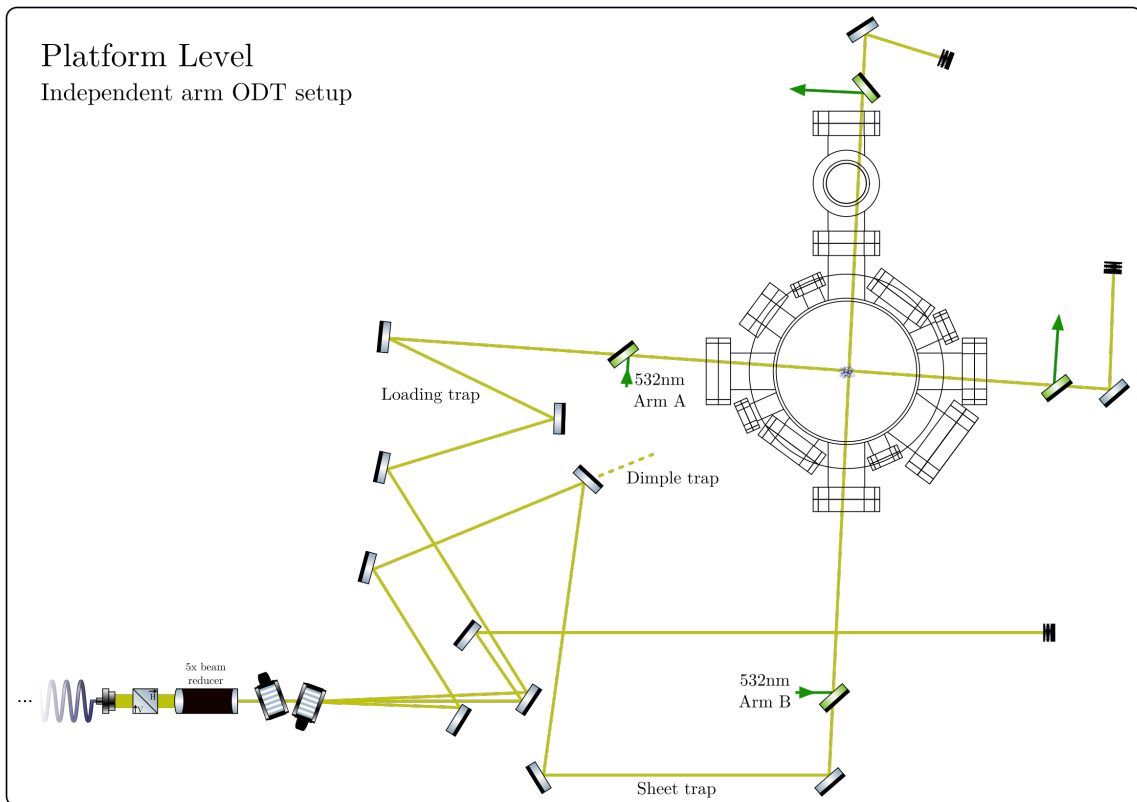


Figure 2.19 : 1064 nm optical dipole trap schematic

Paths for the loading and sheet traps are shown as they are realized on the apparatus. Also shown is the dimple trap path which is an optional configuration of the sheet trap [86].

For our experiments with strontium-86, the evaporation timescales were on the order of 1-2 seconds for achieving sample temperatures near 100-200 nK and densities as high as 10^{12} cm^{-3} .

2.3.3.1 Modeling the potential

Optical dipole traps result from the AC stark shift present whenever an atom interacts with a light field [76]. In the simple two-level dressed atom model, the AC stark shift can be viewed as a mixing of the bare atomic states by the light field. Fig. 2.20 shows a schematic avoided crossing of a two-level system near resonance. Here the separation between states is defined as Ω , or the Rabi frequency given by

$$\Omega = \frac{1}{\tau} \sqrt{\frac{I}{2I_{sat}}} \quad (2.2)$$

where τ is the lifetime of the excited state, I_{sat} is the saturation intensity of the transition, and I is the applied intensity. Using this we can understand the origin of the potential which provides the trapping force in ODTs.

Considering an atom in the ground state, $|1\rangle$, a light field with red detuning, $\Delta < 0$, and the intensity dependence of Eq. 2.2. We see that at low-intensity, Ω^{low} , the energy of state $|1\rangle$, E^{low} , is nearly unchanged from the non-interacting case. However, as intensity is increased, Ω^{high} , the energy of state $|1\rangle$ decreases. Thus, atoms in $|1\rangle$ will experience a force, $F(\mathbf{r}) = -\nabla U(\mathbf{r})$, directed towards higher intensity regions when there is a spatial dependence of the potential energy.

With respect to the detuning, Δ , from resonance, the potential energy of the atom scales as

$$U(r) \propto \frac{\Gamma}{\Delta} I(r) \quad (2.3)$$

where, Γ is the natural linewidth of the transition determined by it's spontaneous

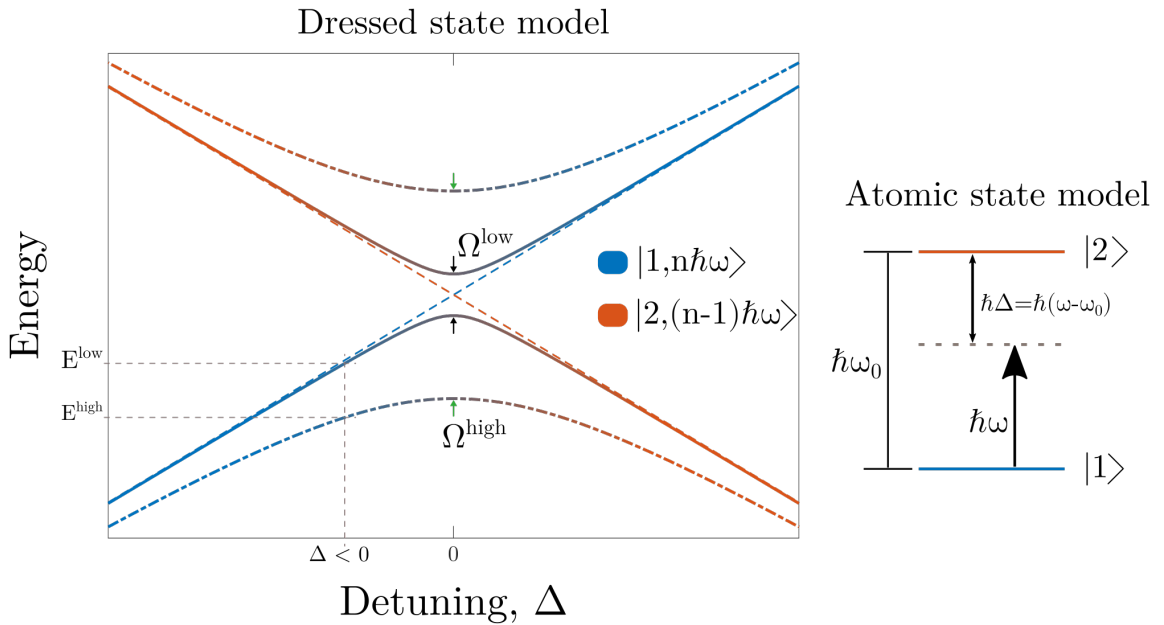


Figure 2.20 : Two-level avoided crossing

The dressed state energy of each level is shown for several different cases of coupling strength, represented by the three different line types: dashed lines represent the non-interacting case, solid lines represents a weak (low) coupling between states, and the dashed-dot line represents a stronger (high) coupling. The color of the lines indicates the makeup of the eigenstates of the system. Starting from the left of the plot, the bare atomic states are the eigenstates that are shifting with the photon energy. Moving to the right, in the region of the avoided crossing, the pure atomic states $|1\rangle$ and $|2\rangle$ become mixed. This mixing is represented schematically with the gradient between blue and red. Continuing to the left, the bare states have again become the eigenstates, but switched in energy due to one fewer photons. The coupling between the bare atomic states $|1\rangle$ and $|2\rangle$ results in an energy gap determined by the coupling strength Ω .

decay lifetime, and $I(r)$ is the spatial dependence of the light intensity. Optical dipole traps are also characterized by their off-resonant scattering rate. This rate is proportional to

$$\Gamma(r) \propto \left(\frac{\Gamma}{\Delta} \right)^2 I(r) \quad (2.4)$$

Comparing Eqs. 2.3 & 2.4, we find a favorable scaling for far off-resonant optical traps since the potential energy varies as $1/\Delta$ and the scattering rate varies as $1/\Delta^2$.

The spatial dependence of $U(\mathbf{r})$ derives from the TEM₀₀ Gaussian intensity profile of the incident lasers given by

$$I(r, z) = \frac{2P}{\pi w(z)^2} \exp \left(\frac{-2r^2}{w(z)^2} \right) \quad (2.5)$$

where z is oriented along the beam propagation axis and r is transverse to this axis. Additionally, P is the incident laser power, w_0 is the waist radius at $z = 0$, and the axial profile $w(z)$ is given by

$$w(z) = w_0 \sqrt{1 + \left(\frac{z\lambda}{\pi w_0^2} \right)^2} \quad (2.6)$$

where λ is the laser wavelength.

Combining Eqs. 2.3 & 2.5 we find the three dimensional potential generated by two orthogonal lasers to be

$$U(x, y, z) = mgz + \frac{\alpha(\lambda)}{2\epsilon_0 c} \frac{2}{\pi} \left[\frac{P_1}{w_1^y(x) w_1^z(x)} \exp \left(\frac{-2(y^2 + z^2)}{[w_1^y(x)]^2 [w_1^z(x)]^2} \right) + \frac{P_2}{w_2^x(y) w_2^z(y)} \exp \left(\frac{-2(x^2 + z^2)}{[w_2^x(y)]^2 [w_2^z(y)]^2} \right) \right] \quad (2.7)$$

where mgz accounts for the influence of gravity on the atoms of mass m , labels 1, 2 specify the two intersecting laser, i.e. the load and sheet traps as illustrated in Fig. 2.19, $\alpha(\lambda)$ is the AC polarizability of the ground state at a given wavelength, ϵ_0 is the vacuum permittivity, and c is the speed of light. This polarizability encapsulates

the natural linewidth, detuning, and resonant behavior of the light field interaction with the bare atomic states [76]. Sec. 2.3.1 and App. A of Pascal Mickelson's PhD thesis [128] outlines a calculation of the AC polarizability, which at 1064 nm is $\frac{\alpha(\lambda=1064\text{ nm})}{2\epsilon_0 c} = -10.9 \text{ Hz}/(\text{W/cm}^2) = -5.23 \times 10^{-8} \mu\text{K}/(\text{W/cm}^2)$ * [204]. Furthermore, $w_{(1,2)}^{(x,y,z)}$ generalizes Eqs. 2.5 and 2.6 for astigmatic laser profiles whereby the waist position and size are not common to both beam axes as assumed in these simple equations†.

The effects of gravity are a significant limiting factor for ultracold atoms as it is the dominant force that must be counteracted by the optical dipole trap. Fig. 2.21a shows the effects of gravity considering a simple one-dimensional Gaussian potential, $U(z) = mgz + A \exp\left(\frac{-z^2}{2\sigma^2}\right)$. Here we've chosen a general form of the Gaussian for illustrative purposes. From the figure we see that, due to gravity, there is a maximum energy of the trap at U_{\max} . Particles with energy above U_{\max} are not effected by the trapping potential and will fall under the influence of gravity. We may then define a trap depth $U_{\text{depth}} = U_{\max} - U_{\min}$, where U_{\min} is the minimum energy of the trap. Fig. 2.21b illustrates a realistic three-dimensional profile of an optical trap. From the 3D profiles, we find the maximum trappable energy U_{\max} is given by a saddle point that may not be along the $X = 0$ line. This is particularly important for shallow traps (low power) as the trap depth is more greatly influenced by gravity and therefore U_{\max} is likely to be defined by a saddle point along a non-trivial trajectory. This realization has important repercussion for our analysis of the halo binding energy described in

*Units here are convenient lab units for quick calculation of trap parameters. Polarizability of 1S_0 in atomic units is $\alpha = 232.857 \text{ au}$.

†Eq. 2.7 is given assuming a coordinate system where one beam propagates along X , another along Y , and Z is parallel to gravity.

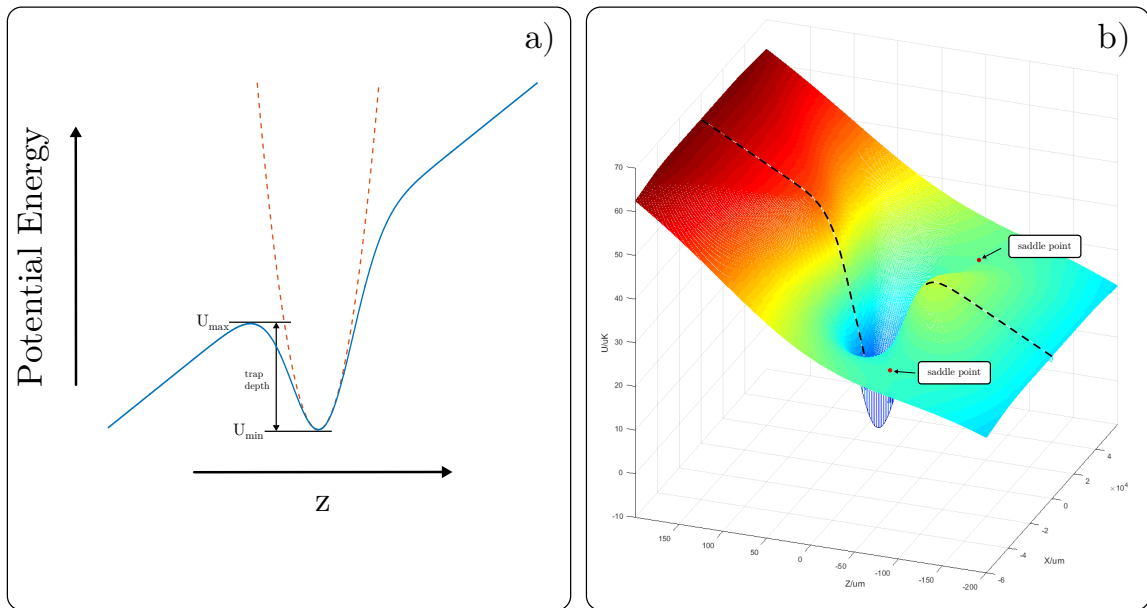


Figure 2.21 : Modeling an optical dipole potential

a) A one-dimensional view along the trap axis parallel to gravity. The trap depth is defined between the trap minimum and the nearest saddle point. Also shown is the harmonic approximation used for defining trap frequencies. b) A pseudo-color volumetric plot of a three-dimensional potential. Here we see a saddle point similar to the 1D case along $X = 0$ but there is also a lower saddle point indicated by the black arrows.

Ch. 5.

2.3.3.2 Trap frequency calibration

Fig. 2.21a shows a harmonic approximation, dashed line in the figure, commonly made for ODT potentials. This approximation is related to the realistic potential by Taylor expanding the exponentials in Eq. 2.7 and relating the beam parameters to a trap frequency ω . From the figure, we see that for deep traps or cold samples this is an excellent approximation and a readily measurable characteristic. Thus, measurement of the trap frequencies provides the link between our theoretical models and the experimental realization of the optical dipole trap. Previously, these measurements were performed by parametric heating via intensity modulation of the optical dipole trap [86]. This process causes atom loss via resonant heating when the modulation frequency matches a trap oscillation frequency. While convenient and simple, parametric heating can lead to a complicated spectrum to decipher since the heating process does not discriminate directional information and causes coupling of higher harmonics of the trap frequencies.

Recently, we have found excitation of center-of-mass (COM) oscillations to be a robust mechanism for measuring trap frequencies. Fig. 2.22 shows an example of trap frequency measurements taken via center-of-mass oscillations. This example illustrates the long-lived nature of these collective modes which can extend for hundreds of milliseconds. Furthermore, the frequency discrimination provides an unambiguous estimate of the underlying trap frequency.

Exciting vertical trap frequencies, along Z , is a straightforward process whereby we excite oscillations by quickly extinguishing one arm of the optical dipole trap for 1-2 ms before turning it back on and allowing the cloud to evolve in time. We measure

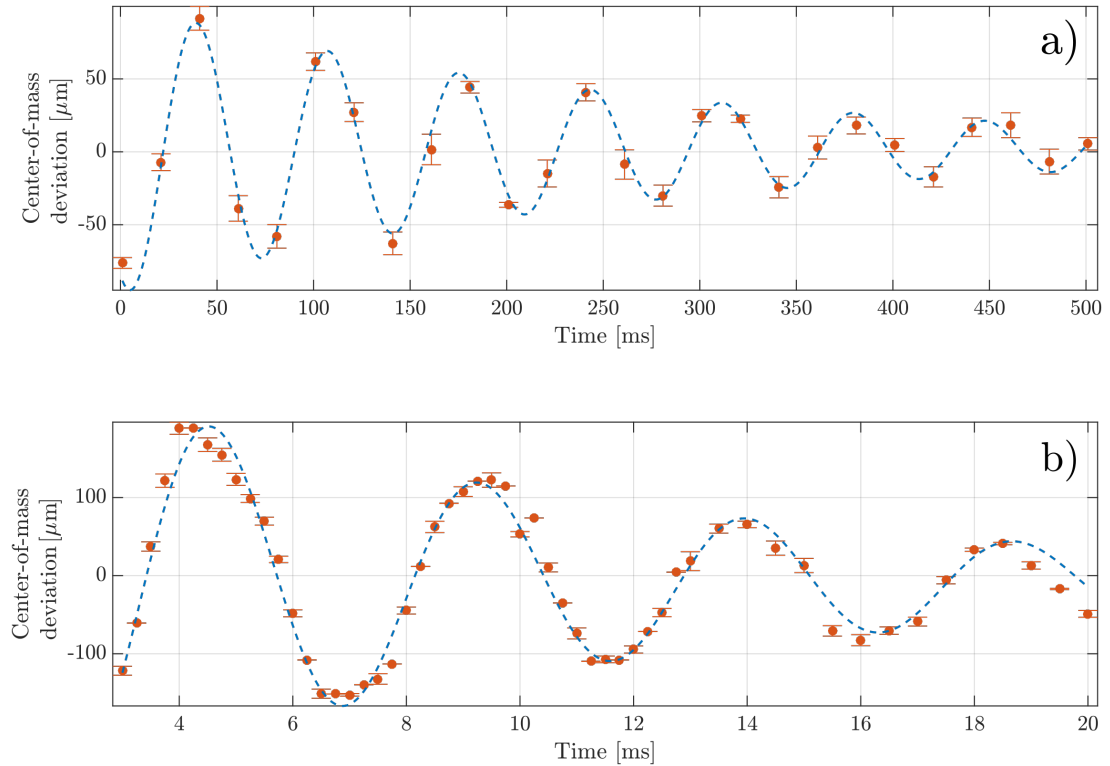


Figure 2.22 : Example center-of-mass oscillations

These measurements were taken in the independent arm ODT with strontium-84. This isotope has a scattering length $a = 124 a_0$ leading to slow decay of the oscillations.

a) Horizontal trap frequency of ~ 13 Hz extending over 500 ms. This mode was excited via the kicking method. b) Vertical trap frequency of ~ 220 Hz. This mode was excited by momentarily pulsing one of the ODT beams off. Further details are given in the text.

the trap frequency by varying this evolution time subsequently performing a standard time-of-flight absorption imaging step[‡].

Exciting oscillations along the horizontal directions, is a bit more challenging. We have developed two mechanisms for exciting these modes which we call the kicking method and the pulling method. The following sections provide further detail[§].

Kicking method: The kicking method has been primarily used for measuring the trap frequencies of the independent arm ODT. In this configuration the two ODT beams intersect in a horizontal plane parallel to the optical table and orthogonal to one another. Excitation of the center-of-mass oscillation occurs via an abrupt step of the AOM drive frequency. This changes the deflection angle of the IR beam out of the AOM which, in turn, "kicks" the cloud. Briefly, the kicking procedure is

- I. During the ODT loading phase, load into a trap with one beam offset
 - A. In our current configuration, an offset of the AOM frequency by ≈ 1 MHz results in a reasonable excitation amplitude.

- II. Once the red MOT is extinguished and ODT loading is complete, evaporate down to the trap or intensities of interest in the offset trap.
 - A. It is useful to follow the evaporation trajectory for the experiment at hand. This allows adequate modeling of the experimental potential and evaluation of the trap depth at various points of interest.

[‡]On a technical note, we find that this rapid on-off of the beams results in a brief overshoot of the power locks due to the reacquisition. However, the power lock equilibrium is restored after a few milliseconds and therefore we evolve for a time long compared to this perturbative behavior.

[§]Note that timescales specified below are given with strontium-84 as the example. This isotope has favorable scattering properties and is typically our prototyping isotope for new techniques.

III. After evaporation, let the atoms equilibrate for ≈ 250 ms then suddenly switch the frequency of the trap and hold for a variable evolution time before releasing and imaging.

- A. This offset will excite oscillations along the opposite beam and measure the confinement due to the beam being shifted.

Pulling method: With the recent addition of the high power 532 nm for the optical lattice, we have explored an alternative method of inducing a center-of-mass oscillation. This method uses a single pass of vertically propagating green light (Arm C) to pull the atoms out of equilibrium to excite an oscillation. Details of the 532 nm setup are given in Ch. 6.

The pulling method has become our preferred method of trap frequency measurement, as it does not require us to change any AOM frequency sources unlike the kicking method[¶]. Additionally, the pulling method can be applied to traps where the 1064 nm light is recycled whereas previously our only recourse in this configuration was to measure trap frequencies via intensity modulation. Briefly, the pulling procedure is

- I. Using an unmodified ODT, load and evaporate down to the trap of interest.

- A. While evaporating, apply slightly mis-aligned lattice Arm C light to the atoms.

[¶]The loading trap uses a VCO so changing the voltage source is enough. However, the sheet/dimple is run from a IntraAction driver with a fixed digital synthesizer as the input. For kicking with the sheet, we temporarily replace the synth with a VCO, but be careful as this will also change the gain of the power lock circuit (Synth outputs ≈ 0 dbm but VCO outputs ≈ 10 dbm)

II. After evaporation, ramp up Arm C to high power over 250 ms then allow the atoms to equilibrate for another 250 ms in the combined two beam IR, one beam 532 ODT.

A. The final power of the 532 nm beam when enabled should be adjusted to provide an adequate force without collapsing the IR ODT.

III. Diabatically extinguish the 532 nm beam and hold in the optical dipole trap for varying evolution times before releasing and performing time-of-flight imaging.

The controlled mis-alignment of the 532 nm Arm C beam is facilitated by an absolute positioning mirror (model: Newport Conex-AG-M100D). This mirror provides a computer controllable interface for reproducibly changing the Arm C beam alignment and exciting center-of-mass oscillations along each of the IR beam directions.

Historical notes and tips for usage

IPG failure: In the fall of 2018, the IPG YLR-20-LR, which had been in use for about a decade, died due to a thermal issue that caused the internal fiber amplifier to overheat and burn. As of April 2019, this laser is being replaced by an IPG YLR-50-1064-LR which is a diode pumped, multi-mode, linearly polarized Ytterbium fiber laser with a maximum power output of 50 W. This system is being installed by Josh Hill, who is also reconstructing some elements of the paths reported in Ying Huang's thesis.

2.3.4 Optical toolbox

2.3.4.1 Absorption imaging system

Absorption imaging is a destructive measurement process that is predicated on measuring the spatially dependent attenuation of laser light after passing through an atomic cloud. In this section we will discuss the technical details of the Neutral absorption system and postpone the theoretical description of the process to Sec. 3.2.1.

Fig. 2.23 shows a simplified schematic of the absorption imaging system. Light is derived from the MOT path subsystem and guided to the atom chamber via freespace propagation. After passing through the atoms, an imaging system shapes and focuses the image onto a Cooke PixelFly CCD camera. The PixelFly is a 12 bit 1280x1024 CCD with a pixel size of $6\mu\text{m}$. The imaging relay system shown after the atomic sample was developed by Mi Yan and is outlined in detail in App. A of his PhD thesis [199]. Much of the imaging sequence is a standard procedure, however, day to day operation may be affected by system performance.

When taking images, we measure the optical depth to extract the properties of the atomic cloud. Sec. 3.2.1 will develop the theoretical approach for determining these properties. For now, we take as a given that each experimental sequence acquires one image with the atoms in frame and another background image without the atoms. In the ideal scenario these two images would be identical except in the region of the atom cloud, allowing us to easily fit and infer properties about the gas. Practically, we must wait for the atoms to exit the frame before taking a background image. This introduce a time delay between the consecutive images, which we seek to minimize. For this reason we utilize a special feature of the PixelFly called "double-shutter" mode. This particular imaging mode of the camera utilizes a second hidden set of pixels that are

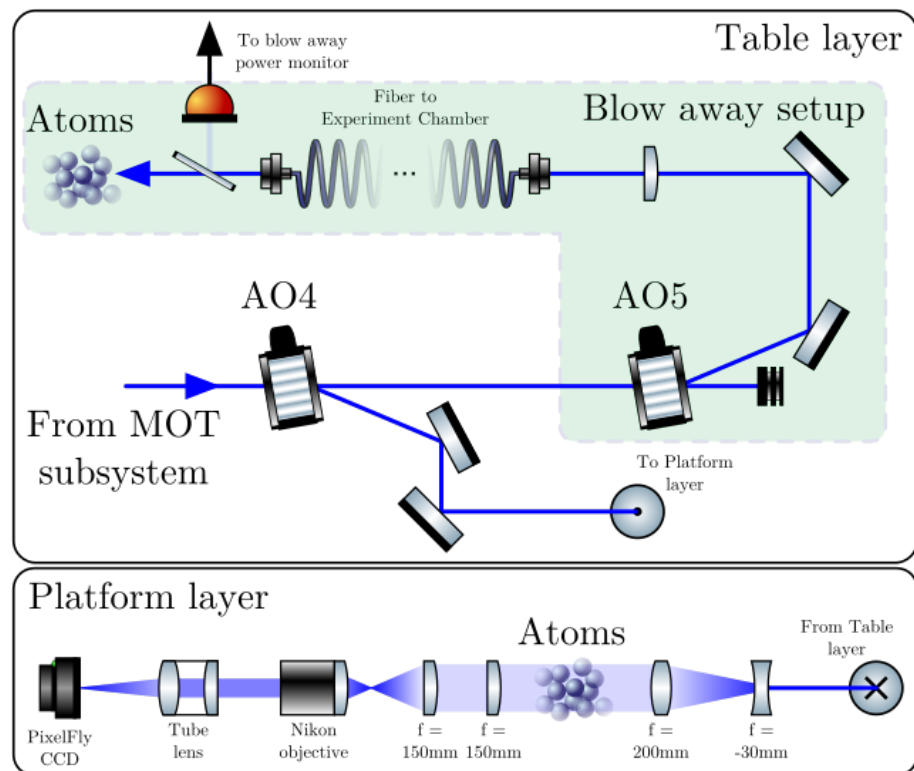


Figure 2.23 : Absorption imaging and blow away pulser optical schematic

Details on the construction and characterization of the blow away setup are available in Josh Hill's masters thesis [82]. Details on the construction and characterization of the imaging system are available in App. A of Mi Yan's PhD thesis [199].

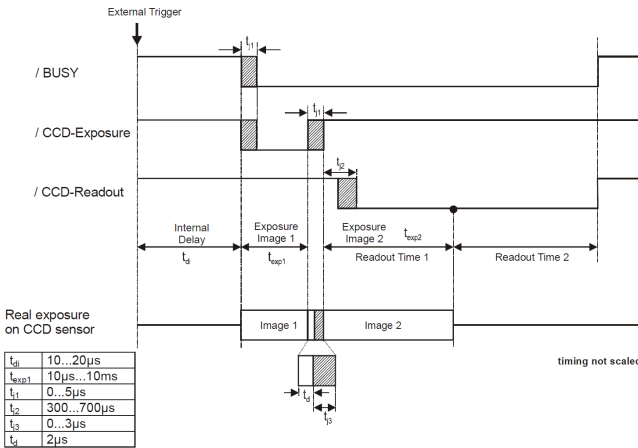


Figure 2.24 : Timing diagram of PixelFly doubleshutter mode

t_j refers to timing jitter inherent to the camera. In this scheme the first exposure can be controlled via the external trigger but the second image exposure is fixed to the readout time of the first image.

interleaved with the active pixels of the CCD. Typically the acquisition time between consecutive images taken with a CCD is limited by the analog-to-digital conversion time needed to readout the image from the pixels into the camera's memory. However, because of the PixelFly's set of hidden pixels, after the first image is taken, it is simply shifted one row down from the active pixels into the hidden area. Once shifted down, the active pixels are free to be exposed again. With this process, the time between images is reduced to 5μ s. Fig. 2.24 shows a full overview of this process. The drawback of this scheme is that for exposure times less than the readout time of an image, the second image is forced to have a minimum exposure of the readout time. This presents a challenge as our exposure time is about four orders of magnitude faster than the readout time. To overcome this, we rely on the fast response of the imaging system AOMs, a high extinction ratio of the 461 nm photons, and a narrow line filter centered

at 461 nm attached directly to front of the CCD. Fig. 2.23 shows two AOM's along the imaging path before the atoms. We found two AOM's necessary to attenuate leakage light along the path to acceptable levels while maintaining fast response times that a physical shutter cannot replicate.

Great care is taken to reduce the time between images since the laser intensity and frequency might drift between the atom and background images. Variations in intensity have straightforward implications for errors in measuring the optical depth since the characterization of the atomic number density assumes the only difference between the images is due to the presence of scattering particles and does not account for fluctuating photon number.

A more insidious source of error is variation of the optical frequency. Coherent, frequency-stabilized radiation is used to illuminate the atom cloud so that we may control the optical absorption cross section and accurately model the atomic number density. However, this laser light is passed through many optical components on its path to the atoms and ultimately the imaging camera. Small reflections along this path result in a multitude of interferometers that cause small scale spatial intensity variation across the beam. Exacerbating this problem are short time frequency drifts that may occur between the atom and background images that result in slightly different fringe patterns in the atom and background images. Fringe patterns are a well known nuisance in experimental AMO images and it has become routine to use linear algebra techniques (PCA, ICA, etc.) to create a composite background image for each atom image during analysis in order to create a higher quality image of the optical depth [171]. A brief discussion of the principal component analysis (PCA) algorithm employed by the Neutral analysis routine is outlined below.

Briefly, the PCA approach is as follows:

- I. Find a basis set of background images from a large set of raw background images.
- II. For a single atom image, construct an initial guess at a composite background image using coefficients to weight each basis image resulting in a superposition of the basis images.
- III. Segment the atom image into multiple regions by separating out the region of interest that includes the atom cloud.
- IV. Comparing regions of the composite background and the region excluding the atom cloud, perform a least-squares minimization by varying the weighting coefficients of the composite background.
- V. Once a suitable composite background has been found, calculate the optical depth using the region including the atom cloud and the corresponding region of the minimized composite background image.

This procedure is repeated for each atom image using a static background basis set that is computed for each scan. Fig. 2.25 shows an example of this technique with a background set of 20 other images (not shown). While PCA does not completely eliminate the visible fringe patterns, there is a noticeable reduction of the fringes in the PCA image versus the partner-in-time method.

2.3.4.2 Highly tunable 689 nm spectroscopy system

The spectroscopy laser is derived from a dedicated slave diode and is our primary 689 nm probe for bosonic isotopes, with the spin manipulation laser described below being used for fermions. This laser system is used for general intercombination line spectroscopy, photoassociation, Bragg scattering, and Rabi oscillation measurements.

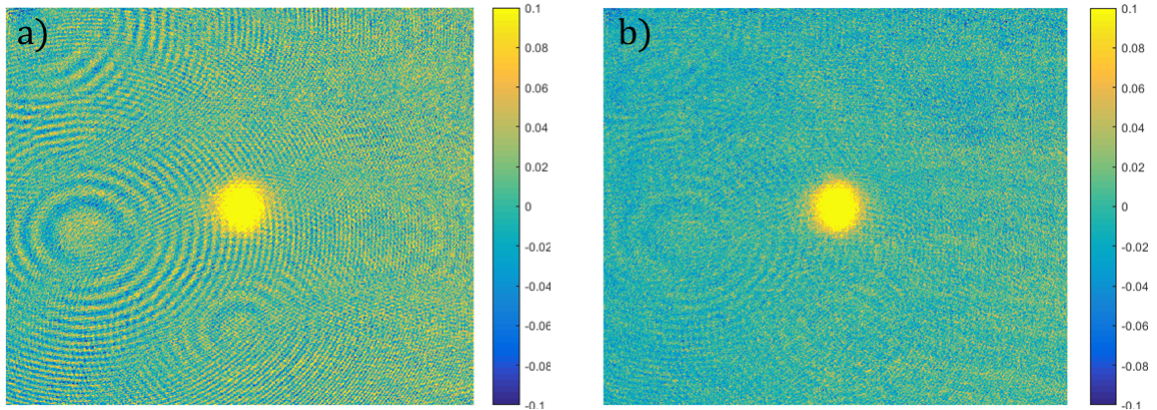


Figure 2.25 : Comparison of background subtraction methods

Background subtraction on the same image performed using two different methods and plotted on the same color scale. a) The partner-in-time background to the atom image is used. b) A composite background image formed via PCA is used.

Fig. 2.26 shows a simplified optical diagram. We found it necessary to increase the isolation out of the laser as the injection lock became unstable when coupling into fiber due to back reflections. We typically get $\sim 25\text{ mW}$ of usable power past the second isolator. As this is our primary spectroscopy laser, its optical setup tends to be in flux but a couple of noteworthy innovations have been implemented in recent years. These include the development of an infinite sample and hold for intensity stabilization, a versatile injection locking scheme, and a shallow angle Bragg scattering setup which are discussed below.

Infinite sample and hold: The infinite sample and hold (ISH) circuit is used in conjunction with an intensity stabilization lock circuit and was built to allow for intensity stabilized pulses on timescales much faster than the acquisition time of the intensity lock circuitry, typically $\sim 70\text{ ms}$. This circuit was developed and built by

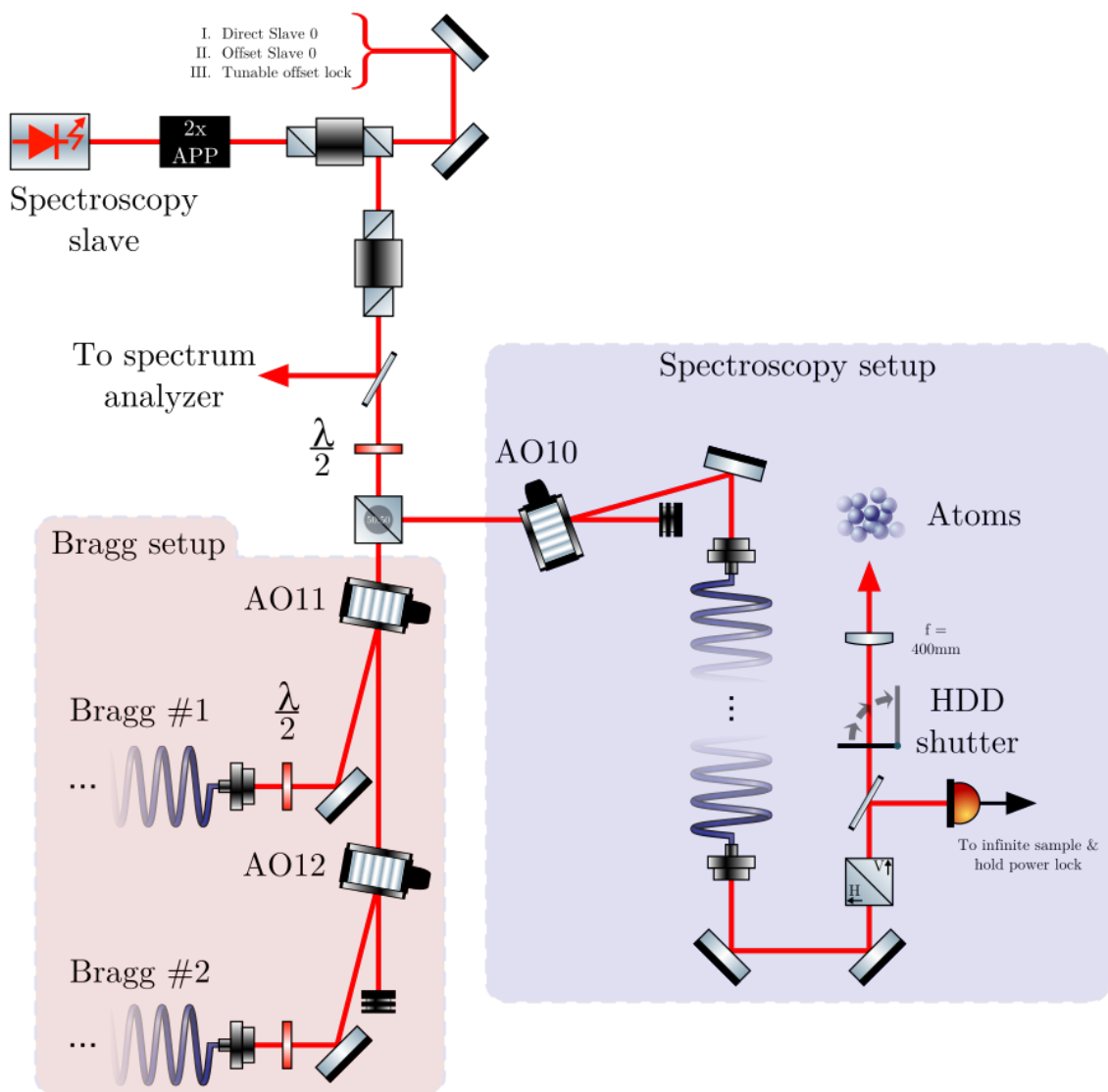


Figure 2.26 : Optical schematic: 689 spectroscopy laser

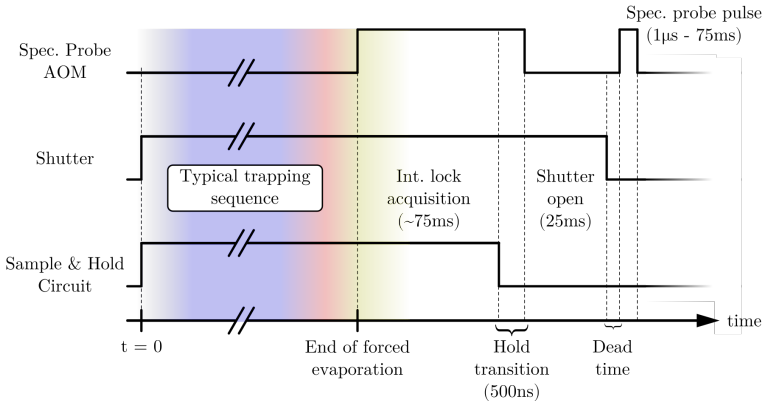


Figure 2.27 : Infinite sample and holding timing diagram

The HDD shutter in use has a full open time of ~ 15 ms and the acquisition time of the sample and hold chip is on the order of ~ 500 ns.

Josh Hill and is based on the LTC1417 which is a low power 14-bit 400 kS/s ADC.

The ISH is currently placed on our spectroscopy probe and is situated between the intensity stabilization lock circuit and RF voltage controlled attenuator. This allows the ISH to passively sample the control voltage from the lock circuit. In sample mode the ISH output follows the input from the lock circuit. When the ISH is transitioned into hold mode, it begins ignoring changes on its input and outputs the last voltage that was sampled before the transition. A timing diagram of the infinite sample and hold usage is outlined in Fig. 2.27. Following our typical preparation sequence we place the ISH in sample mode and enable the spectroscopy probe with the HDD shutter blocking the beam. This allows the lock circuit time needed to acquire and stabilize the feedback voltage required to maintain the present intensity setpoint. Following lock acquisition, we transition the ISH into hold mode, open the shutter, and pulse the RF onto the spectroscopy AOM (AO10) via a fast RF switch, where the RF amplitude is attenuated via a voltage controlled attenuator and the voltage input is the fixed

output value from the ISH. This momentary transition to open-loop operation of the intensity stabilization circuit does suffer from slow long term fluctuations shot to shot, but provides a marked improvement on the intensity reproducibility without placing restrictions on the minimum pulse time required. Furthermore, by monitoring and recording the slowly varying intensity fluctuations, we can model any error introduced by the reduced intensity variation.

Versatile injection locking scheme: This scheme allows us to change the seed laser frequency via three different methods outlined below.

I. Directly following slave 0

A. A small amount of light from slave 0 is coupled directly into the rejected port of the spectroscopy slave isolator, resulting in the frequency of spectroscopy slave following slave 0. Fig. 2.18 shows the position of this pick-off before the boson red MOT AOM. Recalling that slave 0 is always positioned +82 MHz of the bosonic isotope of interest, the direct method will position the frequency of the spectroscopy slave to also be +82 MHz.

II. Slave 0 minus 40 MHz

A. The light sent from slave 0 is shifted down 40 MHz by the spectroscopy offset AOM. This positions the spectroscopy slave frequency at +42 MHz of the intercombination line of interest.

III. Programmable offset

A. In 2018 we re-purposed the original homemade 689 master ECDL described in Natali de Escobar's thesis as a slave ECDL and directed light from this

setup as a tertiary method for tuning the frequency of the spectroscopy slave.

There are several things to note concerning the above descriptions. First, the "of interest" designation specifically refers to the variability of the laser frequency of slave 0, which is dependent on the configuration of the isotope selector AOM. Second, switching between case I and II is surprisingly trivial given the realized setup on the table. In practice, a flipper mirror and clever optical path alignment allow us to switch between these two injection methods in a matter of seconds and has demonstrated remarkable stability. Finally, while the programmable offset is the most versatile of the presented schemes, it also has the greatest frequency uncertainty and is fundamentally a different approach that we are still in the process of exploring.

The slave ECDL, beatnote generation, and phase locked loop (PLL) integrated circuit was a project begun by a visiting student and later completed by Josh Hill. It is based on the 2009 work of Appel et al. [3] which outlines a versatile optical phase locked loop with a claimed frequency range of sub-MHz to 7 GHz.

As a brief reminder, phase locking is a feedback scheme which seeks to maintain the a fixed and phase relationship frequency between two sources. This process is heavily used in the telecommunications industry and analog phase locking is a common technique in atomic physics laboratories as well. In atomic physics, the general idea is to generate a beatnote by interfering two single frequency lasers on a high bandwidth photodiode. From this optical beatnote we observe the difference frequency of the two lasers as the summing frequency is well outside the bandwidth of photodiodes. The difference frequency can then be further interfered against an RF reference frequency and low-passed to generate an error signal that can be used to stabilize the difference frequency against the RF reference.

The versatile OPLL is a digital realization of this approach which, we have used to lock the relative frequency difference between the Toptica master and slave ECDL from approximately 1 MHz to 1.2 GHz. The upper limit is currently bandwidth limited by our AC coupled photodiode and not by the OPLL circuitry. Fig. 2.28a shows an example of the optical beatnote monitored via an RF spectrum analyzer. Notably, while we do observe suppression of frequency components around the set point which is characteristic of locking, we also see resonant peaking instead of a single narrow frequency peak as expected. Further investigations showed that the individual frequencies were fairly narrow as shown in Fig. 2.28b where we observed atom loss on the $F = 9/2 \rightarrow F' = 11/2$ transition with linewidths on the order of 60 kHz.

Finally, we note that this system has also been used to perform Bragg spectroscopy as reported in the PhD thesis of Brian DeSalvo [49].

2.3.4.3 Spin-manipulation laser with dynamic polarization control

Fermionic strontium-87 has become of particular interest for experiments studying quantum magnetism in a highly degenerate SU(N) system. Key to these studies is the creation and manipulation of arbitrary spin mixtures. We have recently implemented a spin manipulation laser probe (spin-man) acting on the $F = 9/2 \rightarrow F' = 9/2$ hyperfine transition of the intercombination line for the purpose of creating well defined spin mixtures.

Fig. 2.18 illustrates the optical schematic of the spin-manipulation system which is derived from slave 1 and is related to the stir MOT system. The original construction of the output optics is outlined in Ch. 5 of Josh Hill's masters work [82] and is part of the layered optical systems added to the top of the optical chamber in 2017.

A key component of this layered system is the liquid crystal retarder (model:

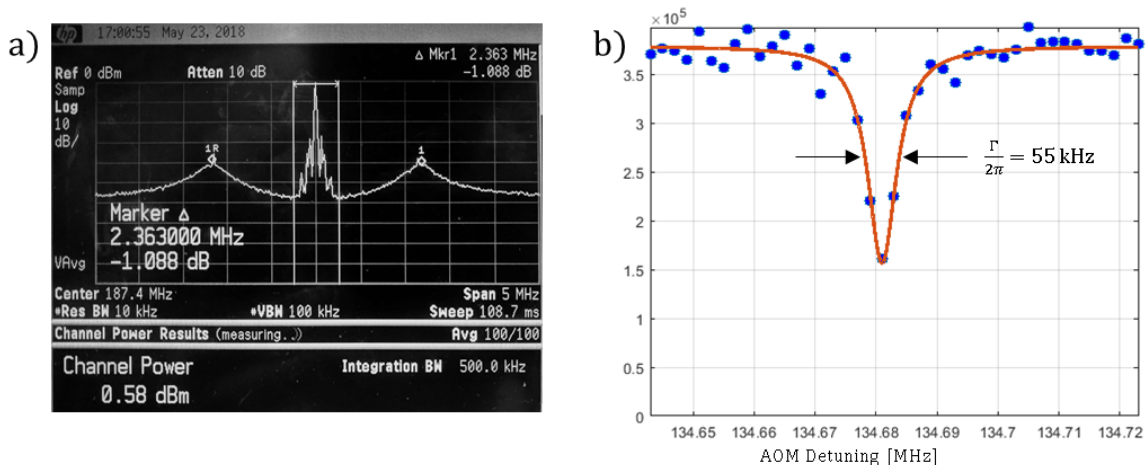


Figure 2.28 : Characterization of the OPLL performance

a) RF spectrum of the optical beatnote when the OPLL is engaged. Resonant peaking can be seen in the 500 kHz band around the center frequency. b) Atom loss spectrum which shows that the central peak is narrow. Differences between the AOM detuning shown and the center frequency of the OPLL are due to various AOM shifts between components.

MeadowLark Optics LV-300 LCR), which allows us to dynamically control the polarization incident on the atoms. Additionally, a configurable high precision RF system for dynamically changing the spin-manipulation laser frequency allows us to perform optical pumping in a magnetic field by addressing each Zeeman transition independently. The RF tunability for optical pumping is based on the "table mode" feature of the Novatech 409B digital synthesizers which can be externally triggered to progress through a table of configured frequencies.

In concert, these devices allow us to, for instance, polarize to the $^1S_0 (F = 9/2, m_F = 9/2)$ using $\sigma+$ and once polarized use the LCR to rotate the light polarization to $\sigma-$ and probe the polarized ground state along the $^1S_0 (F = 9/2, m_F = 9/2) \rightarrow ^3P_1 (F' = 9/2, m_F = 7/2)$. An example spectrum where we demonstrate optical pumping of 6 states is given in Fig. 2.29. For this experiment we applied a large bias field $\sim 5 G$ and performed optical pumping on each m_F level for 2 ms with a 1 ms hold between each level. Thus, the spin-polarization laser was stepped through 6 different m_F resonance frequencies as determined by the "no pumping" spectrum. After pumping, the laser was then set to a frequency as shown along the x-axis to probe the population of each level via shelving population to the $^3P_1 (F = 9/2)$ state for 9 μs and blowing away the remaining ground state atoms with a 1 μs pulse of 461 nm light^{||}.

^{||}More details may be found in OneNote under 87Sr Spin Manipulation. These experiments were performed on 2018.02.22.

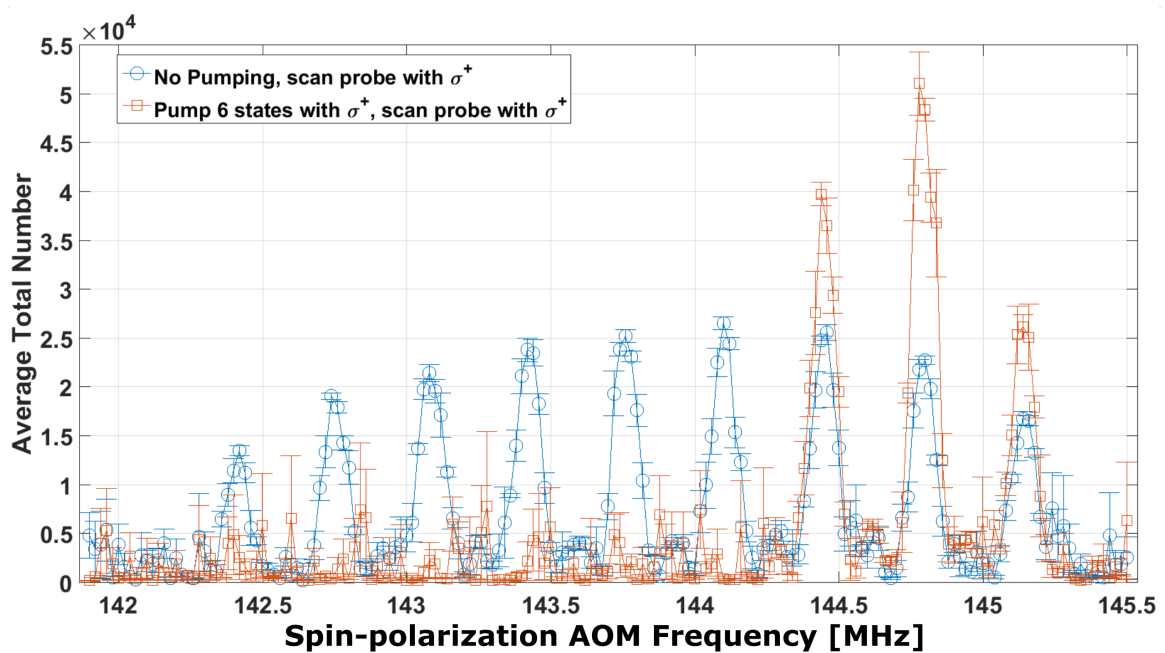


Figure 2.29 : Spin polarization of strontium-87

A comparison of unpolarized and partially polarized ^{87}Sr . These experiments were performed in a bias field $B \approx 5\text{ G}$ to separate the m_F states. Each of the first six states were individually addressed and pumped during the second experiment. For these experiments, the light polarization was fixed.

2.4 Apparatus interface

The Neutral apparatus interfaces to our digital infrastructure via specialized hardware implementations and custom written software. Over the last seven years nearly all of this digital infrastructure has been refactored, upgraded, or replaced. Therefore, the following sections will briefly outline these new constructs, providing references to code repositories when possible. However, detailed discussions on the usage of this infrastructure will be relegated to their respective appendices.

2.4.1 Software

The primary control software is a custom built Labview application based on a synchronous state machine*. The Neutral implementation of this software is called neuKLEIN (Neutral Killian Lab Experimental Interface) and is based on a major overhaul, by Joe Whalen, of the original control software.

In short, an experimental sequence begins with serially programming each voltage output device. The pulseblasters are programmed last and are triggered via the global experimental trigger discussed in 2.4.3.2 below. Once all devices are ready the pulseblasters become the global clock and the neuKLEIN software begins polling the PixelFly camera waiting for a new image. Once an image is received various experimental parameters are recorded into text files and saved to disk. This process continues within the primary WHILE loop of the state machine and steps through the predetermined experimental settings array. Primary exit conditions for the loop are encountering an error, conclusion of the settings array, or manual abortion.

Once the files are written to disk, we perform image analysis using a custom

*Currently this project can be found at <https://github.com/KillianRice/neuKlein>

MatlabTM routine imaginatively named Neutral imagefit routine[†].

2.4.2 Hardware control and measurement systems

The hardware control system is composed of several primary components including the experimental clock, voltage output devices, and measurement instruments. We use a series of National InstrumentsTM data acquisition cards (NI-DAQs) and a re-configurable FPGA for generating output voltages. The experimental clock is based on a pair of SpinCore PulseBlaster TTL generators and a Cooke PixelFly camera is used for collecting absorption images. We also have access to a PicoScope 5000 digital oscilloscope for high resolution signal monitoring and recording. Typically this is used for recording experiment specific photodiode signals for later analysis.

Table 2.7 gives the models of the NI-DAQ cards and additional details such as the resolution, the shared FIFO (first-in, first out) buffer sizes, and the maximum sample rates as a function of the number of channels in use. Though these cards are known as acquisition cards, we instead rely heavily on the arbitrary waveform generation capabilities for dynamically generating analog output voltages. Furthermore, we do not stream data to cards during the experimental sequence but use only the on-board FIFO buffer for storing the arbitrary waveform.

Importantly, the finite buffer size and maximum sample rate define two extremes for time-based waveform generation due to the discretization of the waveform. For short times, the maximum sample rate sets the minimum possible time step between two points on the voltage output. At long times, a fixed number of points between the start and end points may lead to unacceptably large voltage steps between two points on the voltage output. Balancing these two tradeoffs is essential and is the

[†]Currently this project can be found at https://github.com/KillianRice/neutral_imagefit_routine

Model	Resolution		FIFO buffer Size	Max sample rate	
	Bit depth	Voltage [mV]		Channels used	Rate [kS/s]
6713	12	5	16,384	1 - 5	1,000
				6	952
				7	833
				8	740
6221	16	0.03	8,191	1	833
				2	740
6229	16	0.03	8,191	1	833
				2	740
				3	666
				4	625
6733	16	0.03	16,384	1 - 5	1,000
				6	952
				7	869
				8	769

Table 2.7 : Arbitrary waveform generation details

All cards specified are the PCI model and interface with the experiment control computer directly through the motherboard or via a PCI expansion bin (model: StarTech PEX2PCIE4L). Sample rates are given in kilosample per second (kS/s) and are the same across all enabled channels. The FIFO buffer stores the individual waveform points and is also shared amongst all enabled channels. Full voltage output range is $\pm 10\text{ V}$.

primary driver for the plethora of various cards so that we may dedicate their finite resources to specific tasks.

While arbitrary waveform generation is useful for dynamically varying voltages during an experimental sequence, there are a number of applications where a static voltage is needed or smoothly varying between two or more voltages is not required. Until recently, the NI-6713 was our only source of experimentally controlled static voltages (in contrast to a static voltage from a supply) and switching between driving voltages was done via a bank of standalone fast analog IC switches (primarily the ADG419). Fast switching of the set point voltage has traditionally been how we control a number of systems through their feedback circuitry. For example, the 922 nm frequency is jumped from the optimal trapping frequency to the optimal imaging frequency at the end of the experimental sequence via the saturated absorption cell solenoid current. The change in magnetic field shifts the resonance frequency of the loss feature and the 922 nm frequency lock responds by varying the master laser frequency to restore the resonance condition. However, the NI-6713 + switch bank limited the number of controlled static voltages to eight and the simple standalone switches were insufficient for applying application logic or dynamically choosing driving voltages[‡].

These shortcomings led us to develop a real-time based NI-FPGA for the development of custom reconfigurable logic and static voltage output. This system is based on a NI cRIO-9063 with integrated Artix-7 FPGA, a NI-9403 32ch TTL input/output (I/O) module, and a NI-9264 16ch analog output module. The cRIO device manages the control layer of the system, hosts the embedded operating system and allows us

[‡]An example of this application logic might be any set point that could be controlled via boolean logic conditioning.

to easily develop, compile, and deploy our custom control logic to the FPGA via Labview. The FPGA (field programmable gate array) executes the user-defined logic on a user-defined loop-time (minimum 50 μ s.) with the 32 TTL I/O channels and 16 analog output available for reading and writing each cycle. We typically do not use the output functionality of the TTL channels and instead opt for 32 input channels which can be dynamically assigned to control the 16 analog outputs. These analog outputs may be conditioned as static, simple switched, cascading switched, or simple boolean controlled outputs all configurable via software. Additional features include logic inputs which can be shared to multiple outputs and simple waveform generation such as linear ramps.

2.4.3 Ancillary laboratory systems

2.4.3.1 Trim coils

The trim coils are a cubic, 11.5" cage with current coils providing B-field in a Helmholtz configuration. These coils are used to trim out static residual magnetic fields and to apply dynamic and well controlled bias magnetic fields. We commonly use the coils along the Z-direction to apply bias magnetic fields during spectroscopy as shown in Fig. 2.30a.

The narrow linewidth of the 3P_1 states provide a very sensitive probe for precisely zeroing the residual magnetic field. We determine the required bias fields by performing loss spectroscopy with unpolarized light along the $^1S_0 \rightarrow ^3P_1$ transition using a bosonic isotope. Next we fit the $m_j = \pm 1$ spectral features to a loss line-shape (either Gaussian or Lorentzian) and plot the line center as a function of applied magnetic field along each dimension. Fig. 2.30b shows an example of the change in Zeeman splitting of the m_j levels using strontium-84. Finally, we perform a linear fit to the

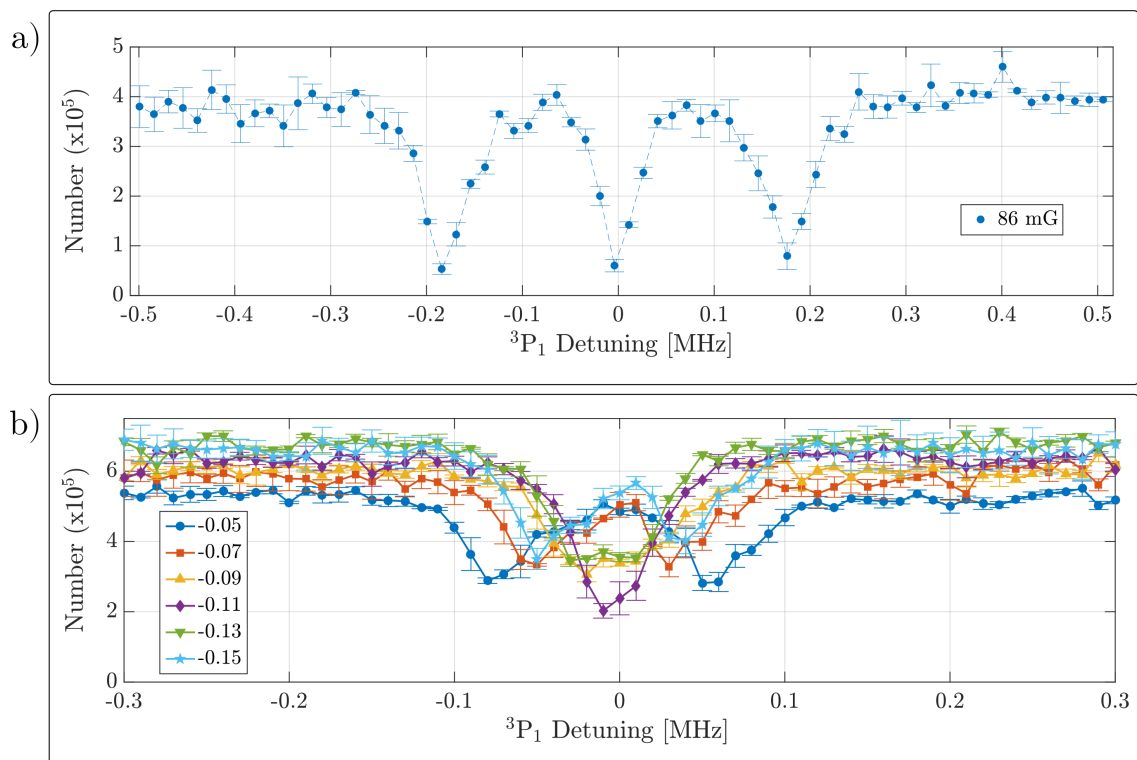


Figure 2.30 : Zeroing residual magnetic fields

Loss spectroscopy in various bias fields. a) Example of resolved Zeeman splitting of the 3P_1 magnetic sub-levels. b) Typical B field variation for determining the zero field position. The applied bias is increased for each subsequent scan and a clear zero crossing is observed. The legend has been left in arbitrary lab units to emphasize the B-field zero crossing which occurs around -0.11.

line center variation and extract the intercept which nulls the residual field and the slope which calibrates our applicable field strength per ampere. We have found these calibrations to be $[\delta B_z = 0.985, \delta B_y = 0.982, \delta B_z = 0.987]$ G/A[§].

2.4.3.2 Zero crossing AC line trigger

Fig. 2.31 shows the circuit used to start the Neutral experimental sequence. It is based on deriving a TTL pulse at the positive-going zero crossing of the 60 Hz building line. Manual triggering is essential since we do not share the same clock source between the two independent pulseblasters (PB0 & PB1). Instead relying on their relative precision and low timing jitter to maintain experimental synchronicity when triggered from a shared source.

Fig. 2.32 shows a comparison of the timing uncertainty when a short 200 ns pulse is output from both pulseblasters and the oscilloscope is triggered from the zero crossing of the AC line. While this measurement does not reveal the cause of the relative instability between the three sources (PB0, PB1, or AC line), we do observe a relative instability of $\sim 1\ \mu\text{s}$. For most use cases with ultracold matter, this timing uncertainty presents no practical limitation. However, we have observed this small jitter to lead to shot-to-shot fluctuations when timing signals for the optical lattice are mixed between the two PulseBlasters. This is due to short timescales becoming relatively more important for the evolution of a quantum state at the large energy scales accessible in a lattice. As an example, an unstable delay up to $1\ \mu\text{s}$ during the abrupt extinction of two arms of a deep lattice potential, can lead to irregular and seemingly erratic behavior of the population oscillations between plane waves.

[§]Further details available in Onenote under Research Projects → Routine Studies → B-field zeroing → Zeroing summary

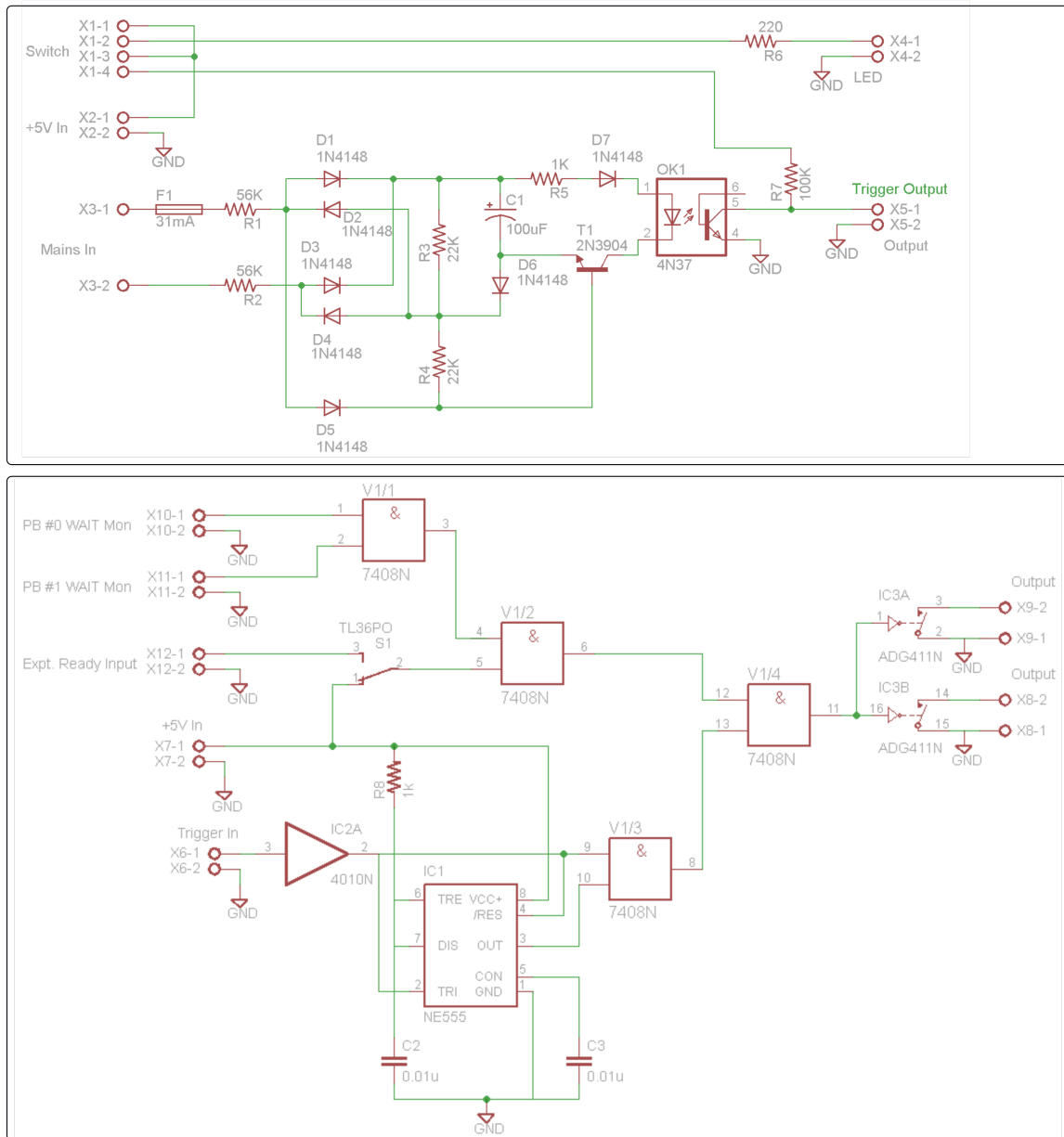


Figure 2.31 : Circuit diagram of the zero crossing AC line trigger

Top - 120 Hz square wave pulser which generates a short pulse on the 60 Hz zero crossing. Bottom - Synchronizer circuit between both pulseblasters, an optional experiment-ready trigger (which ensures the atom shutter is open), and the AC zero-crossing trigger. Trigger input is from the top circuit and is used with the 555 timer in a one-shot configuration. This ensures only every other pulse from the AC trigger produces a TTL high output past the AND gate V1/3.

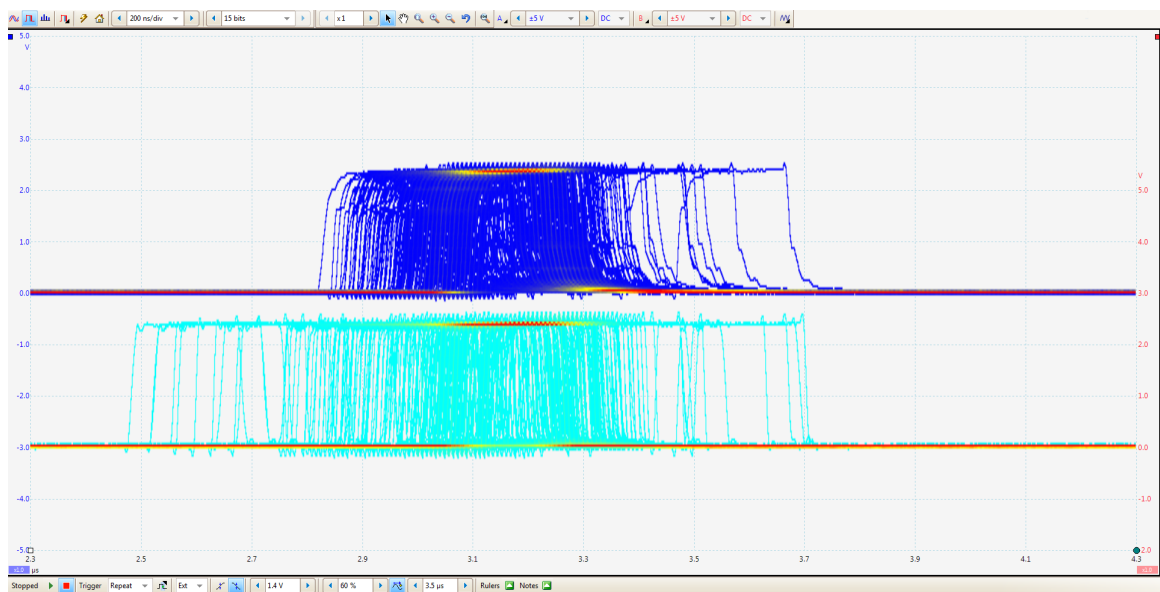


Figure 2.32 : Comparison of PulseBlaster timing jitter

A persistent oscilloscope trace showing repeated measurements of a 200 ns logic pulse from each PulseBlaster. The upper signal is PB0 and the lower is PB1. The scope is externally triggered by the zero crossing AC line trigger.

We account for and mitigate this instability by taking care to trigger all related processes from the same PulseBlaster where the timing guarantees are more stringent and timing uncertainty is reduced to 50 ns[¶].

This is similarly related to the discretization and finite sampling rate of the DAQ cards, whereby dependent on the dynamics under investigation, small errors in timing between the DAQ clock or sampling rate and PulseBlaster clock(s) may lead to significant variation in the observed behavior of the sample.

We choose to trigger off the building wide 60 Hz line in order to maintain a fixed phase relationship from shot to shot. This is thought to act as a common-mode rejection of electrical noise that could couple into our measurements via intensity or frequency noise. Although, we have not rigorously evaluated this hypothesis and no significant change was observed when changing the global experimental trigger.

Finally, the additional logic gates ensure that the pulseblasters trigger at the same time since they are programmed serially by the neuKLEIN software. This process is enabled by a WAIT signal that each PulseBlaster outputs when in this state, which is used to ensure proper initialization of the system before starting an experimental sequence.

2.4.3.3 Pneumatic actuated mirror mounts

The lattice arms in the plane of the atoms (A & B) are combined and separated along the 1064 nm ODT path using harmonic beamsplitters as shown in Fig. 6.5. Alignment of the vertical propagating beam presents a challenge as the optical access into the chamber is limited and position of the MOT beams require waveplates along the vertical axis. This places prohibitive constraints on the availability of passive optical

[¶]Quoted in the PulseBlaster specifications provided in the manual.

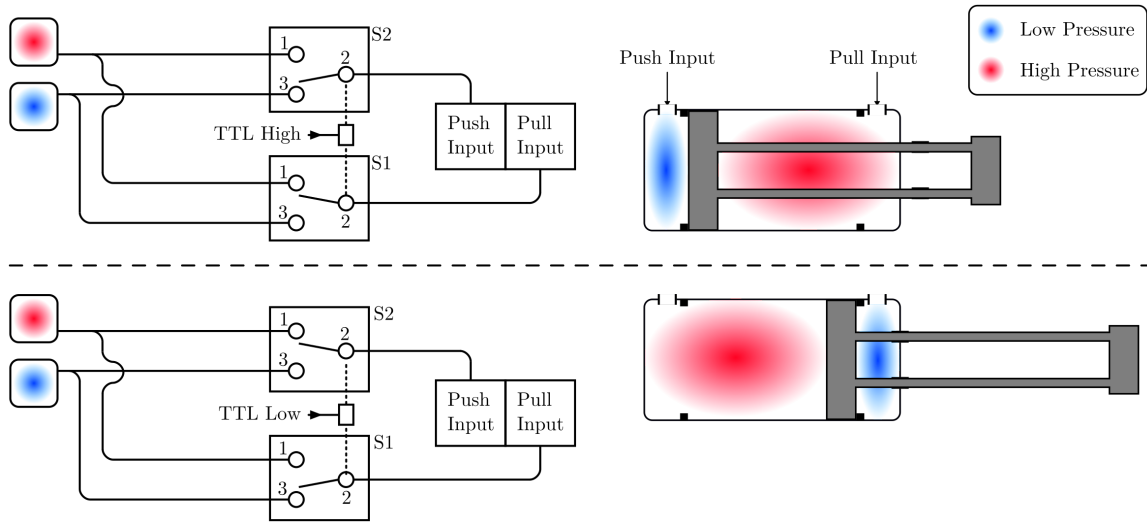


Figure 2.33 : Pneumatic actuators diagram

Example schematic for a single actuator. Three actuators are used on the apparatus to move several components simultaneously. Not shown is the 4-way cross which splits the output from each valve (S1 and S2) to each actuator.

components that might combine the MOT and lattice traps along the vertical path. To overcome this, we employ pneumatic valves and actuators to move the waveplates and requisite MOT mirrors out of the path before turning on the 532 nm light.

Fig. 2.33 shows the flow diagram for switches S1 and S2 for this system where the default position is the lower figure with the actuators extended. As one might expect, this abrupt movement does impart vibrations into to the table which we dampen by slowing the movement and cushioning the stops. In practice we find that the system is fairly robust against these small "kicks" ||.

|| Although occasionally the air pressure must be adjusted if the lasers are behaving erratically.

Chapter 3

Photoassociation in ultracold gases

3.1 Introduction

Recall from Ch. 1 that photoassociation describes the process of creating molecular states from colliding free atoms. This process tends to create long-range weakly-bound molecules due to the excitation rate of photoassociation depending on the overlap of the initial scattering state and the bound state. Fig. 3.1 illustrates the PA process outlined previously and adds schematic wavefunctions. This highlights the interparticle spacing with the strongest contribution to the overlap integral, known as the Condon point (radius) R_c , which is situated around the classical turning point of the molecule [16, 18]. Contribution to the overlap in the region $r < R_c$ is negligible due to the fast oscillations in the interior region of either wavefunction. Furthermore, the Condon point moves inward as the binding energy of the bound state molecules is increased. This causes overlap with the initial scattering state to decrease and consequently a reduction in the rate of molecular formation may be observed [88, 94, 97, 145].

Thus, while a conceptual description of photoassociation as colliding particles associating to a bound-state is straightforward, a rigorous theoretical understanding of the process requires discussion of several fundamental topics related to the behavior of ultracold gases. In particular, the rate of photoassociation of a trapped gas is sensitive to a number of energetic effects including the distribution of thermal kinetic energy,

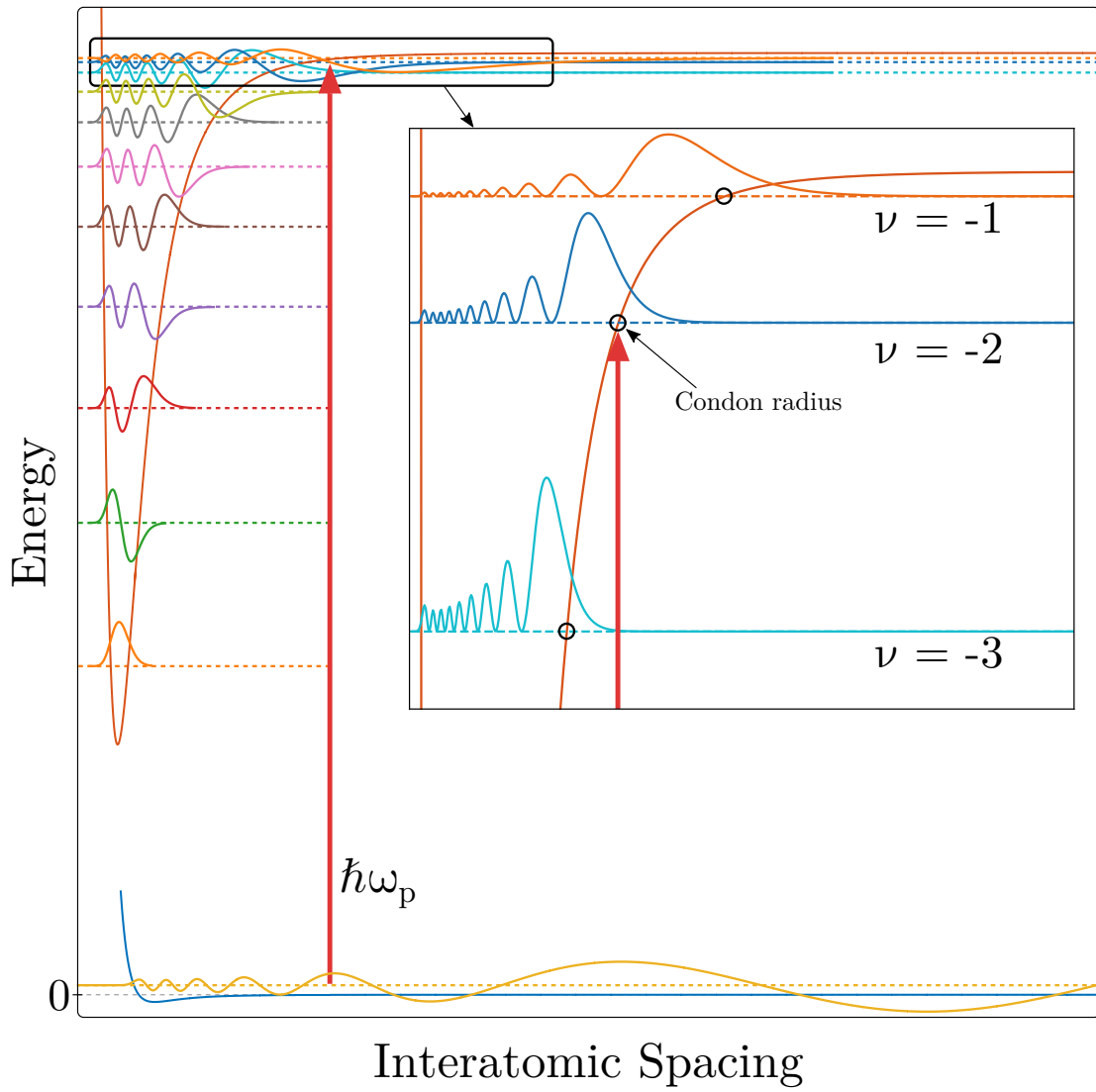


Figure 3.1 : Schematic of the photoassociation process

The photoassociation process relies on favorable overlap between the initial free particle state and the final bound state. An example incoming wavefunction at collision energy $\epsilon > 0$ is shown in yellow along the lower potential. This state is then coupled to a vibrationally excited bound-state wavefunction in the upper potential using a photoassociation laser at frequency ω_p . The inset shows the probability density of the excited states and the Condon point (radius) for each bound state.

differences in potential energy due to trapping potentials, and internal interaction energy due to interparticle scattering [97]. The remainder of this chapter will discuss these considerations and end by formulating analytic descriptions for describing one- and two-photon photoassociation spectra.

3.2 Theory of trapped boson gases

This section briefly covers the statistical mechanics describing a trapped thermal bosonic gas. From this description we discuss the evolution of the atomic densities during free expansion and discern how to extract physical parameters of the gas from absorption images.

In the limit of large, fixed particle number, the trapped density distribution $n(\mathbf{r})$ is given by

$$n_{th}(\mathbf{r}) = \int \frac{d\mathbf{p}}{(2\pi\hbar)^3} \frac{1}{\exp((E_p(\mathbf{r}) - \mu)/k_B T) - 1} \quad (3.1)$$

where $E_p(\mathbf{r}) = \frac{p^2}{2m} + V(\mathbf{r})$. This semi-classical description assumes negligible occupation of the trap ground state. This integral can be evaluated by defining the quantities

$$x = \frac{p^2}{2mk_B T} \quad z(\mathbf{r}) = e^{[\mu - V(\mathbf{r})]/k_B T} = \xi e^{-V(\mathbf{r})/k_B T}$$

where ξ is known as the fugacity [153]. After a change of variables from p to the dimensionless quantity x , Eq. 3.1 reduces to

$$n_{th}(\mathbf{r}) = \frac{2}{\sqrt{\pi}} \frac{1}{\lambda_T^3} \int dx \frac{\sqrt{x}}{z^{-1}e^x - 1} \quad (3.2)$$

where $\lambda_T = \sqrt{\frac{2\pi\hbar^2}{mk_B T}}$ is the de Broglie wavelength. This is a common integral in

problems of this type and may be rewritten as [48, 101, 153]

$$\begin{aligned} \int_0^\infty dx \frac{x^{\gamma-1}}{z^{-1}e^x - 1} &= \sum_{n=1}^\infty \int_0^\infty dx x^{\gamma-1} e^{-nx} z^n \\ &= \Gamma(\gamma) \text{Li}_\gamma[z] \end{aligned} \quad (3.3)$$

where $\text{Li}_\gamma[z]$ is the polylogarithm function defined by $\text{Li}_\gamma[z] = \sum_{n=1}^\infty \frac{z^n}{n^\gamma}$ and $\Gamma(\gamma)$ is the Euler gamma function. This function is also known as the Bose enhancement function [101] and describes the bunching of bosonic particles near degeneracy. The thermal distribution is then given by

$$\begin{aligned} n_{th}(\mathbf{r}) &= \frac{\text{Li}_{\frac{3}{2}}[z(\mathbf{r})]}{\lambda_T^3} \\ &= \frac{1}{\lambda_T^3} \text{Li}_{\frac{3}{2}}[\xi \exp(-V(\mathbf{r})/k_B T)] \end{aligned} \quad (3.4)$$

For harmonic traps $V(\mathbf{r}) = \frac{m}{2} \sum_i \omega_i^2 r_i^2$ and the *in situ* density profile is

$$n_{th}(\mathbf{r}) = \frac{1}{\lambda_T^3} \text{Li}_{\frac{3}{2}} \left[\xi \exp \left(\sum_i \frac{-m\omega_i^2 r_i^2}{2k_B T} \right) \right] \quad (3.5)$$

In the classical, or high-temperature limit, $\text{Li}_{\frac{3}{2}}[z(\mathbf{r})] \approx z(\mathbf{r})$ and we recover the classical Maxwell-Boltzmann description [153].

$$n_{MB}(\mathbf{r}) = \frac{\xi}{\lambda_T^3} \exp \left(\sum_i \frac{-m\omega_i^2 r_i^2}{2k_B T} \right) \quad (3.6)$$

3.2.1 Extracting data from column densities

This description of thermal bosons in a trapping potential is useful but we must continue a step further and see how Eq. 3.5 evolves when released from the trap and allowed to expand in free space. Once the trapping potential is removed, neglecting any collisions, atoms will follow trajectories according to

$$\frac{d\mathbf{r}}{dt} = \frac{\mathbf{p}}{m} \quad \text{and} \quad \frac{d\mathbf{p}}{dt} = 0 \quad (3.7)$$

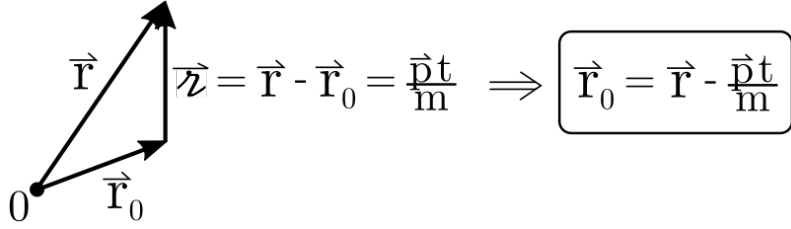


Figure 3.2 : Ballistic expansion of particles

Schematic representation particle displacement vectors used to determine how time-of-flight expansion transforms the initial density distribution

Thus, an atom measured at position \mathbf{r} after the time-of-flight, t , will have traveled a distance $\boldsymbol{\zeta} = \frac{\mathbf{p}t}{m} = \mathbf{r} - \mathbf{r}_0$ from its initial position \mathbf{r}_0 . This is shown schematically in Fig. 3.2. The spatial density then evolves to

$$\begin{aligned} n'_{th}(\mathbf{r}, t) &= \int \frac{d^3\mathbf{r} d^3\mathbf{p}}{(2\pi\hbar)^3} \frac{1}{\exp\left(\left[\frac{p^2}{2m} + V(\mathbf{r}') - \mu\right] \frac{1}{k_B T}\right) - 1} \delta^3\left(\mathbf{r} - \frac{\mathbf{p}t}{m} - \mathbf{r}'\right) \\ &= \int \frac{d^3\mathbf{p}}{(2\pi\hbar)^3} \frac{1}{\exp\left(\left[\frac{p^2}{2m} + V\left(\mathbf{r} - \frac{\mathbf{p}t}{m}\right) - \mu\right] \frac{1}{k_B T}\right) - 1} \end{aligned} \quad (3.8)$$

where $n'_{th}(\mathbf{r}, t)$ is simply the time-evolved thermal density such that $n'_{th}(\mathbf{r}, t = 0) = n_{th}(\mathbf{r})$. Adding the harmonic potential, the free expansion after release from a harmonic trap is found to be self-similar and amounts to rescaling the the spatial coordinates [48]. Thus the scaled spatial profile is given by

$$n'_{th}(\mathbf{r}, t) = \frac{1}{\lambda_T^3} \left(\prod_{j=1}^3 \frac{1}{1 + \omega_j^2 t^2} \right) \text{Li}_{\frac{3}{2}} \left[\xi \exp \left(\sum_{i=1}^3 \frac{-m\omega_i^2 r_i^2}{2k_B T} \frac{1}{1 + \omega_i^2 t^2} \right) \right] \quad (3.9)$$

From this description of the spatial distribution after time-of-flight expansion, we may now consider the relation of absorption images to the physical characteristics of the gas. Absorption imaging is a technique whereby a spatially resolved image of (resonant or near-resonant) laser light is recorded after it has passed through a gas of

atoms. When illuminated, the atomic sample will absorb and scatter photons out of the laser beam resulting in the imprint of the atoms "shadow" on the laser's recorded image. Then using Beer's law [59, 87, 160], the total absorption of photons may be related to the product of the number density of scattering particles along the optical path and the absorption cross section [128]. This results in a measurement of the "optical depth" of the gas along a column density. Notably, this measurement occurs along a particular direction through the gas, which limits our analysis of the gases properties to the two-dimensional plane orthogonal to the laser beam.

Experimentally, the optical depth (OD) is computed by taking the natural logarithm of a ratio of the images obtained from the camera (Sec. 2.3.4.1). This OD may then be fit using the analytic form of the expanded density profile in Eq. 3.9 to extract physical quantities. To see this, we equate the OD image to be proportional to the spatial density profile after the time-of-flight expansion integrated along the optical path through the atoms.

$$\begin{aligned} \text{OD} &= \ln \left(\frac{\text{Atom Image}}{\text{Background Image}} \right) = \sigma_{abs} \int_{-\infty}^{\infty} dz n'_{th}(\mathbf{r}, t) \\ &= \frac{\sigma_{abs}}{\lambda_T^3} \left(\prod_{j=1}^3 \frac{1}{1 + \omega_j^2 t^2} \right) \int_{-\infty}^{\infty} dz \text{Li}_{\frac{3}{2}} \left[\xi \exp \left(\sum_{i=1}^3 \frac{-r_i^2}{2\sigma_i^2} \right) \right] \end{aligned} \quad (3.10)$$

where $\sigma_i^2 = \frac{k_B T}{m\omega_i^2}(1 + \omega_i^2 t^2)$ and σ_{abs} is the optical absorption cross section dependent on the imaging laser frequency.

Before proceeding, let us rewrite the polylogarithm in terms of its series representation and integrate over a single dimension to replicate the column density image of the experimental data.

$$\int_{-\infty}^{\infty} dz \text{Li}_{\frac{3}{2}} \left[\xi \exp \left(\sum_{i=1}^3 \frac{-r_i^2}{2\sigma_i^2} \right) \right] = \int_{-\infty}^{\infty} dz \sum_{n=1}^{\infty} \frac{\xi^n}{n^{3/2}} \exp \left(\frac{-x^2}{2\sigma_x^2} - \frac{y^2}{2\sigma_y^2} - \frac{z^2}{2\sigma_z^2} \right)^n \quad (3.11)$$

Defining $\rho = \exp\left(\frac{-x^2}{2\sigma_x^2} - \frac{y^2}{2\sigma_y^2}\right)$ and expanding

$$= \int_{-\infty}^{\infty} dz \xi \rho e^{\frac{-z^2}{2\sigma_z^2}} + \frac{\xi^2}{2^{3/2}} \rho^2 e^{\left(\frac{-z^2}{2\sigma_z^2}\right)^2} + \frac{\xi^3}{3^{3/2}} \rho^3 e^{\left(\frac{-z^2}{2\sigma_z^2}\right)^3} + \dots \quad (3.12)$$

This expansion readily shows the dependence on z . By considering each term separately and integrating each along z , we find $\int_{-\infty}^{\infty} dz \sum_{n=1}^{\infty} \exp\left(\frac{-nz^2}{2\sigma_z^2}\right) = \frac{\sqrt{2\pi}}{n^{1/2}} \sigma_z$ [68, 101]. Rewriting Eq. 3.12 and using this result

$$\begin{aligned} &= \int_{-\infty}^{\infty} dz \sum_{n=1}^{\infty} \frac{\xi^2 \rho^n}{n^{3/2}} \exp\left(\frac{-nz^2}{2\sigma_z^2}\right) \\ &= \sqrt{2\pi} \sigma_z \underbrace{\sum_{n=1}^{\infty} \frac{\xi^n \rho^n}{n^2}}_{\text{Li}_2[\xi \rho]} \end{aligned} \quad (3.13)$$

Returning to Eq. 3.9, the optical depth is given by

$$OD(x, y) = \frac{\sqrt{2\pi}}{\lambda_T^3} \sigma_{abs} \sigma_z \left(\prod_{j=1}^3 \frac{1}{1 + \omega_i^2 t^2} \right) \text{Li}_2\left[\xi \exp\left(\frac{-x^2}{2\sigma_x^2} - \frac{y^2}{2\sigma_y^2}\right)\right] \quad (3.14)$$

This equation still has one unknown, σ_z , that we cannot readily measure. This is overcome by measuring a specific value of the optical depth, the peak optical depth, $OD_{\text{peak}} = OD(x=0, y=0)$.

$$OD_{\text{peak}} = \frac{\sqrt{2\pi}}{\lambda_T^3} \sigma_{abs} \sigma_z \left(\prod_{j=1}^3 \frac{1}{1 + \omega_i^2 t^2} \right) \text{Li}_2[\xi] \quad (3.15)$$

Thus the relation between the measured optical depth and the spatial density distribution is given by

$$OD(x, y) = \frac{OD_{\text{peak}}}{\text{Li}_2[\xi]} \text{Li}_2\left[\xi \exp\left(\frac{-x^2}{2\sigma_x^2} - \frac{y^2}{2\sigma_y^2}\right)\right] \quad (3.16)$$

with $\sigma_i^2 = \frac{k_B T}{m \omega_i^2} (1 + \omega_i^2 t^2)$. In the limit of long expansion time during time-of-flight, namely $t \gg \omega_x^{-1}, \omega_y^{-1}, \omega_z^{-1}$ then the widths approach $\sigma_i^2 \rightarrow \frac{k_B T}{m} t^2$. From this long-time expansion, the atom temperature is given along each axis by

$$T_i = \frac{m \sigma_i^2}{k_B t^2} \quad (3.17)$$

In general, the limiting factor for the maximum allowed expansion time is caused by center-of-mass motion of the cloud under the influence of gravity. On the Neutral apparatus, we typically utilize drop times $\approx 30\text{ ms}$ before we are no longer able to view the atoms. For shallow traps, ω_i on the order of $< 10\text{ Hz}$, the applicability of the above long-time approximation should be verified before claiming temperatures, as cold atoms may not approach the long-time limit of expansion, $\omega_i^2 t^2 \gg 1$, before falling out of frame.

Finally, we determine the total number of atoms in the trapping potential by formally requiring the particle number to be fixed as $n_{th}(\mathbf{r}) \Rightarrow n'_{th}(\mathbf{r}, t)$.

$$\begin{aligned} N &= \int_{-\infty}^{\infty} d^3\mathbf{r} n_{th}(\mathbf{r}) = \int_{-\infty}^{\infty} d^3\mathbf{r} n'_{th}(\mathbf{r}, t) \\ &= \int_{-\infty}^{\infty} d^3\mathbf{r} \frac{\sigma_{abs}}{\lambda_T^3} \left(\prod_{j=1}^3 \frac{1}{1 + \omega_i^2 t^2} \right) \sum_{n=1}^{\infty} \frac{\xi^n}{n^{3/2}} \exp \left(-\frac{x^2}{2\sigma_x^2} - \frac{y^2}{2\sigma_y^2} - \frac{z^2}{2\sigma_z^2} \right)^n \end{aligned} \quad (3.18)$$

Applying the same expansion and identity as in Eq. 3.12, then

$$N = \frac{(2\pi)^{3/2}}{\lambda_T^3} \sigma_{abs} \left(\prod_{j=1}^3 \frac{\sigma_i}{1 + \omega_i^2 t^2} \right) \text{Li}_3[\xi] = 2\pi \frac{\sigma_x \sigma_y}{\sigma_{abs}} OD_{\text{peak}} \frac{\text{Li}_3[\xi]}{\text{Li}_2[\xi]} \quad (3.19)$$

3.3 Atomic collisions

Atomic collisions may be envisioned as an interferometer of the incoming and outgoing waves due to reflection by the short-range interatomic potential [94]. Through interference of these waves, a standing wave pattern is established that extends infinitely far into space. With this picture in mind, we begin to understand how the effects of short-range couplings between atoms can influence their long-range behavior, as any small change in the "interferometer" is reflected across the entire far-reaching wavefunction. Fig. 3.3 shows several examples of scattering state wavefunctions at various energies that illustrate the effect of the potential.

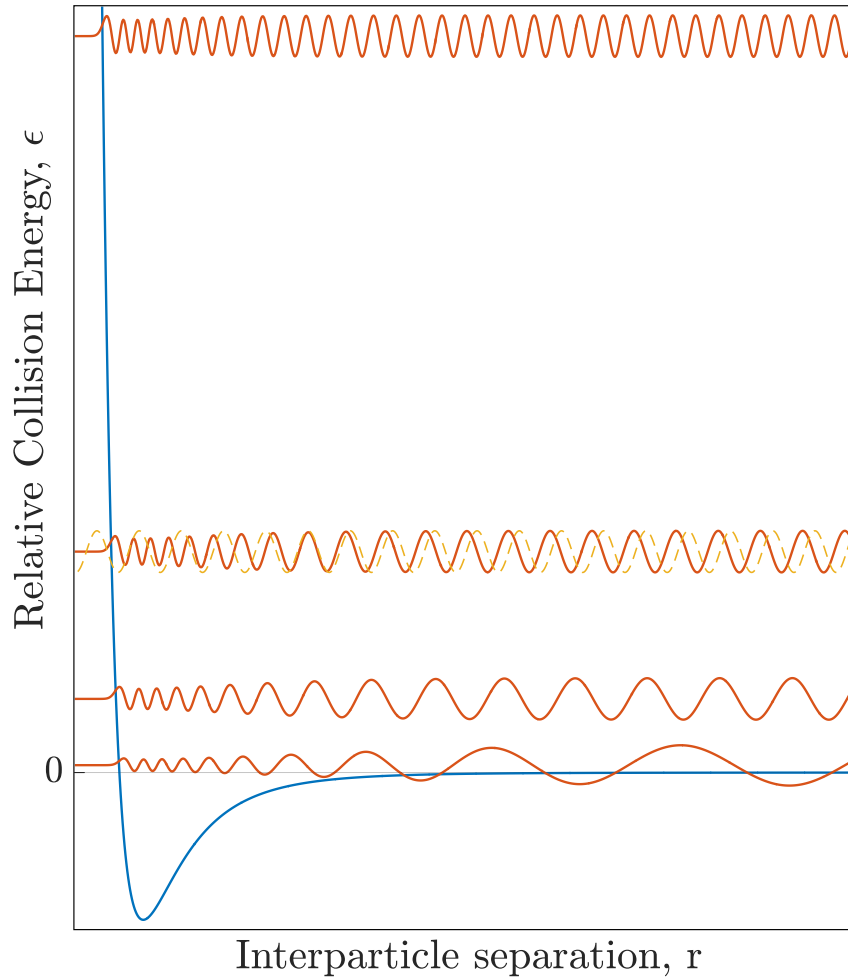


Figure 3.3 : Examples of scattering state solutions

Schematic examples of scattering states for several different collision energies undergoing single-channel scattering. At high collision energy the incoming wavefunction is not significantly perturbed by the $\epsilon < 0$ part of the potential and simply reflects off the barrier. As collision energy is decreased, the potential begins to effect the incoming wave and results in a compression of the local de Broglie wavelength, $\lambda_{\text{local}} = 2\pi\hbar/\sqrt{2\mu(E - V(r))}$, in the vicinity of the well. Note, the dashed line shown with the middle scattering state is the unscattered wavefunction for comparison. The phase shift, resulting from scattering from the potential, is apparent as $r \rightarrow \infty$.

A notable achievement of atomic collision theory has been the successful separation of the scattering interaction into regions that exhibit very different characteristic length and energy scales [97]. Through this separation, a great deal of insight has led to the development of many practical methods for studying the scattering states and weakly-bound molecular states near zero-energy [16, 63, 64, 97, 99, 136, 192, 194]. In the following, we will outline the critical results of these treatments of atomic collisions.

3.3.1 Single channel scattering near threshold

Consider the collision of two structureless atoms interacting by a single adiabatic Born-Oppenheimer potential, which at long-range is described by a van der Waals potential, $V(r)_{\text{long}} = -\frac{C_6}{r^6}$. We are interested in understanding the van der Waals interaction as it is the dominant term in the long-range interaction between two ground state neutral atoms. This potential has a characteristic length, $R_{\text{vdW}} = \frac{1}{2} \left(\frac{2\mu C_6}{\hbar^2} \right)^{1/4}$, and energy, $E_{\text{vdW}} = \frac{\hbar^2}{2\mu R_{\text{vdW}}^2}$. However, the closely related characteristic scales from Gribakin and Flambaum [17, 75] prove to be more useful

$$\bar{a} = \frac{4\pi}{\Gamma(1/4)^2} R_{\text{vdW}} \quad \bar{E} = \frac{\hbar^2}{2\mu \bar{a}^2} \quad (3.20)$$

where $\Gamma(x)$ is the Euler Gamma function. The wavefunction for relative motion is found by solving the radial Schrödinger equation

$$-\frac{\hbar^2}{2\mu} \frac{d^2\phi_\ell}{dr^2} \left(V(r) + \frac{\hbar^2 \ell(\ell+1)}{2\mu r^2} \right) \phi_\ell = E \phi_\ell \quad (3.21)$$

Solutions of Eq. 3.21, for energies $E > 0$, are scattering states $\phi_\ell(E)$ with collision wavevector $k = \sqrt{2\mu E / \hbar^2}$. In the region $r \gg \bar{a}$, the scattering states approach the free particle states but with the additional phase shift η_ℓ

$$\phi_\ell(E) \rightarrow \frac{\sin(kR - \pi\ell/2 + \eta_\ell)}{\sqrt{k}} \quad (3.22)$$

with de Broglie wavelength $\lambda = 2\pi/k$. Fig. 3.4 gives an example scattering state for ^{86}Sr undergoing a collision at 10 nK. Note the significant differences in length-scales between each result despite the range of the interaction being restricted to $< 100 \text{ a}_0$.

A physical intuition for origin of the phase shift η_ℓ in Eq. 3.22 may be gained by considering the scattering state ϕ_ℓ for different energies as shown in Fig. 3.3. Starting with atoms in the asymptotic region, where the interparticle spacing is large, we see that for atoms approaching one another with low energy, as they near $r \sim \bar{a}$ they begin to be accelerated by the interatomic potential due to increasing potential energy. This acceleration results in a compression of the local de Broglie wavelength to $\lambda_{\text{local}} = 2\pi\hbar/\sqrt{2\mu(E - V(r))}$ which in turn results in a change of the overall phase of the wavefunction as the scattered state wavelength is pulled inward relative to the unscattered state wavefunction. In the limit $E \rightarrow 0$, $V(R)$ becomes the dominant energy scale such that $E - V(r) \approx V(r)$ and the local de Broglie wavelength becomes independent of the incident energy. Therefore near threshold, small changes in the relative collision energy do not compress the wavefunction any further in the region $r \lesssim \bar{a}$ and the imparted phase shift, due to acceleration by the potential, is constant. This is the origin of the *s*-wave scattering length, a . The scattering phase shift may be related to the *s*-wave scattering length a by

$$a = -\frac{\tan \eta_0(k)}{k} \quad (3.23)$$

where $\eta_{\ell=0}$ is the additional phase in Eq. 3.22 and $k = \sqrt{2\mu E/\hbar^2}$ is the collision wavevector. The value of the *s*-wave scattering length may also be seen as a measure of the peak-to-peak shift between the asymptotic wavefunction and the unscattered wavefunction at long-range as shown in Figs. 3.3 & 3.4. Finally, as energy is increased, the effect of the potential on the scattering state is reduced and the de Broglie wavelength once more remains constant, at a specific energy, for all interatomic distances.

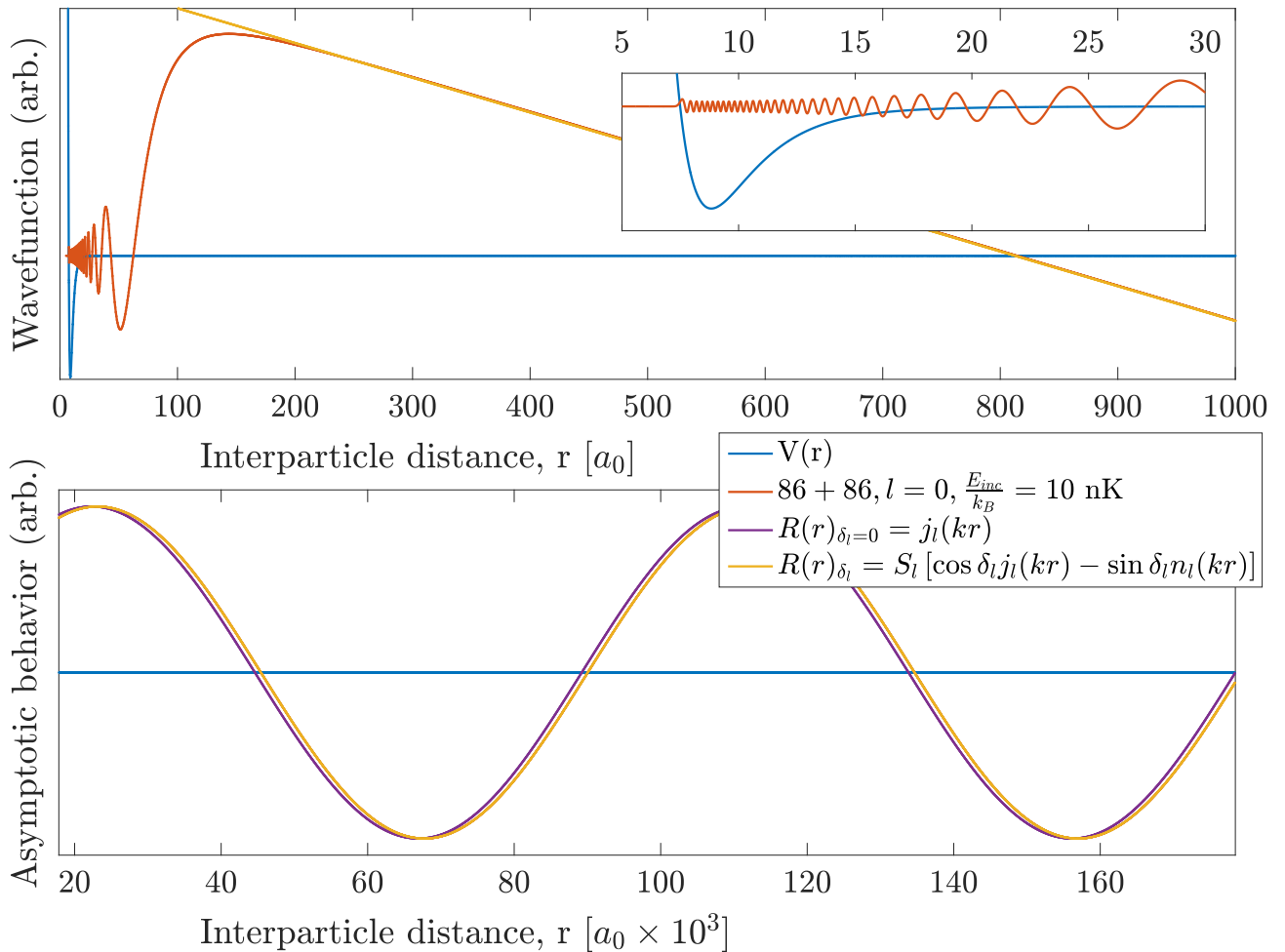


Figure 3.4 : ^{86}Sr radial scattering wavefunction near $E = 0$

The radial wavefunction for $\ell = 0$ at $E/k_B = 10 \text{ nK}$ for a colliding pair of strontium-86 atoms. The top panel shows the region of the wavefunction near the last node which is related to the s -wave scattering length. The inset shows a close up view of the wavefunction in the short-range portion of the $X^1\Sigma_g^+$ ground state potential where the oscillations and amplitude of the wavefunction are strongly effected by the potential. In the asymptotic range, shown in the bottom panel, the scattered wavefunction (red) and the asymptotic free particle state (yellow) are overlapping and shifted with respect to the unscattered free particle wavefunction (purple). Note that the form of the asymptotic wavefunctions given in the legend is equivalent to that given in Eq. 3.22 [77, 168].

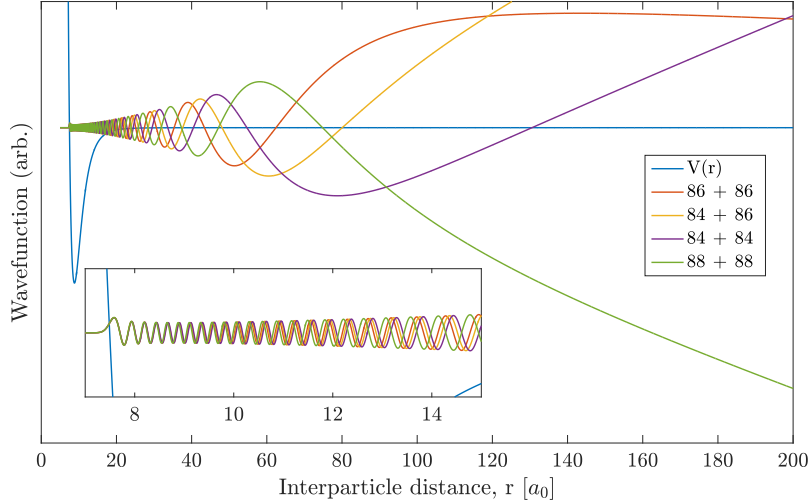


Figure 3.5 : Effects of mass-scaling on strontium scattering wavefunctions

Varying the reduced mass of the colliding particles leads to vastly different scattering properties between the atoms. From the inset, the wavefunctions start with the same amplitude and phase and quickly begin to oscillate at different frequencies due to the mass differences leading to the large differences in the asymptotic wavefunctions.

From this simple physical picture, we can also understand how changing a particle's mass will effect it's scattering behavior. Changes to the reduced mass μ while keeping $V(r)$ fixed, also lead to a change in the local de Broglie wavelength since $\lambda_{\text{local}} = 2\pi\hbar/\sqrt{2\mu(E - V(r))}$ and therefore a change in the s -wave scattering length. This approach of mass-scaling to predict the scattering lengths of various isotopes of many atomic species has been remarkably successful and narrowed the problem of modeling atomic collisions to one of measuring the interaction potential [97]. Fig. 3.5 shows the effect of mass-scaling for a selection of strontium isotopic combinations.

Moreover, a change in the reduced mass is not isolated to affecting the scattering states. For bound states, a change in μ will result in shifting of the binding energies as

the solutions to Eq. 3.21 when $E < 0$ will also be different. In some cases this may even lead to changing the number of supported states within the potential well. Gribakin and Flambaum [75] calculated the relationship between the s -wave scattering length and the van der Waals potential to be

$$a = \bar{a} \left[1 - \tan\left(\Phi - \frac{\pi}{8}\right) \right] \quad (3.24)$$

where

$$\Phi = \int_{R_i}^{\infty} \sqrt{\frac{-2\mu V(R)}{\hbar^2}} \quad (3.25)$$

and R_i is the inner turning point of the potential where $V(R_i) = 0$. The binding energy of the least-bound state of a potential plays an important role in the characterization of scattering from a potential. In the simplest approximation, the s -wave scattering length and the binding energy of the least-bound state are related by

$$E_{-1} = -\frac{\hbar^2}{2\mu a^2} \text{ as } a \rightarrow +\infty \quad (3.26)$$

However, accounting for the phase accumulation due to the long-range part of the van der Waals potential modifies the binding energy with \bar{a} [75].

$$E_{-1} = -\frac{\hbar^2}{2\mu(a - \bar{a})^2} \quad (3.27)$$

This approaches the universality limit when $a \gg \bar{a}$. Higher-order analytical corrections to the van der Waals potential have also been worked out [64], which relate the binding energy and scattering length through

$$E_{-1} = -\frac{\hbar^2}{2\mu(a - \bar{a})^2} \left[1 + \frac{g_1 \bar{a}}{a - \bar{a}} + \frac{g_2 \bar{a}^2}{(a - \bar{a})^2} + \dots \right] \quad (3.28)$$

where $g_1 = \frac{\Gamma(1/4)^4}{6\pi^2} - 2$ and $g_2 = \frac{5g_1^2}{4} - 2$. Ch. 5 will employ each of these estimates in analysis of the $^{86}\text{Sr}_2$ halo molecule.

3.3.2 Remarks on S -matrix

In the previous section, we focused on interactions restricted to a single channel without any decay mechanism. Such interactions are necessarily elastic as the two-body scattering wavefunction cannot couple outside of its originating channel. However, most atoms used in laser-cooling exhibit a high degree of internal structure and a quantitative description of their short-range interactions requires consideration of coupling among many different channels. While a full characterization of such methods is left to Refs.[35, 77, 89, 148, 157, 191], here we give the high-level results which will be useful for describing photoassociation in the next section.

In this formalism, atoms are considered to be initially prepared in a single quantum state, which may be characterized by several quantum numbers. This state is labeled the entrance channel and defined to have energy $E = 0$ in the limit $r \rightarrow \infty$. Scattering channels are specified by a collective set of quantum numbers, α , which represents the state of both atoms in the collision. Channels with $E > 0$ are labeled closed, while those with $E < 0$ are open. Upon solving a matrix formulation of the Schrödinger equation, the effect of all short-range interactions due to scattering with relative collision energy $E > 0$ is summarized in the unitary S -matrix, and reflected in the scattering wavefunctions as $r \rightarrow \infty$. Thus the S -matrix is the generalization of the energy-dependent phase shift, $\eta_\ell(k)$, across all the channels [97].

In the case of a single open channel scattering near threshold the S -matrix is reduced to a single element $S(k) = e^{2i\eta(k)}$ represented by the complex energy-dependent phase shift $\eta(k)$. This phase shift also defines a complex energy-dependent scattering length

$$\alpha(k) = a(k) - ib(k) = -\frac{\tan \eta_0(k)}{k} = \frac{1}{ik} \frac{1 - S(k)}{1 + S(k)} \quad (3.29)$$

This is an incredibly useful result in the theory of magnetic and optical Feshbach resonances, the latter of which is closely related to photoassociation [35, 148].

Finally, the S -matrix is related to the elastic and inelastic cross sections by [150]

$$\sigma_{\alpha}^{\text{el}}(k) = \frac{\pi g_{\alpha}}{k^2} |1 - S_{\alpha\alpha}(k)|^2 \quad (3.30)$$

$$\sigma_{\alpha}^{\text{in}}(k) = \frac{\pi g_{\alpha}}{k^2} (1 - |S_{\alpha\alpha}(k)|^2) \quad (3.31)$$

where g_{α} is a channel specific collisional symmetry factor which is equal to 2 for describing inelastic collisions in a Maxwellian gas of two atoms of the same species in identical spin states [35].

3.4 Modeling of photoassociation lineshapes

This section develops the theory used to describe one- and two-photon photoassociative spectra with a focus on developing the equations necessary for modeling atomic-loss lineshapes presented in the following chapters.

Recall the classical result for the rate of two-body collisions in a mono-energetic gas is given by $\Gamma = v \sigma n = Kn$, where v is the velocity of each particle, σ is the scattering cross-section, and n is the particle density. Here K is identified as the two-body collision rate constant, which for inelastic collisions governs the evolution of the density through $\dot{n} = -Kn^2$.

Similarly, for scattering of quantum particles, the inelastic collision rate constant* for a specific channel α , is given by [148]

$$K_{\alpha}^{\text{in}}(k) = v \sigma_{\alpha}^{\text{in}}(k) \quad (3.32)$$

*also called the loss rate constant in literature

where $v = \hbar k \mu$ is the relative collision velocity in the center-of-mass frame for the atom pair with reduced mass μ and $\sigma_\alpha^{in}(k)$ is given by Eq. 3.31. We see that the inelastic cross section simply characterizes the coupling of channel α to all other channels by recalling that the scattering S -matrix is unitary and thus

$$1 - |S_{\alpha\alpha}|^2 = \sum_{\alpha' \neq \alpha} |S_{\alpha\alpha'}|^2 \quad (3.33)$$

In the case of ultracold photoassociation, we are concerned with the evolution of a single ground state undergoing s -wave collisions that is coupled to one or few internal states leading to decay. Thus, at a fixed collision energy $\epsilon = \hbar^2 k^2 / 2\mu$, the loss rate constant due to inelastic collisions may be written as

$$K_{\text{loss}}(k) = g \frac{\pi \hbar}{\mu k} \sum_{\alpha' \neq \alpha} |S_{\alpha\alpha'}|^2 \quad (3.34)$$

Finally, in order to compare to experimental data, we must consider a thermal average of the loss rate constant given by [88, 96, 97]

$$\begin{aligned} \langle K \rangle_{\text{thermal}} &= \int_0^\infty d^3 \mathbf{v} f_{v,\text{two}}(\mathbf{v}) |\mathbf{v}| \sigma_{in} \\ &= \int_0^\infty d\epsilon f_{E,\text{two}}(\epsilon) g \frac{\pi \hbar}{\mu} \frac{\hbar}{\sqrt{2\mu\epsilon}} \sum_{\alpha' \neq \alpha} |S_{\alpha\alpha'}|^2 \\ &= \frac{g}{h Q_T} \int_0^\infty d\epsilon \sum_{\alpha' \neq \alpha} |S_{\alpha\alpha'}|^2 e^{-\epsilon/k_B T} \end{aligned} \quad (3.35)$$

where $Q_T = \left(\frac{2\pi k_B T \mu}{\hbar^2}\right)^{3/2}$ is the partition function. Here we have performed a change of variables using $\epsilon = \mu v^2 / 2$. Eq. 3.35 assumes the relative collision energy distribution, $f_{E,\text{two}}(\epsilon)$, is a Maxwell-Boltzmann distribution.

$$f_{E,\text{two}}(\epsilon) = \frac{2}{\sqrt{\pi}} \frac{\sqrt{\epsilon}}{(k_B T)^{3/2}} e^{-\epsilon/k_B T} \quad (3.36)$$

With the expression for $\langle K \rangle_{\text{thermal}}$ in Eq. 3.35, a description of photoassociation reduces to determining the relevant channel couplings and matrix elements needed from

the scattering S -matrix. The general approach when evaluating the S -matrix for scattering problems involving two or more channels is the coupled-channel method [88]. Alternatively, analytic approximations for S may be found if the scattering problem can be considered in the isolated resonance regime. The isolated resonance approximation assumes that each molecular bound state is far from any molecular states and can be described by a local strength parameter independent of energy and molecular detuning [16, 148]. Photoassociation is well described by an isolated resonance treatment as specific resonances are targeted and the number of relevant channels is relatively few. For the case of one- and two-color photoassociation, Bohn and Julienne have derived approximate analytic expressions of the S -matrix elements by considering a multi-channel description of resonant scattering and applying an isolated resonance type treatment to approximate the wavefunctions in all channels [15, 16, 98].

One- and two-photon PAS of ultracold atoms may be modeled by first considering the evolution of a local density given by

$$\dot{n} = -Kn^2 - \Gamma_1 n \quad (3.37)$$

where Γ_1 is the one-body loss rate due to background collisions and K is the two-body loss rate constant. Integrating over the trapping volume, the evolution of the total number of trapped atoms is then

$$N(t) = \frac{N_0 e^{-\Gamma_1 t}}{1 + \frac{2N_0 \langle K \rangle V_2}{\Gamma V_1^2} (1 - e^{-\Gamma_1 t})} \quad (3.38)$$

where N_0 is the initial number of trapped atoms, $\langle K \rangle$ is an averaged loss rate constant, and V_q is the effective trap volume given by

$$V_q = \int_V d^3 \mathbf{r} \exp \left(-\frac{qU(\mathbf{r})}{k_B T} \right), \quad (3.39)$$

for trapping potential $U(\mathbf{r})$. A derivation of these trapping volumes is given in App. B.

In one-color photoassociation, a single laser at frequency ω_1 couples pairs of colliding ground state atoms with relative kinetic energy ϵ to an excited bound state b_1 with energy E_{b1} and decay rate γ_1 . Here, $\Delta_1 = \omega_1 - E_{b1}/\hbar$ is used to characterize the single photon detuning from the target state. Following the approach of Bohn and Julienne [16], the theoretical description of the bound state b_1 is modeled as being coupled to an artificial, purely repulsive, potential a_1 used to simulate decay from the bound state. State b_1 is then allowed to couple to both the artificial channel and the ground state, while the ground state is defined to only couple to state b_1 [†]. Thus the scattering probability $|S_{\epsilon,a_1}|^2$ is the only relevant S -matrix element for describing inelastic loss due to one-photon PAS. This matrix element characterizes the probability that an atom pair in the ground state with relative collision energy ϵ scatters into the loss channel a_1 and is given by

$$|S_{\epsilon,a_1}|^2 = \frac{\gamma_1 \gamma_s(\epsilon)}{(\Delta_1 + \epsilon/\hbar)^2 + \left(\frac{\gamma_1 + \gamma_s(\epsilon)}{2}\right)^2} \quad (3.40)$$

where $\gamma_s(\epsilon)$ is the stimulated width of b_1 due to coupling to the initial scattering state by the PAS lasers, which for low energy can be expressed as [21, 40, 150, 151]

$$\gamma_s(\epsilon) = 2k\ell_{\text{opt}}\gamma_1, \quad (3.41)$$

Where $k = (2\mu\epsilon)^{1/2}/\hbar$ and the optical length ℓ_{opt} parameterizes the coupling strength between the scattering states and the bound state b_1 and is related to the overlap between them. Plugging $|S_{\epsilon,a_1}|^2$ into Eq. 3.35 then the thermally averaged loss rate constant for one-photon PA is given by

$$\langle K \rangle_{\text{thermal}} = \frac{g}{h Q_T} \int_0^\infty d\epsilon e^{-\epsilon/k_B T} \frac{\gamma_1 \gamma_s(\epsilon)}{(\Delta_1 + \epsilon/\hbar)^2 + \left(\frac{\gamma_1 + \gamma_s(\epsilon)}{2}\right)^2} \quad (3.42)$$

[†]This is discussed near Eq. 3.1 for one-photon PA scattering matrix in [16]

Similarly, two-color photoassociation also considers pairs of colliding atoms undergoing collisions in the presence of light fields. In this scenario, an additional laser at frequency ω_2 is applied to couple a transition between state b_1 and another bound state b_2 with energy E_{b2} and decay rate γ_2 . However, whereas in one-color PAS the frequency ω_1 is swept across the resonant energy of the bound state b_1 , two-color PAS is most commonly performed in the Raman regime with a fixed intermediate state detuning $\Delta_1 = \omega_1 - E_{b1}/\hbar$ from b_1 . The two-photon detuning is given by $\Delta_2 = \omega_1 - \omega_2 - E_{b2}/\hbar$. As before, the bound states b_1 and b_2 are coupled to artificial loss channels a_1 and a_2 respectively. Thus the relevant scattering probabilities for two-color PAS are $|S_{\epsilon,a_1}|^2$ and $|S_{\epsilon,a_2}|^2$. Plugging these into $\langle K \rangle_{\text{thermal}}$, a formal form of the loss rate constant is specified by

$$\langle K \rangle_{\text{thermal}} = \frac{g}{h Q_T} \int_0^\infty d\epsilon [|S_{\epsilon,a_1}|^2 + |S_{\epsilon,a_2}|^2] e^{-\epsilon/k_B T} \quad (3.43)$$

where the explicit form of the matrix elements, $S_{\epsilon,a_i}(\epsilon, \gamma_1, \gamma_2, \omega_1, \omega_2, \dots)$, may be found in equations 4.8 and 4.9 of Ref. [16].

Typically, a simplifying assumption is applied to Eq. 3.43 by considering loss from the state b_2 at rate γ_2 to be negligible on the experimental timescales or in comparison to loss due to scattering from b_1 . While this is usually a valid assumption for PAS in alkali systems, it is not necessarily true in alkaline-earth system when using bound states of a narrow intercombination line transition as the two-photon intermediate state. However, taking $\gamma_2 = 0$, we recover the standard expressions for two-photon PA with scattering probability [94, 118, 146, 150].

$$|S_{\epsilon,a_1}|^2 = \frac{(\Delta_2 + \epsilon/\hbar)^2 \gamma_1 \gamma_s}{\left[(\Delta_1 + \epsilon/\hbar + \delta_1)(\Delta_2 + \epsilon/\hbar) - \frac{\Omega_{12}^2}{4} \right]^2 + \left[\frac{\gamma_1 + \gamma_s}{2} \right]^2 (\Delta_2 + \epsilon/\hbar)^2} \quad (3.44)$$

which includes a shift of the intermediate state Δ_1 induced by laser 1 and the molecular Rabi frequency between states b_1 and b_2 . Finally, the thermally averaged loss

rate constant simplifies to

$$\langle K \rangle_{\text{thermal}} = \frac{g}{h Q_T} \int_0^\infty d\epsilon |S_{\epsilon,a_1}|^2 e^{-\epsilon/k_B T} \quad (3.45)$$

3.4.0.1 PAS near narrow intercombination transitions

In the previous section, Eq. 3.35 was presented with an implicit assumption that the loss rate is dependent only on the relative collision energy distribution. This is, once again, typically a good approximation for photoassociation with alkali atoms using dipole-allowed transitions, as the consideration of single-particle kinetic energy may be neglected due to the natural width of the transition dominating small shifts due to Doppler effect or photon recoil. On the other hand, photoassociation to bound states near a narrow intercombination line transitions may exhibit sensitivity to Doppler shifts and photon recoil due to the long-lifetime of the excited molecular state, which will effect the observed photoassociative lineshape [21, 41, 148, 150, 164].

PAS lineshapes utilizing such transitions is described by considering both the center-of-mass momentum of particle pairs in addition to the relative-momentum. We proceed by considering the individual momenta of each particle using Eq. 3.35 written as a thermal average,

$$\langle K \rangle_{\text{thermal}} = \int_0^\infty d^3 \mathbf{p}_1 \int_0^\infty d^3 \mathbf{p}_2 \frac{2\pi\hbar^2}{\mu|\mathbf{p}_1 - \mathbf{p}_2|} f_{\text{p,two}}(\mathbf{p}_1, \mathbf{p}_2) |S(\mathbf{p}_1, \mathbf{p}_2, \omega_1, \omega_2, \dots)|^2 \quad (3.46)$$

Assuming that particle collisions are not correlated, or equivalently, that collisions occur rapidly enough that \mathbf{p}_1 and \mathbf{p}_2 are independent, then the two-particle momentum distribution function, $f_{\text{p,two}}(\mathbf{p}_1, \mathbf{p}_2)$, is written as the product of two single-particle

distributions [26, 37, 53].

$$\begin{aligned} f_{\text{p,two}}(\mathbf{p}_1, \mathbf{p}_2) &= f_{\text{p,one}}(\mathbf{p}_1)f_{\text{p,one}}(\mathbf{p}_2) \\ &= \left(\frac{1}{2\pi m k_B T} \right)^3 \exp \left(\frac{-(p_1^2 + p_2^2)}{2m k_B T} \right) \end{aligned} \quad (3.47)$$

where m is the single-particle mass for a sample at temperature T .

Eq. 3.46 may be reduced to the earlier equations for $\langle K \rangle_{\text{thermal}}$ by performing a coordinate transform into center-of-mass and relative coordinates and integrating over the center-of-mass, as shown in App. A.1. We will consider a special case of this procedure in Ch. 5 when discussing the truncation of the single-particle kinetic energy and how this truncation effects the relative collision energy distribution in a trapped gas.

We've taken care to note this specific example of considering the center-of-mass momentum, as our approach to the treatment of single-particle kinetic energy truncation was informed and motivated by this common consideration for one-photon intercombination line PAS in strontium. Although, we emphasize that for these particular two-photon experiments, we are not sensitive to Doppler shifts or photon recoil. Refs. [21, 41] develop a rigorous extension of the standard Bohn and Julienne theory for one-photon photoassociation near an intercombination line which accounts for Doppler broadening and photon recoil.

Chapter 4

High-intensity photoassociation spectroscopy of a halo molecule

4.1 Probing the ground state potential

In this chapter we study the least-bound vibrational level of the $X^1\Sigma_g^+$ electronic ground state of the $^{86}\text{Sr}_2$ dimer in a high-intensity regime. Previous studies of the molecular states of the $X^1\Sigma_g^+$ ground state potential have been performed using strontium-88, due to its high natural abundance, and strontium-84, because of it's amenable scattering properties. [120, 121, 161, 162, 177].

This work presents the first two-photon photoassociation study of the ground state of ^{86}Sr . All previous PA experiments with this isotope have been one-photon photoassociation to excited electronic states [21, 130, 164]. The large *s*-wave scattering length, $\sim 800 \text{ a}_0$, for this isotope is indicative of a near-threshold bound state known as a halo molecule. Direct photoassociation to this halo state revealed several unanticipated phenomena including AC Stark shifts comparable to the halo molecule binding energy and multi-photon resonance processes [107].

The experiments presented in this chapter are expanded upon in Ch. 5 with a low-intensity study that precisely determined the halo binding energy. In these initial experiments, we explore some of the novel effects of photoassociation to a halo state with a focus on understanding the AC Stark shifts and developing a useful theoretical framework for describing this unique photoassociation regime.

As discussed in previous chapters, two-photon PAS can be used to directly populate molecular levels and may be described with the formalism of Bohn and Julienne [16]. However, this approach assumes the two driving lasers are of sufficiently different frequencies that each independently drives a specific transition, as in the typical Λ -model [15, 197]. In the regime of PAS to a halo state, the laser frequencies differ by only up to ~ 300 kHz, much smaller than the typical intermediate state detuning of several MHz. Thus, both lasers must be considered to act on each leg of the transition simultaneously. The effects of this two-frequency coupling were explored through a collaboration with the theory group of Kaden Hazzard to develop simple models that are able to reproduce the key experimental observations and features.

In the following, we present the experimental results of high-intensity PAS to the halo state and develop lineshape models based on the theory of Bohn and Julienne to extract the halo state binding energy. Next, we'll compare our experimental data to numerical simulations of a three-level model. This model subsequently becomes the basis of a Floquet treatment which results in an analytic form for describing and predicting AC Stark shifts of the halo state. This is used to consider the observed frequency dependence of the halo state energy and estimate the bound-bound coupling strength between the intermediate and halo states.

4.2 Experimental setup

Fig. 4.1 shows the excitation scheme used to probe the halo state in ^{86}Sr using two-photon Raman photoassociation [94], in which two laser fields couple colliding atoms to the least-bound state of the ground molecular potential. ^{86}Sr has no nuclear spin and a 1S_0 electronic ground state, leading to a single $X^1\Sigma_g^+$ ground electronic molecular potential. The target state for the two-photon transition has total angular

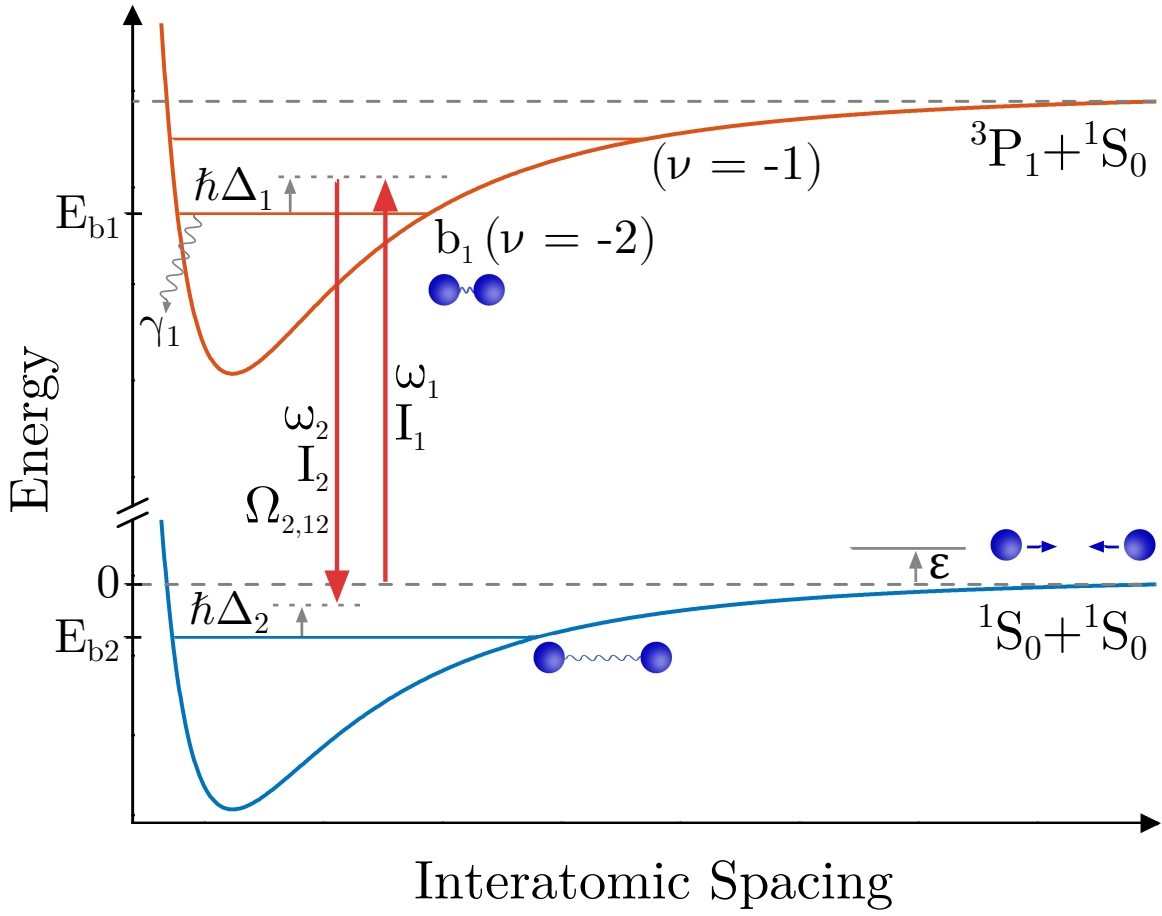


Figure 4.1 : $^{86}\text{Sr}_2$ halo molecule excitation scheme

Two-photon photoassociation diagram. The energy of two well-separated 1S_0 atoms at rest is taken as zero. ϵ is the kinetic energy of the colliding atom pair. E_{b1} is the unperturbed energy of the bound state of the excited molecular potential that is near resonance with the free-bound laser, which in these experiments is the second-least-bound level of the excited molecular potential $\nu = -2$. $E_{b2} (< 0)$ is the energy of the least-bound state of the ground molecular potential. The photon of energy $\hbar\omega_1$ is detuned from E_{b1} by $\hbar\Delta_1$ for $\epsilon = 0$, while the two-photon detuning from E_{b2} is $\hbar\Delta_2$. The decay rate of b_1 is γ_1 . Stark and collisional frequency shifts are neglected in this schematic.

momentum $J = 0$ and halo state energy $E_{b2}(< 0)$, which we label as b_2 . The dominant intermediate state, b_1 , with energy E_{b1} , is the $J = 1$ rotational state of the second least-bound $\nu = -2$ vibrational level on the 0_u^+ molecular potential, which asymptotically connects to the ${}^1S_0 + {}^3P_1$ asymptote at long range [118]. This state is bound by 44.246(10) MHz [21, 164]. We define $\Delta_1 = \omega_1 - E_{b1}/\hbar$ and $\Delta_2 = \omega_1 - \omega_2 - E_{b2}/\hbar$ as the one-photon detuning from state b_1 and two-photon detuning from state b_2 respectively for an initial scattering state with collision energy $\epsilon = 0$. The Rabi frequency, $\Omega_{2,12}$, characterizes coupling between states b_1 and b_2 due to the laser field at ω_2 with single-beam intensity I_2 . Because the binding energy of the halo molecule is very small compared to Δ_1 , both laser frequencies are near resonance with the $\nu = -2$ state. The least-bound $\nu = -1$, $J = 1$ excited molecular state, bound by 1.633(1) MHz, and the excited atomic state lie near enough in energy to the $\nu = -2$ state that they can also effect our observations.

The small detuning between ω_1 and ω_2 results in an atypical consideration of the accessible resonance conditions during the Raman process. Fig. 4.2a shows the two scenarios which lead to resonance with the halo state when ω_1 is held fixed and ω_2 is varied. The left panel, when $\omega_2 \geq \omega_1$, shows Δ_1 remains fixed while scanning the two-photon energy. This holds constant the bound-bound coupling between the halo and intermediate state. In the opposite case, when $\omega_2 \leq \omega_1$, the halo resonance condition can still be satisfied as ω_2 is varied, though at the expense of also varying Δ_1 . This behavior is equivalent to fixing ω_2 and scanning ω_1 in a typical Λ -type Raman scheme, but warrants our attention because of the interchangeability of the excitation lasers.

The latter configuration, which couples ω_2 and Δ_1 , was used during our photoassociation experiments. The effects on the observable spectra between these two

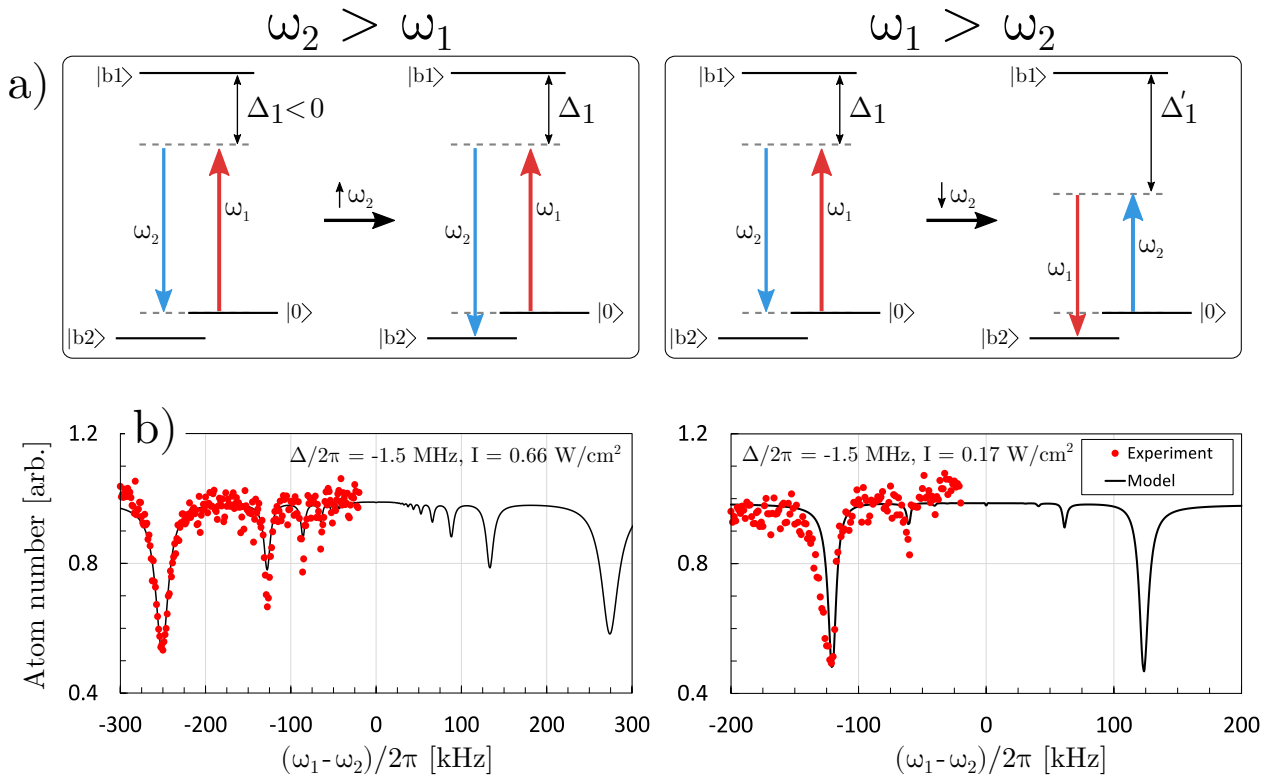


Figure 4.2 : Accessible halo resonance PAS processes

Effects of fixing ω_1 and varying ω_2 . Consider the state $|b2\rangle$ to be fixed. a) The left and right panels illustrate scanning ω_2 relative to ω_1 . Within each panel, the lasers start with $\omega_1 = \omega_2$ and $\Delta_2 = -E_b/\hbar$. Scanning ω_2 will fulfill the resonance condition in both scenarios but also lead to a change in Δ_1 if $\omega_1 > \omega_2$. b) Example simulated spectra compared with experimental PAS. The development of the model is described in Sec. 4.4. For both simulations, the "positive" axis is the configuration where $\omega_2 \geq \omega_1$ and the negative axis is the opposite. An asymmetry in resonance frequencies is noticeable for the largest loss features of the $I = 0.66$ W/cm² data.

schemes was considered using a three-level model, Sec. 4.4, to evaluate both scenarios of laser detuning across the complete range of our data. Fig. 4.2b shows two simulated spectra in the regime of strongest perturbation accessible by our experiments. The higher intensity spectrum, $I = 0.66 \text{ W/cm}^2$, shows that coupling between Δ_1 and ω_2 can noticeably shift the resonance energy of the halo state. Importantly, this prediction is in a regime where $E_{b2} \sim \Delta_1$, which applies to only a small subset of our measurements. Most of our data is in a regime where $\Delta_2 \ll \Delta_1$ thus we neglect variation of the AC Stark shift with ω_2 .

Spectroscopy is performed in a crossed beam optical dipole trap generated from a 1064 nm laser propagating perpendicular to gravity with spot sizes at the atoms of $300 \mu\text{m} \times 60 \mu\text{m}$ and $400 \mu\text{m} \times 40 \mu\text{m}$, with both short axes parallel to gravity. Further details are available in Sec. 2.3.3. Typical atom numbers are several hundred thousand and sample temperatures of approximately 300 nK. Peak densities are between $n_0 = 1 - 2 \times 10^{12} \text{ cm}^{-3}$. Following forced evaporative cooling, the atoms are allowed to thermally equilibrate before being illuminated by the photoassociation lasers for $\approx 1 - 10$ milliseconds. The number of remaining ground state atoms and the sample temperature are measured using absorption imaging after release from the trap and subsequent expansion during time-of-flight. Trap oscillation frequencies are determined by measuring dipole and breathing collective mode frequencies, which allow determination of trap volume and sample density.

We generate the two photons for spectroscopy as shown in Fig. 4.3. Using an AOM, these photons are derived from the output of a slave diode laser that is injection locked from the master 689 nm laser. Two precisely controlled RF frequencies are applied to a single AOM to generate both beams. These frequencies are separated by less than 300 kHz, and the diffracted beams corresponding to each frequency

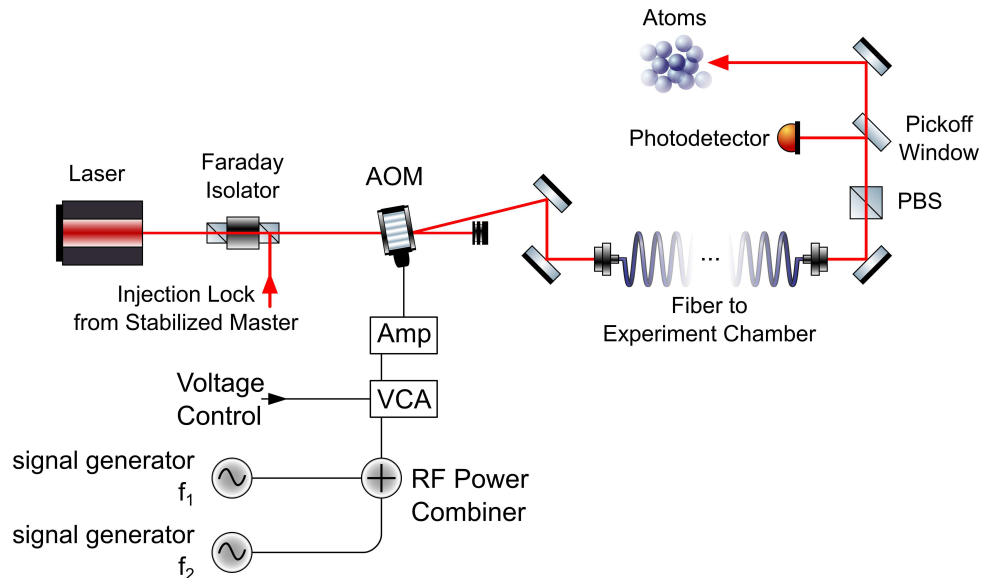


Figure 4.3 : Schematic of PAS light generation

Light for these experiments is generated by the spectroscopy slave laser setup discussed in Sec. 2.3.4.2. Light at two controllable frequencies is generated with a single acousto-optic modulator (AOM) and delivered to the atoms with an optical fiber. The beat note between the two frequencies is monitored after the fiber.

component are unresolved and appear as a single beam that is coupled into a single-mode, polarization-maintaining optical fiber. This fiber output is launched near the science chamber and shaped with output optics that yield a $450 \mu\text{m}$ spherical waist at the atoms, much larger than the size of the atom cloud. The light from this fiber is linearly polarized such that the polarization vector is parallel to gravity. The optical fiber ensures that the wavevector of the two photons will be parallel. This allows us to neglect any effects of Doppler broadening that might result from photoassociation near an intercombination line.

By using a single laser source and applying both frequencies to a single acousto-

optic modulator, we establish phase coherence and RF precision frequency differences between the ω_1 and ω_2 photons. Reduction of the beat note contrast is the primary limiting factor of the accessible range of Δ_2 for this spectroscopy setup. This is due to misalignment into the optical fiber resulting from the varying angular deviation out of the AOM as the RF frequency difference is increased. We partially compensate for this misalignment by increasing the RF amplitude of one drive frequency to maintain high beat note contrast. However, we observe significant reduction in contrast, which we were unable to compensate for, when the two drive frequencies differ by more than ≈ 300 kHz.

During the course of our experiments we found that mild environmental perturbations resulted in slow variation (on the order of 1 s) of the light intensity through the optical fiber. Such amplitude modulations are not uncommon in laser systems and are typically compensated by using a closed-loop intensity stabilization circuit. However, this circuit was inadequate for short-time exposures due to the acquisition process being long compared to our desired pulse width. This led us to implement the digital based infinite sample and hold mechanism for reduced intensity variability described in Sec. 2.3.4.2. The sample and hold system provided increased intensity stability with a 5% standard deviation during a typical experiment. The beat signal of the two light fields after the fiber was monitored on a photodiode and the RF powers adjusted to ensure matched intensities for the two frequency components ($I_1 = I_2 \equiv I$). Fig. 4.4 shows a typical histogram of the recorded intensities during an experimental scan along with a sample beat note showing the contrast.

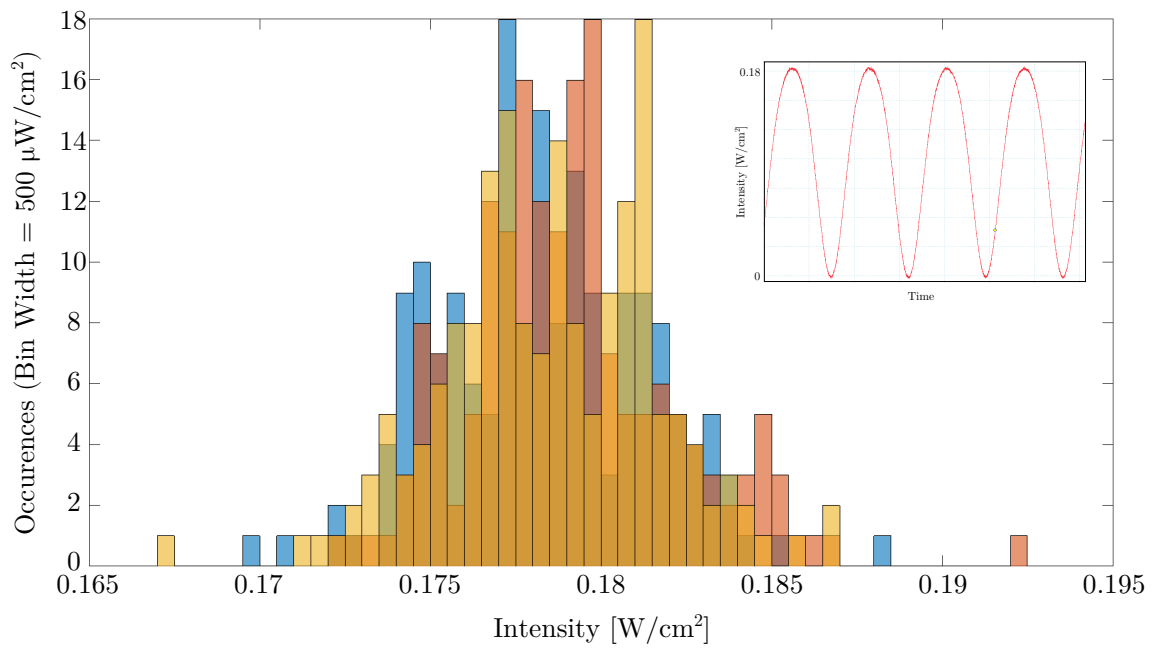


Figure 4.4 : Histogram of PAS beam intensity variation

Sample intensity variation during a set of photoassociation scans. Different colors denote multiple scans separated in time which are averaged. The inset shows a sample beat note and typical contrast.

4.3 Modeling the photoassociative loss

We observe the effects of photoassociation as a loss of atoms from the optical dipole trap as a function of the frequency difference, Δ_2 , between the two excitation lasers. Fig. 4.5 shows several spectra resulting from photoassociation to the $^{86}\text{Sr}_2$ halo state as the excitation beam intensity is varied. Intensities are specified by the single-beam intensities, I as defined in the previous section, with the average total near-resonant intensity illuminating the atoms given by $I_{689} = 2I$. In each of the spectra, the characteristic asymmetric tail of a photoassociation process sensitive to the relative collision energy distribution of the trapped atoms can be observed. Each spectra are averaged over several scans and the error bars give the standard error calculated for each detuning Δ_2 .

We model the rate of atom loss following the two-color PA theory of Bohn and Julienne and introduced in Sec. 3.4. Recall that the time-evolution of the total number of trapped atoms is given by Eq. 3.38

$$N(t) = \frac{N_0 e^{-\Gamma_1 t}}{1 + \frac{2N_0 \langle K \rangle V_2}{\Gamma_1 V_1^2} (1 - e^{-\Gamma_1 t})}$$

with Γ_1 the one-body loss rate, N_0 the initial number of trapped atoms before applying the PAS lasers, and V_q the effective volumes defined in Eq. 3.39. When fitting to experiments, we calculate the two-body average density distribution within the trap by considering the thermally averaged $\langle K \rangle_{\text{thermal}}$ (Eq. 3.45) at each \mathbf{r} contained within the trapping volume. The trap averaged $\langle K \rangle_{\text{trap}}$ is given by

$$\langle K \rangle_{\text{trap}} = \frac{1}{V_2} \int_V e^{-2U(\mathbf{r})/k_B T} \frac{1}{h Q_T} \int_0^{U_{\text{depth}}} d\epsilon |S|^2 e^{-\epsilon/k_B T} \quad (4.1)$$

The partition function $Q_T = \left(\frac{2\pi k_B T \mu}{h^2}\right)^{3/2}$ is determined for sample temperature T and reduced mass $\mu = m/2$ with mass m the mass of ^{86}Sr . We assume a fixed temperature

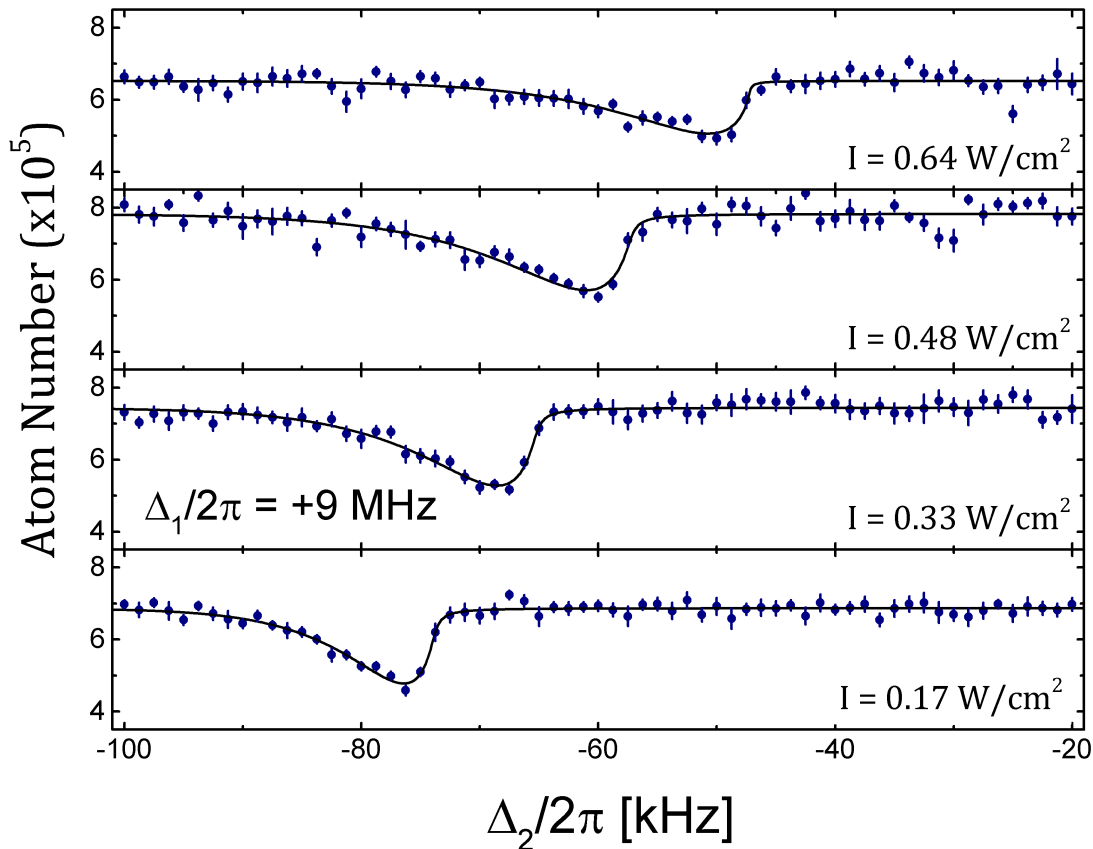


Figure 4.5 : Atom-loss spectra due to halo molecule spectroscopy

The resulting atom number in the ODT following continuous exposure of the photoassociation lasers for exposure times on the order of several milliseconds at a fixed intermediate state detuning $\Delta_1/2\pi = +9 \text{ MHz}$. As the single-beam intensity I , is increased the atom-loss lineshape noticeably shifts to lower binding energies. The procedure used to fit these lineshapes is discussed in the text.

throughout the exposure time. Consideration of the temperatures measured from time-of-flight images showed no more than 15% variation as Δ_2 was scanned. Finally, $U(\mathbf{r})$ is the trapping potential of the optical dipole trap and U_{depth} is the overall trap depth defined in Sec. 2.3.3.1. For this analysis, a harmonic approximation was applied to $U(\mathbf{r})$. This is an accurate representation of the trap when the ratio of trap depth to sample temperature is large, $U(\mathbf{r})/k_B T > 4$, as was true for these experiments.

We assume the dominant loss process to occur via the intermediate state b_1 and therefore use the scattering probability, $|S|^2$ given in Eq. 3.44

$$|S|^2 = \frac{(\Delta_2 + \epsilon/\hbar)^2 \gamma_1 \gamma_s}{\left[(\Delta_1 + \epsilon/\hbar)(\Delta_2 + \epsilon/\hbar) - \frac{\Omega_{12}^2}{4} \right]^2 + \left[\frac{\gamma_1 + \gamma_s}{2} \right]^2 (\Delta_2 + \epsilon/\hbar)^2} \quad (4.2)$$

where $\gamma_1 = 2\gamma_{\text{atomic}}$, and $\gamma_{\text{atomic}} = 4.7 \times 10^4 \text{ s}^{-1}$ is the decay rate of the atomic 3P_1 level. $\gamma_s(\epsilon)$ is the stimulated width of b_1 due to coupling to the initial scattering state by the PAS lasers, which for low energy can be expressed as [15, 16, 18, 55, 146]

$$\gamma_s(\epsilon) = 2kl_{\text{opt}}\gamma_1 \quad (4.3)$$

where the optical length ($l_{\text{opt}} \propto I_{689}$) is related to the overlap between the initial colliding state and b_1 , and $k = \sqrt{2\mu\epsilon/\hbar^2}$. Our chosen intermediate state has optical length $l_{\text{opt}}/I = (1.5 \pm 0.3) \times 10^4 a_0/(\text{W/cm}^2)$ [21], where $a_0 = 5.29 \times 10^{-11} \text{ m}$ is the Bohr radius.

Since we are primarily concerned with measuring light shifts on the halo state, the statement of $|S|^2$ above omits any explicit inclusion of light shifts in contrast to the original theory. This includes the shift of b_1 due to coupling to the ground state scattering continuum which was found to be a sufficient approximation for describing previous two-photon spectroscopy in ${}^{88}\text{Sr}$ [118]. Furthermore, lacking a model of coupling outside of our system, the scattering probability neglects dependence on

shifts due to the trapping or photoassociation lasers coupling to states outside of this model.

The standard approach to describing photoassociation spectra is to consider the complete lineshape as a sum over Lorentzians shifted by the thermally distributed collision energy [45, 99, 146]. However, Eq. 4.2 is not a true Lorentzian due to the form of its dependence on Δ_2 . We may recover the more intuitive approach to the lineshape by noting that for the experiments reported here, we maintain significant intermediate state detuning, Δ_1 , for which $|\Delta_1| \gg \Omega_{12}$. Thus we are in the Raman regime and may further simplify Eq. 4.2 by considering its behavior as a function of Δ_2 . A maximum for this function occurs when $\Delta_2 + \epsilon/\hbar = \Omega_{12}^2/4\Delta_1$. In the regime of this maximum Eq. 4.2 behaves similarly to a Lorentzian, thus by restricting the range of Δ_2 to be near two-photon resonance and maintaining $|\Delta_1| \gg \Omega_{12}, \gamma_1, \gamma_s$, we can approximate $|S|^2$ by [150, 151].

$$|S|^2 \approx \frac{A(\epsilon)}{\left(\Delta_2 + \epsilon/\hbar - \frac{\Omega_{12}^2}{4(\Delta_1 + \epsilon/\hbar)}\right)^2 + [\Gamma_L(\epsilon)/2]^2} \quad (4.4)$$

where

$$A(\epsilon) = \frac{\Omega_{12}^4 \gamma_1 \gamma_s(\epsilon)}{16(\Delta_1 + \epsilon/\hbar)^4} \quad (4.5)$$

$$\Gamma_L(\epsilon) = \frac{\Omega_{12}^2 [\gamma_1 + \gamma_s(\epsilon)]}{4(\Delta_1 + \epsilon/\hbar)^2} \quad (4.6)$$

There remains several concerns regarding this formulation of the Bohn and Julienne theory for our experiment. First, it assumes an isolated intermediate state, which is not strictly a valid approximation due to the proximity of the intermediate state b_1 to the ${}^1S_0 + {}^3P_1$ asymptote and to the $\nu = -1$ state. Second, Eq. 4.2 is derived assuming only a single near-resonant laser beam along each leg of the two-photon transition. This condition is clearly violated for two-photon spectroscopy to a halo state

where $\omega_1 - \omega_2 \approx -E_{b2} \ll |\Delta_1|$. Thus, we expect pairs of colliding atoms will experience inelastic scattering processes in both fields simultaneously which will contribute to the overall observed transition strengths and light shifts. During the photoassociation exposure, the total 689 nm intensity, I_{689} , oscillates with near 100% contrast according to $I_{689} = I_1 + I_2 + 2\sqrt{I_1 I_2} \cos[(\omega_1 - \omega_2)t] = 2I \{1 + \cos[(\omega_1 - \omega_2)t]\}$. When fitting the spectra, we assume an ansatz dependence of the bound-bound coupling, $\Omega_{12} \propto \langle I_{689} \rangle^{1/2}$ where $\langle I_{689} \rangle$ is the time averaged intensity which neglects the interference term between the lasers.

In the absence of a more rigorous theory treating these effects, we analyze loss spectra using the effective expression given by Eq. 4.7, where the observed molecular binding energy, E'_{b2} , includes any perturbations due to AC Stark shifts.

$$|S|^2 = \frac{\Gamma_L(\epsilon) + \gamma_{\text{eff}}}{\Gamma_L(\epsilon)} \frac{\eta A(\epsilon)}{(\omega_1 - \omega_2 + \epsilon/\hbar - E'_{b2}/\hbar)^2 + \left[\frac{\Gamma_L(\epsilon) + \gamma_{\text{eff}}}{2}\right]^2} \quad (4.7)$$

This formulation of the $|S|^2$ has been further modified with two additional parameters, η and γ_{eff} , while maintaining the required unit normalization of the scattering probability [88, 157]. The additional width, γ_{eff} , was added to allow for broadening which may have been neglected in this treatment of the inelastic scattering. The amplitude scaling parameter η accounts for additional phenomenological loss that is typically measured during photoassociation [12, 21, 102, 148, 188, 202, 205].

When performing fits of the atomic loss lineshapes using Eqs. 4.3, 4.1, and 4.7, we utilize independently determined simulations of the trapping potential $U(\mathbf{r})$. The sample temperature, T , is measured from the time-of-flight and used to characterize the energy distribution of $\langle K \rangle_{\text{thermal}}$. As a check of our lineshape model, we allowed the sample temperature to vary as a fit parameter and found reasonable agreement between the temperature estimated by the asymmetric tail of the lineshape and the

time-of-flight temperature. However, this process makes the fitting routine proceed much more slowly so we generally fix it to the value measured via time-of-flight. The one-body loss rate Γ was also measured and found to be $\approx 5\text{ s}^{-1}$. All other values such γ_s , γ_1 , Ω_{12} , etc. are calculated for each spectrum using known physical values or locally measured estimates. Thus, the remaining parameters E'_{b2} , N_0 , η , and γ_{eff} are independently fit and estimated for each spectrum.

Note that for each set of experimental conditions, I_{689} and Δ_1 , several scans of the photoassociation process were accumulated. When determining the parameter estimates, E'_{b2} , N_0 , etc., for a specific set of conditions, we independently fit and extract the coefficient values from each of the individual scans. Then calculate the average and standard error for each parameter for a given set of conditions, I_{689} and Δ_1 .

In this work, we are primarily concerned with variation of the halo resonance energy with the excitation laser intensity and intermediate state detuning as shown in Fig. 4.6. The estimate of E'_{b2} from the spectra is largely determined by the sharp edge on the blue side of the spectrum. While we cannot determine if the halo resonance energies are sensitive to other interactions causing shifts of the halo state, we do observe a striking dependence on the 689 nm excitation intensity, I_{689} , as demonstrated in Figs. 4.5 & 4.6. The relationship between the measured resonance positions and the unperturbed binding energy E_{b2} is modeled as

$$E'_{b2} = E_{b2} + h\chi_{689}I_{689} \quad (4.8)$$

We characterize the change in the AC Stark shift due to varying Δ_1 , by estimating the rate of change of the halo resonance energy with respect to I_{689} using the linear fitting function Eq. 4.8. When fitting, only intensities which exhibit linear scaling are included for each value of Δ_1 . This estimates the susceptibility of the halo state,

$\chi_{689}(\Delta_1)$, which are plotted as a function of Δ_1 in Fig. 4.6.

4.4 Frequency dependence of the binding energy

Collaborating with Kon Wen Yu, of the Hazzard group, the data shown in Fig. 4.6 was used to develop and assess several theoretical descriptions in order to reproduce and predict the resonance positions and susceptibility of the halo molecule state. Additionally, we evaluated the effect of the two-frequency drive on the observed halo resonance energies and reproduced the emergence of higher-order loss processes observed in the experiment.

These theoretical approaches began with the setup and numerical evaluation of a time-dependent three-level system. This model was then analyzed using Floquet and perturbation theory to develop an approximate analytic formula for predicting the halo resonance shift. Throughout this analysis, we neglect the motional degrees of freedom for the initial state of two free atoms. This greatly simplifies the physical processes we must consider and allows us to deduce an analytic result for the scaling of the binding energy. For the remainder of this chapter, our discussion will focus on the results of Yu's analyses and leave the details of his derivation to Ref. [107].

The photoassociation experiment is modeled using a three-level system composed of two well-separated atoms $|0\rangle$, an intermediate dimer state in an excited electronic potential $|b1\rangle$, and a dimer in the ground electronic state $|b2\rangle$. This setup is outlined in Fig. 4.1 where we have defined $|0\rangle$ to be a pair of atoms with $\epsilon = 0$ relative collision energy. The Hamiltonian for this system is

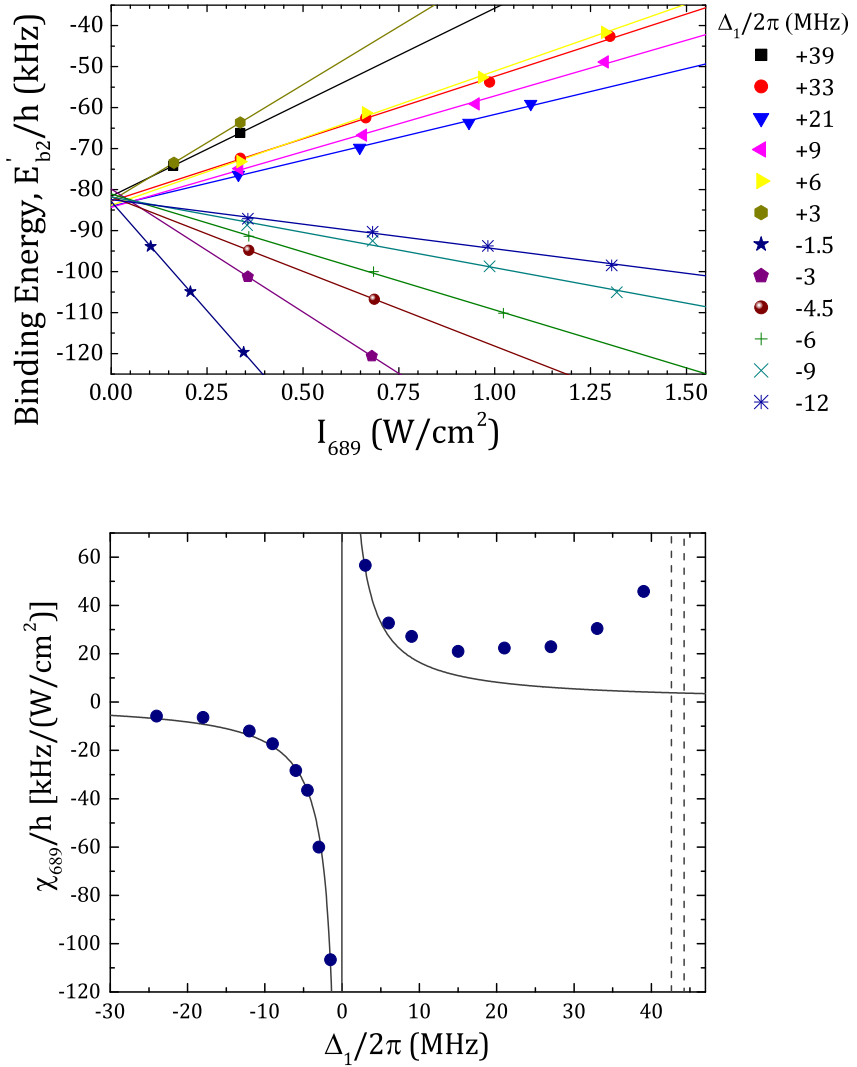


Figure 4.6 : Halo state resonances and susceptibilities, χ_{689}

Summary of the halo PAS experimental results. Top: A selection of two-photon PA resonance positions as a function of twice the single-beam excitation intensity, $I_{689} = 2I$, for various intermediate state detunings Δ_1 . The solid lines are fits used to determine χ_{689} at each detuning. Bottom: The susceptibility, χ_{689} , across all intermediate state detunings probed in this study. Dashed lines indicate the positions of the $\nu = -1$, $J = 1$ excited molecular state, bound by 1.633(1) MHz, and the ${}^1S_0 + {}^3P_1$ continuum. Dark solid line is a guide to the eye $\propto 1/\Delta_1$.

$$H = \begin{bmatrix} 0 & \Omega_{1,01}\cos(\omega_1 t) + \Omega_{2,01}\cos(\omega_2 t) & 0 \\ \Omega_{1,01}\cos(\omega_1 t) + \Omega_{2,01}\cos(\omega_2 t) & E_{b1} - i\frac{\gamma_1}{2} & \Omega_{1,12}\cos(\omega_1 t) + \Omega_{2,12}\cos(\omega_2 t) \\ 0 & \Omega_{1,12}\cos(\omega_1 t) + \Omega_{2,12}\cos(\omega_2 t) & E_{b2} - i\frac{\gamma_2}{2} \end{bmatrix} \quad (4.9)$$

Unlike the typical Λ -model considered in the Bohn and Julianne formalism, Eq. 4.9 considers both lasers 1 and 2 to drive the transition $|0\rangle \rightarrow |b1\rangle$ and $|b1\rangle \rightarrow |b2\rangle$. Decay terms are included to describe atom loss with γ_1 representing spontaneous emission from the intermediate bound state due to natural decay and γ_2 representing loss from the halo state due to collisions with background atoms.

The time-evolution of Eq. 4.9 begins in $|0\rangle$ and proceeds for a time τ using similar optical couplings and oscillating optical intensity as present during the photoassociation experiments. The model is numerically solved to generate a simulated spectrum as shown in Fig. 4.2. From these spectra, we estimate the halo resonance energy by determining the frequency of peak loss. The results of these simulations are shown in Fig. 4.7. The predicted halo resonance energies generally agrees with experimental data and reproduces a linear scaling of the binding energy consistent with the experimental observations. This indicates that effects missing from this theory – the motion of the atoms [15, 16], interaction shifts due to molecules and atoms scattering off of other molecules and atoms [197], and the varying density within the trap [118] – are not necessarily relevant for considering the gross effects of the two-frequency drive and determination of the internal interaction strengths.

Using this model, we find that as intensity is increased the predicted resonance energy begins to deviate significantly from the experimental data, limiting its regime of applicability. Fig. 4.7b shows an example where the three-level model tends to

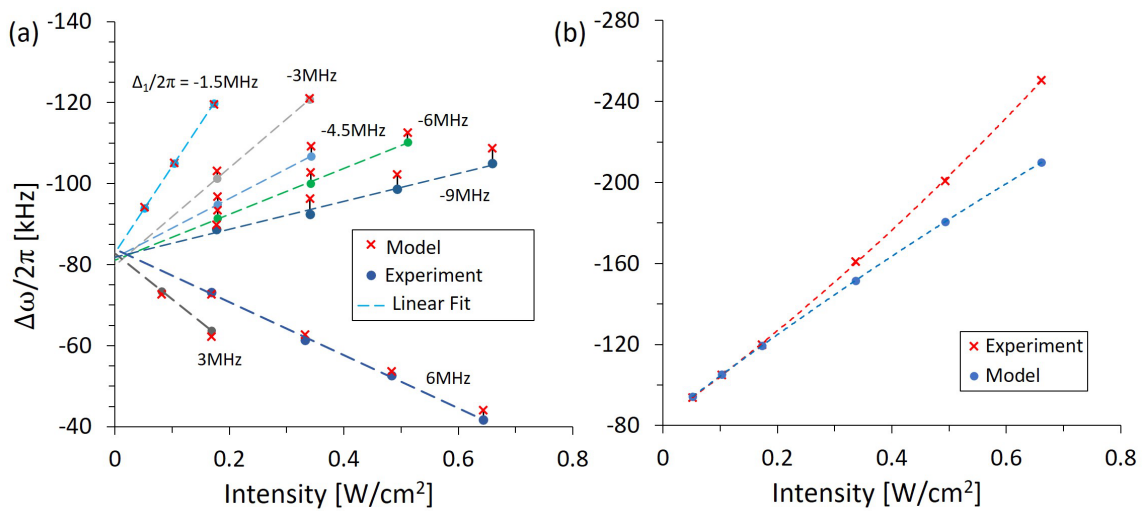


Figure 4.7 : Comparison of a three-level model to experimental halo PAS

a) The resonance energies, E'_{b2} , determined from the experiments is compared to the predicted resonance frequency determined from numerical simulation of the three-level model given by Eq. 4.9. This is the same data and linear fits as shown in Fig. 4.6. b) The resonance energy positions for $\Delta_1/2\pi = -1.5 \text{ MHz}$ data over a larger range of intensities for which the experimental results are not well described by linear scaling as predicted by the three-level model. Quadratic fits are shown as a guide to the eye. The experimental spectra for all six intensities plotted here are given in Fig. 4.9.

underestimate the resonance energy at higher intensities. This behavior is suggestive of additional interactions between the halo molecule state and one or more levels outside of the model as it is formulated.

We expect the predictive capability of the three-level system to prove useful for future studies of the ^{86}Sr halo molecule. Although, the numerical time-evolution is intensive and would require solving multiple simulations when including the halo resonance energy in the development of future theories. Thus, to obtain analytic insight into the three-level model, the Hamiltonian of Eq. 4.9 was treated under Floquet theory. We leave the details of this analysis to Ref. [107] but note that once the Floquet Hamiltonian has been found, a perturbative expansion can be applied in the region around $|\omega_1 - \omega_2| \approx -E_b^0$ by assuming $|\Delta_1| \gg \Omega_{01}, \Omega_{12}, \Delta_2, |\omega_1 - \omega_2|$, where $\Delta_2 = \omega_1 - \omega_2 - E_b^0$. Additionally, we assume $\Omega_{12} \gg \Omega_{01}$. The resulting expression for the shift of the halo resonance energy is then

$$\Delta\omega = \frac{\Omega^2}{4} \left(\frac{1}{\Delta_1 + E_b^0 + \Delta\omega} + \frac{1}{\Delta_1 + E_b^0} \right) \quad (4.10)$$

where $\Delta\omega$ is the shift from the natural binding energy E_b^0 and we have defined $\Omega_{1,12} = \Omega_{2,12} = \Omega$ in the case that $I_1 = I_2$. Comparison of this analytic formula with results from the numerical simulations show excellent agreement, even outside the region of strict validity of the perturbative expansion. Eq. 4.10 also confirms our initial hypothesis, applied when fitting the halo molecule lineshapes in the previous section, that the AC Stark shift scales as nearly twice the single-beam intensity. This is consistent with approximations of light shifts made in previous similar experiments [103, 197].

As an application of Eq. 4.10, we note that $\frac{d\Delta\omega}{dT}$ gives the susceptibility $\chi_{689}(\Delta_1)$ of the halo state. Fig. 4.8 plots the analytic susceptibility over Δ_1 resulting from fitting the coupling parameter in $\frac{d\Delta\omega}{dT}$. Once more we see that the three-level model cannot

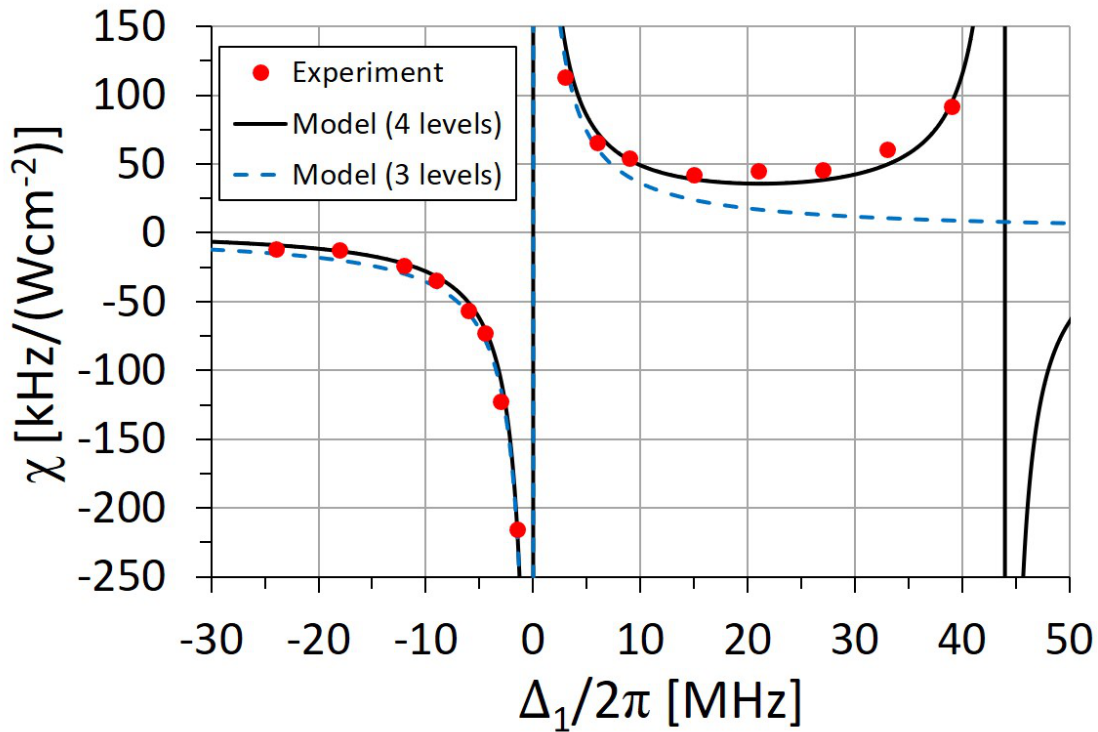


Figure 4.8 : Analytic approximation of the susceptibility

Plot of the experimental susceptibility data shown in Fig. 4.6. These points are fit with the analytic susceptibility predicted from the Floquet treatment of the three-level and four-level models. The coupling from the four-level model is estimated to be $\Omega_{12}/2\pi = 850 \text{ kHz}$ for $I = 1 \text{ W/cm}^2$

reproduce the experimental observations as intermediate state detuning is increased. This is most likely due to coupling with the $\nu = -1, J = 1$ excited molecular state and the ${}^1S_0 + {}^3P_1$ continuum. Experimentally we were unable to isolate and determine the separate effects of these states. Thus, as an approximate theoretical approach, the three-level model is extended with a virtual fourth-level, $|X\rangle$, specified by

$$H' = H_0 + E_X |X\rangle\langle X| + [\Omega_{1,0X} \cos(\omega_1 t) + \Omega_{2,0X} \cos(\omega_2 t)] |0\rangle\langle X| + \text{h.c.} \quad (4.11)$$

where H_0 is the three-level Hamiltonian in Eq. 4.9. The virtual state $|X\rangle$ may, in general, have couplings Ω_{0X} and Ω_{2X} . We choose to set $\Omega_{2X} = 0$ in Eq. 4.11 and consider the dominant coupling as being between states $|0\rangle$ and $|X\rangle$. This approximation is motivated by the positive slope of the observed susceptibilities as Δ_1 is varied towards the ${}^1S_0 + {}^3P_1$ asymptote which suggests that the ground state is shifting faster than the halo state. If instead we assumed that $\Omega_{2X} \gg \Omega_{0X}$, the sign of the AC Stark shift would be negative at red-detuning, which is inconsistent with our observations. Additionally, we choose to set the energy of the virtual state to the energy of the ${}^1S_0 + {}^3P_1$ asymptote, $E_X = E_{b1} + 2\pi\hbar \times 44.2 \text{ MHz}$.

A fit of the Floquet treatment of the four-level model is shown in Fig. 4.8 and yields $\Omega_{12}/2\pi = 850 \text{ kHz}$ for $I = 1 \text{ W/cm}^2$. Note that Ω_{12} as defined here would be the splitting of the Autler-Townes doublet [118, 151], which differs from the Bohn-Julienne definition of the molecular Rabi coupling [15, 16].

Using the measured Ω_{12} , one can extract the Franck-Condon factor, f_{FCF} , reflecting the overlap of the ground and intermediate molecular states through

$$\Omega_{12} = \sqrt{f_{\text{ROT}}} \sqrt{f_{\text{FCF}}} \gamma_{\text{atomic}} \sqrt{\frac{I}{2I_{\text{sat,atom}}}} \quad (4.12)$$

where $I_{\text{sat,atom}} = 2\pi^2\hbar c\gamma_{\text{atomic}}/(3\Lambda^3) = 3 \mu\text{W/cm}^2$ is the atomic saturation intensity for the ${}^1S_0 \rightarrow {}^3P_1$ transition and $I = I_{689}/2$ is the single-beam intensity. The rota-

tional factor f_{ROT} accounts for the change in dipole moment from atom to molecule due to symmetry of the wave function and projection on a rotating molecular axis. Following the formalism described in [151, 164], $f_{\text{ROT}} = 2$ for the $J = 1 \rightarrow 0$ bound-bound molecular transition studied here. This yields $f_{\text{FCF}} = 0.03$.

4.5 Multi-photon loss processes

In the regime of strongest perturbation between the halo state and intermediate excited molecular state, we observe the emergence of higher order loss features absent in the typical Λ -model due to the separability of the excitation lasers. Fig. 4.9 shows a series of spectra close to resonance which demonstrates the appearance of these loss features. At low-intensity a single prominent PAS lineshape around $\Delta_2 \approx -100$ kHz is observed. Then, as the intensity is increased, the resonance energy of the primary loss feature, defined as E_{b2} , shifts significantly more deeply into the ground state potential. Accompanying this shift, additional loss features continue to emerge in the spectrum as the intensity is further increased. These satellite features also appear to scale with intensity and the position of the primary loss feature. Increasing intensity also results in an increase in the linewidth as the lineshape broadens from an asymmetric feature into a fully symmetric profile. This is indicative of power broadening of the two-photon transition as population is cycled between the halo and continuum states.

Two conclusions may be drawn from these spectra that are of particular note. First, the shift of the halo state to a binding energy of ≈ 250 kHz for the highest intensity spectrum represents a significant change in the scattering length of freely scattering atoms in the ${}^1S_0 + {}^1S_0$ continuum. In the next chapter, we will discuss our precise determination of the halo molecule resonance energy which we measure to be $E_{b2} = -83$ kHz. Presuming this value of E_{b2} for the moment, we can estimate

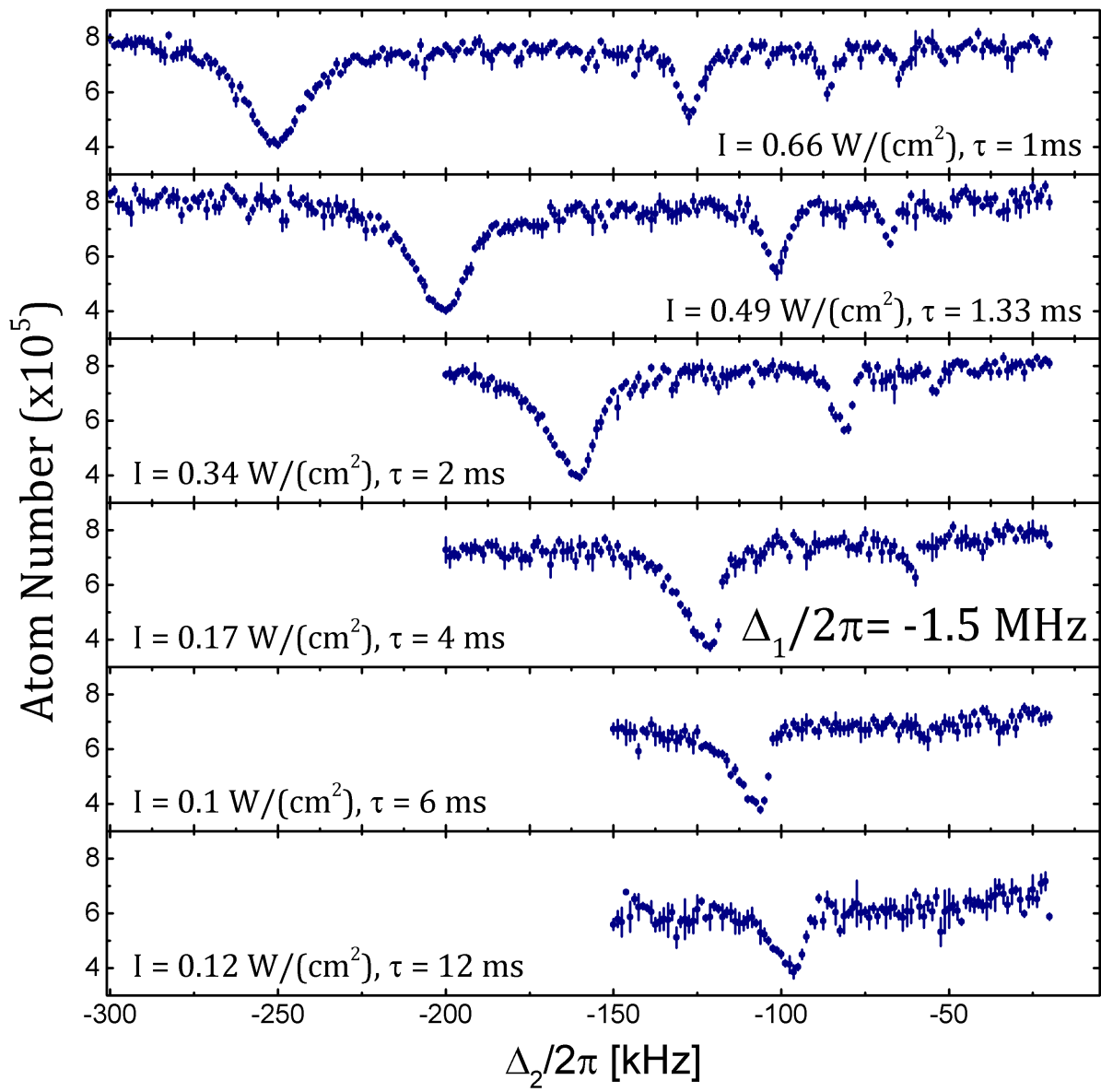


Figure 4.9 : Observation of higher order Raman processes

the change in scattering length due to a 250 kHz change in the halo state resonance energy using $E_{b2} = -\hbar^2/(2\mu a^2)$, where μ is the reduced mass of the strontium-86 halo molecule and a is the s -wave scattering length. From the highest intensity spectrum, the primary loss feature is shifted by approximately $3 \times$ the natural binding energy. This reduces the 86-86 scattering length to $\sim 500 a_0$, or approximately 60% of its natural value. The proximity of ^{86}Sr to a scattering resonance and the susceptibility of the halo binding energy to the intensity of the excitation light suggests using light to tune the binding energy and scattering length as was done with optically assisted magnetic Feshbach resonances [6, 42]. This complements previous work on the use of optical Feshbach resonances in strontium [12, 55, 188, 198, 202].

Second, consideration of the peak loss positions in Fig. 4.9 shows that each higher order process is related to the position of the primary loss by approximately $E_{b2}/2$. $E_{b2}/3$, This scaling suggests a non-linear process whereby multiple photons from the excitation light fields are absorbed and emitted to reach the final state. This is possible because of the small overall detuning, Δ_2 , and favorable coupling between the halo and intermediate state. This hypothesis can be tested using time-evolution of the three-level model to predict the spectra under similar conditions. Fig. 4.10 shows a schematic example of the multi-photon process as well as the result of the numerical evaluation for a selection of the spectra shown in Fig. 4.9. Despite its simplicity, the three-level model captures the relevant physics and accurately predicts the emergence of multi-photon loss features near the positions of the experimentally measured loss. Furthermore, at high-intensity, this model reproduces the symmetric lineshape profile indicating that power broadening is becoming the dominant source of the width. This shows that at high-intensity, the scattering nature of the problem, in which the initial state is embedded in a continuum of free atoms, is relatively unimportant.

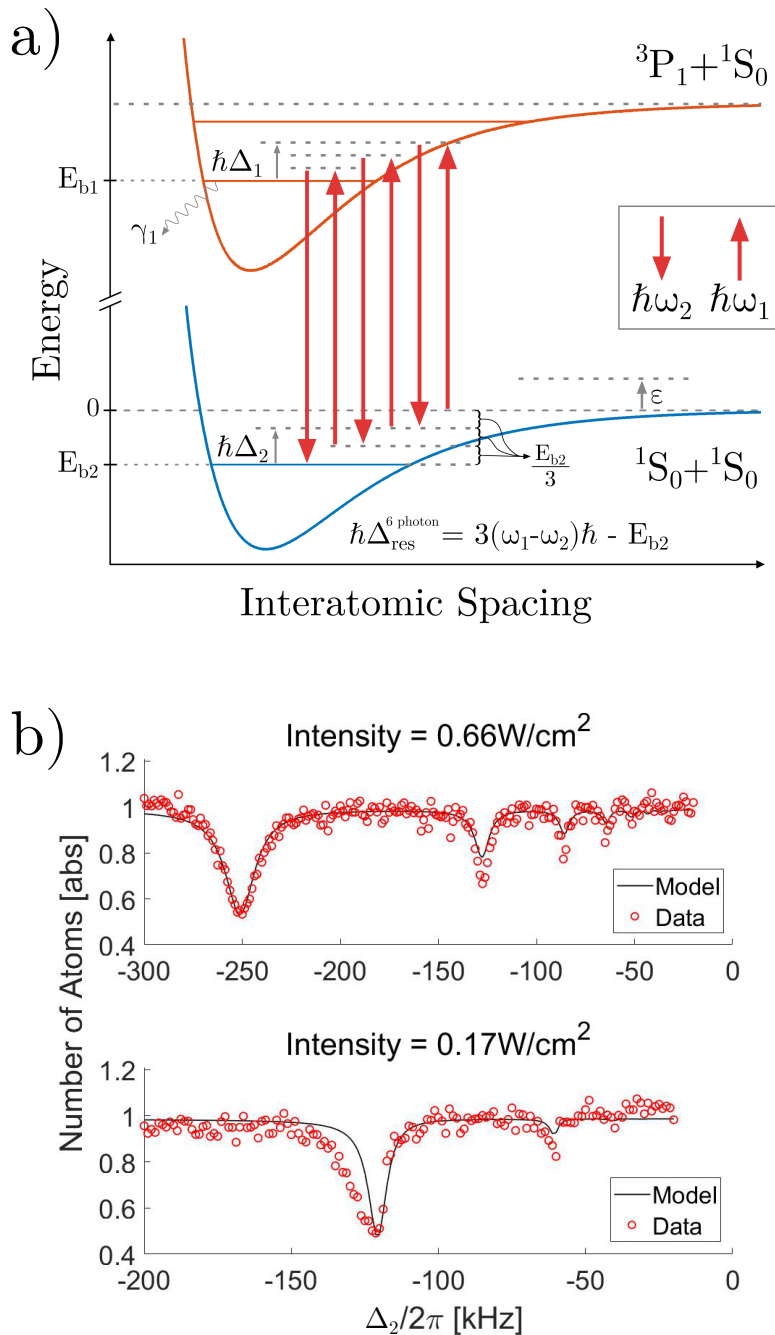


Figure 4.10 : Multi-photon Raman processes

- a) The excitation process for observing multi-photon Raman processes. Shown is a 6-photon process which results in atom loss at $E'_{b2}/3$ where E'_{b2} is the AC stark shifted halo molecule resonance energy of the fundamental process. b) Numerical simulation of the three-level model which reproduces the observed higher order loss processes.

Chapter 5

Binding energy of the $^{86}\text{Sr}_2$ halo molecule

Atomic interactions are generally quite complex and difficult to accurately calculate for all but the simplest of systems. Nonetheless, a parameterization of atomic interactions in ultracold atomic gases is possible using a single quantity known as the *s*-wave scattering length, a , that characterizes the complete interatomic potential [97]. For ground state atoms at large distances, interactions between atoms are well described by the van der Waals form, $V(r) = -C_6/r^6$. Therefore, once the effects of the overall potential are known through the *s*-wave scattering length, the threshold bound state and scattering properties are determined mainly by the long-range portion of the potential [94].

For systems near a scattering resonance, where the scattering length is much larger than the characteristic length-scale of the van der Waals potential, $\bar{a} = \frac{2\pi}{\Gamma(1/4)^2} \left(\frac{2\mu C_6}{\hbar^2}\right)^{1/4}$, it has been shown that the binding energy of the least-bound molecular state may be related to the scattering length by the universal formula $E_b = -\hbar^2/2\mu a^2$ [55, 64, 98]. Thus in ^{86}Sr , the large *s*-wave scattering length of $\sim 800a_0$ [175], provides a naturally occurring system for probing the interplay of the long-range potential, the scattering length, and the binding energy of the least-bound state.

In the previous chapter, we explored the coupling of the intermediate state and halo state via measuring the halo molecule's susceptibility as a function of the light intensity and detuning from the intermediate state. These measurements probed a strongly perturbed regime and were found to produce large AC stark shifts and multi-

photon Raman loss processes. To determine a precise value of the natural binding energy of the halo molecular state, we repeated similar experiments as before but with much lower excitation beam intensity at a fixed intermediate state detuning.

When describing two-photon spectroscopy to a weakly-bound ground state molecule, it is typical to neglect any potential AC Stark shift between the free ground state atoms and the bound state dimer caused by far off-resonant trapping lasers since the dimerized atoms contribute to the overall polarizability approximately as free atoms [94]. However, in general, AC Stark shifts due to the trapping lasers and collisions with ground state atoms may also shift the molecular resonance, as was considered in a recent, high-precision study of weakly-bound molecular states of ultracold ytterbium atoms [185]. Another recent study in calcium also probed several weakly-bound excited ground state molecules using an intercombination line transition as the intermediate state as is used in this work [151].

In this chapter, we accurately determine the $^{86}\text{Sr}_2$ halo state binding energy, considering possible collisional frequency shifts and AC Stark shifts due to trapping and excitation lasers. Then using the universal prediction for the binding energy, including corrections derived for a van der Waals potential [63, 64, 75], we derive new estimates for the value of the strontium C_6 coefficient of the $\text{X}^1\Sigma_g^+$ potential from Ref. [175]. This modified version of the potential is then used to calculate improved scattering lengths for all strontium isotopes via mass scaling.

5.1 Photoassociation in shallow traps

Excitation of the halo state proceeded using the same methodology as described in Sec. 4.2, with the only difference being that the experiments reported here were performed in a single-beam optical dipole trap to produce a large trapping volume.

The trap is generated from a 1064 nm laser that is aligned perpendicular to gravity with beam waists $260 \mu\text{m} \times 26 \mu\text{m}$. Following forced evaporation, typical atom numbers were several hundred thousand and typical atom temperatures were between 30 nK – 1000 nK. The atom number and sample temperature are measured using time-of-flight absorption imaging and trap oscillation frequencies are determined by measuring dipole and breathing collective mode frequencies. These trap frequencies are confirmed against an independent model of the trapping potential.

The large volume of this single-beam optical trap allowed us to maintain peak densities $\approx n_0 = 1 - 2 \times 10^{12} \text{ cm}^{-3}$, comparable to our previous work, over a range of various 1064 nm intensities. For each trap intensity, two-photon spectroscopy was performed to search for a differential AC Stark shift at 1064 nm between the free-atom asymptote of scattering states and the halo molecule state.

The experiments in the previous chapter revealed that photoassociation using high-intensity and/or large intermediate state detuning led to shifts of the halo molecular resonance that could vary non-linearly and were not explained by a simple three-level model. In this study, the 689 nm excitation beam intensity was kept extremely low, such that the AC Stark shift remained proportional to I_{689} . Additionally, the intermediate state detuning was fixed at $\Delta_1/2\pi = -9 \text{ MHz}$. Thus, these experiments are in the Raman regime with $\Delta_1 \gg \Omega_{12}$ and a theoretical description considering only a single intermediate state should be sufficient.

Loss spectra are modeled using the previously developed lineshape formulas of Bohn and Julienne, Sec. 4.3. Here we restate the main results needed for evaluating the current experiments.

$$\langle K \rangle_{\text{trap}} = \frac{1}{V_2} \int_V \exp\left(\frac{-2U(\mathbf{r})}{k_B T}\right) \frac{1}{h Q_T} \int_0^{\epsilon_{\max}(\mathbf{r})} d\epsilon |S(\epsilon, \mathbf{r})|^2 \exp\left(\frac{-\epsilon}{k_B T}\right) \quad (5.1)$$

$$|S(\epsilon, \mathbf{r})|^2 = \frac{\Gamma_L(\epsilon) + \gamma_{\text{eff}}}{\Gamma_L(\epsilon)} \frac{\eta A(\epsilon)}{(\omega_1 - \omega_2 + \epsilon/\hbar - E'_{b2}(\mathbf{r})/\hbar)^2 + \left[\frac{\Gamma_L(\epsilon) + \gamma_{\text{eff}}}{2} \right]^2} \quad (5.2)$$

$$A(\epsilon) = \frac{\Omega_{12}^4 \gamma_1 \gamma_s(\epsilon)}{16(\Delta_1 + \epsilon/\hbar)^4} \quad (5.3)$$

$$\Gamma_L(\epsilon) = \frac{\Omega_{12}^2 [\gamma_1 + \gamma_s(\epsilon)]}{4(\Delta_1 + \epsilon/\hbar)^2} \quad (5.4)$$

The astute observer may notice that a spatial dependence has been introduced into the collision energy distribution by an energy cutoff $\epsilon_{\text{max}}(\mathbf{r})$ defined by the local trap depth $\epsilon_{\text{max}}(\mathbf{r}) = U_{\text{depth}} - U(\mathbf{r})$. The effect of this will be discussed momentarily. Spatial dependence of the trapping laser intensity $I_{1064}(\mathbf{r})$ and the density $n(\mathbf{r})$ give rise to the spatial dependence of $|S(\epsilon, \mathbf{r})|^2$ and the need for a spatial average in Eq. 5.1. The 689 nm excitation beam is large compared to the atom sample so we neglect effects of spatial variation for this beam.

Recall from Sec. 2.3.3.1, the trapping potential is given by $U(\mathbf{r}) = mgz + \frac{\alpha(\lambda)}{2\epsilon_0 c} I_{1064}(\mathbf{r}) - \tilde{U}_{\text{min}}$, with mgz the gravitational potential, $I_{1064}(\mathbf{r})$ the intensity of the trapping light, and $\alpha(\lambda)$ the polarizability of ground state atoms due to 1064 nm light. Here we have subtracted off the trap minimum, U_{min} , such that the maximum kinetic energy of trapped particles is U_{depth} as previously defined.

The inclusion of a spatially dependent energy cutoff, $\epsilon_{\text{max}}(\mathbf{r})$, in Eq. 5.1 is a result of the shallow trapping potentials used for these experiments. Whether a trap is considered deep or shallow is determined by the ratio of trap depth to sample temperature, $\eta_{\text{trap}} = U_{\text{depth}}/k_B T$, where $\eta_{\text{trap}} \gtrsim 4$ is the approximate transition as will be shown in the next section. The experiments in this chapter were performed in shallow traps where $\eta_{\text{trap}} \sim 1$ for the lowest temperature samples $T \approx 30 \text{ nK}$ and $\eta_{\text{trap}} \sim 3$

for $T \approx 1000 \text{ nK}^*$. Thus, the harmonic approximation is not a valid description of the trapping potential and the full form of the Gaussian beam profile must be used to evaluate $\langle K \rangle_{\text{trap}}$ (Eq. 5.1). This requires several factors to be assessed for their spatial dependence when modeling photoassociation in a shallow trap, including $U(\mathbf{r})$, $\epsilon_{\text{max}}(\mathbf{r})$, and $E'_{b2}(\mathbf{r})$.

5.1.1 Effects of truncation on collision energy

Fig. 5.1 shows a volumetric plot of a trapping potential, $U(\mathbf{r})$, used in the lowest temperature experiments where $\eta_{\text{trap}} \sim 1$. From the plot, we identify a local maximum along the Z -axis with $X = 0$ and saddle points on either side of this peak that define U_{depth} . This atypical geometry impacts equilibration in such a trap as the exit path lies along a non-trivial trajectory. In real space, this trap appears as an elongated bowl in the XY plane with a "hump" in the middle and small "funnels" on either end such that atoms must have low enough energy to fall under the influence of gravity along $-Z$ while simultaneously moving away from the trap center along $|X| > 0$, in order to find the minimum and exit. This geometry is caused by the Gaussian nature of the extremely narrow vertical beam waist, $26 \mu\text{m}$ along the Z -axis. The rapid expansion of the beam intensity in the vertical direction along the Rayleigh length, causes the trap to weaken along the X direction quickly.

In addition to the abnormal trajectory required to leave the trap, atoms trapped in the central region near $X = 0$ see a larger barrier to leaving the trap due to the local maximum. Analysis of the trap revealed that this maximum is $\sim 2 U_{\text{depth}}$. Thus atoms at kinetic energies higher than U_{depth} may remain trapped for a significant

*In the previous experiments at high-intensity, $\eta_{\text{trap}} > 6$ for all data, therefore a harmonic approximation was appropriately applied.

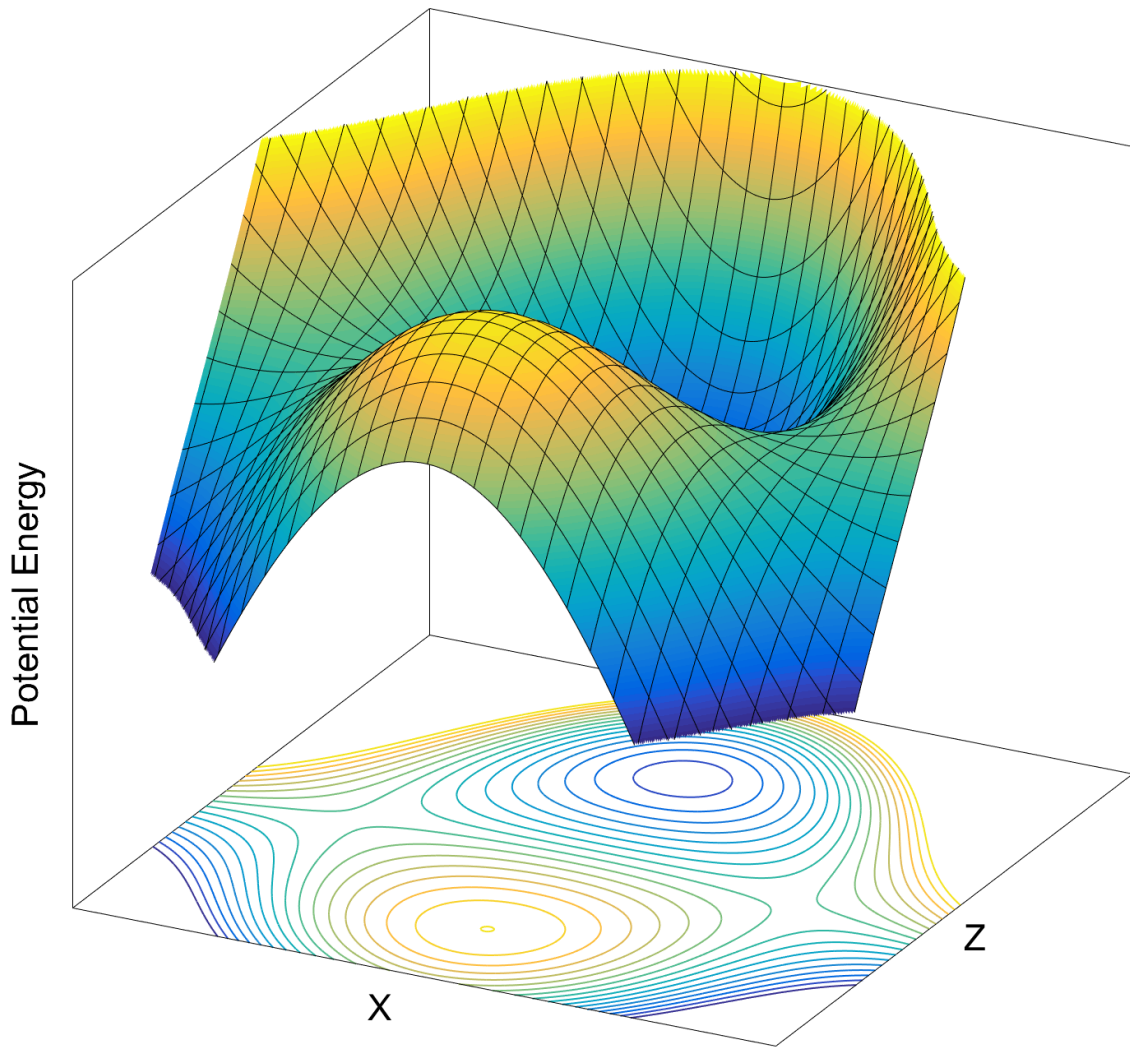


Figure 5.1 : Surface plot of the trapping volume in single-beam trap

The spatial dependence along the XZ plane with $Y = 0$ of the ground state potential energy during the halo molecule excitation. This plane contains the smallest difference between the trap minimum and lowest saddle point and therefore is used to define and visualize the trap depth. The trap depth is defined along a trajectory where a particle is simultaneously moving away from the beam waist and down under the influence of gravity. Note, this coordinate system assumes the laser wavevector is propagating along $+X$ and gravity is aligned along $-Z$.

period of time before eventually finding a path to leave. This is further confirmed by photoassociation spectra that demonstrated a larger thermal tail than was expected based on the temperature measured by time-of-flight (this will be shown shortly). Consideration of the trapping potential and the spectra suggests that our sample was non-ergodic.

Lacking a detailed microscopic model of the atomic density and momentum distribution in this shallow trap, we proceed by assuming the single-particle kinetic energy may be described by a truncated Maxwell-Boltzmann distribution such that energies above a particular cut-off, ϵ_{\max} , do not contribute to the scattering probability in the photoassociation process. Furthermore, we assume the density does not change during the excitation time. This is a reasonable assumption given that our exposure times were short compared to any background change in density and the sample temperature varied by no more than 15% for all values of Δ_2 .

It is helpful to begin our discussion of the truncated relative-momentum distribution by first considering how to treat the simple case of an untruncated gas. Such a system is described by a single-particle momentum distribution $f_{p,\text{one}}(\mathbf{p})$ for a gas at temperature T of particles with mass m given by

$$f_{p,\text{one}}(\mathbf{p}) = \frac{1}{(2\pi mk_B T)^{3/2}} \exp\left(\frac{-p^2}{2mk_B T}\right) \quad (5.5)$$

The two-particle relative-momentum distribution, $f_{p,\text{two}}(\mathbf{p}_R)$, for two similar particles with reduced mass $\mu = m/2$, is also given by a Maxwell-Boltzmann distribution. A derivation of this may be found in App. A.

$$f_{p,\text{two}}(\mathbf{p}_R) = \frac{1}{(2\pi\mu k_B T)^{3/2}} \exp\left(\frac{-p_R^2}{2\mu k_B T}\right) \quad (5.6)$$

Through a change of variables, the relative collision energy distribution is found to

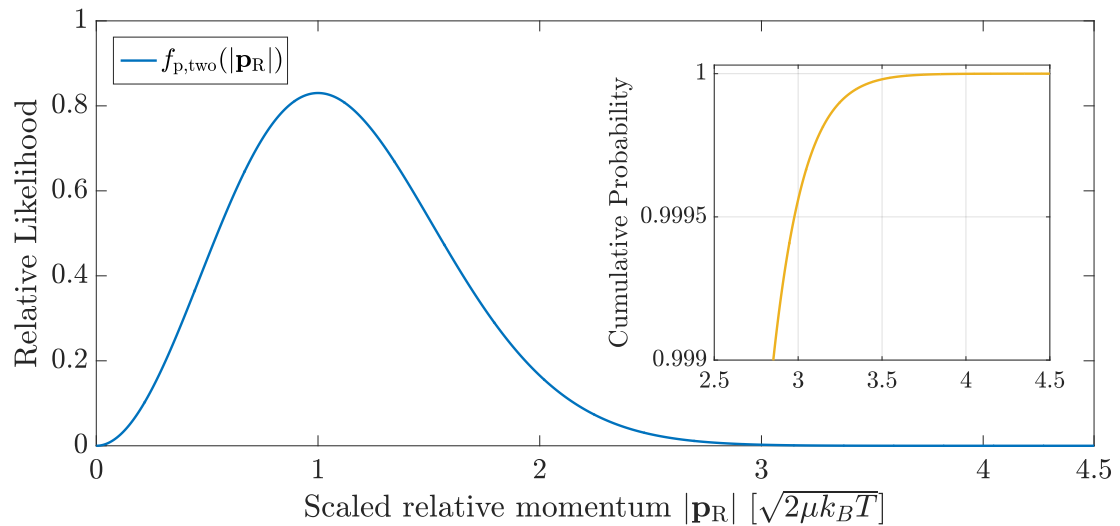


Figure 5.2 : Two-particle Maxwell-Boltzmann distribution

relative-momentum distribution Eq. 5.6. Here $|\mathbf{p}_R|$ is given in units of $\sqrt{2\mu k_B T}$ to emphasize the generality of the distribution. Importantly, the likelihood of finding a particle with a momentum $|\mathbf{p}_R| > 4\sqrt{2\mu k_B T}$ is extremely small. This is corroborated by the inset which shows the integral of the relative likelihood, also known as the cumulative distribution function of $f(\mathbf{p}_R)$. This gives the probability two-particles will have relative-momentum between $0 \rightarrow p_i$ for any specified p_i . Thus the probability for a two-particles to have relative-momentum $|\mathbf{p}_R| < 4\sqrt{2\mu k_B T}$ is ≈ 1 .

be

$$f_{E,\text{two}}(\epsilon) = \frac{2}{\sqrt{\pi}} \frac{\sqrt{\epsilon}}{(k_B T)^{3/2}} \exp\left(\frac{-\epsilon}{k_B T}\right) \quad (5.7)$$

These distributions describe gases with momentum and energy formally extending to infinity. Fig. 5.2 shows the Maxwell-Boltzmann distribution in Eq. 5.6 using scaled units in terms of the system's characteristic momentum $\sqrt{2\mu k_B T}$. This shows that the occupation of momentum states $> 4\times$ the characteristic scale is very small. Therefore, if the ratio of maximum single-particle kinetic energy and sample temperature is greater than four, the relative-momentum and collision energy distributions will be given by a Maxwell-Boltzmann. In trapping of ultracold atoms, we define the ratio of trap depth to sample temperature as $\eta_{\text{trap}} = U_{\text{depth}}/k_B T$ where the trap depth specifies the maximum allowed single-particle kinetic energy. Thus a deep trap is one where $\eta_{\text{trap}} > 4$. When modeling photoassociation performed in deep traps, it is sufficient to use a Maxwell-Boltzmann description of the relative-momentum and collision energy distribution as all non-negligible relative collision energies are integrated over.

For the case of shallow traps, the ratio of single-particle kinetic energy to sample temperature is by definition $\eta_{\text{trap}} < 4$ and the relative-momentum and collision energy distributions are not given by a Maxwell-Boltzmann. Furthermore, a naive truncation of $\langle K \rangle$ such that $\langle K \rangle_{\text{thermal}} \propto \int_0^{\epsilon_{\text{max}}} \exp\left(\frac{-\epsilon}{k_B T}\right) |S(\epsilon)|^2 d\epsilon$, is incorrect as $\int_0^{U_{\text{depth}}} \exp\left(\frac{-\epsilon}{k_B T}\right) |S(\epsilon)|^2 d\epsilon \neq 1$. Thus a naive truncation omits contributions from relative collision energy states above the integration limit ϵ_{max} [118].

Appendix section A.2 presents a derivation of the relative-momentum distribution $\hat{f}_{p,\text{two}}(\mathbf{p}_R)$, and the relative collision energy distribution $\hat{f}_{E,\text{two}}(\epsilon)$, when the single-particle kinetic energies are truncated. The average over collision energies in $\langle K \rangle_{\text{thermal}}$

is then weighted by the distribution $\hat{f}_{\text{E,two}}(\epsilon)$, given by

$$\begin{aligned}\hat{f}_{\text{E,two}}(\epsilon) &= \frac{2}{\sqrt{\pi}} \frac{\sqrt{\epsilon}}{(k_B T)^{3/2}} \exp\left(\frac{-\epsilon}{k_B T}\right) \hat{\mathcal{G}}_{\text{E}}(\epsilon_{\max}, \epsilon) \\ &= f_{\text{E,two}}(\epsilon) \hat{\mathcal{G}}_{\text{E}}(\epsilon_{\max}, \epsilon)\end{aligned}\quad (5.8)$$

where ϵ is the relative collision energy and ϵ_{\max} is the maximum single-particle kinetic energy. Eq. 5.8 collects the effects of truncation into the normalized function $\hat{\mathcal{G}}_{\text{E}}$ given by Eq. A.16. The functions $\hat{f}_{\text{E,two}}$ and $\hat{\mathcal{G}}_{\text{E}}$ are implicitly specified with the characteristic energy scale $k_B T$.

Fig. 5.3 plots the truncated relative collision energy distribution, $\hat{f}_{\text{E,two}}$, for several values of maximum single-particle energy ϵ_{\max} as specified in the legend. For each value of ϵ_{\max} , the collision energy ϵ may take on the range of available energies $[0 \rightarrow 2\epsilon_{\max}]$. The upper bound on collision energy, $2\epsilon_{\max}$, considers the case that both particles have maximum kinetic energy ϵ_{\max} . We see that for the case of maximum single-particle kinetic energy $\epsilon_{\max}/k_B T = 1$ (blue curve), the maximum collision energy is $2\epsilon_{\max}/k_B T$ and the likelihood of collision energies falls to zero for higher energies as required by our definition of the truncation. Furthermore, the relative collision energy distribution converges to the Maxwell-Boltzmann distribution, $f_{\text{E,two}}$, of Eq. 5.7 for cutoff energies $\epsilon_{\max} \gtrsim 4$. This is in agreement with our expectation discussed previously, that for deep traps the single-particle distribution is accurately accounted for and therefore the relative collision energy distribution is given by a Maxwell-Boltzmann. Additional tests of the normalization and behavior of $\hat{\mathcal{G}}_{\text{E}}$ are given with the derivation in the appendix.

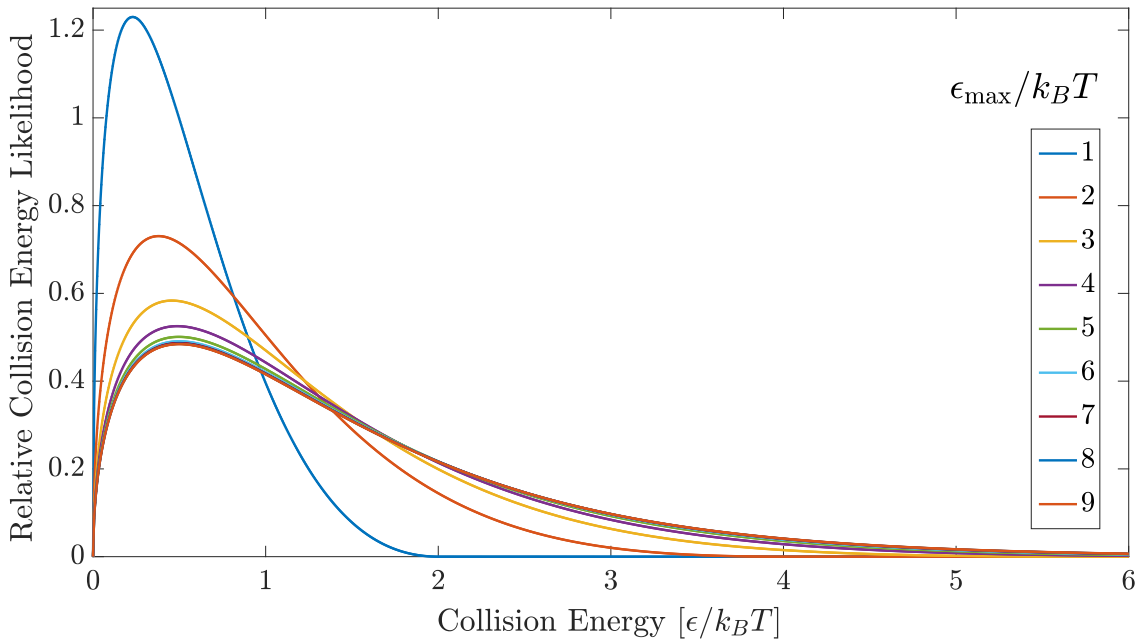


Figure 5.3 : Relative collision energy distributions for various truncations

The effects of single-particle kinetic energy truncation on the likelihood of relative energy collisions at different values of the maximum allowed single-particle kinetic energy ϵ_{\max} . Here the total collision probability for each curve is normalized to unity and energy is given in scaled units of $k_B T$. Each curve has a maximum collision energy of $2 \epsilon_{\max}/k_B T$ between two-particles each with maximum kinetic energy ϵ_{\max} .

5.1.2 Fitting the thermally averaged spectra

The consideration of the relative collision energy distribution for truncated single-particle energies is incorporated into the photoassociation lineshape equations by modifying the thermal average, $\langle K \rangle_{\text{thermal}}$. Recall from Sec. 3.4, that the two-body loss rate is simply given by $K = v\sigma_{in}$ and the thermal average is $\langle K \rangle_{\text{thermal}} = \int_0^\infty dv f(v) v \sigma_{in}$. By replacing $f(v)$ with Eq. 5.8 and modifying the integration bounds, the truncated thermal average is given by

$$\langle K \rangle_{\text{thermal}} = \frac{1}{h Q_T} \int_0^{2\epsilon_{\max}} d\epsilon |S(\epsilon)|^2 \hat{\mathcal{G}}(\epsilon_{\max}, \epsilon) \exp\left(\frac{-\epsilon}{k_B T}\right) \quad (5.9)$$

Note that the above expression only concerns the energy integral. The complete two-body loss rate with average over collision energy, space, and incorporating the effects of localized single-particle kinetic energy truncation becomes

$$\begin{aligned} \langle \hat{K} \rangle_{\text{trap}} &= \frac{1}{V_2} \int_V \exp\left(\frac{-2U(\mathbf{r})}{k_B T}\right) \\ &\quad \times \frac{1}{h Q_T} \int_0^{2\epsilon_{\max}(\mathbf{r})} d\epsilon |S(\epsilon, \mathbf{r})|^2 \hat{\mathcal{G}}(\epsilon_{\max}(\mathbf{r}), \epsilon) \exp\left(\frac{-\epsilon}{k_B T}\right) \end{aligned} \quad (5.10)$$

where $\epsilon_{\max}(\mathbf{r}) = U_{\text{depth}} - U(\mathbf{r})$ and U_{depth} is a global parameter describing the trap depth. The energy integral is now evaluated at each position within the trapping volume, \mathbf{r} , and the maximum single-particle kinetic energy is the difference $U_{\text{depth}} - U(\mathbf{r})$. This ensures that the total energy of the particle is the sum of the potential and kinetic energies and results in a spatially dependent energy cutoff.

As mentioned previously, our spectra indicate that the sample may be non-ergodic and there are significant numbers of atoms with kinetic energies above U_{depth} . We find that the data is well fit using a single-particle kinetic energy cutoff (ϵ_{\max}) that exceeds U_{depth} . Figure 5.4a shows fits for several different single-particle kinetic energy limits. Clearly the inclusion of higher energy collisions results in a more appropriate

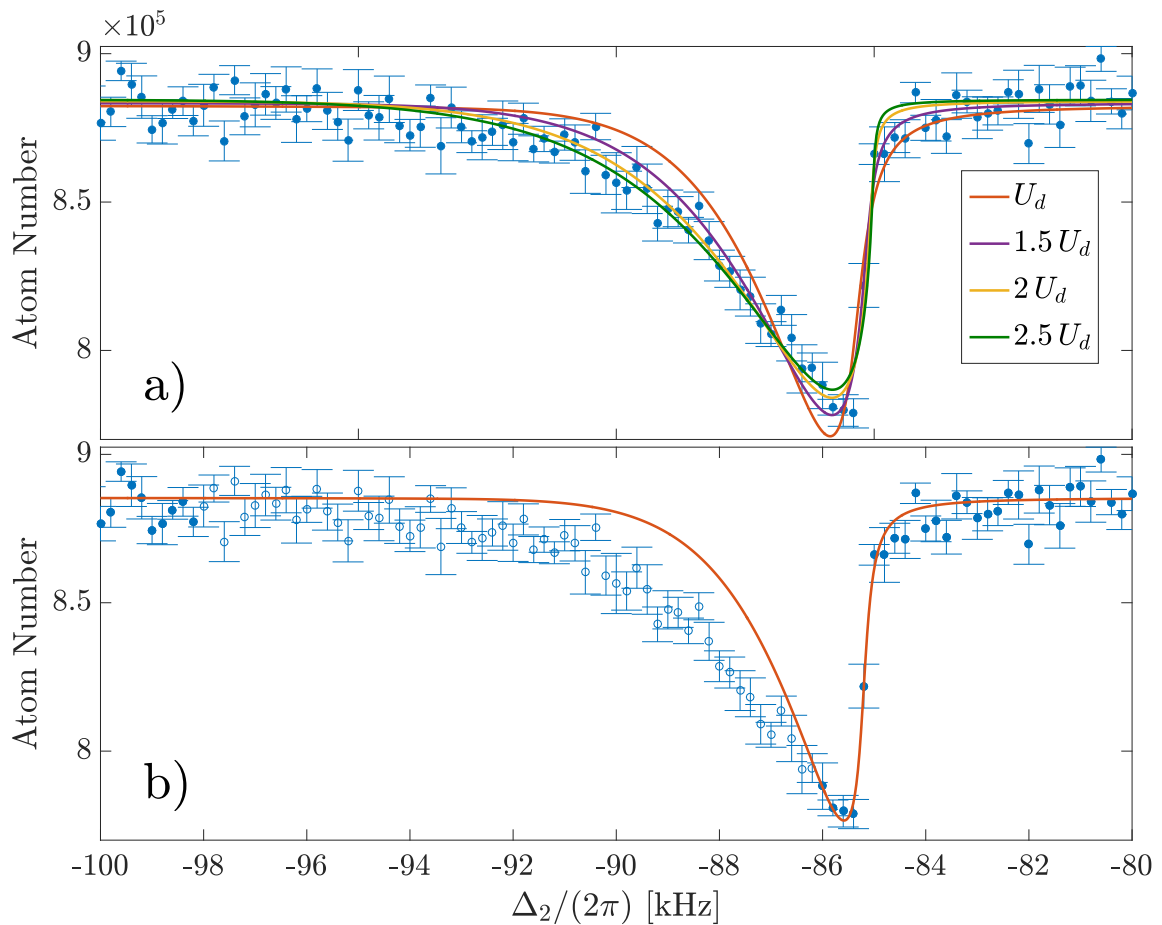


Figure 5.4 : Comparison of lineshape fits at various ϵ_{\max}

Using a constant trap geometry (eg. Fig. 5.1) with a trap depth U_d . Sample temperature determined from time-of-flight is 100 nK. a) The spectrum is fit with various maximum single-particle collision energy, $\epsilon_{\max}(\mathbf{r})$, shown by the solid lines and labeled in the legend. b) The spectrum is fit, neglecting the effects of truncation, using only the filled data points.

fit of the spectrum. However, it is not clear what the best description of the effective trap depth would be. Therefore, we proceed by fitting each spectra with limiting values of the single-particle kinetic energy cutoffs, $\epsilon_{\max}(\mathbf{r})$, equal to $[U_{\text{depth}} - U(\mathbf{r})]$ and $2[U_{\text{depth}} - U(\mathbf{r})]^{\dagger}$. The upper value of trap depth was chosen due to the height of the local maximum, $\sim 2 U_{\text{depth}}$, that was discussed previously. To estimate the systematic uncertainty introduced by this treatment of the non-ergodicity, we take the mean of the two results as the best value for the binding energy and half the difference as a systematic uncertainty $\sigma_{\epsilon_{\max}} \approx 100 \text{ Hz}$. This procedure does not correctly represent the overall normalization of $|S|^2$, but we are not concerned with overall signal amplitude in this study.

The method just outlined provides a description of the broad thermal tail, but fortunately the binding energy derived from the spectral fit is determined mostly by the contribution to the spectrum from low-energy collisions and is thus relatively insensitive to our choice of cutoff, ϵ_{\max} . To show this, we also fit the data excluding the broad thermal tail of the spectra and instead used only the sharp blue edge of the spectrum where low-energy collisions dominate. This provides a method to check the systematic uncertainty introduced by our incomplete understanding of the collision energy distribution and likely non-ergodicity. This "edge only" method provides a good estimate of the binding energy since broadening to the blue side of the spectrum is mostly sensitive to decay of the intermediate state $\Gamma_L(\epsilon)$, and the additional broadening term γ_{eff} . Thus the binding energy is strongly determined by this edge and is relatively insensitive to the description of the thermal portion of the spectrum.

[†]Note that with the 2 in the upper bound of the energy integral in Eq. 5.10, the integral is evaluated for relative collision energies from $[0 \rightarrow 2[U_{\text{depth}} - U(\mathbf{r})]]$ and $[0 \rightarrow 4(U_{\text{depth}} - U(\mathbf{r}))]$ respectively.

An example of such a fit is shown in Fig. 5.4b where the analysis neglects any effects of truncation and assumes the relative collision energy distribution is given by an unmodified Maxwell-Boltzmann. The long lifetime of the excited state and the significant detuning Δ_1 result in a width $\Gamma_L(\epsilon) < 5 \text{ Hz}$ for all conditions. This is extremely small compared to the observed width, which is determined by the fit of γ_{eff} to be on the order of 300 Hz. We hypothesize that the observed width reflects decay of molecules in the electronic ground state due to collisions with background atoms.

Table 5.1 gives a comparison of the resonances frequencies from each of these fitting methods. Here we give the estimated resonance position found by fitting the individual spectra for each set of experimental parameters (approximately 10 scans per row) and calculating the mean and standard error for the set. We see that the resulting estimates of the edge fit generally lie between the two values found via truncation. Note that the quoted uncertainty is statistical as no systematic error has been applied at this point. This provides confidence that our approach may reasonably estimate the $^{86}\text{Sr}_2$ binding energy. Furthermore, using only the values from the edge fit method does not substantively change our conclusions in the following sections.

5.2 Determination of energy shifts

We estimate the halo resonance energy of the atom-loss spectra using Eq. 3.38 for the evolution of atom number with time, Eq. 5.10 for the average two-body loss rate constant over the trap volume and locally truncated single-particle kinetic energy, and the phenomenological expression Eq. 5.2 for the scattering probability. We follow the fitting routine outlined just above whereby the quoted value of the binding energy is determined from the average of two fits where $\epsilon_{\text{max}}(\mathbf{r})$ is set equal to $[U_{\text{depth}} - U(\mathbf{r})]$

Label	Estimated halo state resonance from fit [kHz]		
	Scan	Edge fit	Truncated
		$U_{\text{depth}} - U(\mathbf{r})$	$2[U_{\text{depth}} - U(\mathbf{r})]$
1	-83.85 ± 0.1	-84.01 ± 0.02	-83.82 ± 0.03
2	-84.37 ± 0.04	-84.47 ± 0.03	-84.25 ± 0.03
3	-84.82 ± 0.02	-84.96 ± 0.03	-84.73 ± 0.02
4	-85.11 ± 0.07	-85.29 ± 0.02	-85.06 ± 0.02
5	-85.59 ± 0.02	-85.73 ± 0.02	-85.49 ± 0.02
6	-84.1 ± 0.03	-84.29 ± 0.05	-84 ± 0.02
7	-85.09 ± 0.03	-85.15 ± 0.03	-84.99 ± 0.01
8	-85.04 ± 0.03	-85.11 ± 0.04	-84.99 ± 0.01
9	-84.97 ± 0.03	-85.04 ± 0.04	-84.95 ± 0.01
10	-85.03 ± 0.07	-85.08 ± 0.05	-84.97 ± 0.03
11	-84.08 ± 0.05	-84.14 ± 0.04	-84.07 ± 0.05
12	-84.11 ± 0.07	-84.04 ± 0.02	-84.06 ± 0.01

Table 5.1 : Comparison of fitted resonance energies

The fit resonance position E'_{b2}/h , is given for each type of fitting routine used to analyze the data shown in Figures 5.6 and 5.8. The scan label column corresponds to the same label used in Table 5.2 that provides more detailed experimental conditions and the "Truncated" columns give the maximum single-particle kinetic energy ϵ_{max} that was allowed when fitting. Comparison of the "edge fit" method to the truncated method shows the edge method typically falls between the two limiting cases. Note that the quoted uncertainty is statistical.

and $2[U_{\text{depth}} - U(\mathbf{r})]$. The shifted resonance energy E'_{b2} , η , and γ_{eff} are taken as fit parameters. Table 5.2 gives the fit results and pertinent experimental parameters used in evaluating this data. In the final analysis, temperatures are set to values determined from time-of-flight imaging of the atoms (as given in the table), but when they are allowed to vary, the fit values differ by no more than 10%. Approximately 10 spectra are recorded and independently fit for each set of experimental parameters. The spread of resulting parameter estimates from the fits are used to determine best values and uncertainties. All error bars shown are the standard error determined from the set of individual scans.

5.2.1 AC Stark shift due to excitation lasers

The most significant perturbation to the resonance position is the AC Stark shift due to the excitation laser intensity, as shown in Fig. 5.5. We fit each spectrum to find the binding energies with fixed parameters, temperature ($T = 30 \text{ nK}$), initial peak sample density ($n_0 = 2 \times 10^{12} \text{ cm}^{-3}$), and excitation time 50 ms. Fig. 5.6 gives the best fit value of the binding energies versus the single-beam intensity where we varied the single-beam excitation intensity from $I = 0.02 - 0.06 \text{ mW/cm}^{-2}$. The susceptibility to 689 nm intensity, in Hz per unit intensity, is determined from Fig. 5.6 by taking I_{689} as twice the single-beam intensity $I_{689} = 2I$ and the functional form for the AC Stark shift due to the excitation lasers as discussed in Sec. 4.4. The observed shifts are comparable to the thermal width of the spectrum, allowing a precise determination of $\chi_{689} = -21(1)(2) \text{ kHz/(W/cm}^2)$ from a linear fit to the resonance positions, $\Delta E'_{b2} \propto h\chi_{689}I_{689}$ as shown in Fig. 5.6. This value of the susceptibility is in agreement with the estimate of the Floquet model presented in Sec. 4.4. The first quoted uncertainty is statistical and it arises from variations in parameters and fluctuations in the measured

Scan	E'_{b2}/h	$\gamma_{\text{eff}}/2\pi$	T	U_{depth}/k_B	Initial Number	$\langle n(\mathbf{r}) \rangle$	$\langle I_{1064}(\mathbf{r}) \rangle$	I_{689}
Label	(kHz)	(kHz)	(nK)	(μ K)	($\times 10^6$)	($\times 10^{12} \text{ cm}^{-3}$)	(kW/cm 2)	(mW/cm 2)
1	-83.91 ± 0.03	0.45 ± 0.1	30	0.033	0.231	1.29	3.4	44 ± 3
2	-84.36 ± 0.04	0.38 ± 0.13	29	0.033	0.231	1.31	3.4	64 ± 3
3	-84.85 ± 0.04	0.29 ± 0.1	32	0.033	0.233	1.28	3.4	83 ± 4
4	-85.18 ± 0.03	0.35 ± 0.12	32	0.033	0.273	1.5	3.4	104 ± 4
5	-85.61 ± 0.03	0.44 ± 0.09	32	0.033	0.225	1.24	3.4	123 ± 7
6	-84.15 ± 0.06	0.49 ± 0.18	70	0.113	0.64	1.08	4.1	51 ± 3
7	-85.07 ± 0.03	0.32 ± 0.11	78	0.145	0.753	1.06	4.4	97 ± 4
8	-85.05 ± 0.04	0.34 ± 0.13	104	0.219	0.949	0.98	4.8	97 ± 4
9	-85 ± 0.04	0.21 ± 0.12	129	0.298	1.096	0.89	5.2	97 ± 4
10	-85.02 ± 0.06	0.29 ± 0.17	154	0.384	1.226	0.84	5.6	97 ± 4
11	-84.11 ± 0.06	0.21 ± 0.13	211	0.572	1.524	0.79	6.3	51 ± 3
12	-84.05 ± 0.02	0.23 ± 0.12	402	1.4	2.05	0.66	9.1	51 ± 3

Table 5.2 : Experimental parameters for evaluating the $^{86}\text{Sr}_2$ halo binding energy
Select list of relevant experimental conditions for the experiments summarized in
Figs. 5.6 (scans 1-5) and 5.8 (scans 6-12). Parameters such as the intermediate state
detuning, $\Delta/2\pi = -9$ MHz, intermediate state decay rate $\gamma_1/2\pi = 15$ kHz, and
one-body loss rate, $\Gamma_1 = 2 \text{ s}^{-1}$ are considered fixed for each sample. Additionally,
the stimulated width, γ_s is calculated using $\ell_{opt} = 15 \times 10^3 a_0 / (\text{W/cm}^2)$ and the
Rabi frequency $\Omega_{12}/2\pi = 850$ kHz for $I_{689} = 1 \text{ W/cm}^2$ as found in the previous
chapter. $\langle I_{1064}(\mathbf{r}) \rangle$ and $\langle n(\mathbf{r}) \rangle$ are weighted averages of the 1064 nm trapping
intensity and number density respectively. These weighted averages are taken over
the trapped sample, with weighting given by the square of atom density.

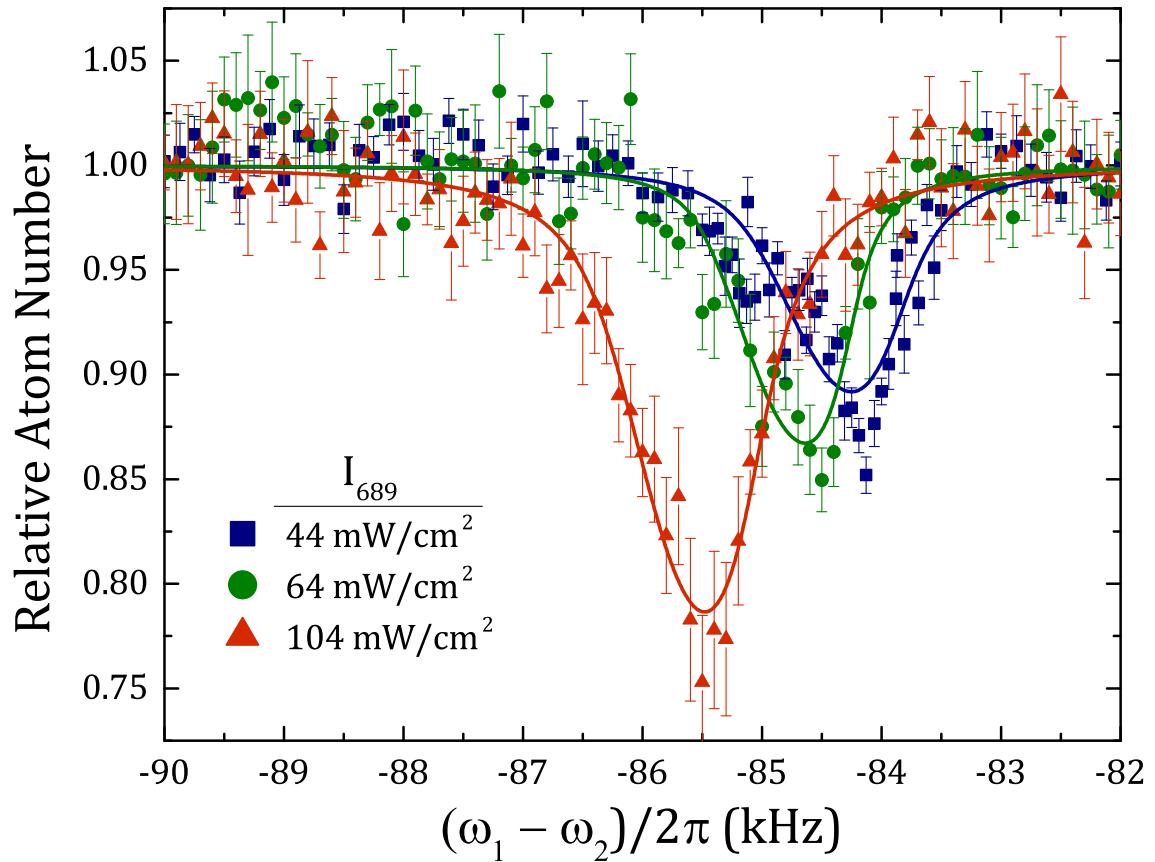


Figure 5.5 : Atom-loss spectra with varying 689 nm intensity

Atom-loss spectra as a function of two-photon difference frequency $(\omega_1 - \omega_2)/2\pi$ for intermediate detuning $\Delta_1/2\pi = -9 \text{ MHz}$ and various 689 nm excitation laser intensities. Twice the single-beam intensity $I_{689} = 2I$ is indicated in the legend.

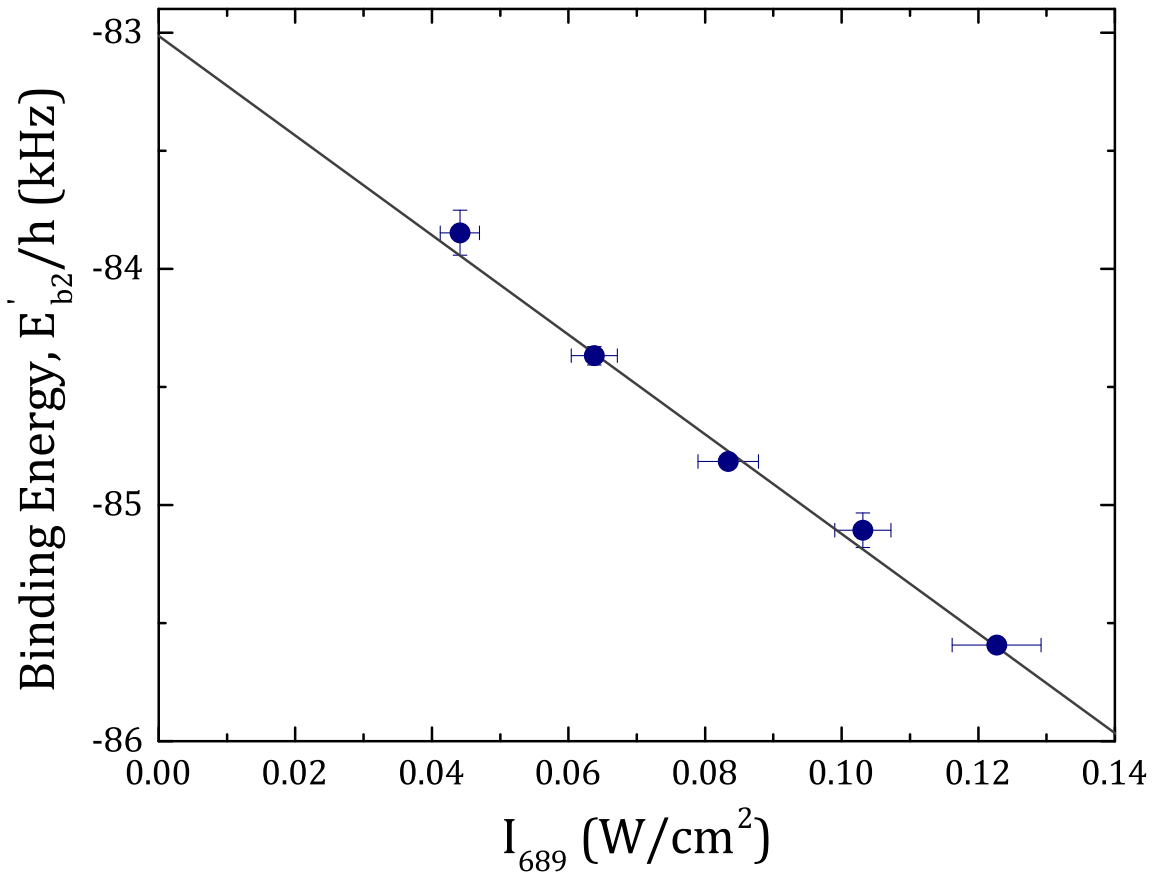


Figure 5.6 : Fit of 689 nm AC Stark shift

Measured resonance position E'_{b2} plotted versus twice the single-beam intensity $I_{689} = 2I$. The linear fit provides the AC Stark shift parameter χ_{689} .

intensity during the scans. The second value is systematic, reflecting uncertainty in laser-beam size and intensity profile at the atoms.

All parameters beside the 689 nm laser intensity are held fixed for this data, the AC Stark shift is not sensitive with any other variable, such as density or trap intensity. We thus obtain an accurate measure of χ_{689} without attempting to account for other systematic shifts of E'_{b2} in this data.

5.2.2 Density-dependent frequency shift

A shift of the two-photon resonance position is possible due to differing mean-field shifts of initial atomic and final molecular states arising from interaction with the background of ground state atoms. Such a shift would be proportional to the atom density, $\Delta E_{b2} \propto \hbar \chi_n n$, where χ_n depends upon the *s*-wave scattering lengths for atom-atom and atom-dimer collisions, a_{86} and a_{ad} respectively. This was observed in a Rb Bose-Einstein condensate in Ref. [197]. For a non-degenerate gas, this effect yields $\chi_n = \hbar(\frac{a_{\text{ad}}}{\mu_{\text{ad}}} - 4\frac{a_{86}}{\mu_{\text{aa}}}) = \frac{\hbar}{m}(\frac{3}{2}a_{\text{ad}} - 8a_{86})$, where μ_{ad} and μ_{aa} are the reduced masses for molecule-atom and atom-atom collisions respectively. Note that the shift would vanish for $a_{\text{ad}} = (16/3)a_{86}$. The largest densities used in these experiments was $\sim 1 - 2 \times 10^{12} \text{ cm}^{-3}$. This is relatively low compared to typical BEC densities, and at this time we are unable to accurately measure a variation of resonance position with density. However, the atom-atom scattering is close to resonance and thus Efimov physics can provide information on a_{ad} [24, 144] and an estimate of the systematic error introduced by any residual density-dependent frequency shifts. For a zero-range interaction, the atom-dimer scattering length is related to the atom-atom scattering length through the three-body Efimov parameter κ_* according to [24]

$$a_{\text{ad}} = a_{86} \{1.46 + 2.15 \cot[s_0 \ln(14.1 \kappa_* a_{86})]\} \quad (5.11)$$

where $s_0 = 1.006$ [‡].

In principle, the atom-dimer scattering length can take any value. However, for a deep atom-atom potential, such as for the ground state strontium dimer [175], there is a universality of the three-body physics that sets $\kappa_* = 0.226(2)/R_{\text{vdW}}$ [193]. Here,

[‡]The Efimov parameter is related to E_{3b}^0 through $\kappa_* = (m|E_{3b}^0|/\hbar^2)^{1/2}$, where E_{3b}^0 is the binding energy the lowest Efimov trimer would have in the case of resonant atom-atom interactions.

$R_{\text{vdW}} = (2\mu C_6/\hbar^2)^{1/4}/2 = 74.6 a_0$ is the van der Waals length associated with the C_6 coefficient of the long-range Sr_2 ground state potential. Using $C_6 = 3164 \text{ a.u.}$ from a fit of potential parameters to spectroscopic data [175], yields $\kappa_* = 5.72 \times 10^7 \text{ m}^{-1} = (330 a_0)^{-1}$. Eq. 5.11 then predicts $a_{\text{ad}} = 6.4 a_{86}$, which leads to a small density-dependent frequency shift parameter of $\chi_n = 50 \text{ Hz}/(10^{12} \text{ cm}^{-3})$. A numerical calculation including a finite-range correction for the atom-atom interaction [124] results in $a_{\text{ad}} = 3.5 a_{86}$ and $\chi_n = -90 \text{ Hz}/(10^{12} \text{ cm}^{-3})$. Thus, a very small shift is expected for the densities used here.

We incorporate $\chi_n = 0 \pm 90 \text{ Hz}/(10^{12} \text{ cm}^{-3})$ as a set parameter in our model of the spectrum, where we set the systematic uncertainty to reflect the spread of theory predictions. This uncertainty is the most significant source of error for our determination of the unperturbed halo binding energy.

5.2.3 AC Stark Shift due to Trapping Lasers

The final effect we considered accounts for spatial dependence of the AC Stark shift due to the intensity $I(\mathbf{r})$ of the 1064 nm trapping laser. We modeled the effect of the AC Stark shift from the trapping laser as $\Delta E_{b2} = \chi_{1064} \times \langle I_{1064} \rangle$ where $\langle I_{1064} \rangle$ is a two-body weighted average intensity of the 1064 nm laser that is used to characterize the average shift experienced by the atoms due to the trapping potential. Fig. 5.7 shows a series of spectra for different final trap depths (values of $\langle I_{1064} \rangle$) and sample temperatures. For the lowest temperature data, the effects of truncation discussed in Sec. 5.1.1 is evident. We illustrate the fit results from the two different limits of collision energy by bounding each fit with a solid line and shading the region between.

With an accurate determination of χ_{689} , a value for χ_n , and a method for characterizing the trapping intensity, we use the data shown in Fig. 5.7 to determine the

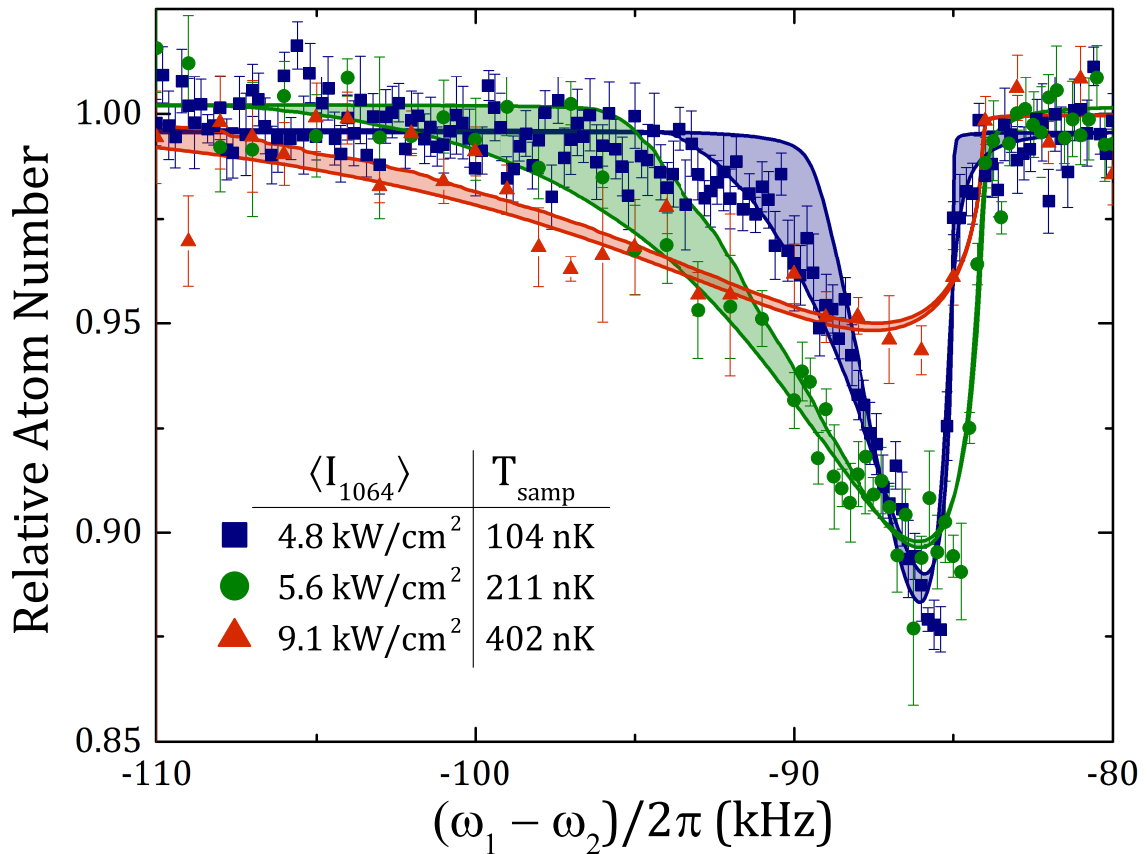


Figure 5.7 : Atom-loss spectra with varying 1064 nm intensity

Sample temperature and average trapping laser intensity are indicated in the legend. The single-beam excitation laser intensity is $I = 25 \text{ mW/cm}^2$ for the 104 nK spectrum and $I = 48 \text{ mW/cm}^2$ for the 211 nK and 402 nK spectra. The two boundaries of each band give the fits with collision-energy truncation ϵ_{\max} equal to $2[U_{\text{depth}} - U(\mathbf{r})]$ and $U_{\text{depth}} - U(\mathbf{r})$.

susceptibility for the AC Stark shift from the trapping laser, χ_{1064} , and the unperturbed halo binding energy E_{b2} . Fig. 5.8 shows a plot of $E''_{b2} = E'_{b2} - \chi_{689}I_{689} - \chi_n\langle n \rangle$ versus $\langle I_{1064} \rangle$, where E'_{b2} is the resonance position from each fit and $\langle \dots \rangle$ indicates a weighted average of the quantity over the trapped sample, with a weighting given by the square of atom density. The plotted uncertainties in E''_{b2} are from statistical variation in the fit parameters.

The typical average density is $\langle n \rangle \approx 1 \times 10^{12} \text{ cm}^{-3}$. The linear fit function is to $E''_{b2} = E_{b2} + \chi_{1064}\langle I_{1064} \rangle$ where E_{b2} is the unperturbed energy of the halo molecule. In addition to statistical uncertainty, we account for the systematic uncertainty from χ_n and our treatment of the truncation of the collision-energy integral by performing linear fits to values of $E'_{b2} - \chi_{689}I_{689} - \chi_n\langle n \rangle$ to determine by assuming these parameters are shifted up and down by the limiting estimates for each parameter.. The dashed lines shown in Fig. 5.8 show the results of these fits. The resulting value for the unperturbed binding energy is $E_{b2}/h = -83.00(7)(20) \text{ kHz}$, where the first uncertainty is statistical, and the second is systematic. We estimate a susceptibility to I_{1064} of $\chi_{1064} = 0 \pm 10 \text{ Hz/(kW/cm}^2)$.

5.3 Discussion of the halo binding energy

In the limit of extremely small binding energy and resonant atom-atom interactions, the binding energy of a halo molecule is approximately given by [35, 85, 105]

$$E_b = \frac{\hbar^2}{2\mu a^2} \quad (5.12)$$

For interactions described at long-range by a van der Waals potential $V(r) = -C_6/r^6$, as with ultracold atoms, a convenient figure of merit for quantifying how accurate Eq. 5.12 should be is given by the ratio of the *s*-wave scattering length to the inter-

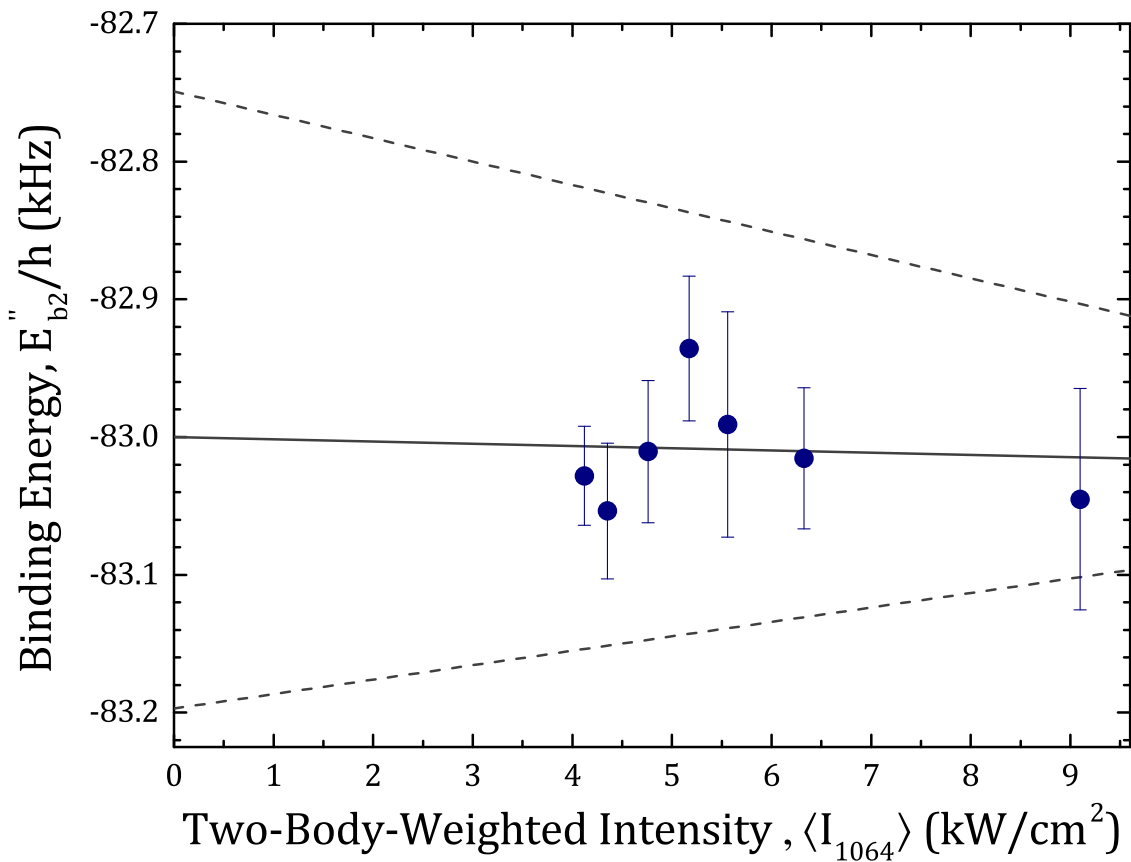


Figure 5.8 : Measurement of halo state susceptibility, χ_{1064}

Measured resonance positions corrected for excitation-laser AC Stark shift and collisional frequency shift, $E''_{b2} = E'_{b2} - \chi_{689}I_{689} - \chi_n\langle n \rangle$, as a function of average trap laser intensity $\langle I_{1064} \rangle$ for the data such as in Fig. 5.7 . The trend line and confidence intervals are described in the text.

action range \bar{a} that is closely related to the van der Waals length [36, 75].

$$\bar{a} = \frac{4\pi}{\Gamma(1/4)^2} R_{\text{vdW}} \quad (5.13)$$

Slightly away from resonance, corrections to the binding energy for the van der Waals potential were worked out in [63, 64], yielding

$$E_{b2} = -\frac{\hbar^2}{2\mu(a - \bar{a})^2} \left[1 + \frac{g_1 \bar{a}}{a - \bar{a}} + \frac{g_2 \bar{a}^2}{(a - \bar{a})^2} + \dots \right], \quad (5.14)$$

where $g_1 = \Gamma(1/4)^4 / 6\pi^2 - 2 = 0.918\dots$ and $g_2 = (5/4)g_1^2 - 2 = -0.947\dots$. The range of validity of this expression is $a \gtrsim 2\bar{a}$. The accuracy of the first term in this expansion has been experimentally confirmed for various systems such as ^{85}Rb [43, 104], ^{40}K [137, 159] and ^6Li [5]. The derivation of Eq. 5.14 assumes that the influence of short-range physics, which can be expressed through a quantum defect, varies negligibly from threshold to the molecular binding energy. We expect this to be an excellent approximation, since, as shown in Ref. [63] the corrections are typically less than about 1% even for GHz binding energies.

For ground state ^{86}Sr atoms, $\bar{a} = 71.3 a_0$. The most accurate value available for the *s*-wave scattering length is $a = 798(12) a_0$ [175], satisfying the requirement of $a \gg \bar{a}$ for the least-bound state on the ground molecular potential to be a halo molecule. Nonetheless, $\bar{a}/(a - \bar{a}) = 0.10$, and the corrections given by Eq. 5.14 are significant (Fig. 5.9). Using the previous best value of the scattering length, Eq. 5.14 predicts a binding energy of $E_{b2} = -86(3)$ kHz. This agrees with our measurement, but by inverting Eq. 5.14, we can use our increased accuracy in E_{b2} to extract an improved value of the scattering length of $a = 810.6(3)(9) a_0$, where uncertainties reflect statistical and systematic uncertainties in E_{b2} respectively. The next higher-order term in $x_0 = \bar{a}/(a - \bar{a})$ is likely to introduce a correction on the order of 100 Hz

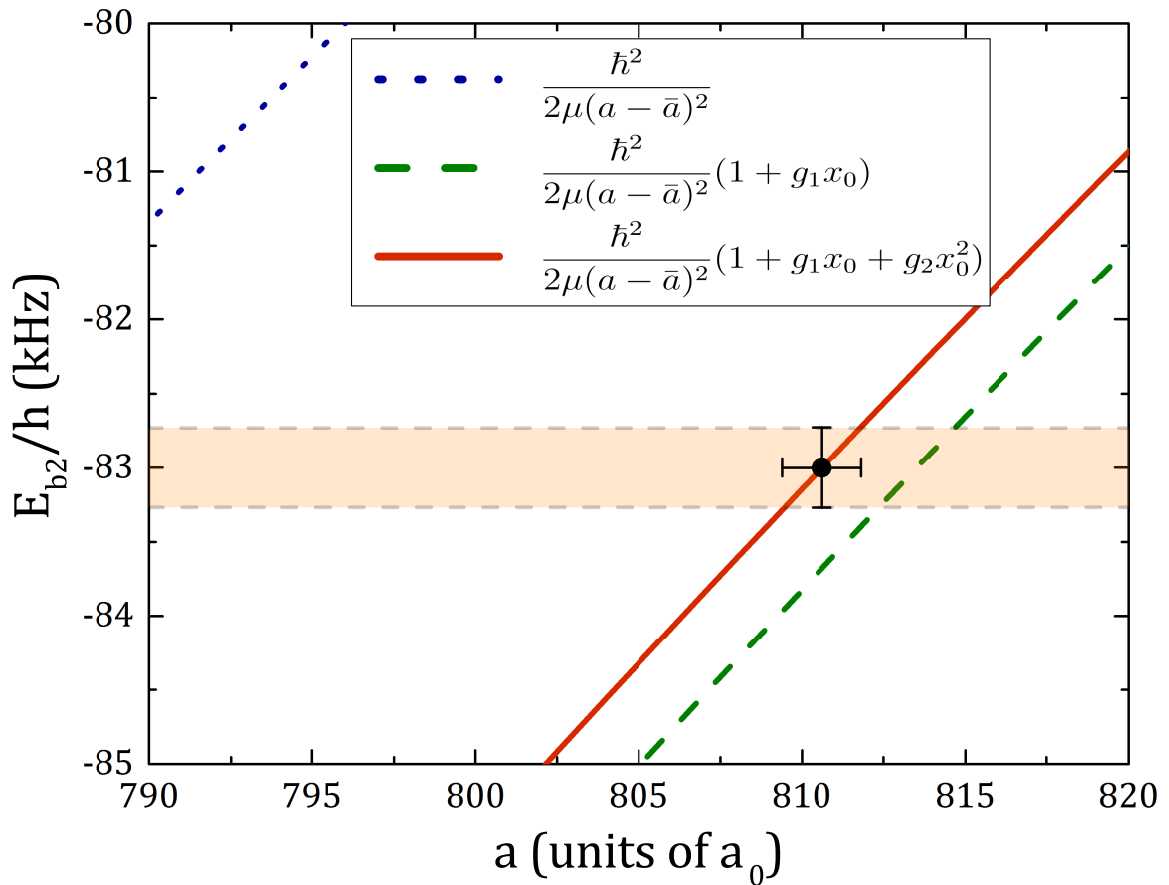


Figure 5.9 : Determination of 86 s-wave scattering length

Halo binding energy versus s -wave atom-atom scattering length for ^{86}Sr . The shaded region indicates our experimental measurement. The lines are predictions of Eq. 5.14 retaining up to the first, second, and third terms as indicated in the legend [$x_0 = \bar{a}/(a - \bar{a})$]. The data point is the prediction of Eq. 5.14 for the recommended value of the measured binding energy.

in Eq. 5.14, creating a systematic uncertainty in a that is about one third of the uncertainty from our measurement.

This binding energy can be used to determine the value of the ground state potential C_6 parameter for strontium. As previously discussed in Sec. 3.3.1, the relationship between the scattering length and the potential is given by

$$a = \bar{a} \left[1 - \tan(\Phi - \frac{\pi}{8}) \right] \quad \Phi = \int_{R_i}^{\infty} dR \sqrt{\frac{-2\mu V(R)}{\hbar^2}} \quad (5.15)$$

where R_i is the inner turning point of the potential such that $V(R_i) = 0$. Therefore, given the potential, we can use these equations to calculate the s -wave scattering length with Eq. 5.15 and the binding energy of the halo state with Eq. 5.14.

Stein et al. (2010) [175], gives two piece-wise estimates of the strontium ground state $X^1\Sigma_g^+$ potential with separately defined functional forms for the inner, central, and long-range portions where the model coefficients are determined from molecular spectroscopy data. The two model potentials are labeled "freely varied" and "recommended" and differ in their treatment of the long-range coefficients. The "freely varied" model results from allowing all coefficients, including the long-range coefficients, to be treated as fit parameters and subsequently estimated by the fitting routine (details of this routine may be found in [175]). The "recommended" model is an averaged model where the value of either C_6 or C_8 were fixed to *ab initio* calculations from Refs. [155, 203] and the remaining unconstrained long-range coefficients were fit using the transition data. The recommended model also determines the inner and central coefficients via fitting.

Using these two forms of the strontium ground state potential, the binding energy for the halo state can be determined with Eq. 5.14 using a numerical integration of Φ to find a (Eq. 5.15). Fig. 5.10 shows the predicted binding energy when varying C_6 and holding all other parameters of each model constant. This analysis assumes that all

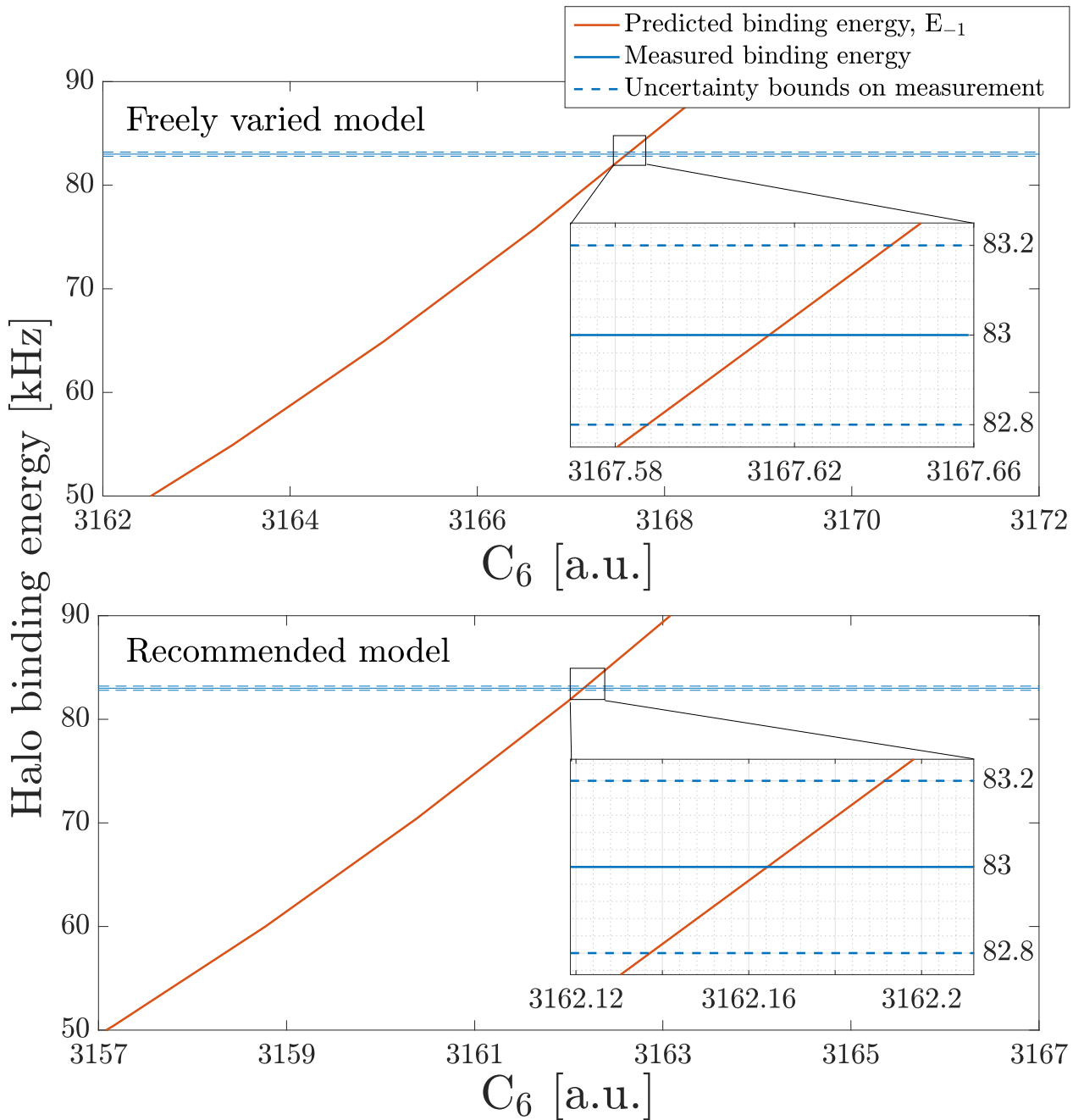


Figure 5.10 : Comparison of C_6 coefficient estimates

The ^{86}Sr halo state predicted binding energy is calculated using Eq. 5.14 and numerical integration of the piece-wise potentials from Stein et al. (2010) [175]. Comparing the measured halo state binding energy to these predictions gives an estimate of the underlying C_6 underlying value.

other parameters of the potentials from Ref. [175], particularly the inner portion of the potential, are well determined, which may not necessarily be true. Thus, additional analysis of least-bound states of other isotopes should provide a robust measure of the long-range portion of the $X^1\Sigma_g^+$ potential. However, the extremely small binding energy of the ^{86}Sr halo molecule is a sensitive probe of the strontium C_6 parameter so in lieu of a more complex analysis, we consider the rest of the potential parameters to be fixed and only the vary the C_6 parameter.

From Fig. 5.10 we can determine a C_6 value for each form of the potential that shows the precision of our measurement exceeds that of the available models and suggests that this work could be useful to further develop a theoretical understanding of the long-range portion of the strontium $X^1\Sigma_g^+$ potential. Table 5.3 shows all published values, and errors where available, for the strontium C_6 coefficient. We have included both values from Fig. 5.10 for completeness and show that they are in agreement with a majority of the published literature. The quoted C_6 values are found from Fig. 5.10 by applying a linear fit, in the region of the binding energy, to the C_6 curves. From these fits we find the intersection of C_6 and the binding energies at 83 ± 0.2 kHz for both models.

Next, using our values of C_6 given in Table 5.3 we compute the s -wave scattering lengths for each isotopic combination of strontium through mass-scaling, Table 5.4. Interestingly, despite our estimated values for C_6 being model dependent, the calculated scattering lengths from each model are found to be nearly identical, differing by $< 0.5\%$ across all isotopes. The scattering length for each model are given in Table 5.4 and Fig. 5.11 plots the mass-scaled scattering lengths as a function of the reduced mass. The quoted values of a are calculated for each model using the appropriate value of C_6 as given in Table 5.3. These C_6 estimates are used to construct

C_6 [a.u.]	Reference	Type
3212	Stanton (1994) [174]	Theory
3170 ± 197	Porsev et al. (2002) [154]	Theory
3249	Mitroy et al. (2003) [135]	Theory
3131 ± 41	Lima et al. (2005) [111]	Theory
3103 ± 7	Porsev et al. (2006) [155]	Theory
3130 ± 20	Martinez de Escobar et al. (2008) [118]	Experiment
3164 ± 10	Stein et al. (2010) [175]	Experiment
3142	Skomorowski et al. (2012) [172]	Theory
3107 ± 30	Zhang et al. (2014) [207]	Theory
3162.16 ± 0.03 - Freely varied	Aman et al. (2018) [1]	Experiment
3167.61 ± 0.03 - Recommended		

Table 5.3 : Comparison of C_6 values from literature

All values are given in atomic units. Note that the uncertainty of the present measurement reflects the uncertainty in the binding energy of the halo molecule.

	"Freely varied"	"Recommended"	Average value
	$C_6 = 3162.16 \text{ a.u.}$	$C_6 = 3167.61 \text{ a.u.}$	
84 + 84	122.94	122.89	122.92 ± 0.06
84 + 86	31.63	31.62	31.62 ± 0.02
84 + 87	-57.48	-57.44	-57.46 ± 0.07
84 + 88	1715	1716	1716 ± 5
86 + 86	810.7	810.6	810.6 ± 1
86 + 87	162.6	162.5	162.58 ± 0.09
86 + 88	97.44	97.41	97.43 ± 0.1
87 + 87	96.27	96.23	96.25 ± 0.05
87 + 88	54.8	54.78	54.79 ± 0.05
88 + 88	-2.025	-2.019	-2.022 ± 0.025

Table 5.4 : Comparison of calculated s -wave scattering lengths

All scattering lengths are given in units of a_0 , the Bohr radius. The average of the two calculated values is given as the scattering length in the final column. The uncertainty is estimated by summing the calculated uncertainty and the difference between each model. The calculated uncertainty is found by calculating scattering lengths using the values of C_6 plus uncertainty given in Table 5.3.

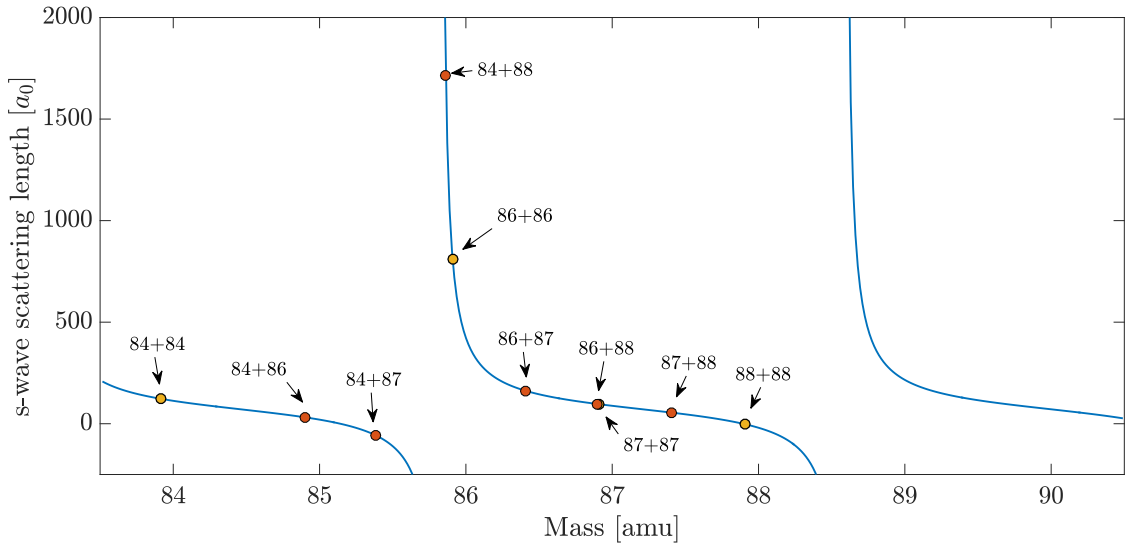


Figure 5.11 : Estimation of scattering lengths via mass scaling

and numerically integrate the potential from $R_i \rightarrow \infty$ according to Eq. 5.15, where $R_i = 7.5 a_0$ is the inner turning point of both models (as given in Ref. [175]). Finally, the average estimate of the scattering length (given in the last column of Table 5.4) is calculated by taking the average of the two scattering lengths as the quoted value and the difference of the scattering lengths as a systematic uncertainty. This difference is then summed with the uncertainty derived from our uncertainty in the determination of C_6 .

Chapter 6

Installation of a 532 nm lattice

Optical lattices are formed by a standing wave of light which creates a defect free periodic potential. These traps are extremely versatile and have enabled the observation of the superfluid - Mott insulator transition [72], artificial gauge fields for neutral atoms [112], quantum microscopy with single-site resolution [4], and investigations of quantum magnetism [69, 79]. They are among the most well-established techniques for controlling a quantum state and have proven to be great tools for exploring the connection between few- and many-body systems [13].

Until recently, experiments on the Neutral apparatus were confined to work with bulk gases in an optical dipole trap. While optical dipole traps are useful for efficient evaporation and thermalization of an ultracold gas, optical lattices greatly extend our capabilities for studying ultracold molecules and novel many-body quantum states [30, 109, 134, 138, 187, 207]. A straightforward extension of the work presented in this thesis would be to introduce an optical lattice, which with appropriate parameters could isolate halo molecules from atom-molecule collisions and allow for improved study of their properties. It would also enable studies of $SU(N)$ quantum magnetism with fermionic strontium. This chapter will detail our installation and characterization of this laser system.

6.1 Background

An optical lattice is created by counter-propagating two laser beams to form a standing wave pattern, which for two plane waves if the same polarization in one-dimension results in a periodic potential given by

$$V(x) = V_{lat} \sin^2(k_L x) \quad (6.1)$$

where V_{lat} is the lattice depth determined by the polarizability of the atom for a given trapping wavelength λ and laser intensity I , and $k_L = 2\pi/\lambda$ is the lattice wavevector. This potential can be readily extended to three dimensions using two additional pairs of counter-propagating laser beams along the y and z directions which results in a 3D cubic lattice. Depth of the trapping potential, V_{lat} , is controlled by varying the intensity of the lattice beams.

Periodic potentials are powerful because they break the translational invariance of space which results in the formation of band structure and the opening of bandgaps or disallowed particle energies [8]. Because of this broken invariance, p is no longer a good quantum number and must be replaced by two new quantum numbers: the band index, n , and the quasimomentum, q . In one-dimension, quasimomentum is specified by $q = p - nG$, where $G = 2\pi/a$ is a reciprocal lattice vector, and a is the real space lattice constant. Fig. 6.1 shows how the band structure varies as the lattice depth is increased. Optical lattices have a lattice spacing $a = \lambda/2$ which determines the reciprocal lattice vector $G = 4\pi/\lambda = 2\hbar k_L$ and a natural energy scale $E_r = \frac{\hbar^2 k_L^2}{2m}$ where m is the atomic mass and k_L the lattice wavevector. From the band structure, we see that the bandwidth of each band, given by $\Delta E = E_{q=\hbar k_L} - E_{q=0}$, decreases as the lattice depth is increased. In the limit that $V_{lat} \rightarrow \infty$ the band structure reduces to a ladder of harmonic oscillator levels spaced by $\hbar\omega_{ho} = \sqrt{4V_{lat}E_r}$, where ω_{ho} is the

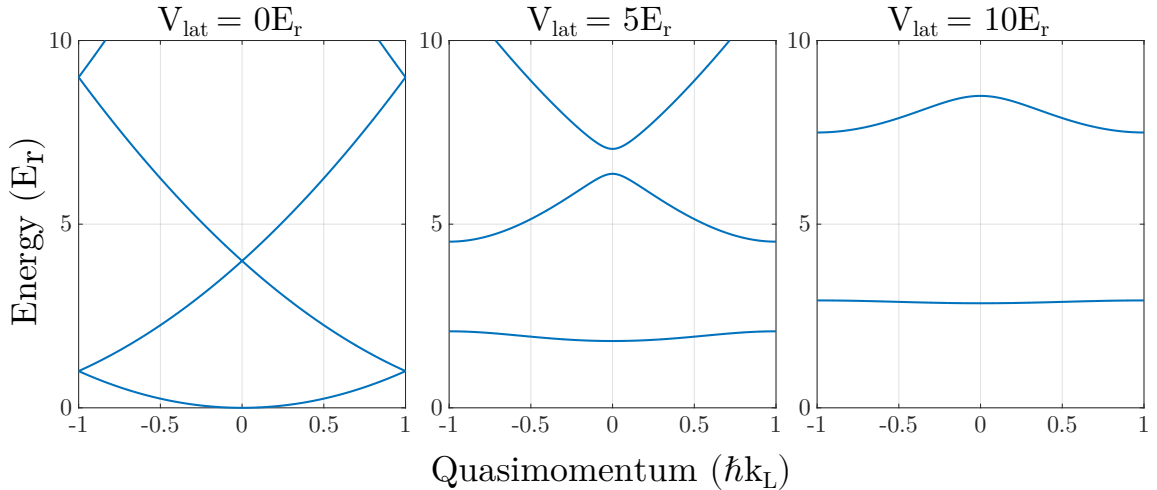


Figure 6.1 : 1D band structure as a function of lattice depth

One-dimensional band structure for an optical lattice as the lattice depth is increased. The band energies are found by solving the Schrödinger equation using the Bloch functions of Eq. 6.2.

trapping frequency within a single site. For moderately deep lattices, $V_{\text{lat}} \gtrsim 5 E_r$, this approximation is valid near the center of the Brillouin zone, $q = 0$, and provides a simple form to estimate the energy gaps between bands [91, 92, 92].

Solutions to the Schrödinger equation in a periodic potential are given by the Bloch functions [8]

$$\phi_q^{(n)}(x) = e^{iqx/\hbar} u_q^{(n)}(x) \quad (6.2)$$

These eigenstate wavefunctions are specified for a given quasimomentum q , and band index n . Their corresponding energy eigenvalues define the band structure of the lattice shown in Fig. 6.1. From Eq. 6.2 we see that the Bloch functions are the product of plane waves modulated by a function $u_q^{(n)}(x)$, which shares the periodicity of the underlying lattice potential [8]. For an optical lattice this modulating function can

be expanded in a basis of plane waves through a Fourier decomposition of the lattice potential in Eq. 6.1, which gives [70],

$$u_q^{(n)}(x) = \sum_l c_l^{(n,q)} e^{i2lk_L x} \quad (6.3)$$

Here $c_l^{(n,q)}$ are the coefficients for each plane wave in the basis expansion that are found by diagonalizing the lattice Hamiltonian [70].

Often, we are interested in the dynamics of particles on a particular lattice site, but since Bloch functions are delocalized over the entire lattice, it is useful to instead use the Wannier functions. These functions provide an orthogonal and normalized set of wavefunctions that are maximally localized to a specific lattice site. The Wannier function for a localized particle in the n^{th} band of a lattice site located at position x_i is given by [92]

$$w_n(x - x_i) = \mathcal{N}^{-1/2} \sum_q e^{iqx_i/\hbar} \phi_q^{(n)}(x) \quad (6.4)$$

where \mathcal{N} is a normalization constant and $\phi_q^{(n)}(x)$ are the Bloch functions of Eq. 6.2. This localized description of particles allows us to calculate important physical quantities which govern dynamical properties of the lattice such as the tunneling rate, J/\hbar , and on-site interaction energy, U . As $V_{lat} \rightarrow \infty$, the Wannier functions approach the eigenfunctions of the harmonic oscillator, which allows us to estimate the spatial extent of an atomic wavefunction by $a_{ho} = \sqrt{\frac{\hbar}{m\omega_{ho}}}$ [92].

When bosons are confined to the lowest energy band of a lattice, a particularly simple model known as the Bose-Hubbard Hamiltonian is used to describe the lattice system [91].

$$H_{BH} = -J \sum_{\langle i,j \rangle} (\hat{b}_i^\dagger \hat{b}_j + \hat{b}_j^\dagger \hat{b}_i) + \frac{U}{2} \sum_i \hat{n}_i(\hat{n}_i - 1) \quad (6.5)$$

Where $\langle i, j \rangle$ denotes a sum over nearest-neighbors. This model is the simplest example of a non-trivial interacting many-body system for dynamics in a lattice. The first

term describes hopping of bosons from site to site at a rate J/\hbar . The second term describes an interaction energy which is related to the s -wave contact interaction term, $g = 4\pi\hbar^2 a_s/m$, where a_s , is the s -wave scattering length of the particles. J and U can be calculated directly using the Wannier functions of Eq. 6.4 and are given by [92]

$$\begin{aligned} J_{ij} &= - \int d^3x w_0(x - x_i) \left(\frac{p^2}{2m} + V(x) \right) w_0(x - x_j) \\ U &= \frac{4\pi\hbar^2 a_s}{m} \int d^3x |w_0(x - x_i)|^4 \end{aligned} \quad (6.6)$$

Using Eq. 6.6, the expected tunneling rates and interaction energies for atomic strontium are shown in Fig. 6.2 for homonuclear samples of strontium as a function of lattice depth. This single band calculation is valid under the assumption that the interaction energy of a site is smaller than the bandgap between the $n = 0$ and 1 bands, namely $UN \lesssim \hbar\omega_{ho}$ where N is the mean number of particles per site and $\hbar\omega_{ho}$ is the approximate energy spacing between bands [165]. Alternatively, Eq. 6.6 can be simplified through considering appropriate limits to the Bose-Hubbard model. In the limit that $U \rightarrow 0$, the Bose-Hubbard model becomes exactly solvable and the energy of the $n = 0$ band is given by $E_q^{(0)} = -2J \cos(qa)$ [92]. Thus, the tunneling rate, J , can be related to the bandwidth of the lowest band as expressed in Eq. 6.7. Under a separate limit, $V_{lat} \rightarrow \infty$, then the tunneling rate goes to zero and the localized wavefunctions can be approximated by a Gaussian wavefunction which yields the form for the on-site interaction U given in Eq. 6.7 [165].

$$\begin{aligned} J &= \frac{E_{q=\hbar k_L} - E_{q=0}}{4} \\ U &= \frac{\hbar a_s}{\sqrt{2\pi}} \frac{\bar{\omega}_{ho}}{\bar{a}_{ho}} \end{aligned} \quad (6.7)$$

Here \bar{a}_{ho} and $\bar{\omega}_{ho}$ are the geometric means of the harmonic oscillator length and frequency given previously.

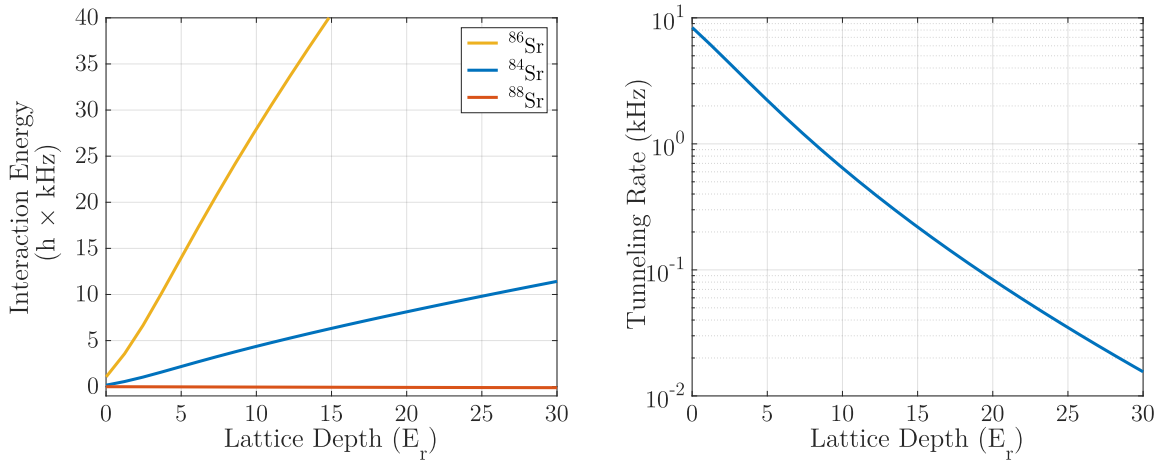


Figure 6.2 : Tunneling rate, J , and interaction energy, U , for strontium in a 532 nm optical lattice

Calculated tunneling rate and interaction energies for homonuclear pairs of each bosonic isotope. The interaction energy shows a large variation due to its dependence on the s -wave scattering length.

6.2 Kapitza-Dirac scattering

Much of the previous discussion has focused on describing the evolution of a quantum coherent state in the presence of an optical lattice which may be characterized with the lattice depth. Thus, in practice, measurement of this lattice depth is paramount for an accurate parameterization of the behavior of an atomic sample loaded into an optical lattice potential. Kapitza-Dirac diffraction is a well-known technique for measuring the depth of an optical lattice [80] and may be viewed as a diabatic projection between eigenstates. Typically one consider the case of a Bose-Einstein condensate, described by an initial $p = 0$ plane wave eigenstate, that is projected on the Bloch eigenstates of the lattice, which results in an oscillation of the wavefunction probability amplitude over the new Bloch eigenstates of the lattice [70, 71, 165]. This coherent oscillation

evolves for some period and is then projected back onto the plane wave states by extinguishing the lattice laser. Since each of the Bloch states may be written as a superposition of particular free particle plane wave states, this projection populates specific momentum states which may be imaged directly after a time-of-flight.

Theoretically, this process is described by a pure $p = 0$ plane wave, $|\phi_{p=0}\rangle$, suddenly loaded into an optical lattice and written as a superposition of the Bloch states given by Eq. 6.2, here denoted by $|n, q\rangle$.

$$|\Psi(t=0)\rangle = \sum_{n=0}^{\infty} |n, q\rangle \langle n, q| \phi_{p=0} \rangle \quad (6.8)$$

The time evolution of this state is then given by

$$|\Psi(t)\rangle = \sum_{n=0}^{\infty} |n, q\rangle \langle n, q| \phi_{p=0} \rangle \exp\left(\frac{-iE_n(q)t}{\hbar}\right) \quad (6.9)$$

where $E_n(q)$ is the energy of the Bloch state at a specified q and n shown in Fig. 6.1. The exponential factor of Eq. 6.9 introduces the oscillations among Bloch states and after the second diabatic projection back to the plane wave basis, we relate evolution of plane wave populations to the lattice bandgap energy at $q = 0$. From this analysis we find that for relatively weak lattices, $V_{lat} \lesssim 10E_r$, the plane wave population will be constrained to the $n = 0$ and $n = \pm 2\hbar k_L$ plane waves and their population will vary as $\omega_{osc} = (E_2 - E_0)/\hbar$, where E_i is the band energy of the i^{th} band at $q = 0$.

Fig. 6.3 shows a typical Kapitza-Dirac oscillation pattern which we use to maximize retro-reflected beam overlap near the atoms and use to calibrate our achievable lattice depths. Kapitza-Dirac is useful as an alignment tool since measurement of the population oscillation frequency can be highly accurate and directly relates to the bandgap energy in the lattice, shown in Fig. 6.1. This bandgap energy is in turn is related to the lattice depth.

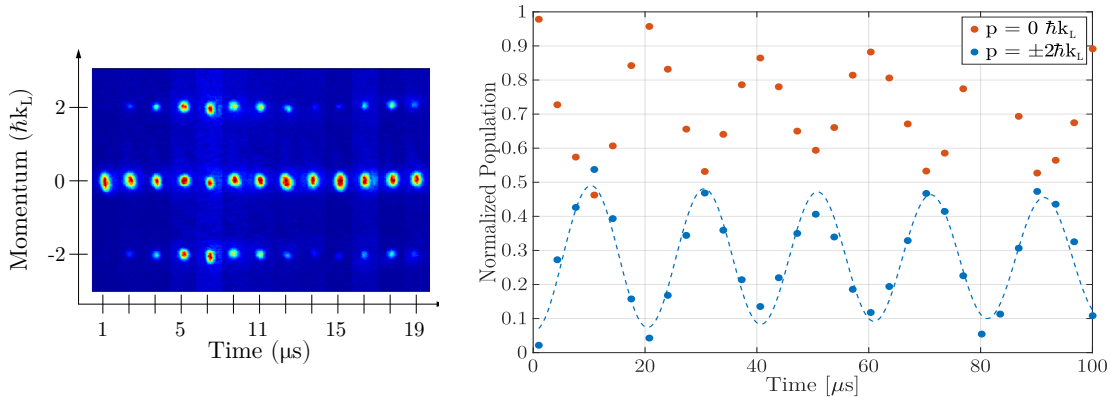


Figure 6.3 : Evolution of plane wave population using Kapitza-Dirac diffraction
 Left: Kapitza-Dirac diffraction result after a time-of-flight expansion following the specified hold time in the lattice. Right: Normalized population from fits of time-of-flight images. Oscillations are fit with a decaying sinusoidal and the best-fit frequency is used to determine the lattice depth.

6.3 Setup and alignment

Setup

Our optical lattice operates at $\lambda = 532\text{ nm}$ and is derived from a Coherent Verdi V-18 single-mode laser which is sent through separate AOMs for intensity control of each arm before propagating in free space to the atoms. We label these arms A, B, & C as noted in Fig. 6.5. Figs. 6.6 - 6.8 show the detailed beam profiles for the lattice and specify the spot size at the atoms for each pass of all three arms. All three arms are linearly polarized with the polarization vector aligned along the z direction, parallel to gravity. With this configuration we can achieve lattice depths $> 30E_r$ in an isotropic lattice. Finally, for reference, Fig. 6.9 shows the resulting lattice depth calibration for our most recent alignment.

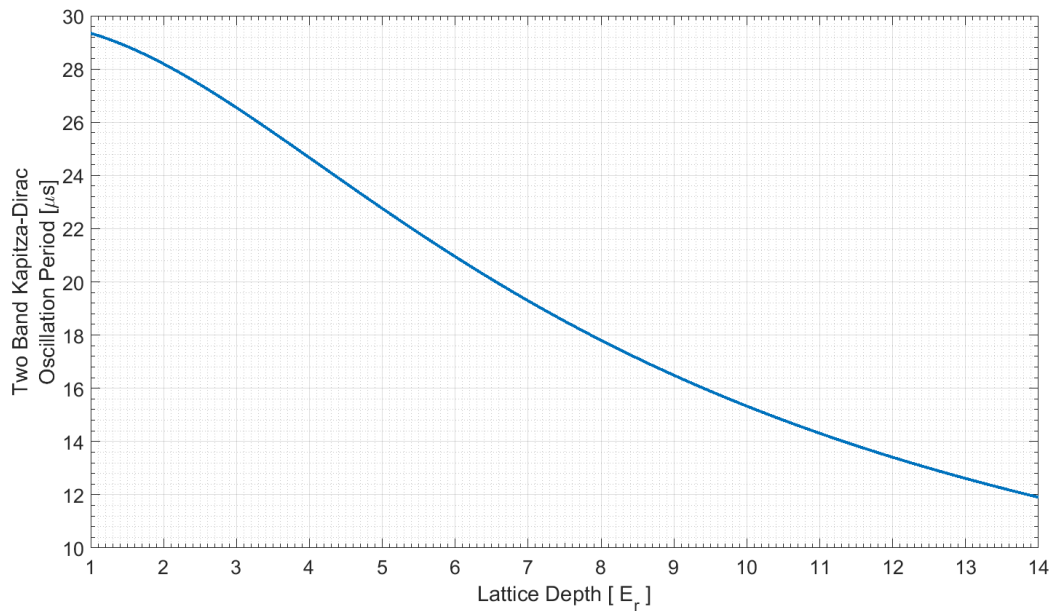


Figure 6.4 : Oscillation period between $n = 0 \rightarrow n = 2$ band at $q = 0$

This period is calculated for a 532 nm lattice acting on strontium-84 and is useful as a guide for estimating the lattice depth during retro-reflection alignment.

	Label	Part	Position [cm]	Distances [cm]	
Arm A	AOM	IntraAction AFM-804A1	-126.5	AOM → A1	24.1
	PBS	Thorlabs PBS12-532-HP	-117.8	A1 → A2	22.3
	Lens	CVI PLCX-25.4-772.6-UV-532	-106.5	A2 → A3	35
	Dichroic - 1	Thorlabs HBSY12	-30.6	A3 → A4	4.5
	Dichroic - 2	Thorlabs HBSY12	43.6	A4 → AD1	10
	Retro mirror	CVI Y2-1025-0-0.30CC	69.9	AD1 → Atoms	30.6
Arm B				Atoms → AD2	43.6
				AD2 → ARM	26.3
	AOM	IntraAction AFM-803A1	-167.1	AOM → B1	19
	PBS	Newport PBS-5811	-154.6	B1 → B2	25
	Lens	CVI PLCX-25.4-772.6-UV-532	103.1	B2 → B3	46
	Dichroic - 1	Thorlabs HBSY12	-36.1	B3 → B4	23.5
Arm C	Dichroic - 2	Thorlabs HBSY12	30.5	B4 → B5	14
	Retro mirror	CVI Y2-1025-0-0.30CC	73.5	B5 → BD1	3.5
				BD1 → Atoms	36.1
				Atoms → BD2	30.5
				BD2 → B6	25
				B6 → BRM	18
Arm C	AOM	IntraAction AFM-803A1	-117.5	AOM → C1	45.5
	PBS	Thorlabs PBS12-532-HP	-109.5	C1 → C2	25.5
	Lens-1	CVI PLCX-25.4-772.6-UV-532	-89.5	C2 → C3	15
	Retro lens	CVI PLCX-25.4-149.9-UV-532	14.6	C3 → C4	5.5
	Retro mirror	CVI Y2-1025-0	18.2	C4 → Atoms	26
				Atoms → CRM	18.2

Table 6.1 : Inventory of 532 nm lattice optics

All distances are specified in centimeters and are labeled by the optics labels given in Fig. 6.5. Optical path position is given with respect to zero defined at the atoms.

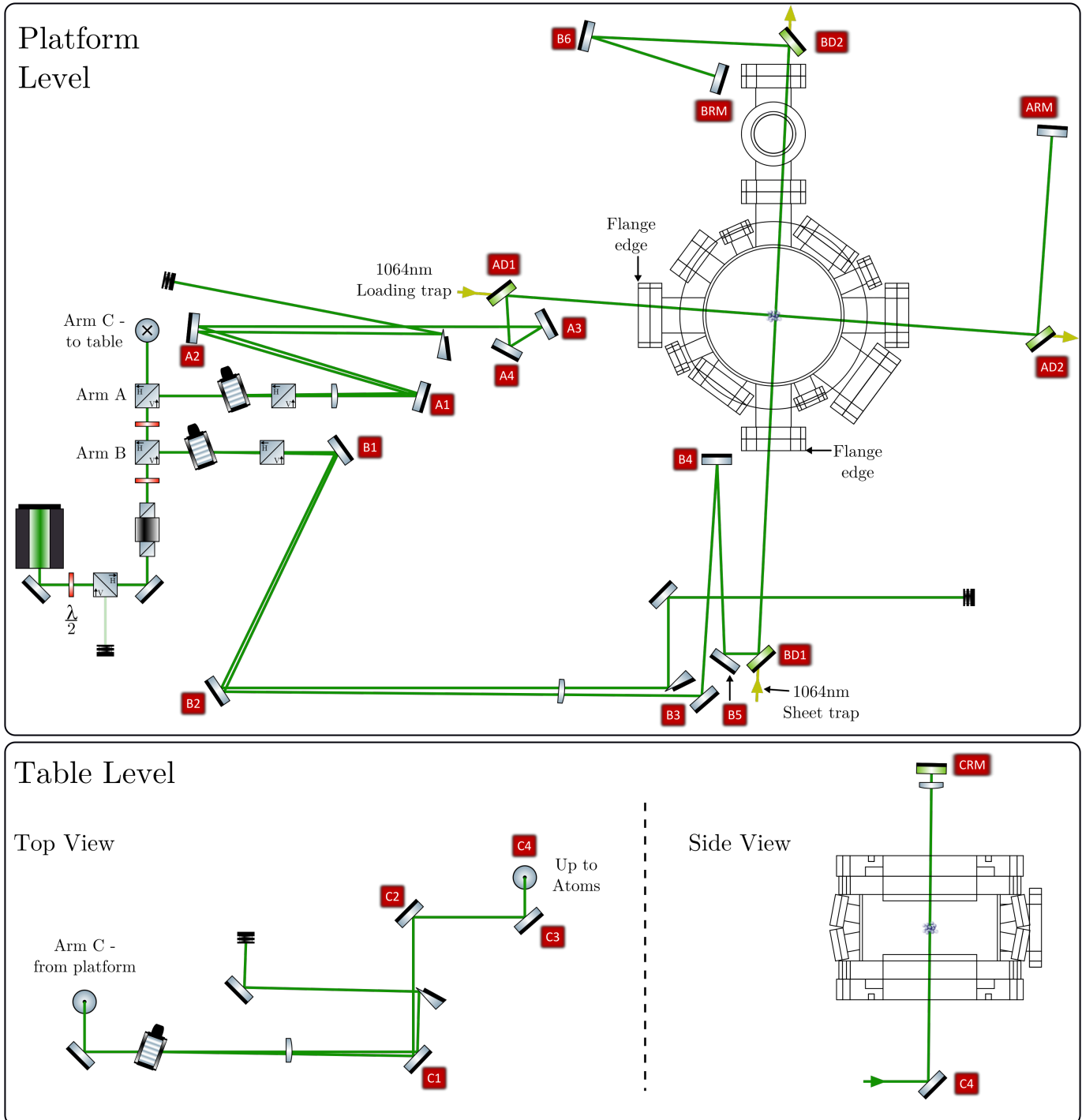


Figure 6.5 : Lattice optical schematic

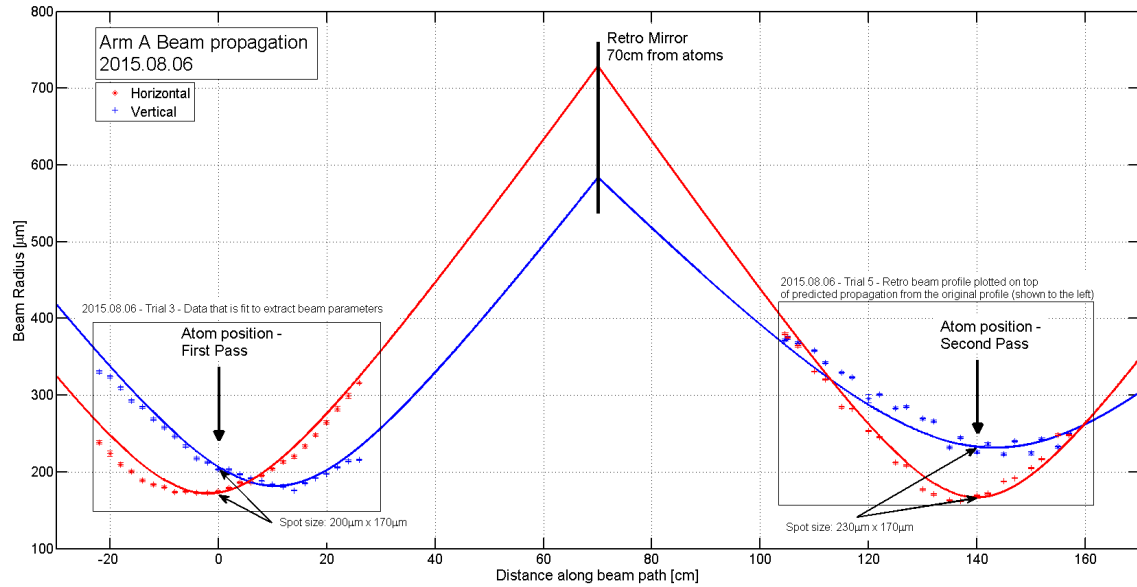


Figure 6.6 : Lattice Arm A profile

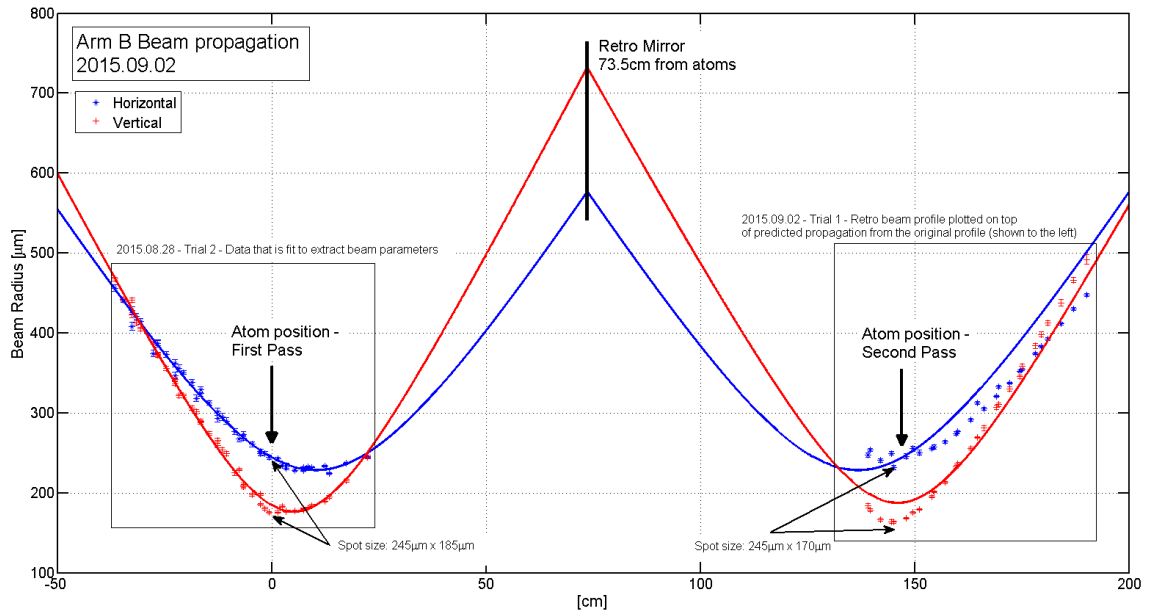


Figure 6.7 : Lattice Arm B profile

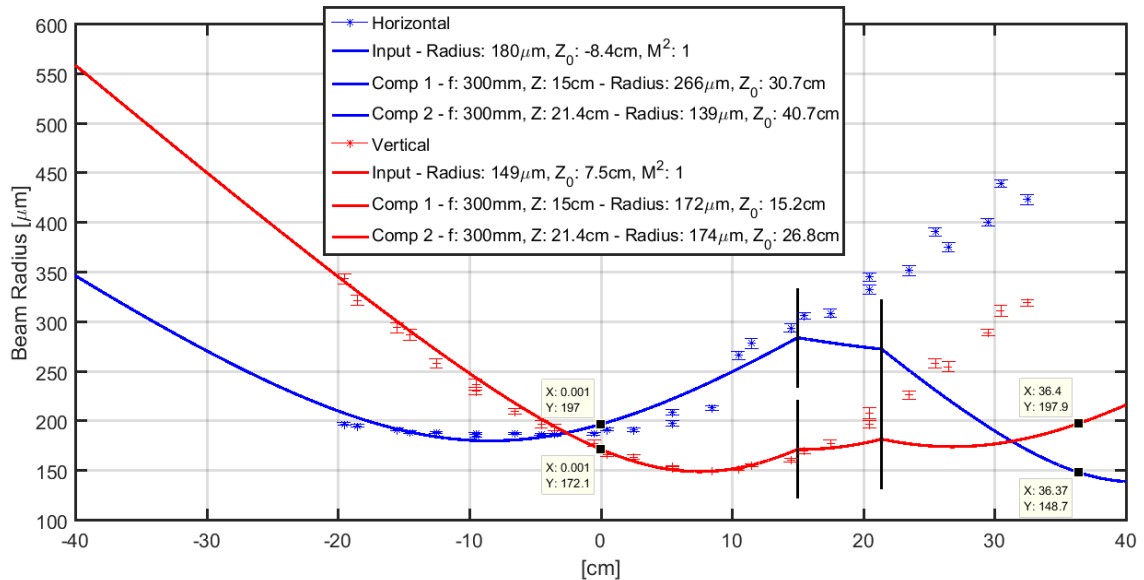


Figure 6.8 : Lattice Arm C profile

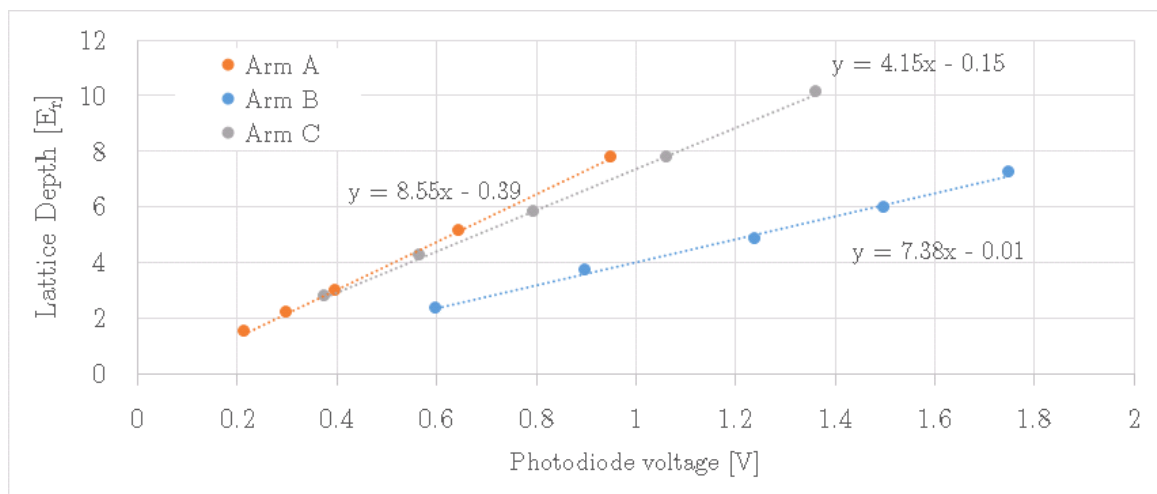


Figure 6.9 : Lattice depth calibration

Calibration was performed using the two-band Kapitza-Dirac technique. Maximum photodiode voltage for each arm is 10 V

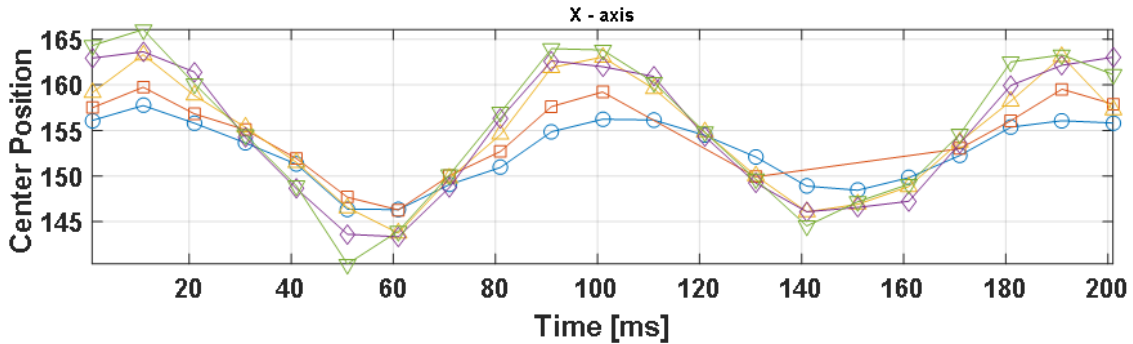


Figure 6.10 : Center-of-mass amplitude suppression when overlapping traps

From green symbols to blue symbols, each subsequent scan is a small variation in the pointing of the last mirror directing the 532 nm light before the chamber. Note that the Y-axis is in arbitrary units.

Aligning the first pass:

We align the first pass of the optical lattice to maximize overlap with the 1064 nm optical dipole trap. This process relies on observing the change in amplitude of center-of-mass oscillations due to misalignment between the 532 nm and 1064 nm traps as shown in Fig. 6.10. Additionally, we have observed breathing mode oscillations when the 532 nm and 1064 nm traps are well overlapped due to the change in trap depth, and correspondingly the potential energy of the atoms, when flashing off the 532 nm light. Below is our prescription for overlapping the first pass of the lattice with the IR trap.

I. This process requires the oscillations start from a consistent equilibrium. We achieve this through the following experimental sequence:

- A. Typical trapping sequence of blue MOT, repump, red MOT broadband, red MOT single frequency + ODT load

- B. In order to allow for any thermal effects on the ODT beams that cause the trapping volume to move slightly with changing 1064 nm laser intensity, it is best to align the lattice at the ODT laser intensity at which experiments will be performed. Thus, after loading the ODT, evaporate to a reasonable depth for the given loading time.
 - C. Following the forced evaporation, hold in the 1064 nm trap while ramping up the lattice arm being studied to full power. We generally find a ramp of $\sim 200 - 300$ ms worked best for strontium-84.
 - D. Once the green is at full power, hold for ~ 250 ms in the combined 532 + Crossed IR ODT trap to allow for the equilibration of the atoms in the modified trapping potential.
 - E. After the 250 ms hold, the green is flashed off to excite an oscillation within the IR ODT.
 - F. Image the cloud after various evolution times to allow for the cloud to oscillate. Usually this is done after a time-of-flight to magnify small displacements but may also be performed *in situ* if the cloud expansion is hindering determination of the cloud position.
- II. The procedure just outlined has been successful for aligning the lattice, but to setup the procedure first focus on *in situ* where atoms are held in the combined 1064 + 532 nm trap. Then use the tools in Labview to identify adequate excitation amplitude and ensure that the cloud is settled in each trap before exciting

the oscillation.*.

III. As the alignment is improved the maximum displacement is minimized, this is the signature of improving the overlap. After the period is known, one can speed up the process by making single-point measurements at a quarter-period of the oscillation. This is the point of maximum displacement and provides the most sensitive probe for observing how changes to the alignment may vary the oscillation amplitude.

IV. Each lattice arm (A,B,C) can then be varied along both dimensions (horizontal and vertical) while monitoring the oscillation amplitude. Lower oscillation amplitude indicates better alignment, but one must be extremely careful, as it is possible to obtain a flat response of the oscillation amplitude when severely misaligned. We have found that around the minimum in the oscillation amplitude, we are able to flip the phase of the quarter-period oscillation as we move through the minimum. This phase flip along with the emergence of breathing mode oscillation are robust measures of good overlap between the two traps.

Fig. 6.10 shows an example of the above process where for each scan we have varied the beam alignment slightly and can clearly observe a suppression of the oscillation amplitude. Additionally, Fig. 6.11 shows the emergence of a breathing mode when the traps are well overlapped. Observation of oscillatory behavior of the cloud radius with reduced deviation of the cloud center is a robust measure of the overlap of the 532 nm and 1064 nm traps.

*Start by moving the VI cursor positions to be on the cloud center and drawing a box around the cloud location. This will help to identify small movements of the cloud as well as recording your start position.

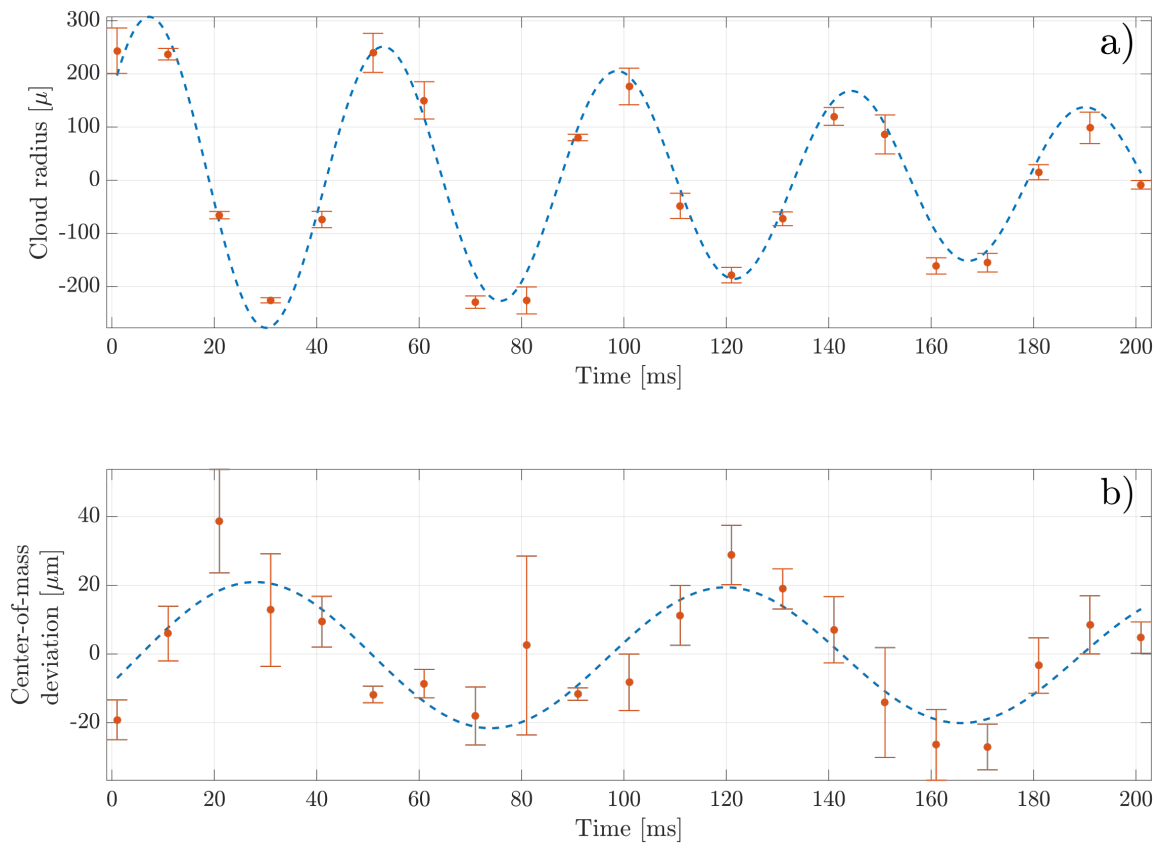


Figure 6.11 : Observation of breathing mode oscillation

a) The cloud radius and b) the cloud center deviation as measured along a horizontal axis of the trap.

Aligning the retro-reflection:

The lattice retro-reflection is optimized via the 2-band Kapitza-Dirac method described in Sec. 6.2. For this, we pulse the lattice on to project a $p = 0$ BEC onto the $q = 0$ Bloch states, let it evolve for a short time in the lattice, turn off the lattice to project the state back onto the plane wave basis, and then image after a time-of-flight to resolve the different momentum states. For a quantum degenerate gas in shallow lattice depths, $< 10 E_r$, only the ± 1 plane waves are populated following the second diabatic projection from the Bloch states to free plane wave [54, 80]. Furthermore, for short pulses the amplitude of the population in these plane waves is linearly increasing with lattice depth. This provides a simple single-point measurement which can be used for optimizing the lattice depth. However, an iterative approach may be needed to ensure that the alignment is only optimized during the first quarter-period before the population of the orders is maximized. Fig. 6.3 shows an example oscillation.

As our lattice is in free space, the first order alignment of the retro-reflection is to overlap the incoming and retro-reflected beam over a long distance. This tends to overlap the two beams closely enough in the region of the atoms so as to begin observing diffraction effects when performing a short high-intensity pulse of the 532 nm light.

Second, once we can observe diffraction, gimbal mounted retro mirrors are adjusted to maximize the population of the diffracted plane waves[†]. As the diffracted population is oscillatory and depends on laser intensity, we have found that using an exposure time of approximately $2 - 3 \mu\text{s}$ and varying the laser intensity leads to the most successful alignments of the retro mirror. We generally start with this short

[†]This alignment is extremely sensitive and may ultimately benefit from a more reproducible method of adjustment as mount backlash can strongly effect this process.

time pulse of a few microseconds using the highest intensity pulse possible and systematically decrease the laser power of the particular lattice arm as the alignment is improved. Finally, we note that, as Kapitza-Dirac diffraction happens on very short timescales, the power stabilization circuits must be bypassed for this procedure. Instead, we directly drive the RF sources with fast analog IC switches (switching time on the order of 10 ns) to apply the desired power to the lattice arm.

6.4 Measurement and results

Higher order Kapitza-Dirac: The simple two-band model in Sec. 6.2 is a straightforward method for determining the lattice depth but one that requires a time-series measurement over varying lattice depths. Gadway et al. [62] derived a complimentary depth calibration method which requires only a single time-series measurement at high lattice depth. This process relies on the quantum interference of the oscillating populations which produces a complex beat note. An undergraduate student from our lab, Alex Wikner [195], developed an algorithm using MatlabTM for applying this technique to the Neutral apparatus. The cited report provides sample code as well as benchmark calculations for comparison. However, application of this work to calibrate the lattice depth has been stymied by a consistent heating concern we have observed when applying the lattice beams for significant periods at high lattice depths.

Observation of Mott insulator transition: Competition between J and U results in a phase transition known as the superfluid - Mott insulator transition [57, 72]. When $J/U \gg 1$ atoms are free to delocalize over the lattice and the many-body ground state is a superfluid. In the opposite limit that $J/U \ll 1$, particle fluctuations

between sites are no longer energetically accessible and the system transitions into an interaction induced insulating state. This state is characterized by fixed particle number per site and in a 3D cubic lattice near unit filling, this phase transition occurs at $U/J \approx 35$ [11]. For ^{84}Sr this corresponds to a lattice depth of $V_{lat} \approx 13E_r$ [57]. Fig. 6.12 shows an observation of this transition using a lattice depth of $16E_r$. In this procedure the lattice is ramped up linearly for 200 ms before being immediately ramped down for an additional 200 ms. The figure shows absorption images at several points along this trajectory.

Heating of a quantum degenerate gas

For many experiments it is important to be able to slowly ramp up the lattice laser and adiabatically transform the initial quantum state ground state into a different ground state in the new lattice basis. Thus slowly ramping up the lattice laser intensity will approximately adiabatically transform a plane wave ground state into the ground Bloch state of the lattice [168]. Strictly speaking, in order to adiabatically connect the free space eigenstates and the lattice eigensates, the lattice must be turned on infinitely slowly due to the infinitesimal bandgaps which open near the band edges. Although near the band center, $q = 0$, the adiabaticity requirement relaxes to $\frac{dV_{lat}}{dt} \ll \frac{16E_r^2}{\hbar}$, [80] which for strontium in a 532 nm lattice is $\approx 5\mu\text{s}/E_r$. We do not observe adiabaticity unless the potentials are ramped much more slowly than this, typically on a timescale of about 100 ms [11]. We have experimented with various functional forms of this pulse shape and currently rely on an S-shaped curve given by Eq. 6.10

$$V_{sCurve}(A, B, C, t) = \frac{A - C}{2} [\tanh(2\pi B[t - 1]) + 1] + C \quad (6.10)$$

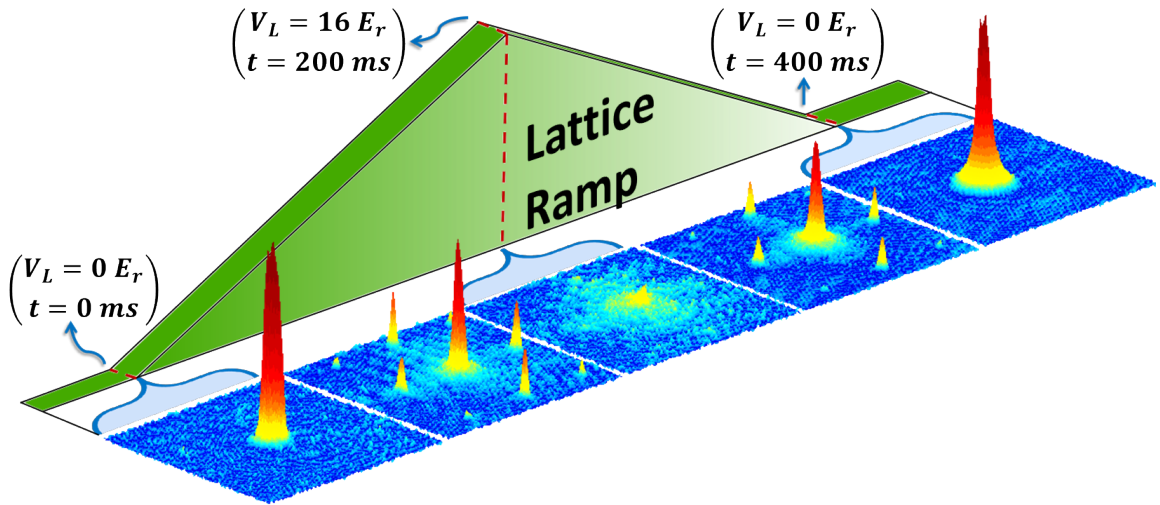


Figure 6.12 : Superfluid to Mott insulator transition

A Bose-Einstein condensate of ^{84}Sr is adiabatically loaded into the lattice potential using a linear ramp over 200 ms. Each absorption image is the result of a time-of-flight expansion after diabatically projecting the lattice eigenstates back to free plane wave states. At low lattice depth, in the superfluid regime, the coherence of the lattice states causes quantum interference during the time-of-flight and spatially resolved momentum peaks are visible. In the insulating state, this coherence is lost and the resulting momentum states do not interfere. This is the classic signature of this quantum phase transition [72, 73].

where A is the overall amplitude starting from zero, B is the timescale for one period, and C is a constant offset term.

As shown in Fig. 6.13, we observe a large condensate fraction after ramping the lattice up and back down in this manner to demonstrate restoration of BEC coherence. Further characterization of the lattice required us to measure the reduction of atom population over long times due off-resonant light scatter. For our red detuned optical lattice, we expect the off-resonant scattering rate to be well approximated by a simple two level approach. In this model, the effective scattering rate is given by [92]

$$\Gamma_{eff} \approx \frac{\Gamma V_{lat}}{\hbar \delta_{lat}} \quad (6.11)$$

where Γ is linewidth of the dipole transition between the two states, V_{lat} is the lattice depth, and δ_{lat} is the detuning of the optical lattice from the two level transition frequency. In strontium, the $^1S_0 \rightarrow ^1P_1$ transition strongly dominates the polarizability of the ground state and therefore can be used to estimate the effective off-resonant scattering rate. For this transition $\Gamma = 2\pi \times 30.5$ MHz and a 532 nm lattice is detuned by $\delta_{lat} \approx 2\pi \times 87$ THz. With a lattice depth of $V_{lat} = 10 E_r$ we expect a scattering rate of $\Gamma_{eff} \approx 2 \times 10^{-1}$ s⁻¹, which is negligible for the timescales of our proposed experiments. From Fig. 6.13, we see that there is not an appreciable loss of atoms over a one second timescale but there is a reduction of the condensate fraction by $\sim 25\%$. We have additionally observed that attempts to load a degenerate gas into a deep lattice, $\gtrsim 15 E_r$, and hold over long timescales leads to unacceptable heating of the atomic sample. We hypothesize that this may stem from alignment instability of the free space lattice or an intrinsic instability (frequency or power) of the Verdi laser. The latter hypothesis has been tested by monitoring the 532 nm light in a spectrum analyzer where no obvious deficiencies have been observed. To test the stability hypothesis, we are currently investigating fiber coupling one of the arms of the lattice

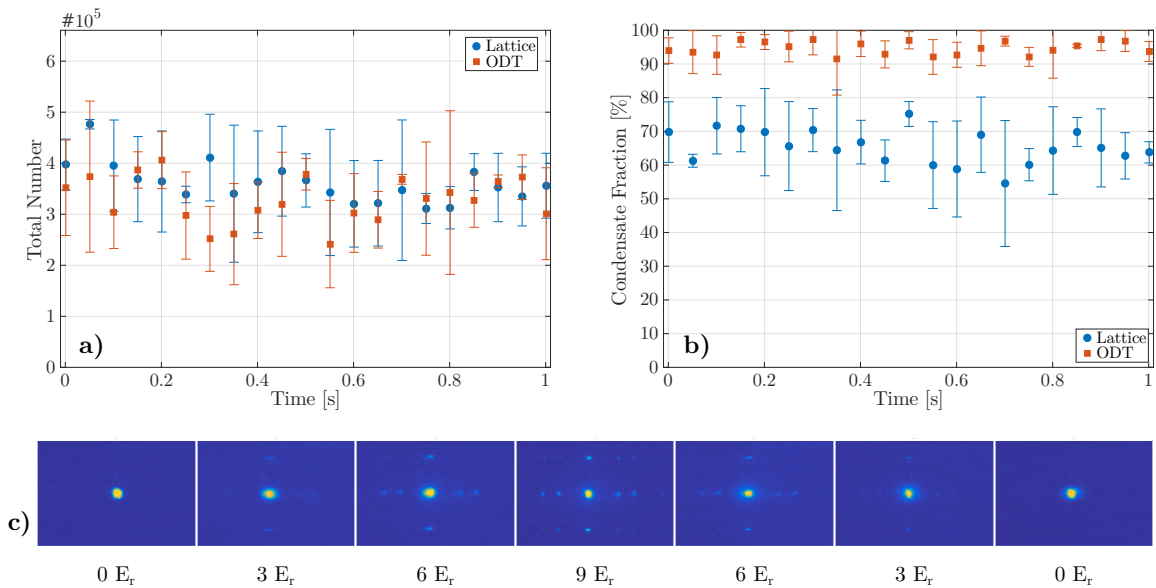


Figure 6.13 : Characterization of heating in the optical lattice

Evolution of condensate fraction over time after adiabatically ramping on the lattice to $9 E_r$. a,b) Comparison of total number and condensate fraction for a sample held in the optical dipole trap (red squares) or in a deep lattice (blue circles). c) Time of flight images after ramping on the lattice and diabatically projecting back to plane wave states.

but as of spring 2019, this project is ongoing.

Chapter 7

Conclusion

This thesis presents studies probing the least-bound vibrational level of the ground electronic state of the $^{86}\text{Sr}_2$ molecule using two-photon photoassociative spectroscopy. The large *s*-wave scattering length of ^{86}Sr reveals this to be a naturally occurring halo molecular state. Using a precise measurement of the binding energy of this extremely weakly-bound state, we estimate an improved value of the strontium long-range C_6 coefficient from the best-known descriptions of the ground state $\text{X}^1\Sigma_g^+$ potential and the universal prediction for the binding energy of a halo state, accounting for corrections derived for a van der Waals potential. This work points to the need for an improved theoretical understanding of the Sr ground state molecular potential, which could be compared with this high-accuracy measurement of the halo binding energy. Despite uncertainty in the applicable model potential, we use mass-scaling to predict the *s*-wave scattering lengths for each isotopic combination of strontium and find them to be model invariant for the chosen description of the strontium ground state potential.

We also characterized the AC Stark shift of the halo state binding energy due to light near-resonant with the single-photon photoassociation transition. Through numerical simulation of a three-level model and focusing on a regime where the AC Stark shift is comparable to the halo binding energy, we find it is important to consider intermediate state coupling due to both excitation lasers. Subsequent analysis of this theoretical model using Floquet theory and a perturbative expansion about the halo

resonance position allowed us to derive a simple analytic form for the binding energy which showed that the light shift is a sum of independent AC Stark shifts from each of the excitation lasers [20, 103, 197]. These simulations also predict higher-order loss structures arising from multi-photon resonant processes, as was also observed in our experiments. However, a three-level model only accounting for a single excited state channel [15] cannot explain the full range of the observed frequency dependence of the AC Stark shift, which may be attributed to the proximity of nearby excited states.

Large AC Stark shifts of the halo state point to the possibility of optically tuning the ^{86}Sr scattering length, similar to recent demonstrations of optical tuning of magnetic Feshbach resonances [6, 42]. This is attractive because ground state strontium lacks magnetic Feshbach resonances. With improved measurement of the photoassociation resonance frequency and its dependence on background atom density, perhaps combined with optical manipulation of the scattering length, it may be possible to study the landscape of Efimov trimers associated with this naturally occurring scattering resonance [24, 124, 144, 193]. Experiments such as these are natural extensions of previous work from our lab controlling states of quantum matter using an optical Feshbach resonance and coherent one-color photoassociation [83, 148, 201, 202].

Although not as well-studied as other strontium isotopes, ^{86}Sr is a promising candidate for the creation of a novel type of Feshbach molecule originating from the manipulation of the halo state energy via optical coupling. This is of fundamental interest to complete the analogy between optical and magnetic Feshbach resonances. Studies in this regime include measuring the binding energy of these optical Feshbach molecules by modulating the laser frequency at a fixed detuning as was done with MFRs [105, 106, 180]. This will allow us to test the binding energy of Feshbach

molecules near the universal regime as well as to explore scaling with coupling strength through variation of the laser intensity [35, 94, 148, 150, 163].

Related to the creation of Feshbach molecules in the universal regime, adiabatic internal state transfer presents an intriguing possibility of creating large populations of $^{86}\text{Sr}_2$ halo molecules [110, 156, 157]. These dimers are interesting intermediaries for further study using STIRAP or related protocols to create deeply bound or absolute ro-vibrational ground state strontium molecules, which can serve as excellent metrological tools [52, 162, 172, 177, 206].

Moreover, additional insight might also be drawn from revisiting OFR and photoassociation in an optical lattice and employing new measurement techniques in the lattice [183]. By working in an optical lattice with fewer than three atoms per site, we may eliminate atom-molecule and molecule-molecule collisions and accurately measure molecular lifetimes [109, 187] allowing us to test our understanding of the mechanisms that provide stability to Feshbach molecules when the closed channel is naturally decaying [106]. Halo molecule formation in sites with two atoms can be nearly 100% efficient with MFRs [35, 133], and we expect OFRs should behave similarly. Using the fast temporal control of optical fields and the spatial confinement provided by a lattice we may also explore out of equilibrium unitarity quenches [115] and strongly interacting Bose gases stabilized by the quantum Zeno effect [56, 182, 196, 208].

Finally, utilizing recently developed tools for photoassociation in our lab, we have begun probing the photoassociation spectrum of ^{87}Sr . We have observed several molecular transitions targeting the $^1S_0 \rightarrow ^1P_1$ transition in a regime of large detuning from the asymptotic transition frequency, $\approx 4 - 12$ GHz, where the effects of the small hyperfine splitting of the 1P_1 , $\approx \pm 30$ MHz, are not resolved. With further investigation of this spectrum, we hope to develop improved predictions of the posi-

tions of molecular states near the $^1S_0 (F = 9/2) \rightarrow ^3P_1 (F' = 9/2)$ intercombination transition which has not yet been successfully demonstrated [163]. A recent study of intercombination line photoassociation of ^{173}Yb suggests that the ^{87}Sr intercombination line PAS spectrum is likely to exhibit rich structure [60, 78, 102]. Photoassociation of degenerate or nearly degenerate gases of fermionic strontium-87 loaded into an optical lattice may be the key to overcoming the low excitation strength of the bound-state transitions [19, 184]. It is anticipated that these resonances are likely to be individually resolved [78] and therefore may prove invaluable in studies of quantum magnetism as a means of breaking the naturally occurring $SU(N)$ symmetry. Even further still, with the installation of an additional one-dimensional lattice at twice the wavelength of our current lattice, $2 \times 532 \text{ nm} = 1064 \text{ nm}$, we hope to detect exotic spin phases unique to these highly degenerate systems [10, 30, 32, 33, 58, 67, 152, 169].

The experiments presented in this thesis and our planned future work demonstrate the versatility and variety of interactions accessible in ultracold and quantum degenerate neutral strontium. When loaded into optical lattices and illuminated with near-resonant laser light, an exceptional degree of dynamic spatial control and state selectivity can be achieved, particularly when coupling through narrow intercombination transitions. This ability to engineer and manipulate novel quantum states for investigating the extremes of universality and collisions of particles with large symmetries, makes strontium an invaluable experimental probe for exploring questions of fundamental physics concerning the interactions of few-body systems.

Bibliography

- [1] Aman, J. A., J. C. Hill, R. Ding, W. Y. Kon, K. R. Hazzard, and T. C. Killian, 2018, Physical Review A **98**(5), 053441, ISSN 24699934, URL <https://link.aps.org/doi/10.1103/PhysRevA.98.053441>.
- [2] Anderson, M. H., J. R. Ensher, M. R. Matthews, C. E. Wieman, and E. A. Cornell, 1995, Science **269**(5221), 198, ISSN 00368075, URL <http://www.ncbi.nlm.nih.gov/pubmed/17789847>.
- [3] Appel, J., A. MacRae, and A. I. Lvovsky, 2009, Measurement Science and Technology **20**(5), 055302, ISSN 0957-0233, URL <http://stacks.iop.org/0957-0233/20/i=5/a=055302?key=crossref.adae87159f5fcf9ab105ed053c6c98dd>.
- [4] Bakr, W. S., J. I. Gillen, A. Peng, S. Fölling, and M. Greiner, 2009, Nature **462**(7269), 74, ISSN 0028-0836, URL <http://www.nature.com/doifinder/10.1038/nature08482>.
- [5] Bartenstein, M., A. Altmeyer, S. Riedl, R. Geursen, S. Jochim, C. Chin, J. H. Denschlag, R. Grimm, A. Simoni, E. Tiesinga, C. J. Williams, and P. S. Julienne, 2005, Physical Review Letters **94**(10), 103201, ISSN 00319007, URL <https://link.aps.org/doi/10.1103/PhysRevLett.94.103201>.
- [6] Bauer, D. M., M. Lettner, C. Vo, G. Rempe, and S. Dürr, 2009, Nature Physics **5**, 339, URL <https://doi.org/10.1038/nphys1232>.

- [7] Beloy, K., A. W. Hauser, A. Borschevsky, V. V. Flambaum, and P. Schwerdtfeger, 2011, Physical Review A **84**(6), 062114, ISSN 10502947, URL <https://link.aps.org/doi/10.1103/PhysRevA.84.062114>.
- [8] Bergman, D. J., and D. Stroud, 1992, *Solid state Physics* (Saunders College), ISBN 047141526X.
- [9] Bertelsen, J. F., 2007, *Ultracold Atomic Gases*, Ph.d thesis, Danish National Research Foundation Center for Quantum Optics, URL http://phys.au.dk/fileadmin/site{_}files/forskning/ltc/theses/Jesper{_}Fevre{_}Bertelsen.pdf.
- [10] Beverland, M. E., G. Alagic, M. J. Martin, A. P. Koller, A. M. Rey, and A. V. Gorshkov, 2016, Physical Review A **93**(5), 051601, ISSN 24699934, URL <http://link.aps.org/doi/10.1103/PhysRevA.93.051601>.
- [11] Blakie, P. B., and J. V. Porto, 2004, Physical Review A **69**(1), 013603, ISSN 1050-2947, URL <https://link.aps.org/doi/10.1103/PhysRevA.69.013603>.
- [12] Blatt, S., T. L. Nicholson, B. J. Bloom, J. R. Williams, J. W. Thomsen, P. S. Julienne, and J. Ye, 2011, Physical Review Letters **107**(7), 073202, ISSN 00319007, URL <http://link.aps.org/doi/10.1103/PhysRevLett.107.073202>.
- [13] Bloch, I., J. Dalibard, and W. Zwerger, 2008, Reviews of Modern Physics **80**(3), 885, ISSN 00346861, URL <http://link.aps.org/abstract/RMP/v80/p885> <http://link.aps.org/doi/10.1103/RevModPhys.80.885>.
- [14] Boffard, J. B., M. L. Keeler, G. A. Piech, L. W. Anderson, and C. C. Lin, 2001,

- Physical Review A **64**(3), 032708, ISSN 1050-2947, URL <https://link.aps.org/doi/10.1103/PhysRevA.64.032708>.
- [15] Bohn, J. L., and P. S. Julienne, 1996, Physical Review A **54**(6), R4637, ISSN 10941622, URL <http://link.aps.org/doi/10.1103/PhysRevA.54.R4637>.
- [16] Bohn, J. L., and P. S. Julienne, 1999, Physical Review A **60**(1), 414, ISSN 10941622, URL <https://link.aps.org/doi/10.1103/PhysRevA.60.414>.
- [17] Boisseau, C., E. Audouard, J. Vigué, and V. V. Flambaum, 2000, European Physical Journal D **12**(2), 199, ISSN 14346060, URL <http://www.springerlink.com/index/10.1007/s100530070014>.
- [18] Boisseau, C., E. Audouard, J. Vigué, and P. S. Julienne, 2000, Physical Review A **62**(5), 052705, ISSN 10502947, URL <http://link.aps.org/doi/10.1103/PhysRevA.62.052705>.
- [19] Bonnes, L., K. R. A. Hazzard, S. R. Manmana, A. M. Rey, and S. Wessel, 2012, Physical Review Letters **109**(20), 205305, ISSN 0031-9007, URL <http://link.aps.org/doi/10.1103/PhysRevLett.109.205305>.
- [20] Borkowski, M., R. Ciuryło, P. S. Julienne, S. Tojo, K. Enomoto, and Y. Takahashi, 2009, Physical Review A **80**(1), 1, ISSN 10502947, URL <http://arxiv.org/abs/0905.0958>.
- [21] Borkowski, M., P. Morzyński, R. Ciuryło, P. S. Julienne, M. Yan, B. J. Desalvo, and T. C. Killian, 2014, Physical Review A **90**(3), 032713, ISSN 10941622, URL <http://link.aps.org/doi/10.1103/PhysRevA.90.032713>.

- [22] Bourdel, T., L. Khaykovich, J. Cubizolles, J. Zhang, F. Chevy, M. Teichmann, L. Tarruell, S. J. J. M. F. Kokkelmans, and C. Salomon, 2004, Physical Review Letters **93**(5), 050401, ISSN 0031-9007, URL <https://link.aps.org/doi/10.1103/PhysRevLett.93.050401>.
- [23] Braaten, E., and H.-W. Hammer, 2006, Physics Reports **428**(5-6), 259, ISSN 03701573, URL <https://linkinghub.elsevier.com/retrieve/pii/S0370157306000822>.
- [24] Braaten, E., and H.-W. Hammer, 2007, Annals of Physics **322**(1), 120, ISSN 00034916, URL <http://linkinghub.elsevier.com/retrieve/pii/S0003491606002387>.
- [25] Bradley, C. C., C. A. Sackett, J. J. Tollett, and R. G. Hulet, 1995, Physical Review Letters **75**(9), 1687, ISSN 00319007, URL <http://link.aps.org/doi/10.1103/PhysRevLett.75.1687>.
- [26] Brown, H. R., and W. Myrvold, 2008, **0809.1304**, URL <https://arxiv.org/abs/0809.1304>.
- [27] Burnett, K., P. S. Julienne, P. D. Lett, E. Tiesinga, and C. J. Williams, 2002, Nature **416**(6877), 225, ISSN 00280836, URL <https://doi.org/10.1038/416225a><http://10.0.4.14/416225a>.
- [28] Camargo, F., 2015, *Strontium Laser Cooling and Trapping Apparatus*, Masters, Rice University, URL <http://ultracold.rice.edu/publications/2015CamargoMasters.pdf>.
- [29] Camargo, F., 2017, *Rydberg Molecules and Polaron in Ultracold Strontium*

- Gases*, Ph.d thesis, Rice University, NIHMS150003, URL http://ultracold.rice.edu/publications/Camargo{_}PhD.pdf.
- [30] Cappellini, G., M. Mancini, G. Pagano, P. Lombardi, L. Livi, M. Siciliani de Cumis, P. Cancio, M. Pizzocaro, D. Calonico, F. Levi, C. Sias, J. Catani, *et al.*, 2014, Physical Review Letters **113**(12), 5, ISSN 10797114, URL <http://link.aps.org/doi/10.1103/PhysRevLett.113.120402><http://arxiv.org/abs/1406.6642>.
 - [31] Cazalilla, M. A., R. Citro, T. Giamarchi, E. Orignac, and M. Rigol, 2011, Reviews of Modern Physics **83**(4), 1405, ISSN 0034-6861, URL <https://link.aps.org/doi/10.1103/RevModPhys.83.1405>.
 - [32] Cazalilla, M. A., and A. M. Rey, 2014, Reports on Progress in Physics **77**(12), 124401, ISSN 0034-4885, URL <http://arxiv.org/abs/1403.2792>.
 - [33] Chen, G., K. R. A. Hazzard, A. M. Rey, and M. Hermele, 2016, Physical Review A **93**(6), 061601, ISSN 2469-9926, URL <https://link.aps.org/doi/10.1103/PhysRevA.93.061601>.
 - [34] Chin, C., M. Bartenstein, A. Altmeyer, S. Riedl, S. Jochim, J. H. Denschlag, and R. Grimm, 2004, Science **305**(5687), 1128, URL <http://www.sciencemag.org/cgi/content/abstract/305/5687/1128>.
 - [35] Chin, C., R. Grimm, P. Julienne, and E. Tiesinga, 2010, Reviews of Modern Physics **82**(2), 1225, ISSN 00346861, URL <https://link.aps.org/doi/10.1103/RevModPhys.82.1225>.
 - [36] Chin, C., and P. S. Julienne, 2005, Physical Review A **71**(1), 012713, ISSN 1050-2947, URL <https://link.aps.org/doi/10.1103/PhysRevA.71.012713>.

- [37] Chliamovitch, G., O. Malaspinas, and B. Chopard, 2017, Entropy **19**(8), 381, ISSN 1099-4300, URL <http://www.mdpi.com/1099-4300/19/8/381>.
- [38] Ciamei, A., A. Bayerle, C.-C. Chen, B. Pasquiou, and F. Schreck, 2017, Physical Review A **96**(1), 013406, ISSN 2469-9926, URL <http://link.aps.org/doi/10.1103/PhysRevA.96.013406>.
- [39] Ciamei, A., A. Bayerle, B. Pasquiou, and F. Schreck, 2017, EPL (Europhysics Letters) **119**(4), 46001, ISSN 0295-5075, URL <http://stacks.iop.org/0295-5075/119/i=4/a=46001?key=crossref.f6416ca9549dd206a78f42682d6d0a1e>.
- [40] Ciuryło, R., E. Tiesinga, and P. S. Julienne, 2006, Physical Review A **74**(2), 022710, ISSN 1050-2947, URL <https://link.aps.org/doi/10.1103/PhysRevA.74.022710>.
- [41] Ciuryło, R., E. Tiesinga, S. Kotochigova, and P. S. Julienne, 2004, Physical Review A **70**(6), 062710, ISSN 10941622, URL <http://link.aps.org/doi/10.1103/PhysRevA.70.062710https://link.aps.org/doi/10.1103/PhysRevA.70.062710>.
- [42] Clark, L. W., L.-C. Ha, C.-Y. Xu, and C. Chin, 2015, Physical Review Letters **115**(15), 155301, ISSN 0031-9007, URL <https://link.aps.org/doi/10.1103/PhysRevLett.115.155301>.
- [43] Claussen, N. R., S. J. J. M. F. Kokkelmans, S. T. Thompson, E. A. Donley, E. Hodby, and C. E. Wieman, 2003, Physical Review A **67**(6), 60701, ISSN 1050-2947, URL <https://link.aps.org/doi/10.1103/PhysRevA.67.060701>.

- [44] Cooper, A., J. P. Covey, I. S. Madjarov, S. G. Porsev, M. S. Safronova, and M. Endres, 2018, Physical Review X **8**(4), 041055, ISSN 2160-3308, URL <https://link.aps.org/doi/10.1103/PhysRevX.8.041055>.
- [45] Côté, R., A. Dalgarno, Y. Sun, and R. G. Hulet, 1995, Physical Review Letters **74**(18), 3581, ISSN 00319007, URL <https://link.aps.org/doi/10.1103/PhysRevLett.74.3581>.
- [46] Cubizolles, J., T. Bourdel, S. J. J. M. F. Kokkelmans, G. V. Shlyapnikov, and C. Salomon, 2003, Physical Review Letters **91**(24), 240401, ISSN 0031-9007, URL <http://link.aps.org/doi/10.1103/PhysRevLett.91.240401>.
- [47] Davis, K. B., M. O. O. Mewes, M. R. Andrews, N. J. Van Druten, D. S. Durfee, D. M. Kurn, and W. Ketterle, 1995, Physical Review Letters **75**(22), 3969, ISSN 00319007, URL <http://link.aps.org/doi/10.1103/PhysRevLett.75.3969>.
- [48] Demarco, B., 1998, *Quantum Behavior of an Atomic Fermi Gas*, Ph.d thesis, University of Colorado.
- [49] Desalvo, B. J., 2015, *Ultralong-Range Molecules and Rydberg Blockade in Ultracold Sr*, Ph.d thesis, Rice University, URL <https://hdl.handle.net/1911/87766>.
- [50] DeSalvo, B. J., M. Yan, P. G. Mickelson, Y. N. Martinez de Escobar, and T. C. Killian, 2010, Physical Review Letters **105**(3), 030402, ISSN 0031-9007, URL <https://link.aps.org/doi/10.1103/PhysRevLett.105.030402>.
- [51] Drever, R. W. P., J. L. Hall, F. V. Kowalski, J. Hough, G. M. Ford, A. J. Munley, and H. Ward, 1983, Applied Physics B **31**(2), 97, ISSN 1432-0649, URL <https://doi.org/10.1007/BF00702605>.

- [52] Dürr, S., T. Volz, A. Marte, and G. Rempe, 2004, Physical Review Letters **92**(2), 20406, ISSN 0031-9007, URL <http://link.aps.org/doi/10.1103/PhysRevLett.92.020406>.
- [53] Ehrenfest, P., and T. Ehrenfest, 2015, *The Conceptual Foundations of the Statistical Approach in Mechanics* (Dover Publications), new editio edition.
- [54] Fallani, L., C. Fort, J. Lye, and M. Inguscio, 2005, Optics express **13**(11), 4303, ISSN 1094-4087, URL <http://www.ncbi.nlm.nih.gov/pubmed/21902335>.
- [55] Fedichev, P. O., Y. Kagan, G. V. Shlyapnikov, and J. T. Walraven, 1996, Physical Review Letters **77**(14), 2913, ISSN 10797114, URL <http://link.aps.org/doi/10.1103/PhysRevLett.77.2913>.
- [56] Fischer, M. C., B. Gutiérrez-Medina, M. G. Raizen, M. C. Fischer, M. G. Raizen, B. Gutiérrez-Medina, and M. G. Raizen, 2001, Physical Review Letters **87**(4), 1, ISSN 0031-9007, URL <http://link.aps.org/doi/10.1103/PhysRevLett.87.040402>.
- [57] Fisher, M. P., P. B. Weichman, G. Grinstein, and D. S. Fisher, 1989, Physical Review B **40**(1), 546, ISSN 01631829, URL <http://link.aps.org/doi/10.1103/PhysRevB.40.546>.
- [58] Fölling, S., S. Trotzky, P. Cheinet, M. Feld, R. Saers, A. Widera, T. Müller, and I. Bloch, 2007, Nature **448**(7157), 1029, ISSN 1476-4687, URL <http://www.ncbi.nlm.nih.gov/pubmed/17728753>.
- [59] Foot, C. J., 2005, *Atomic Physics* (Oxford University Press, New York).

- [60] Franchi, L., L. F. Livi, G. Cappellini, G. Binella, M. Inguscio, J. Catani, and L. Fallani, 2017, New Journal of Physics **19**(10), 103037, ISSN 1367-2630, URL <https://iopscience.iop.org/article/10.1088/1367-2630/aa8fb4>.
- [61] Franzen, A., ????, ComponentLibrary, URL <http://www.gwoptics.org/ComponentLibrary/>.
- [62] Gadway, B., D. Pertot, R. Reimann, M. G. Cohen, and D. Schneble, 2009, Optics Express **17**(21), 19173, ISSN 1094-4087, URL <http://arxiv.org/abs/0907.3507>{%}0A<http://dx.doi.org/10.1364/OE.17.019173>.
- [63] Gao, B., 2001, Physical Review A **64**(1), 010701, ISSN 1050-2947, URL <https://link.aps.org/doi/10.1103/PhysRevA.64.010701>.
- [64] Gao, B., 2004, Journal of Physics B: Atomic, Molecular and Optical Physics **37**(21), 4273, ISSN 0953-4075, URL <https://iopscience.iop.org/article/10.1088/0953-4075/37/21/004>.
- [65] Gibson, S., 2016, PyDiatomic: PyDiatomic initial release, URL [#}.XSws8J7Is8A.mendeley](https://doi.org/10.5281/zenodo.56871).
- [66] Giorgini, S., L. P. Pitaevskii, and S. Stringari, 2008, Reviews of Modern Physics **80**(4), 1215, ISSN 00346861, URL <http://link.aps.org/doi/10.1103/RevModPhys.80.1215>.
- [67] Gorshkov, A. V., M. Hermele, V. Gurarie, C. Xu, P. S. Julienne, J. Ye, P. Zoller, E. Demler, M. D. Lukin, and A. M. Rey, 2010, Nature Physics **6**(4), 289, ISSN 17452481, URL <http://dx.doi.org/10.1038/nphys1535>.

- [68] Gotlibovych, I., 2014, *Degenerate Bose Gases in a Uniform Potential*, Ph.D. thesis, University of Cambridge, URL <http://www-amop.phy.cam.ac.uk/amop-zh/Publications/igorthesis.pdf>.
- [69] Greif, D., G. Jotzu, M. Messer, R. Desbuquois, and T. Esslinger, 2015, Physical Review Letters **115**(26), 260401, ISSN 0031-9007, URL <https://link.aps.org/doi/10.1103/PhysRevLett.115.260401>.
- [70] Greiner, M., 2003, *Ultracold quantum gases in three-dimensional optical lattice potentials*, Ph.d thesis, Ludwig-Maximilians-Universität München, URL http://greiner.physics.harvard.edu/assets/theses/PhD{_}greiner.pdf.
- [71] Greiner, M., and S. Fölling, 2008, Nature **453**(June), 736, URL <https://www.nature.com/articles/453736a>.
- [72] Greiner, M., O. Mandel, T. Esslinger, T. W. Hansch, I. Bloch, T. Rom, A. Altmeier, A. Widera, T. W. Hänsch, and I. Bloch, 2002, Nature **415**(6867), 39, ISSN 09214526, URL <http://www.nature.com/doifinder/10.1038/415039a>.
- [73] Greiner, M., O. Mandel, T. W. Hänsch, and I. Bloch, 2002, Nature **419**(6902), 51, ISSN 0028-0836, URL <http://www.nature.com/articles/nature00968>.
- [74] Greiner, M., C. A. Regal, and D. S. Jin, 2003, Nature **426**(6966), 537, ISSN 0028-0836, URL <http://www.nature.com/articles/nature02199>.
- [75] Gribakin, G. F., and V. V. Flambaum, 1993, Physical Review A **48**(1), 546, ISSN 1050-2947, URL <http://link.aps.org/doi/10.1103/PhysRevA.48.546>.

- [76] Grimm, R., M. Weidemüller, and Y. B. Ovchinnikov, 1999, *Optical dipole traps for neutral atoms*, Technical Report, 9902072, URL <https://arxiv.org/abs/physics/9902072>.
- [77] H., M., and Alexander, 2014, p. 49, URL <http://www2.chem.umd.edu/groups/alexander/teaching/index.html>.
- [78] Han, J. H., J. H. Kang, M. Lee, and Y. Shin, 2018, Physical Review A **97**(1), 013401, ISSN 24699934, URL <https://link.aps.org/doi/10.1103/PhysRevA.97.013401>.
- [79] Hart, R. A., P. M. Duarte, T.-L. Yang, X. Liu, T. Paiva, E. Khatami, R. T. Scalettar, N. Trivedi, D. A. Huse, and R. G. Hulet, 2015, Nature **519**(7542), 211, ISSN 0028-0836, URL <https://doi.org/10.1038/nature14223>.
- [80] Hecker Denschlag, J., J. E. Simsarian, H. Häffner, C. McKenzie, A. Browaeys, D. Cho, K. Helmerson, S. L. Rolston, and W. D. Phillips, 2002, Journal of Physics B: Atomic, Molecular and Optical Physics **35**(14), 3095, ISSN 09534075, URL <http://stacks.iop.org/0953-4075/35/i=14/a=307?key=crossref.143851fb4f795110e47d745ef41278c>.
- [81] Herbig, J., T. Kraemer, M. Mark, T. Weber, C. Chin, H.-C. H. C. Nägerl, and R. Grimm, 2003, Science **301**(5639), 1510, ISSN 1095-9203, URL <http://www.ncbi.nlm.nih.gov/pubmed/12934014>.
- [82] Hill, J. C., 2017, *Design and Construction of an Apparatus for Optically Pumping ^{87}Sr* , Masters, Rice University, URL http://ultracold.rice.edu/publications/Hill{_}MS.pdf.

- [83] Höfer, M., L. Riegger, F. Scazza, C. Hofrichter, D. R. Fernandes, M. M. Parish, J. Levinsen, I. Bloch, and S. Fölling, 2015, Physical Review Letters **115**(26), 1, ISSN 10797114, URL <http://arxiv.org/abs/1509.04257>.
- [84] Huang, B., R. Grimm, S. Stellmer, F. Schreck, and M. K. Tey, 2009, Physical Review Letters **103**(20), 200401, ISSN 0031-9007, URL <http://link.aps.org/doi/10.1103/PhysRevLett.103.200401>.
- [85] Huang, K., and C. N. Yang, 1957, Physical Review **105**(3), 767, ISSN 0031-899X, URL <https://link.aps.org/doi/10.1103/PhysRev.105.767>.
- [86] Huang, Y., 2013, *A New Optical Trap System for Ultracold Strontium*, Masters, Rice University, URL <http://ultracold.rice.edu/publications/Ying{ }Huang{ }master.pdf>.
- [87] Hueck, K., N. Luick, L. Sobirey, J. Siegl, T. Lompe, H. Moritz, L. W. Clark, and C. Chin, 2017, Optics Express **25**(8), 8670, ISSN 1094-4087, URL <https://www.osapublishing.org/abstract.cfm?URI=oe-25-8-8670>.
- [88] Hutson, J., 2010, in *Cold Molecules*, edited by R. V. Krems, B. Friedrich, and W. C. Stwalley (CRC Press, Boca Raton, Fla.), chapter 1, 1st edition, ISBN 9781420059038 1420059033, pp. 3–38.
- [89] Hutson, J. M., 2007, New Journal of Physics **9**(5), 152, ISSN 1367-2630, URL <http://stacks.iop.org/1367-2630/9/i=5/a=152?key=crossref.21a092de740716c0280b5f41edc5d848>.
- [90] Ido, T., Y. Isoya, and H. Katori, 2000, Physical Review A **61**(6), 4, ISSN 10941622, URL <http://link.aps.org/doi/10.1103/PhysRevA.61.061403>.

- [91] Jaksch, D., C. Bruder, J. I. Cirac, C. W. Gardiner, and P. Zoller, 1998, Physical Review Letters **81**(15), 3108, ISSN 10797114, URL <http://journals.aps.org/prl/abstract/10.1103/PhysRevLett.81.3108>.
- [92] Jaksch, D., and P. Zoller, 2005, Annals of Physics **315**(1), 52, ISSN 00034916, URL <http://linkinghub.elsevier.com/retrieve/pii/S0003491604001782>.
- [93] Johnson, B. R., 1978, The Journal of Chemical Physics **69**(10), 4678, ISSN 0021-9606, URL <http://aip.scitation.org/doi/10.1063/1.436421>.
- [94] Jones, K. M., E. Tiesinga, P. D. Lett, and P. S. Julienne, 2006, Reviews of Modern Physics **78**(2), 483, ISSN 00346861, URL <http://link.aps.org/doi/10.1103/RevModPhys.78.483>.
- [95] Jordens, R., N. Strohmaier, K. Gunter, H. Moritz, T. Esslinger, R. Jördens, N. Strohmaier, K. Günter, H. Moritz, and T. Esslinger, 2008, Nature **455**(7210), 204, ISSN 14764687, URL <http://dx.doi.org/10.1038/nature07244>.
- [96] Julienne, P. S., 2009, Faraday Discussions **142**(0), 361, ISSN 13596640, URL <http://dx.doi.org/10.1039/B820917K>.
- [97] Julienne, P. S., 2010, in *Cold Molecules*, edited by R. V. Krems, B. Friedrich, and W. C. Stwalley (CRC Press, Williamsburg), chapter Chapter 6, 1st edition, ISBN 978-1-4200-5903-8, pp. 221–244, [0902.1727](https://arxiv.org/abs/0902.1727), URL [http://arxiv.org/abs/0902.1727](https://arxiv.org/abs/0902.1727).
- [98] Julienne, P. S., and B. Gao, 2006, AIP Conference Proceedings **869**(1), 261, ISSN 0094243X, URL <https://aip.scitation.org/doi/abs/10.1063/1.2400656>.

- [99] Julienne, P. S., and F. H. Mies, 1989, Journal of the Optical Society of America B **6**(11), 2257, ISSN 0740-3224, URL <https://www.osapublishing.org/abstract.cfm?URI=josab-6-11-2257>.
- [100] Katori, H., T. Ido, Y. Isoya, and M. Kuwata-Gonokami, 1999, Physical Review Letters **82**(6), 1116, ISSN 10797114, URL <http://link.aps.org/doi/10.1103/PhysRevLett.82.1116>.
- [101] Ketterle, W., D. S. Durfee, and D. M. Stamper-Kurn, 1999, Proc. Int. School of Physics-Enrico Fermi , 679904034, URL <https://arxiv.org/abs/cond-mat/9904034>.
- [102] Kim, M.-S., J. Lee, J. H. Lee, Y. Shin, and J. Mun, 2016, Physical Review A **94**(4), 042703, ISSN 2469-9926, URL <https://link.aps.org/doi/10.1103/PhysRevA.94.042703>.
- [103] Kitagawa, M., Y. Takahashi, M. Kumakura, Y. Takasu, Y. Kato, S. Tojo, and K. Enomoto, 2006, Physical Review Letters **96**(15), 153201, ISSN 0031-9007, URL <https://link.aps.org/doi/10.1103/PhysRevLett.96.153201>.
- [104] Köhler, T., T. Gasenzer, and K. Burnett, 2003, Physical Review A **67**(1), 13601, ISSN 1050-2947, URL <http://link.aps.org/doi/10.1103/PhysRevA.67.013601>.
- [105] Köhler, T., K. Góral, and P. S. Julienne, 2006, Reviews of Modern Physics **78**(4), 1311, ISSN 00346861, URL <http://link.aps.org/doi/10.1103/RevModPhys.78.1311>.
- [106] Köhler, T., E. Tiesinga, and P. S. Julienne, 2005, Physical Review Letters

- 94(2), 020402, ISSN 00319007, URL <http://link.aps.org/doi/10.1103/PhysRevLett.94.020402>.
- [107] Kon, W. Y., J. A. Aman, J. C. Hill, T. C. Killian, and K. R. A. Hazzard, 2018, Physical Review A ISSN 2469-9926, [1812.11682](https://arxiv.org/abs/1812.11682), URL <http://arxiv.org/abs/1812.11682>.
- [108] Kotchigova, S., T. Zelevinsky, and J. Ye, 2009, Physical Review A 79(1), 012504, ISSN 1050-2947, URL <https://link.aps.org/doi/10.1103/PhysRevA.79.012504>.
- [109] Lang, F., P. V. D. Straten, B. Brandstätter, G. Thalhammer, K. Winkler, P. S. Julienne, R. Grimm, and J. Hecker Denschlag, 2008, Nature Physics 4(3), 22, ISSN 1745-2473, URL <http://www.nature.com/doifinder/10.1038/nphys838>.
- [110] Lang, F., K. Winkler, C. Strauss, R. Grimm, and J. H. Denschlag, 2008, Physical Review Letters 101(13), 133005, ISSN 00319007, URL <http://link.aps.org/doi/10.1103/PhysRevLett.101.133005>.
- [111] Lima, N. A., and M. J. Caldas, 2005, Physical Review B 72(3), 33109, URL <https://link.aps.org/doi/10.1103/PhysRevB.72.033109>.
- [112] Lin, Y.-J., K. Jiménez-García, and I. B. Spielman, 2011, Nature 471, 83, URL <https://doi.org/10.1038/nature09887><http://10.0.4.14/nature09887>.
- [113] Loftus, T. H., T. Ido, M. M. Boyd, A. D. Ludlow, and J. Ye, 2004, Physical Review A 70(6), 063413, ISSN 10502947, URL <http://link.aps.org/doi/10.1103/PhysRevA.70.063413>.

- [114] Luo, F., G. C. McBane, G. Kim, C. F. Giese, and W. R. Gentry, 1993, The Journal of Chemical Physics **98**(4), 3564, ISSN 0021-9606, URL <http://dx.doi.org/10.1063/1.464079>.
- [115] Makotyn, P., C. E. Klauss, D. L. Goldberger, E. A. Cornell, and D. S. Jin, 2014, Nature Physics **10**(2), 116, ISSN 17452473, URL <http://www.nature.com/doifinder/10.1038/nphys2850>.
- [116] Martinez de Escobar, Y., P. Mickelson, M. Yan, B. DeSalvo, S. Nagel, and T. C. Killian, 2009, Physical Review Letters **103**, 200402, ISSN 0031-9007, URL <http://link.aps.org/doi/10.1103/PhysRevLett.103.200402>.
- [117] Martinez de Escobar, Y. N., 2010, *Thesis: Bose-Einstein Condensation of 84Sr*, Ph.d thesis, Rice University, URL <https://hdl.handle.net/1911/62163>.
- [118] Martinez De Escobar, Y. N., P. G. Mickelson, P. Pellegrini, S. B. Nagel, A. Traverso, M. Yan, R. Côté, and T. C. Killian, 2008, Physical Review A **78**(6), 062708, ISSN 10502947, URL <https://link.aps.org/doi/10.1103/PhysRevA.78.062708>.
- [119] Mazurenko, A., 2010, *Molecular Beam Nozzle Optimization*, Undergraduate report, MIT, URL <http://ultracold.rice.edu/publications/2010mazurenkooven.pdf>.
- [120] McGuyer, B. H., M. McDonald, G. Z. Iwata, M. G. Tarallo, A. T. Grier, F. Apfelbeck, and T. Zelevinsky, 2015, New Journal of Physics **17**(5), 055004, ISSN 1367-2630, URL <http://stacks.iop.org/1367-2630/17/i=5/a=055004?key=crossref.c50b50642e24ab939a8feeca800c7eb4>.

- [121] McGuyer, B. H., M. McDonald, G. Z. Iwata, M. G. Tarallo, W. Skomorowski, R. Moszynski, and T. Zelevinsky, 2014, 1407.4752, URL <https://arxiv.org/abs/1407.4752>.
- [122] McGuyer, B. H., C. B. Osborn, M. McDonald, G. Reinaudi, W. Skomorowski, R. Moszynski, and T. Zelevinsky, 2013, Physical Review Letters **111**(24), 243003, ISSN 00319007, URL <https://link.aps.org/doi/10.1103/PhysRevLett.111.243003>.
- [123] Méndez-Visag, C., 2014, Revista Peruana de Medicina Experimental y Salud Pública **31**(4), 725, ISSN 17264642, URL <http://www.ncbi.nlm.nih.gov/pubmed/10481000>.
- [124] Mestrom, P. M. A., J. Wang, C. H. Greene, and J. P. D’Incao, 2017, Physical Review A **95**(3), 032707, ISSN 2469-9926, URL <http://link.aps.org/doi/10.1103/PhysRevA.95.032707>.
- [125] Metcalf, H. J., and P. van der Straten, 1999, *Laser Cooling and Trapping* (Springer-Verlag, New York, New York).
- [126] Michael Viray, 2014, *Zeeman Tunable Saturated Absorption Spectroscopy Cell for Locking Laser Frequency to the Strontium 1S0-1P1 Transition*, Undergraduate report, Rice University, URL <http://ultracold.rice.edu/publications/MichaelVirayREUReport>.
- [127] Mickelson, P., Y.~N.~Martinez de Escobar, M. Yan, and T. Killian, 2009, arXiv.org:0906.1837 URL <http://www.citebase.org/abstract?id=oai:arXiv.org:0906.1837>.

- [128] Mickelson, P. G., 2010, *Trapping and Evaporation of Mixtures Sr*, Ph.d thesis, Rice University, URL <https://hdl.handle.net/1911/62095>.
- [129] Mickelson, P. G., Y. N. M. de Escobar, P. Anzel, B. J. DeSalvo, S. B. Nagel, A. J. Traverso, M. Yan, and T. C. Killian, 2009, Journal of Physics B: Atomic, Molecular and Optical Physics **42**(23), 235001, ISSN 0953-4075, URL <http://stacks.iop.org/0953-4075/42/i=23/a=235001?key=crossref.a02d863a5f28acf3834f8be9018d8045>.
- [130] Mickelson, P. G., Y. N. Martinez, A. D. Saenz, S. B. Nagel, Y. C. Chen, T. C. Killian, P. Pellegrini, and R. Côté, 2005, Physical Review Letters **95**(22), 223002, ISSN 0031-9007, URL <https://link.aps.org/doi/10.1103/PhysRevLett.95.223002>.
- [131] Mickelson, P. G., Y. N. Martinez, A. D. Saenz, S. B. Nagel, Y. C. Chen, T. C. Killian, P. Pellegrini, and R. Côté, 2005, Physical Review Letters **95**(22), 223002, ISSN 0031-9007, URL <https://link.aps.org/doi/10.1103/PhysRevLett.95.223002>.
- [132] Mickelson, P. G., Y.~N.~Martinez de Escobar, M. Yan, B. J. DeSalvo, and T. Killian, 2010, Physical Review. A **81**(5), 051601, ISSN 2469-9926, URL <https://link.aps.org/doi/10.1103/PhysRevA.81.051601>.
- [133] Mies, F. H., and M. Raoult, 2000, Physical Review A **62**(1), 19, ISSN 10941622, URL <https://link.aps.org/doi/10.1103/PhysRevA.62.012708>.
- [134] Mies, F. H., E. Tiesinga, and P. S. Julienne, 2000, Physical Review A **61**(2), 22721, ISSN 1050-2947, URL <http://link.aps.org/doi/10.1103/PhysRevA.61.022721>.

- [135] Mitroy, J., and M. W. J. Bromley, 2003, Physical Review A **68**(5), 52714, URL <https://link.aps.org/doi/10.1103/PhysRevA.68.052714>.
- [136] Moerdijk, A. J., B. J. Verhaar, and A. Axelsson, 1995, Physical Review A **51**(6), 4852, ISSN 10502947, URL <https://link.aps.org/doi/10.1103/PhysRevA.51.4852>.
- [137] Moritz, H., T. Stöferle, K. Günter, M. Köhl, and T. Esslinger, 2005, Physical Review Letters **94**(21), 210401, ISSN 0031-9007, URL <https://link.aps.org/doi/10.1103/PhysRevLett.94.210401>.
- [138] Morsch, O., and M. Oberthaler, 2006, Reviews of Modern Physics **78**(1), 179, ISSN 0034-6861, URL <http://link.aps.org/doi/10.1103/RevModPhys.78.179>.
- [139] Mukaiyama, T., H. Katori, T. Ido, Y. Li, and M. Kuwata-Gonokami, 2003, Physical Review Letters **90**(11), 113002, ISSN 0031-9007, URL <https://link.aps.org/doi/10.1103/PhysRevLett.90.113002>.
- [140] Mukherjee, R., J. Millen, R. Nath, M. P. A. Jones, and T. Pohl, 2011, Journal of Physics B: Atomic, Molecular and Optical Physics **44**(18), 184010, ISSN 0953-4075, URL <http://stacks.iop.org/0953-4075/44/i=18/a=184010?key=crossref.48c64b3448df32d721e72d6d551bc6ab>.
- [141] Nagel, S., 2008, *Ultracold Collisions in Atomic Strontium*, Ph.d thesis, Rice University, URL <http://ultracold.rice.edu/publications/sbndoctoralthesis.pdf>.
- [142] Nagel, S. B., P. G. Mickelson, A. D. Saenz, Y. N. Martinez, Y. C. Chen, T. C. Killian, P. Pellegrini, and R. Côté, 2005, Physical Review Letters **94**(8), 083004,

- ISSN 00319007, URL <http://link.aps.org/doi/10.1103/PhysRevLett.94.083004>.
- [143] Nagel, S. B., C. E. Simien, S. Laha, P. Gupta, V. S. Ashoka, and T. C. Killian, 2003, Physical Review A **67**(1), 011401, ISSN 1050-2947, URL <https://link.aps.org/doi/10.1103/PhysRevA.67.011401>.
- [144] Naidon, P., and S. Endo, 2017, Reports on Progress in Physics **80**(5), 056001, ISSN 0034-4885, URL <http://stacks.iop.org/0034-4885/80/i=5/a=056001?key=crossref.0f4f565c3dc10533719f8c8b91048960>.
- [145] Naidon, P., and F. Masnou-Seeuws, 2006, Physical Review A **73**(4), 43611, ISSN 10502947, URL <http://pra.aps.org/abstract/PRA/v73/i4/e043611http://link.aps.org/doi/10.1103/PhysRevA.73.043611>.
- [146] Napolitano, R., J. Weiner, C. J. Williams, and P. S. Julienne, 1994, Physical Review Letters **73**(10), 1352, ISSN 00319007, URL <https://link.aps.org/doi/10.1103/PhysRevLett.73.1352>.
- [147] Ni, K.-K. K., S. Ospelkaus, M. H. G. de Miranda, A. Pe'er, B. Neyenhuis, J. J. Zirbel, S. Kotobchigova, P. S. Julienne, D. S. Jin, and J. Ye, 2008, Science **322**(5899), 231, ISSN 1095-9203, URL <http://www.sciencemag.org/content/322/5899/231.abstract>.
- [148] Nicholson, T. L., S. Blatt, B. J. Bloom, J. R. Williams, J. W. Thomassen, J. Ye, and P. S. Julienne, 2015, Physical Review A **92**(2), 022709, ISSN 10941622, URL <http://journals.aps.org/prl/abstract/10.1103/PhysRevA.92.022709>.

- [149] O'Hara, K. M., M. E. Gehm, S. R. Granade, J. E. Thomas, K. M. O'Hara, M. E. Gehm, S. R. Granade, and J. E. Thomas, 2001, Physical Review A **64**(5), 4, ISSN 10941622, URL <http://link.aps.org/doi/10.1103/PhysRevA.64.051403>.
- [150] Pachomov, E., 2017, *One and two-color photoassociation spectroscopy of ultracold ^{40}Ca* , Ph.D. thesis, Leibniz Universitat Hannover, URL <https://edocs.tib.eu/files/e01dh17/89419285X.pdf>.
- [151] Pachomow, E., V. P. Dahlke, E. Tiemann, F. Riehle, and U. Sterr, 2017, Physical Review A **95**(4), 043422, ISSN 24699934, URL <http://link.aps.org/doi/10.1103/PhysRevA.95.043422>.
- [152] Paredes, B., and I. Bloch, 2008, Physical Review A **77**(2), 23603, ISSN 1050-2947, URL <http://link.aps.org/doi/10.1103/PhysRevA.77.023603>.
- [153] Pethick, C. J., and H. Smith, 2008, *Bose-Einstein Condensation in Dilute Gases* (Cambridge University Press, Cambridge), ISBN 9780511802850, URL <http://ebooks.cambridge.org/ref/id/CB09780511802850>.
- [154] Porsev, S. G., and A. Derevianko, 2002, Physical Review A **65**(2), 20701, ISSN 10941622, URL <https://link.aps.org/doi/10.1103/PhysRevA.65.020701>.
- [155] Porsev, S. G., and A. Derevianko, 2006, Journal of Experimental and Theoretical Physics **102**(2), 195, ISSN 1090-6509, URL <https://doi.org/10.1134/S1063776106020014>.
- [156] Quéméner, G., 2018, RSC Theoretical and Computational Chemistry Series **2018-Janua**(11), 579, ISSN 2041319X, URL <http://arxiv.org/abs/1703.09174>.

- [157] Quéméner, G., and P. S. Julienne, 2012, Chemical Reviews **112**(9), 4949, ISSN 0009-2665, URL <https://doi.org/10.1021/cr300092g>.
- [158] Regal, C. A., M. Greiner, and D. S. Jin, 2004, Physical Review Letters **92**(4), 040403, ISSN 0031-9007, URL <https://link.aps.org/doi/10.1103/PhysRevLett.92.040403>.
- [159] Regal, C. A., C. Ticknor, J. L. Bohn, and D. S. Jin, 2003, Nature **424**(6944), 47, ISSN 0028-0836, URL <http://www.nature.com/articles/nature01738>.
- [160] Reinaudi, G., T. Lahaye, Z. Wang, and D. Guéry-Odelin, 2007, Optics Letters **32**(21), 3143, ISSN 0146-9592, URL <https://www.osapublishing.org/abstract.cfm?URI=ol-32-21-3143>.
- [161] Reinaudi, G., C. B. Osborn, M. McDonald, S. Kotochigova, and T. Zelevinsky, 2012, Physical Review Letters **109**(11), 115303, ISSN 0031-9007, URL <http://link.aps.org/doi/10.1103/PhysRevLett.109.115303>.
- [162] Reinaudi, G., C. B. Osborn, M. McDonald, S. Kotochigova, and T. Zelevinsky, 2012, Physical Review Letters **109**(11), 115303, ISSN 00319007, URL <http://link.aps.org/doi/10.1103/PhysRevLett.109.115303>.
- [163] Reschovsky, B., 2017, *Studies of Ultracold Strontium Gases*, Ph.d thesis, University of Maryland, URL <http://hdl.handle.net/1903/20742>.
- [164] Reschovsky, B. J., B. P. Ruzic, H. Miyake, N. C. Pisenti, P. S. Julienne, and G. K. Campbell, 2018, **1808.06507**, URL <http://arxiv.org/abs/1808.06507>.

- [165] Rey, A. M., 2004, *Ultracold Bosonic Atoms in Optical Lattices*, Ph.d thesis, University of Maryland, URL <http://hdl.handle.net/1903/1802>.
- [166] Saenz, A., 2005, *461nm Laser For Studies In Ultracold Neutral Strontium*, Masters, Rice University, URL <http://ultracold.rice.edu/publications/adsmastersthesis.pdf>.
- [167] Saffman, M., T. G. Walker, and K. Mølmer, 2010, Reviews of Modern Physics **82**(3), 2313, ISSN 0034-6861, URL <http://link.aps.org/doi/10.1103/RevModPhys.82.2313>.
- [168] Sakurai, J. J., 1994, *Modern Quantum Mechanics* (Pearson), ISBN 978.
- [169] Scazza, F., C. Hofrichter, M. Höfer, P. C. De Groot, I. Bloch, and S. Fölling, 2014, Nature Physics **10**(10), 779, ISSN 17452481, URL <http://arxiv.org/abs/1403.4761>.
- [170] Schöllkopf, W., and J. P. Toennies, 1994, American Association fot the Advancement of Science **266**(5189), 1345, URL <http://science.sciencemag.org/content/sci/266/5189/1345.full.pdf>.
- [171] Segal, S. R., Q. Diot, E. A. Cornell, A. A. Zozulya, and D. Z. Anderson, 2009, [0905.1979](http://dx.doi.org/10.1103/PhysRevA.81.053601), URL <http://dx.doi.org/10.1103/PhysRevA.81.053601>.
- [172] Skomorowski, W., F. Pawłowski, C. P. Koch, and R. Moszynski, 2012, The Journal of chemical physics **136**(19), 194306, ISSN 1089-7690, URL <http://www.ncbi.nlm.nih.gov/pubmed/22612094>.
- [173] Snoke, D., 2002, Science (New York, N.Y.) **298**(5597), 1368, ISSN 1095-9203, URL <http://www.ncbi.nlm.nih.gov/pubmed/12434051>.

- [174] Stanton, J. F., 1994, Physical Review A **49**(3), 1698, URL <https://link.aps.org/doi/10.1103/PhysRevA.49.1698>.
- [175] Stein, A., H. Knöckel, and E. Tiemann, 2010, European Physical Journal D **57**(2), 171, ISSN 14346060, URL <http://www.springerlink.com/index/10.1140/epjd/e2010-00058-y>.
- [176] Stellmer, S., 2013, *Thesis: Degenerate quantum gases of strontium*, Ph.d thesis, University of Innsbruck, URL <http://www.ultracold.at/theses/2013-stellmer.pdf>.
- [177] Stellmer, S., B. Pasquiou, R. Grimm, and F. Schreck, 2012, Physical Review Letters **109**(11), 115302, ISSN 00319007, URL <http://journals.aps.org/prl/abstract/10.1103/PhysRevLett.109.115302>.
- [178] Stellmer, S., F. Schreck, and T. C. Killian, 2013, Annual Review of Cold Atoms and Molecules **Volume 2**(January), 43, ISSN 1094-9194, URL https://doi.org/10.1142/9789814590174{_}0001.
- [179] Stellmer, S., M. Tey, R. Grimm, and F. Schreck, 2010, Physical Review A **82**, 41602, ISSN 1050-2947, URL <http://link.aps.org/doi/10.1103/PhysRevA.82.041602>.
- [180] Stöferle, T., H. Moritz, K. Günter, M. Köhl, T. Esslinger, T. Stoferle, H. Moritz, K. Gunter, M. Kohl, and T. Esslinger, 2006, Physical Review Letters **96**(3), 30401, ISSN 0031-9007, URL <http://link.aps.org/doi/10.1103/PhysRevLett.96.030401>.
- [181] Strecker, K. E., G. B. Partridge, and R. G. Hulet, 2003, Physical Review Letters **90**(19), 190401, ISSN 0031-9007, URL <http://link.aps.org/doi/10.1103/PhysRevLett.90.190401>.

- ters **91**(8), 80406, ISSN 0031-9007, URL <http://link.aps.org/doi/10.1103/PhysRevLett.91.080406>.
- [182] Syassen, N., D. M. Bauer, M. Lettner, T. Volz, D. Dietze, J. J. García-Ripoll, J. I. Cirac, G. Rempe, and S. Dürr, 2008, Science **320**(5881), 1329, ISSN 00368075, URL <http://www.ncbi.nlm.nih.gov/pubmed/18535241>.
- [183] Taie, S., S. Watanabe, T. Ichinose, and Y. Takahashi, 2016, Physical Review Letters **116**(4), 043202, ISSN 10797114, URL <http://link.aps.org/doi/10.1103/PhysRevLett.116.043202>.
- [184] Taie, S., R. Yamazaki, S. Sugawa, and Y. Takahashi, 2012, Nature Physics **8**(11), 825, ISSN 1745-2473, URL <http://www.nature.com/doifinder/10.1038/nphys2430>.
- [185] Takahashi, Y., Y. Kikuchi, A. A. Buchachenko, K. Takahashi, P. S. Julienne, H. Yamada, M. Borkowski, Y. Takasu, and R. Ciuryło, 2017, Physical Review A **96**(6), 63405, ISSN 2469-9926, URL <https://link.aps.org/doi/10.1103/PhysRevA.96.063405>.
- [186] Tey, M. K., S. Stellmer, R. Grimm, and F. Schreck, 2010, Physical Review A **82**(1), 011608, ISSN 10502947, URL <http://link.aps.org/doi/10.1103/PhysRevA.82.011608>.
- [187] Thalhammer, G., K. Winkler, F. Lang, S. Schmid, R. Grimm, and J. H. Denschlag, 2006, Physical Review Letters **96**(5), 050402, ISSN 10797114, URL <http://link.aps.org/doi/10.1103/PhysRevLett.96.050402>.
- [188] Theis, M., G. Thalhammer, K. Winkler, M. Hellwig, G. Ruff, R. Grimm, and

- J. H. Denschlag, 2004, Physical Review Letters **93**(12), 123001, ISSN 0031-9007, URL <http://link.aps.org/doi/10.1103/PhysRevLett.93.123001>.
- [189] Thompson, S. T., E. Hodby, and C. E. Wieman, 2005, Physical Review Letters **95**(19), 190404, ISSN 0031-9007, URL <https://link.aps.org/doi/10.1103/PhysRevLett.95.190404>.
- [190] Traverso, A., R. Chakraborty, Y. N. Martinez de Escobar, P. G. Mickelson, S. B. Nagel, M. Yan, and T. C. Killian, 2009, Physical Review A **79**(6), 060702, ISSN 1050-2947, URL <https://link.aps.org/doi/10.1103/PhysRevA.79.060702>.
- [191] Vaillant, C. L., M. P. Jones, and R. M. Potvliege, 2014, Journal of Physics B: Atomic, Molecular and Optical Physics **47**(15), 22, ISSN 13616455, URL <http://arxiv.org/abs/1402.5802>.
- [192] Vogels, J. M., B. J. Verhaar, and R. H. Blok, 1998, Physical Review A **57**(5), 4049, ISSN 1050-2947, URL <https://link.aps.org/doi/10.1103/PhysRevA.57.4049>.
- [193] Wang, J., J. P. D’Incao, B. D. Esry, and C. H. Greene, 2012, Physical Review Letters **108**(26), 263001, ISSN 0031-9007, URL <https://link.aps.org/doi/10.1103/PhysRevLett.108.263001>.
- [194] Weiner, J., V. S. Bagnato, S. Zilio, and P. S. Julienne, 1999, Reviews of Modern Physics **71**(1), 1, ISSN 00346861, URL <http://journals.aps.org/rmp/abstract/10.1103/RevModPhys.71.1>.
- [195] Wikner, A., 2017, *A MATLAB Script for Calibrating an Optical Lattice using Kapitza-Dirac Diffraction*, Undergraduate report, Rice University, URL <http://ultracold.rice.edu/publications/2017aWiknerKaptizaDirac.pdf>.

- [196] Wong, L. S., B. W. N. Voon, S. C. Teo, and A. Balakrishnan, 2016, Ecology, Environment and Conservation **22**(3), 1107, ISSN 0971765X, URL <http://link.aps.org/doi/10.1103/PhysRevLett.102.040402>.
- [197] Wynar, R., R. S. Freeland, D. J. Han, C. Ryu, and D. J. Heinzen, 2000, Science **287**(5455), 1016 LP , URL <http://science.sciencemag.org/content/287/5455/1016.abstract>.
- [198] Yamazaki, R., S. Taie, S. Sugawa, and Y. Takahashi, 2010, Physical Review Letters **105**(5), 050405, ISSN 00319007, URL <https://link.aps.org/doi/10.1103/PhysRevLett.105.050405>.
- [199] Yan, M., 2013, *Thesis: Optical Feshbach Resonances and Coherent Photoassociation in a BEC*, Ph.d thesis, Rice University, URL <https://hdl.handle.net/1911/77594>.
- [200] Yan, M., R. Chakraborty, A. Mazurenko, P. G. Mickelson, Y. N. De Escobar, B. J. Desalvo, and T. C. Killian, 2011, Physical Review A **83**(3), 1, ISSN 10502947, URL <http://link.aps.org/doi/10.1103/PhysRevA.83.032705>.
- [201] Yan, M., B. J. Desalvo, Y. Huang, P. Naidon, and T. C. Killian, 2013, Physical Review Letters **111**(15), 150402, ISSN 00319007, URL <http://link.aps.org/doi/10.1103/PhysRevLett.111.150402>.
- [202] Yan, M., B. J. Desalvo, B. Ramachandhran, H. Pu, and T. C. Killian, 2013, Physical Review Letters **110**(12), 123201, ISSN 00319007, URL <http://link.aps.org/doi/10.1103/PhysRevLett.110.123201>.
- [203] Yasuda, M., T. Kishimoto, M. Takamoto, and H. Katori, 2006, Physical Re-

- view A **73**(1), 011403, ISSN 1050-2947, URL <https://link.aps.org/doi/10.1103/PhysRevA.73.011403>.
- [204] Ye, J., H. J. Kimble, and H. Katori, 2008, Science **320**(5884), 1734 LP , URL <https://science.sciencemag.org/content/320/5884/1734>.
- [205] Zelevinsky, T., M. M. Boyd, A. D. Ludlow, T. Ido, J. Ye, R. Ciurył, P. Naidon, and P. S. Julienne, 2006, Physical Review Letters **96**(20), 203201, ISSN 00319007, URL <http://link.aps.org/doi/10.1103/PhysRevLett.96.203201>.
- [206] Zelevinsky, T., S. Kotochigova, and J. Ye, 2008, Physical Review Letters **100**(4), 43201, ISSN 00319007, URL <http://link.aps.org/doi/10.1103/PhysRevLett.100.043201>.
- [207] Zhang, X., M. Bishof, S. L. Bromley, C. V. Kraus, M. S. Safronova, P. Zoller, A. M. Rey, and J. Ye, 2014, Science **345**(6203), 1467, ISSN 10959203, URL <http://www.sciencemag.org/cgi/doi/10.1126/science.1254978>.
- [208] Zhu, B., B. Gadway, M. Foss-Feig, J. Schachenmayer, M. L. Wall, K. R. Hazzard, B. Yan, S. A. Moses, J. P. Covey, D. S. Jin, J. Ye, M. Holland, *et al.*, 2014, Physical Review Letters **112**(7), 070404, ISSN 00319007, URL <http://link.aps.org/doi/10.1103/PhysRevLett.112.070404>.
- [209] Zwierlein, M. W., Z. Hadzibabic, S. Gupta, and W. Ketterle, 2003, Physical Review Letters **91**(25), 250404, ISSN 0031-9007, URL <https://link.aps.org/doi/10.1103/PhysRevLett.91.250404>.
- [210] Zwierlein, M. W., C. A. Stan, C. H. Schunck, S. M. F. Raupach, A. J. Kerman,

and W. Ketterle, 2004, Physical Review Letters **92**(12), 120403, ISSN 0031-9007, URL <https://link.aps.org/doi/10.1103/PhysRevLett.92.120403>.

Appendices

Appendix A

Two-particle momentum probability distribution

A.1 Standard form

The following is a derivation of two-particle relative-momentum probability distribution function when the single-particle kinetic energies are allowed to extend to infinity. A quick note on notation conventions, f_p and f_E are used to refer to the momentum and energy forms of the distributions respectively. Additionally, since we will be discussing the single-particle and two-particle distributions at length, each distribution is labeled by a subscript one or two so it is apparent what the physical system under consideration is. Function with hat accents ($\hat{\cdot}$) are used to denote that they are truncated forms of the equation. As an example, the function describing the truncated relative collision energy distribution is labeled by $\hat{f}_{E,\text{two}}$.

Starting with the single-particle Maxwell-Boltzmann momentum probability distribution function for a gas of temperature T with particles of mass m .

$$f_{p,\text{one}}(\mathbf{p}) = \left(\frac{1}{2\pi m k_B T} \right)^{3/2} \exp \left(\frac{-p^2}{2mk_B T} \right) \quad (\text{A.1})$$

This distribution is valid for any momentum \mathbf{p} under the requirement that

$$\int_{-\infty}^{\infty} dp_x \int_{-\infty}^{\infty} dp_y \int_{-\infty}^{\infty} dp_z f_{p,\text{one}}(\mathbf{p}) = 1 \quad (\text{A.2})$$

Extension of this distribution into the two-particle regime may generally be complicated if a particle's trajectory is dependent on other particles trajectories (i. e. particles retain a "memory" of past collisions.) If, however, we assume that particle collisions

are rapid and therefore largely independent of one another, we can approximate the two-particle momentum distribution as the product of two single-particle functions [37, 53]. The two-particle momentum distribution for a homogeneous system is then

$$\begin{aligned} f_{p,\text{two}}(\mathbf{p}_1, \mathbf{p}_2) &= f_{p,\text{one}}(\mathbf{p}_1)f_{p,\text{one}}(\mathbf{p}_2) \\ &= \left(\frac{1}{2\pi m k_B T} \right)^3 \exp \left(\frac{-(p_1^2 + p_2^2)}{2m k_B T} \right) \end{aligned} \quad (\text{A.3})$$

Next, we'd like to consider a center-of-mass frame for the distribution. So we define

$$\begin{aligned} \mathbf{p}_C &= \mathbf{p}_1 + \mathbf{p}_2 & M &= m_1 + m_2 = 2m \\ \mathbf{p}_R &= \frac{\mathbf{p}_1 - \mathbf{p}_2}{2} & \mu &= \frac{m_1 m_2}{m_1 + m_2} = \frac{m}{2} \end{aligned}$$

From these equations we can use conservation of energy to determine the quadrature sum of the two momenta

$$\begin{aligned} \frac{p_1^2}{2m} + \frac{p_2^2}{2m} &= \frac{p_C^2}{2M} + \frac{p_R^2}{2\mu} \\ p_1^2 + p_2^2 &= \frac{p_C^2}{2} + 2p_R^2 \end{aligned}$$

Thus the two-particle momentum probability distribution takes the form

$$f_{p,\text{two}}(\mathbf{p}_C, \mathbf{p}_R) = \left(\frac{1}{2\pi M k_B T} \right)^{3/2} \left(\frac{1}{2\pi \mu k_B T} \right)^{3/2} \exp \left(\frac{-p_C^2}{2M k_B T} \right) \exp \left(\frac{-p_R^2}{2\mu k_B T} \right) \quad (\text{A.4})$$

The relative collision energy distribution is found by integrating over the center-of-mass momentum.

$$\begin{aligned} f_{p,\text{two}}(\mathbf{p}_R) &= \int d^3 \mathbf{p}_C f_{p,\text{two}}(\mathbf{p}_C, \mathbf{p}_R) \\ &= \left(\frac{1}{2\pi \mu k_B T} \right)^{3/2} \exp \left(\frac{-p_R^2}{2\mu k_B T} \right) \end{aligned} \quad (\text{A.5})$$

A.2 Truncated form

Now let's consider the effects on the two-particle relative distribution when the single-particle Maxwell-Boltzmann distributions are truncated. Starting from Eq. A.3, the

two-particle momentum distribution may be written as

$$\begin{aligned}\hat{f}_{p,\text{two}}(\mathbf{p}_1, \mathbf{p}_2) &= \mathcal{N} \left(\frac{1}{2\pi m k_B T} \right)^3 \exp \left(\frac{-(p_1^2 + p_2^2)}{2m k_B T} \right) \\ &\quad \times \Theta \left(\epsilon_{\max} - \frac{p_1^2}{2m} \right) \Theta \left(\epsilon_{\max} - \frac{p_2^2}{2m} \right)\end{aligned}\tag{A.6}$$

We have modified the continuous two-particle distribution, $f_{p,\text{two}}(\mathbf{p}_1, \mathbf{p}_2)$, with a normalization constant \mathcal{N} and Heaviside functions to enforce the truncation for each single-particle kinetic energy. The truncation energy, ϵ_{\max} , is here considered to be the same for both particles. The normalization constant \mathcal{N} is included to ensure that integration over the truncated probability distribution remains equal to one and will be found explicitly at the end of the derivation.

Once more, we are interested in the distribution of relative momenta so following our previous steps for the continuous distribution, we perform a change of variables to a center-of-mass frame so we can integrate out the center-of-mass component.

$$\begin{aligned}\hat{f}_{p,\text{two}}(\mathbf{p}_R) &= \int d^3 \mathbf{p}_C \hat{f}_{p,\text{two}}(\mathbf{p}_1, \mathbf{p}_2) \\ &= \mathcal{N} \left(\frac{1}{2\pi M k_B T} \right)^{3/2} \left(\frac{1}{2\pi \mu k_B T} \right)^{3/2} \int d^3 \mathbf{p}_C \exp \left(\frac{-p_C^2}{2M k_B T} \right) \exp \left(\frac{-p_R^2}{2\mu k_B T} \right) \\ &\quad \times \Theta \left(\epsilon_{\max} - \frac{p_C^2}{8m} - \frac{p_R^2}{2m} - \frac{\mathbf{p}_C \cdot \mathbf{p}_R}{2m} \right) \Theta \left(\epsilon_{\max} - \frac{p_C^2}{8m} - \frac{p_R^2}{2m} + \frac{\mathbf{p}_C \cdot \mathbf{p}_R}{2m} \right)\end{aligned}\tag{A.7}$$

We expect isotropically distributed center-of-mass momenta so we integrate by transforming into spherical coordinates with the radius aligned along the interatomic axis

$$\begin{aligned}\hat{f}_{p,\text{two}}(\mathbf{p}_R) &= \mathcal{N} \left(\frac{1}{2\pi M k_B T} \right)^{3/2} \left(\frac{1}{2\pi \mu k_B T} \right)^{3/2} \exp \left(\frac{-p_R^2}{2\mu k_B T} \right) \\ &\quad \times \int_0^\pi \sin \theta d\theta \int_0^{2\pi} d\phi \int_0^\infty dp_C p_C^2 \exp \left(\frac{-p_C^2}{2M k_B T} \right) \\ &\quad \times \Theta \left(\epsilon_{\max} - \frac{p_C^2}{8m} - \frac{p_R^2}{2m} - \frac{p_C p_R \cos \theta}{2m} \right) \Theta \left(\epsilon_{\max} - \frac{p_C^2}{8m} - \frac{p_R^2}{2m} + \frac{p_C p_R \cos \theta}{2m} \right)\end{aligned}\tag{A.8}$$

Making a change of variables

$$X = \cos \theta$$

$$dX = -\sin \theta d\theta$$

Substitute and integrate over ϕ

$$\begin{aligned} \hat{f}_{p,\text{two}}(\mathbf{p}_R) &= 2\pi\mathcal{N} \left(\frac{1}{2\pi Mk_B T} \right)^{3/2} \left(\frac{1}{2\mu k_B T} \right)^{3/2} \exp \left(\frac{-p_R^2}{2\mu k_B T} \right) \\ &\quad \times \int_{-1}^1 dX \int_0^\infty dp_C p_C^2 \exp \left(\frac{-p_C^2}{2Mk_B T} \right) \\ &\quad \times \Theta \left(\epsilon_{\max} - \frac{p_C^2}{8m} - \frac{p_R^2}{2m} - \frac{p_C p_R X}{2m} \right) \Theta \left(\epsilon_{\max} - \frac{p_C^2}{8m} - \frac{p_R^2}{2m} + \frac{p_C p_R X}{2m} \right) \end{aligned} \quad (\text{A.9})$$

Here we recognize that the two Heaviside functions cancel each other out on either side of the dX integral. However, since $\cos \theta$ is symmetric we may eliminate one of the Heaviside's, change the bounds of integration to go from $0 \rightarrow 1$, and multiply by two without changing the final result.

$$\begin{aligned} \hat{f}_{p,\text{two}}(\mathbf{p}_R) &= 4\pi\mathcal{N} \left(\frac{1}{2\pi Mk_B T} \right)^{3/2} \left(\frac{1}{2\mu k_B T} \right)^{3/2} \exp \left(\frac{-p_R^2}{2\mu k_B T} \right) \\ &\quad \times \int_0^1 dX \int_0^\infty dp_C p_C^2 \exp \left(\frac{-p_C^2}{2Mk_B T} \right) \Theta \left(\epsilon_{\max} - \frac{p_C^2}{8m} - \frac{p_R^2}{2m} - \frac{p_C p_R X}{2m} \right) \end{aligned} \quad (\text{A.10})$$

At this point we can group the effects of truncation into a new function $\hat{\mathcal{G}}_p$ and rewrite using the continuous relative-momentum probability distribution $f_{p,\text{two}}(\mathbf{p}_R)$, Eq. A.5.

$$\begin{aligned} \hat{f}_{p,\text{two}}(\mathbf{p}_R) &= \left(\frac{1}{2\pi\mu k_B T} \right)^{3/2} \exp \left(\frac{-p_R^2}{2\mu k_B T} \right) \hat{\mathcal{G}}_p(\epsilon_{\max}, \mathbf{p}_R) \\ &= f_{p,\text{two}}(\mathbf{p}_R) \hat{\mathcal{G}}_p(\epsilon_{\max}, \mathbf{p}_R) \end{aligned} \quad (\text{A.11})$$

where $\hat{\mathcal{G}}_p(\epsilon_{\max}, \mathbf{p}_R)$ is given by

$$\begin{aligned} \hat{\mathcal{G}}_p(\epsilon_{\max}, \mathbf{p}_R) &= 4\pi\mathcal{N} \left(\frac{1}{2\pi Mk_B T} \right)^{3/2} \int_0^1 dX \int_0^\infty dp_C p_C^2 \exp \left(\frac{-p_C^2}{2Mk_B T} \right) \\ &\quad \times \Theta \left(\epsilon_{\max} - \frac{p_C^2}{8m} - \frac{p_R^2}{2m} - \frac{p_C p_R X}{2m} \right) \end{aligned} \quad (\text{A.12})$$

In photoassociation we are interested in the relative collision energy distribution $f_{\text{E,two}}(\epsilon)$. Assuming the distribution of momenta are isotropic, we change variables once more using

$$\begin{aligned}\epsilon &= \frac{p_{\text{R}}^2}{2\mu} & \mathcal{E} &= \frac{p_{\text{C}}^2}{2M} \\ p_{\text{R}} &= \sqrt{2\mu\epsilon} & p_{\text{C}} &= \sqrt{2M\mathcal{E}} \\ dp_{\text{R}} p_{\text{R}}^2 &= \sqrt{2\mu^3\epsilon} d\epsilon & dp_{\text{C}} p_{\text{C}}^2 &= \sqrt{2M^3\mathcal{E}} d\mathcal{E}\end{aligned}$$

Using these expressions and noting that

$$\begin{aligned}\int d^3\mathbf{p}_{\text{R}} f_{\text{p,two}}(\mathbf{p}_{\text{R}}) &= \int d\epsilon f_{\text{E,two}}(\epsilon) = 1 \\ \Rightarrow 4\pi p_{\text{R}}^2 f_{\text{p,two}}(\mathbf{p}_{\text{R}}) dp_{\text{R}} &= f_{\text{E,two}}(\epsilon) d\epsilon\end{aligned}\tag{A.13}$$

Then $\hat{f}_{\text{E,two}}(\tilde{\epsilon})$ is given by

$$\begin{aligned}\hat{f}_{\text{E,two}}(\epsilon) &= \mathcal{N} \frac{2}{\sqrt{\pi}} \frac{\sqrt{\epsilon}}{(k_B T)^{3/2}} e^{-\epsilon/k_B T} \int_0^1 dX \int_0^\infty d\mathcal{E} \frac{2}{\sqrt{\pi}} \frac{\sqrt{\mathcal{E}}}{(k_B T)^{3/2}} e^{-\mathcal{E}/k_B T} \\ &\quad \times \Theta\left(\epsilon_{\max} - \frac{\mathcal{E} - \epsilon}{2} - X\sqrt{\mathcal{E}\epsilon}\right)\end{aligned}\tag{A.14}$$

We can now determine the normalization constant \mathcal{N} by requiring that

$$\int_0^{2\epsilon_{\max}} d\epsilon \hat{f}_{\text{E,two}}(\epsilon) = 1$$

where we have used an energy cutoff of $2\epsilon_{\max}$ since either particle may have an energy in the range $[0 \rightarrow \epsilon_{\max}]$. With the normalization, the complete expression for $\hat{f}_{\text{E,two}}(\epsilon)$ is then

$$\begin{aligned}\hat{f}_{\text{E,two}}(\epsilon) &= \frac{2}{\sqrt{\pi}} \frac{\sqrt{\epsilon}}{(k_B T)^{3/2}} \exp\left(\frac{-\epsilon}{k_B T}\right) \hat{\mathcal{G}}_E(\epsilon_{\max}, \epsilon) \\ &= f_{\text{E,two}}(\epsilon) \hat{\mathcal{G}}_E(\epsilon_{\max}, \epsilon)\end{aligned}\tag{A.15}$$

where all the effects of the truncation have been moved to $\hat{\mathcal{G}}_E$, given by

$$\hat{\mathcal{G}}_E(\epsilon_{\max}, \epsilon) = \frac{\int_0^\infty d\mathcal{E} \frac{2}{\sqrt{\pi}} \frac{\sqrt{\mathcal{E}}}{(k_B T)^{3/2}} e^{-\mathcal{E}/k_B T} \Theta\left(\epsilon_{\max} - \frac{\mathcal{E} - \epsilon}{2} - X\sqrt{\mathcal{E}\epsilon}\right)}{\int_0^{2\epsilon_{\max}} d\epsilon \frac{2}{\sqrt{\pi}} \frac{\sqrt{\epsilon}}{(k_B T)^{3/2}} e^{-\epsilon/k_B T} \int_0^1 dX \int_0^\infty d\mathcal{E} \frac{2}{\sqrt{\pi}} \frac{\sqrt{\mathcal{E}}}{(k_B T)^{3/2}} e^{-\mathcal{E}/k_B T} \Theta\left(\epsilon_{\max} - \frac{\mathcal{E} - \epsilon}{2} - X\sqrt{\mathcal{E}\epsilon}\right)} \quad (\text{A.16})$$

As a check of the limiting behavior of $\hat{\mathcal{G}}_E$, we expect that $\lim_{\epsilon_{\max} \rightarrow \infty} \hat{\mathcal{G}}_E = 1$. This is simply a requirement that for single-particle distributions where the truncation value is large, then the truncated two-particle relative collision energy distribution should approach the continuous two-particle relative collision energy distribution. This is trivial to verify, recalling that

$$\int_0^\infty dx \sqrt{x} e^{-x/x_0} = \frac{\sqrt{\pi}}{2} (x_0)^{3/2} \quad (\text{A.17})$$

Although the form of Eq. A.16 is rather cumbersome, this equation may be solved numerically. Below are plots exploring the behavior of $\hat{f}_{\text{E,two}}(\epsilon)$ and $\hat{\mathcal{G}}_E$ as ϵ_{\max} and ϵ are varied.

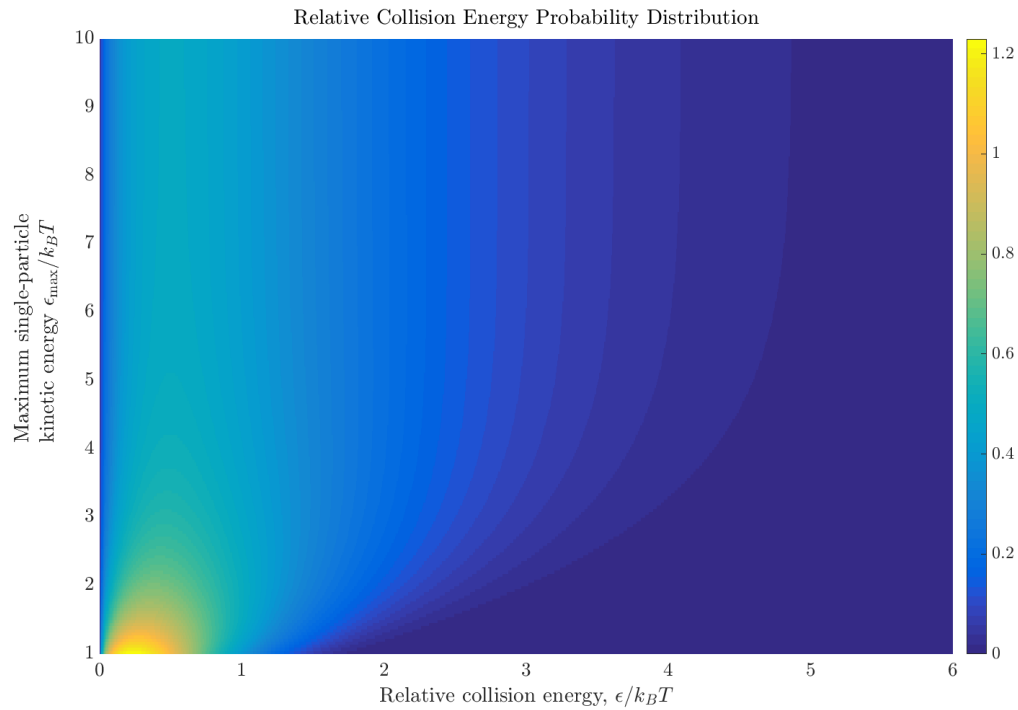


Figure A.1 : 2D Surface plot of the relative collision likelihood

$\hat{f}_{E,\text{two}}(\epsilon)$ is shown with energies scaled by the characteristic energy $k_B T$. The collision likelihood is given for relative collision energy along the bottom axis and the maximum single-particle kinetic energy ϵ_{\max} increasing on the vertical axis. As required, there are no occupied energy states above $2\epsilon_{\max}$ and once the maximum energy is greater than ~ 4 the distribution behaves as expected and appears to become constant. This is discussed in Sec. 5.1.1.

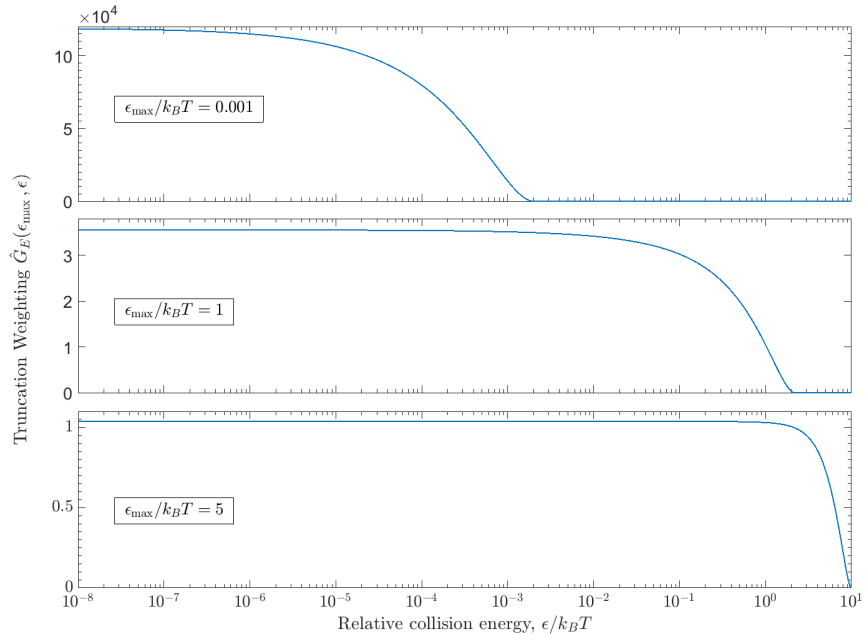


Figure A.2 : Behavior of $\hat{G}_E(\epsilon_{\max}, \epsilon)$ vs. collision energy

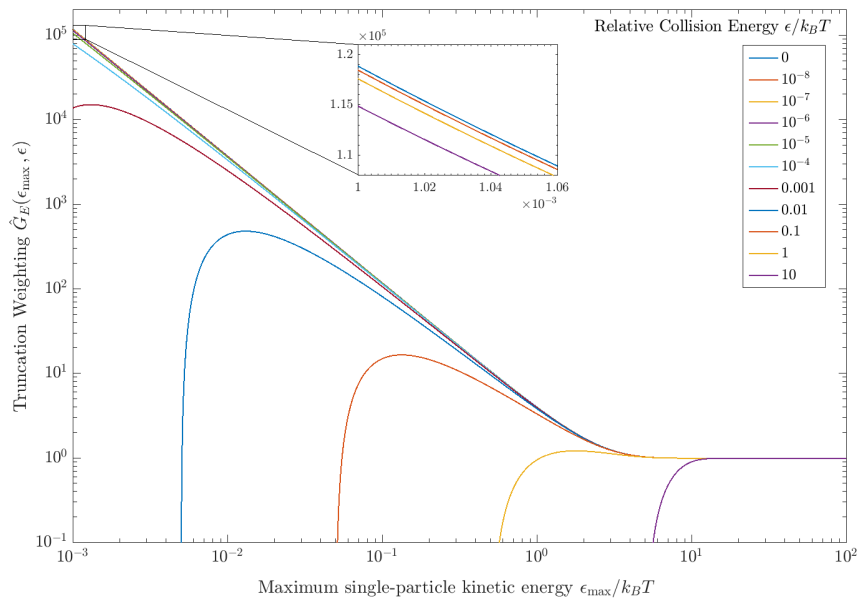


Figure A.3 : Behavior of $\hat{G}_E(\epsilon_{\max}, \epsilon)$ vs. ϵ_{\max}

Appendix B

Concise derivation of effective volumes

The following derivation is meant to serve as a quick reference for finding the analytic form of the effective volumes for ultracold gases held in a optical dipole trap. This section follows the arguments presented in Mi Yan's work on modeling of collisions in an ODT [200]. This work numerically evaluates the general case of power-law potentials and the corresponding density distribution at arbitrary temperatures less than the trap depth.

If instead one restricts to the experimentally reasonable conditions of high- η (recall η is the ratio of trap depth to sample temperature, $\eta = \epsilon_t/k_B T$) and harmonic trapping potentials, then a useful analytic expression can be found for the effective volumes of the gas.

Starting with the definition of effective volumes

$$V_q = \frac{1}{n_{\text{peak}}^q} \int d^3\mathbf{r} [n(\mathbf{r})]^q \quad (\text{B.1})$$

Defining $\eta = \epsilon_t/k_B T$, and integrating over all space we can formally write the number distribution as

$$n(\mathbf{r}) = n_{\text{peak}} A \exp\left(\frac{-U(\mathbf{r})}{k_B T}\right) \left[\operatorname{erf}\left(\sqrt{\eta - \frac{U(\mathbf{r})}{k_B T}}\right) - 2\sqrt{\frac{1}{\pi}} \left(\eta - \frac{U(\mathbf{r})}{k_B T}\right) \exp\left(-\eta + \frac{U(\mathbf{r})}{k_B T}\right) \right] \quad (\text{B.2})$$

$$n_{\text{peak}} = n_0 \left[\operatorname{erf}(\sqrt{\eta}) - 2\sqrt{\frac{\eta}{\pi}} \exp(-\eta) \right] \quad (\text{B.3})$$

where A is a normalization constant defined by

$$\begin{aligned} A &= \frac{n_0}{n_{\text{peak}}} \\ &= \left[\text{erf}(\sqrt{\eta}) - 2\sqrt{\frac{\eta}{\pi}} \exp(-\eta) \right]^{-1} \end{aligned}$$

Plugging these equations into the expression for the effective volume we find

$$V_q = \frac{1}{[\mathcal{P}(\eta, 3/2)]^q} \int d^3\mathbf{r} \exp\left(-q \frac{U(\mathbf{r})}{k_B T}\right) \left[\mathcal{P}(\eta - \frac{U(\mathbf{r})}{k_B T}, 3/2) \right]^q \quad (\text{B.4})$$

where $\mathcal{P}(\eta, a)$ is the incomplete Gamma function. It is easily verifiable in Mathematica that for $\eta \geq 4$ then $\mathcal{P}(\eta, a) \rightarrow 1$. Thus in a deeply trapped regime, we can approximate the effective volume as

$$V_q = \int d^3\mathbf{r} \exp\left(-q \frac{U(\mathbf{r})}{k_B T}\right) \quad (\text{B.5})$$

Considering an anisotropic harmonic potential $U(x, y, z) = \frac{1}{2}m(\omega_x^2x^2 + \omega_y^2y^2 + \omega_z^2z^2)$, then we can find the characteristic length as

$$R_i^2 = \frac{2\epsilon_t}{m\omega_i^2} \quad (\text{B.6})$$

where ϵ_t is the trap depth determined by the lowest saddle point. Thus the effective volume may be written

$$V_q = \int_{-R_x}^{R_x} dx \int_{-R_y}^{R_y} dy \int_{-R_z}^{R_z} dz \exp\left(-q \frac{m(\omega_x^2x^2 + \omega_y^2y^2 + \omega_z^2z^2)}{2k_B T}\right) \quad (\text{B.7})$$

Making a change of variables to $\tilde{r}_i = r_i/R_i$ for each axis we may rewrite V_q as

$$V_q = R_x R_y R_z \int_{-1}^1 d\tilde{x} \int_{-1}^1 d\tilde{y} \int_{-1}^1 d\tilde{z} \exp(-q\eta(\tilde{x}^2 + \tilde{y}^2 + \tilde{z}^2)) \quad (\text{B.8})$$

$$= R_x R_y R_z \left(\frac{\pi}{q\eta} \right)^{3/2} [\text{erf}(\sqrt{q\eta})]^3 \quad (\text{B.9})$$

where recall that $\eta = \epsilon_t/k_B T$. Once more, it is readily verified for $\eta \gg 1$ then $\text{erf}(\sqrt{q\eta}) \rightarrow 1$ and therefore

$$V_q = \left[\frac{2\pi k_B T}{qm\bar{\omega}} \right]^{3/2} \quad (\text{B.10})$$

where $\bar{\omega} = (\omega_x \omega_y \omega_z)^{1/3}$ is geometric mean of the trap frequencies.

Appendix C

Doppler-free spectroscopy

Below we will quickly outline the derivation of the resonance condition when performing Doppler free spectroscopy. This method is commonly used when stabilizing a laser frequency to an atomic transition. In short, counter-propagating laser beams in a pump-probe configuration will can "burn a hole" through an atomic sample and lead to a Lamb dip.

Below we'll derive the resonance condition for when the two lasers will be resonant with the same velocity class. When used in conjunction with frequency modulation, an error signal useful for laser locking can be derived. Therefore, the resonance condition effectively defines the relationship of the laser lock point and any potential offsets.

The first section will cover the case where the two lasers share the same frequency as well as when one beam has an additional offset. Finally, for the case of the 461 nm sat. abs., we'll consider the resonance condition when using a Zeeman tunable transition.

C.1 Common setup

Consider two laser beam at frequencies $f_1 \& f_2 = f_1 + \delta$, driving a 2-level atom with $v \neq 0$ and transition energy $E_0 = hf_0$. Then the resonance condition for $f_1 \& f_2$ is

given by

$$f_1 = f_0 + \mathbf{k}_1 \cdot \mathbf{v}_1 \quad f_2 = f_0 + \mathbf{k}_2 \cdot \mathbf{v}_2 \quad (\text{C.1})$$

Assume the beams are counter propagating such that $k_1 = -k_2 = k$, then the resonance condition becomes

$$f_1 = f_0 + kv_1 \quad f_2 = f_0 - kv_2 \quad (\text{C.2})$$

Finally, consider the case when the 2 beams interact with the same velocity class of atoms $v_1 = v_2 = v$ then

$$f_1 = f_0 + kv \quad f_2 = f_0 - kv \quad (\text{C.3})$$

Rearranging these equation

$$\begin{aligned} kv &= f_1 - f_0 & kv &= f_0 - f_2 \\ &&&= f_0 - f_1 - \delta \end{aligned} \quad (\text{C.4})$$

Finally, combining these equations we find

$$\begin{aligned} f_1 - f_0 &= f_0 - f_1 - \delta \\ 2f_1 &= 2f_0 - \delta \\ f_1 &= f_0 - \frac{\delta}{2} \end{aligned} \quad (\text{C.5})$$

Therefore, if we use a single laser where $f_{\text{laser}} = f_1$ and lock the frequency such that $f_1 \& f_2$ are resonant with the same velocity class of atoms then the laser frequency will be given by $f_{\text{laser}} = f_0 - \delta/2$.

We can also see what would happen if $f_1 = f_2 = f + \delta$. Then instead of locking to $f_0 - \delta/2$ the resonance condition would become $f_{\text{laser}} = f_0 - \delta$.

C.2 Addition of Zeeman shift

Expanding on the previous case we now consider the effects of adding a magnetic field. This addition will let us controllable tune the resonance condition and thereby change the frequency of the locked laser. As before we consider two laser beam, f_1 & f_2 where $f_2 = f_1 + \delta$, and take the beams as counter propagating and interacting with the same velocity class. With the additional Zeeman shift, the previous resonance condition becomes

$$\begin{aligned} f_1 &= f_0 + \mathbf{k}_1 \cdot \mathbf{v}_1 + g_j \mu_B m_1 B = f_0 + kv + g_j \mu_B m_1 B \\ f_2 &= f_0 + \mathbf{k}_2 \cdot \mathbf{v}_2 + g_j \mu_B m_2 B = f_0 - kv + g_j \mu_B m_2 B \end{aligned} \tag{C.6}$$

where g_j is the Lande g-factor, μ_B is the Bohr magneton, m_i is a specified magnetic sub-level, and B is the magnetic field. Proceeding as we did previously, with the additional assumption that $m_1 = m_2 = m$, then we find

$$\begin{aligned} f_1 - f_0 - g_j \mu_B m B &= f_0 - f_1 - \delta + g_j \mu_B m B \\ 2f_1 &= 2f_0 - \delta + 2g_j \mu_B m B \\ f_1 &= f_0 - \frac{\delta}{2} + g_j \mu_B m B \end{aligned} \tag{C.7}$$

As before, the resonant frequency depends on the constant offset δ but now applying a controllable B -field we can tune the frequency f_1 . Therefore, once we include feedback to maintain $f_{\text{laser}} = f_1$ then the tunability gives a knob for dynamically varying the laser frequency.

Note that the above case has only been considered for a simple two-level system, $m_1 = m_2 = m$. Physical systems can simulate this case if the light polarization is well determined. However, non-pure polarization can result in coupling to additional Zeeman sub-levels and may lead to "crossover" resonances.

Appendix D

Repair of 922 Lynx master

In early February 2017, the piezo actuator on the 922 shorted. I suspect it just got old or the Sacher driver killed it but whatever the cause we ordered a new one from Sacher (also ordered a spare which I put in the blue and beige cabinet in the Neutral lab). As of March 1st 2017 it seems that the 922 master is back up and running without issue.

The images below are how I changed the PZT. There was originally some more epoxy around the brass cup but Tom chipped that away so we could unscrew the cup from the flexure arm, this is what holds the PZT. The only other tricky part is removing the back circuit board to get access to the spring terminals that face down. Once you get access here replacing the PZT is fairly trivial.

I also include, at the end, a letter we received from Sacher once they sent us the new PZTs.

Exchanging the Piezo Actuator (PZT)

Purpose of this document is to support users of Sacher Lasertechnik Littrow Laser System with the exchange of the piezo actuator (PZT). Please note that there are security risks for the technician who performs the work as well as for the laser head accompanied with the exchange of the PZT.

- You are working with a Class IIIB laser system. Make sure to wear protective eyewear.
- The PZT is operated with high voltage up to 150V. Make sure to disconnect the laser system from the wall plug power supply prior to any action.
- Consult your security officer on all required security precautions prior to starting the scheduled exchange work.
- Laser Diodes are electrostatic discharge (ESD) sensitive devices. Make sure to take care on ESD protection, e.g. grounded wrist bands.
- The grating attached on the other side of the holder is a sensitive component which may be damaged by a single finger print.
- Avoid electrical short circuits of the piezo cables with the body of the laser head. A single electrical discharge may damage the laser diode.
- Avoid damages of PZT cables by holder's edges.

The customer should keep in mind that she/he are doing the exchange work at their own risk. Sacher Lasertechnik will not be liable in case of any damage to the laser system or any injury to the operating technician.

The holder is composed of diffraction grating, piezo actuator, brass-screw and coarse tuning screw (Figure 1). PZT shall be exchanged in the following procedure:

1. Unscrew the brass-screw (the yellow one) from the holder (Figure 2). You will find the PZT attached with glue within the holder.
2. Detach carefully the PZT from the holder (for example, by slightly waggling PZT from each side).
3. Remove the PZT from the holder (Figure 3).

For exchanging the PZT proceeds in the reverse order.

4. Put the new PZT and attach the front side of the PZT on the holder (using glue).
The back side of the PZT has a small metal-plate attached to it to avoid damage caused by the coarse tuning screw.
5. Screw the brass-screw in.
6. Turn the coarse tuning screw a little bit to confirm the contact of the screw with the PZT.



Figure 1



Figure 2



Figure 3

Document: C:\Dokumente und Einstellungen\icksoon.park\SLT_Arbeits\Tech-Dokus\Exchanging Piezo.doc
Note: Specification are subject to change without further notice



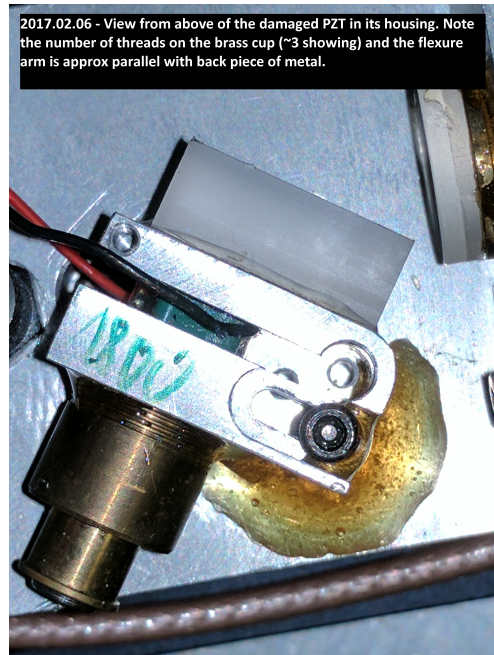


Figure D.1 : Damaged 922 master PZT

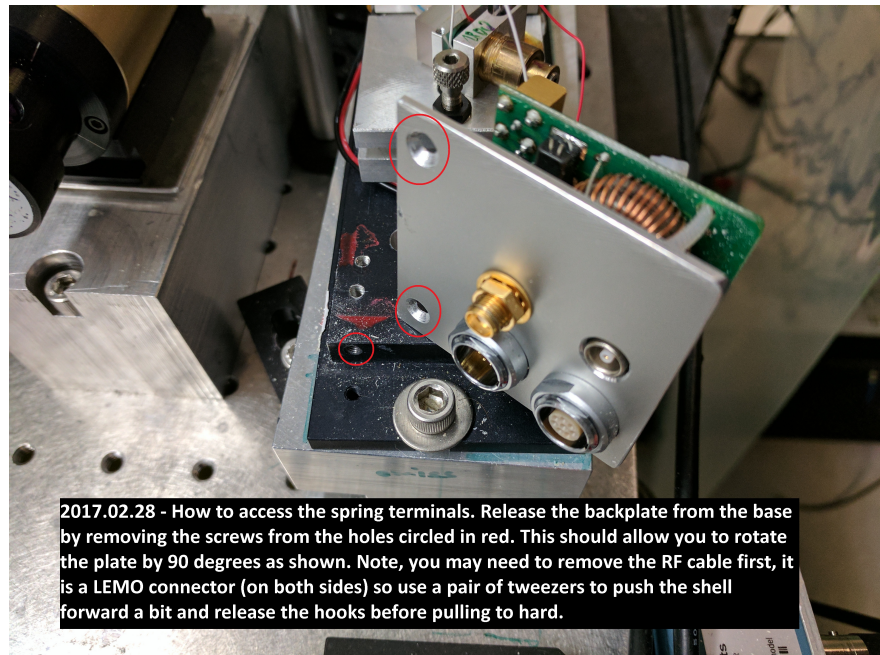


Figure D.2 : Removing the circuit board of the 922 master



Figure D.3 : Newly installed 922 master PZT

Appendix E

Recent changes to the vacuum system

In the following sections, we give some reference data for when the vacuum system was open at the end of 2017. The thermocouple measurements and such are printouts from the OneNote section "Vacuum chamber".

E.1 Nozzle redesign - nuiNozzle 2018

During the downtime from breaking vacuum, we attempted to redesign our atom nozzle to include a heat shield. A CAD image is shown in figure. Unfortunately, due to the high tolerances of the base flange and surrounding enclosure the machining required for this custom piece was deemed prohibitively expensive. A prototype was designed following the machine drawings available in `Drobo:\Neutral\Laboratory Systems\Vacuum Chamber\2017 - Nozzle Redesign - NUI nozzle` but was abandoned due to a bend that developed in the tubing which holds the fire rod.

In addition to the heat shield, we also attempted to incorporate a design feature from Plasma's nozzle redesign which addressed the fragility of the feedthrough connection to the heater wire. This was a problem because the heater wire connection is very thin and we used large clamp type connection for them before which was problematic due to the fragility of the heater wire and the necessity that the bulky clamp couldn't touch the nozzle body (as this would short the heater connection). The new connection would allow us to use a smaller crimp to the heater wire, use the rigidity

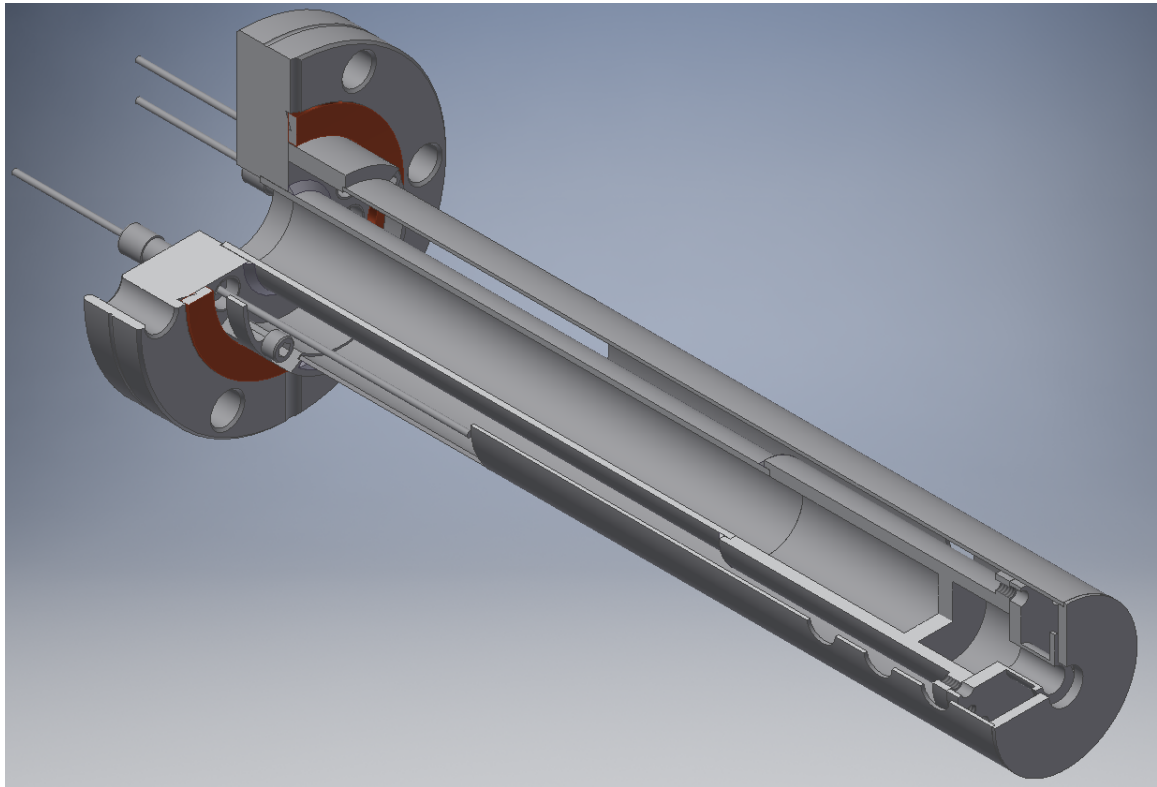


Figure E.1 : nuiNozzle Neutral strontium oven

of the feedthrough itself, and use alumina screws to insulate the connection from the nozzle body.

Finally, I had some trouble finding the part number associated with the firerod in the Neutral chamber but luckily I found one of the broken firerods still had it's part number on it, SK7J-2953. Below is the info from Valin Corporation who seems to be the local reseller of Watlow products.

SPECIAL DIAMETER

HT FIREROD

T/C CENTER CORE LOC \A" TYPE \J"

120 Volts

240 watts

0.580 +/- 0.004 Diameter firerod

7.5" length

12" of MGT leads

12" of TC leads

6 13/32" of no heat section at lead end.

Crimped of leads construction.

E.2 Opening vacuum - data and setup

VACUUM - 2017.11 - Activity reference

Thursday, November 09, 2017 2:40 PM

Today we moved the RGA and turbo pump back onto the system and began pumping. Below I will try to keep a record of pressure and things that we do. Use this sheet as a master reference and if further pictures or extensive notes need to be taken, create a subpage and put the link in the table below.

Date	Time (24 hr)	Action	Gauge read	Pressure [Torr]	Notes																											
2017.11.09	1400	Started scroll pump		760	Dry pump is going without turbo, pressure in pumping tee is steadily going down																											
2017.11.09	1445	Checked pressure	Gauge on scroll pump cross	6.4e-2																												
	1518	Checked pressure	Gauge on scroll pump cross	4.6e-2	Going to turn on the turbo now																											
	1528	Spun up turbo	Gauge on scroll pump cross	1.8e-1	Turbo is fully on and valve to scroll pump is fully open. Will leave to pump and check periodically																											
	1541	Checked ion gauge	RGA ion gauge	1.2e-5																												
2017.11.10	1202	Check pressure	Gauge on scroll cross	2.0e-2																												
	1207	Check ion gauge	RGA ion gauge	1e-6	Ion gauge read 5 min after turning it on when it seemed to have settled																											
	1945	Check pressure	Gauge near scroll cross	1.9e-2																												
	1948	Check ion gauge	RGA ion gauge	8e-7	5 min after turn on																											
2017.11.13	1337	Checked pressure	Gauge near scroll cross	1.5e-2	Turned on ion gauge, letting it settle now																											
	1420	Checked ion gauge	RGA ion gauge	1.5e-7																												
	~1600	Opened bellows valve			Tom wanted to start pumping on the bellows near the source																											
2017.11.14	1313	Checked pressure	Gauge near scroll cross	1.4e-2	Turned on ion gauge																											
	1327	Checked ion gauge	RGA ion gauge	1.1e-7	Degassed ion gauge twice for 30s each, then let it settle for ~5 min																											
2017.11.15	1538	Checked ion gauge	RGA ion gauge	5.4e-8	Degassed ion gauge twice and let it settle. Still pumping on bellows and cross with RGA																											
2017.11.17	1636	Check pressure	Near scroll	1.3e-2	Turned on ion gauge																											
	1703	Checked ion gauge pres.	RGA ion gauge	4.3e-8	Degassed ion gauge three times and let it settle																											
2017.11.20	1638	Checked io gauge press	Near turbo	4e-8	Degassed once																											
2017.12.19	1530	Started turbo and scroll			Replaced the Sr in the nozzle and the zeeman window. Chamber was back filled with dry nitrogen preceded by an LN2 trap. Pumping now to see if pressure can get low enough to turn on the RGA																											
	1800	Checked Pressure	Near scroll	1.2e-2																												
			Chamber ion gauge	9.7e-6	After 5 min warmup																											
2017.12.20	1005	Checked pressure	Near scroll	1.1e-2																												
			Chamber ion gauge	8.5e-7	Degassed for 30s once, let settle for 20min																											
	1357	Checked pressure and turned on firerod	Chamber ion gauge	7e-7	Running 200mA through nozzle heater the nozzle thermocouple was at 166°C and the firerod thermocouple was at 168°C.																											
	1409	Turned off chamber ion gauge	Chamber ion gauge	5e-5	Turning on the nozzle started a lot of outgassing and the chamber ion gauge pressure was getting high so we turned it off to save the filament. Firerod is still heating up.																											
	1417	Reduced firerod variac			Tom was concerned about heating the nozzle too much so we backed off the firerod variac from 40% to 35%																											
	1702	Reading nozzle heaters			Firerod TC settled at 618°C and nozzle TC at 378°C																											
	1734	Check pressure	Chamber ion gauge	1e-5																												
			Scroll gauge	1.1e-2	Flicking between 1.1e-2 and 1.3e-2 Leaving the nozzle heaters on overnight to bake out the nozzle																											
2017.12.21	1039				Firerod TC still stable at 612°C and nozzle TC at 376°C																											
	1100	Checked pressure	Near scroll	1e-2																												
			Chamber ion gauge	6.9e-7	Warmed up for about 20 min (pressure going down consistently). Saw 6.9e-7 then degassed for 30s, pressure quickly got back into the 7.5e-7 range and is now slowly going back down																											
	1105	Turned on gauge	RGA ion gauge	5e-6	Initial pressure when enabling emission. Degassed twice and the pressure is dropping. Going to wait and few minutes and let the reading settle.																											
	1125	Checked pressure	RGA ion gauge	4.1e-7																												
	1127	Turned no ion gauge	Source ion gauge	4e-6	Initial pressure, degassed twice for 30s. Letting the pressure settle now																											
	1145	Checked pressure	Source ion gauge	1.9e-6																												
	1216	Flashing Ti Sub			Watched source ion gauge. Did 3 cycles of flashing using 35A for 1 min with 3 min period. Below are the highest and lowest pressures seen for the first three cycles.																											
					<table border="1"> <thead> <tr> <th>Cycle</th><th>Fil #2</th><th>Fil #3</th></tr> </thead> <tbody> <tr> <td>1</td><td>High</td><td>3e-5</td></tr> <tr> <td>1</td><td>Low</td><td>6.8e-7</td></tr> <tr> <td>2</td><td>High</td><td>2.6e-6</td></tr> <tr> <td>2</td><td>Low</td><td>6.2e-7</td></tr> <tr> <td>3</td><td>High</td><td>3e-6</td></tr> <tr> <td>3</td><td>Low</td><td>6.5e-7</td></tr> <tr> <td></td><td></td><td>4.5e-7</td></tr> </tbody> </table>	Cycle	Fil #2	Fil #3	1	High	3e-5	1	Low	6.8e-7	2	High	2.6e-6	2	Low	6.2e-7	3	High	3e-6	3	Low	6.5e-7			4.5e-7			
Cycle	Fil #2	Fil #3																														
1	High	3e-5																														
1	Low	6.8e-7																														
2	High	2.6e-6																														
2	Low	6.2e-7																														
3	High	3e-6																														
3	Low	6.5e-7																														
		4.5e-7																														
2017.12.22	1127	Checked pressure	Chamber ion gauge	3.4e-7	Degassed 1x for 30s																											
	1130	Ti Sub cycling			Started Ti sub cycling and watched chamber ion gauge for pressure Did 6 cycles using 35A for 1 min with a 3 min period. Below are the highest and lowest pressures seen for these cycles																											
					<table border="1"> <thead> <tr> <th>Cycle</th><th>Fil #2</th><th>Fil #3</th></tr> </thead> <tbody> <tr> <td>1</td><td>High</td><td>8.6e-6</td></tr> <tr> <td>1</td><td>Low</td><td>1.7e-7</td></tr> <tr> <td>2</td><td>High</td><td>1.8e-6</td></tr> <tr> <td>2</td><td>Low</td><td>1.8e-7</td></tr> <tr> <td>3</td><td>High</td><td>1.7e-6</td></tr> <tr> <td>3</td><td>Low</td><td>2e-7</td></tr> <tr> <td>4</td><td>High</td><td>1.7e-6</td></tr> <tr> <td></td><td></td><td>6.6e-7</td></tr> </tbody> </table>	Cycle	Fil #2	Fil #3	1	High	8.6e-6	1	Low	1.7e-7	2	High	1.8e-6	2	Low	1.8e-7	3	High	1.7e-6	3	Low	2e-7	4	High	1.7e-6			6.6e-7
Cycle	Fil #2	Fil #3																														
1	High	8.6e-6																														
1	Low	1.7e-7																														
2	High	1.8e-6																														
2	Low	1.8e-7																														
3	High	1.7e-6																														
3	Low	2e-7																														
4	High	1.7e-6																														
		6.6e-7																														

					4	Low	2.3e-7	1.7e-7
					5	High	1.6e-6	6e-7
					5	Low	2.7e-7	1.8e-7
					6	High	1.6e-6	5.3e-7
					6	Low	1.3e-7	1e-7
1358	Ti sub cycling				Stopped watching the pressure on every cycle and instead switching between the 2 filaments in 20min intervals			
	Checked pressure	Chamber ion gauge	4.7e-8					
1613	Checked pressure	RGA ion gauge	1.3e-7		After 10 min settle and degassing 2x for 30s			
1616	Plugged in source ion				1x degas for 30s and let settle			
1619	Switched Ti sub filament				Turned off #3, #2 on			
1645	Checked pressure	Source ion gauge	1.1e-6					
1700	Started heaters				Grouped heaters by similar resistances at 20% of total			
1745	Check temps				Spot checking of TC showed most about 45'C Increased variacs to ~35% values (these are the values shown in 2017.12.22 - Heater setting #1)			
1810	Checked pressure	Source ion gauge	3e-6					
1835	Checked pressure	Chamber ion gauge	1.3e-7					
1845	Checked pressure	RGA ion gauge	6e-7					
1911	RGA scans				Picture on page "RGA spectra"			
2017.12.23	1342	RGA scans			Picture on page "RGA spectra"			
	1444	Checked pressures	Source ion gauge	8.1e-7				
			Chamber ion gauge	2.4e-7				
			RGA ion gauge	1.9e-7				
1515	Ti sub cycling				Started cycling between filaments in 20min intervals. Started with filament #2			
1522	Check temps				Link to thermocouple readings			
2017.12.24	NA				Did not record activity on these days :/			
2017.12.25	NA				Did not record activity on these days :/			
2017.12.26	1110	Check temps			Link to thermocouple readings			
	1211	Checked pressure	Source ion gauge	1.9e-7				
	1305	Checked pressure	Chamber ion gauge	8.5e-8				
	1346	Checked pressure	RGA ion gauge	6.4e-8				
	1349	Ti sub cycling			Started cycling filaments for 30min intervals using 35A for 1 min with 3 min period			
	1420	Ti sub cycling			#2 off, #3 on			
	1453	Ti sub cycling			#3 off, #2 on Switching to 1 hour intervals			
	1554	Ti sub cycling			#2 off, #3 on			
	1655	Ti sub cycling			#3 off, #2 on			
		Checked pressure	Chamber ion gauge	4e-7				
	1702	RGA scans			Picture on page "RGA spectra"			
	1758	Ti sub cycling			#2 off, #3 on			
	1836	Ti sub cycling			Stopped cycling to leave for the day			
2017.12.27	0936	Checked pressure	Chamber ion gauge	8e-9	Initial reading 4.6e-8, degassed 2x for 30s then let settle for 5 min to get 8e-9. After another 5 min there was a sudden increase to 8.5e-9			
	1008		Chamber ion gauge	8e-9	Pressure still increasing back up to 9.4e-9. Degassed once for 30s and let settle for 6 min before reaching 8e-9 again.			
	1058	Checked pressure	RGA ion gauge	2.7e-8	Degassed for once 30s			
	1135	Checked pressure	Source ion	1e-7	Degassed 2x for 30s			
		Ti sub cycling			Turned on Ti sub using 35A for 1 min with 3 min period on fil #2			
	1152	Check temp			Link to thermocouple readings			
	1239	Ti sub cycling			#2 off, #3 on			
	1346	Ti sub cycling			#3 off, #2 on			
	1449	Ti sub cycling			#2 off, #3 on			
	1550	Ti sub cycling			#3 off, #2 on Noticed the @2 tend to run @ 5.1V and #3 runs at ~3V. Also on the first run of #2 when cycling, the pressure readings tend to shoot up. Perhaps this indicates that #2 is dirtier than #3?			
	1557	RGA Scans			Picture on page "RGA spectra"			
	1648	Ti sub cycling			#2 off, #3 on			
	1709	Check pressure	Source ion gauge	2.5e-7				
	1726	Check pressure	Chamber ion gauge	1.7e-7				
	1743	Ti sub cycling			Stopped cycling protocol			
		Check pressure	RGA ion gauge	1.5e-7				
	1838	Check pressure	RGA ion gauge	2.3e-8				
	1852	Check pressure	Chamber ion gauge	5.6e-9				
2017.12.28	1237	Check temps			Link to thermocouple readings			
	1258	Check pressure	RGA ion gauge	2.2e-8	Degass 3x for 30s. Each time I saw the pressure shoot up to ~1.5e-7 after turning off degassing protocol. The pressure reading then dropped lower than previous reading after about 2 min. Forgot to note this yesterday but I did check that we are still not being limited by back streaming from the turbo. I checked this by closing the gate valve to the system and watching the pressure on the RGA ion gauge fall quickly to about 1e-8. It looked as if the reading would keep going down slowly but I reopened the valve to allow the system to keep pumping.			
	1312	Check pressure	Chamber ion gauge	5e-9	Degassed 2x for 30s			
	1316	Check rpressure	Source ion gauge	8.7e-8	Degassed 2x for 30s			
	1330	Ti sub cycling			Started Ti sub cycling protocol on Fil #3 using 35A for 1 min with 3 min period. Going for 1 hour intervals on each filament			

	1351	RGA scans		Picture on page "RGA spectra"	Saw some weird noise on the baseline that might have been due to having the Ti sub on while running the scans
	1430	Ti sub cycling			#3 off, #2 on
	1530	Ti sub cycling			#2 off, #3 on
	1630	Ti sub cycling			#3 off, #2 on
	1730	Ti sub cycling			#2 off. Stopped protocol
	1810	Check pressure	Chamber ion gauge	7.8e-9	
2017.12.29	1022	Check pressure	Chamber ion gauge	3.5e-9	After degassing 2x for 30s and let settle but then pressure went back up to 4.5e-9. I degassed once more and saw 3.5e-9 after about 5 min.
	1112	RGA scans			Picture on page "RGA spectra"
	1146	Check pressure	Source ion gauge	9e-8	Degassed 1x for 30s and pressure only came down slowly to about 8.7e-8
	1200	Check pressure	RGA ion gauge	2e-8	Degassed 2x for 30s and pressure settled after about 5 min.
		Ti sub cycling			Starting cycling protocol on fil #3 using 35A for 1 min with 3 min period and 1 hour intervals.
	1218	Check temps			Link to thermocouple readings
	1252	Increase temps			After finally getting all of my documentation squared away I was able to see that the tower heat has been consistently low. I am going to try increasing the H2 and H3 variacs to around 50V. This will be referred to as 2017.12.29 - Heater settings #2 H2 will go from 36V (30% of max) to 50V (42% of max) H3 will go from 42V (30% of max) to 50V (36% of max) • Note the different percentages are because the maxes are different between the variacs
	1303	Ti sub cycling			#3 off, #2 on
	1400				#2 off, #3 on
	1513				#3 off, #2 on
	1522	Check temps			Link to thermocouple readings
	1604	Ti sub cycling			#2 off, #3 on
	1658	RGA scans			Picture on page "RGA spectra"
					Wanted to check if the increased temperatures significantly increased the gas load in the chamber. There doesn't seem to be much impact except for hydrogen but the Ti sub is also cycling.
	1707	Ti Sub cycling			#3 off, #2 on
	1749	Check temps			Link to thermocouple readings
	1816	Ti sub cycling			#2 off. Stopped cycling for the evening
	1826	Check pressure	RGA ion gauge	6.8e-8	Degassed 2x 30s and let settle for 7 min Would likely have gone lower as it seemed to be steadily decreasing but degassing did not speed up the process so I moved on
	1836	Check pressure	Chamber ion gauge	3.4e-8	Degassed 2x 30s and let settle for 7 min Increase in pressure is likely due to increasing the temperature on the tower. Will need to let things pump for a little while to see if it comes back down.
2017.12.30	1852	Check temps			
	1930	Check pressure	Chamber ion gauge	5e-9	Bumping the cable changes the pressure reading. Not sure what to make of that
	1933	RGA scans			Picture on page "RGA spectra"
2017.12.31	NA				Didn't take data these days
2018.01.01	NA				Didn't take data these days
2018.01.02	0927	RGA scans			Picture on page "RGA spectra"
	0933	Check temps			Link to thermocouple readings
	0939	Check pressure	Chamber ion gauge	6.0e-9	Degassed 2x for 30s and let settle for 10 min.
	1150	Burp ion Pump	Chamber side ion pump		Chamber side ion pump (black wire, not silver). Turned on this ion pump and the pressure jumped to ~10^-6 Torr briefly. Pump controller made some coughing or clicking noises that may have been it changing ranges. Repeated this on/off cycle two more times. By the third time it was happy at ~2*10^-7 Torr, with a slowly decreasing pressure.
	1155	Check pressure	Source ion gauge	9.4e-8	Before burping the source side ion pump
	1156	Burp ion pump	Source side large ion pump		Watching the source side ion gauge, • first burp of the source side large ion pump for about 5s. Pressure went up to 1e-5. After about 2 min ion gauge read into the mid -7's. • Burping ion pump again for about 15s pressure went up into the -6's then started to come back down. • Third burp after about 2 min for about 15s. Pressure went up into the low -6's before coming back down to 3.4e-7 after 2min • Fourth burp. Pressure went up to high -7's. Leaving ion pump on and the pressure is slowly starting to come down. Left on for about 45s.
	1202	Burp ion pump	Source side small ion pump		Watching source side ion gauge (after burping the large ion pump) • First burp -
	1230	Burp ion pumps			Initial attempts to turn on the ion pump were not successful. At this point we are unsure why. Continued burping both the large ion pumps on the chamber side and source side and watching the pressure on the source ion gauge. Eventually we saw that the ion pumps were not increasing the pressure substantially when they were turned on. We verified they were pumping by watching the pressure stabilize when closing of the gate valve to the turbo. Then we turned off the ion pumps and closed the valve again and saw the pressure only increase.
	1233	Ti sub cycling			Began cycling ti sub using 35A for 1 min with 3 min period. Cycled fil #2 three times and switched to fil #3 for three cycles as well. Watched pressure at the source ion gauge • Fil #2 - high 3e-7 on first cycle • Fil #3 - high: 2e-7 on first cycle Both filaments brought the pressure down to ~8e-7 after a couple cycles
	1249	Turned off all four heaters			
	1256	Check pressure	Source ion gauge	4e-8	After degassing once for 30s
	1746	RGA scans			
	1747	Check pressure	Chamber ion gauge	7.6e-10	That's not a mistake!! We're coming down folks! Pressure is going down nicely after turning off the heaters. Currently the turbo is the only thing pumping on the system. We burped the ion pumps earlier but have them off right now. -
2018.01.03	1200				Turned on ion pumps and left them on. Chamber side pump at 0.1×10^{-9} 0.2uA, Source side is at 3.6×10^{-9} and current of 3.6uA.
2018.01.04	1000				Tightened metal valve to 68 in lbs and turned off the turbo. Currently the chamber side is still 0.1×10^{-9} Torr and 0.2uA and source side is at 2.4×10^{-9} Torr at 2.4uA.

2018.02.01	1600	Filled cryo pump with LN2		Took a lifetime before filling the cryo Picture on page "2018.01.31" and saw a 12-13 second lifetime After filling the cryo pump and flashing the ti sub we took another lifetime Picture on page "2018.02.02" and extended the lifetime to about 15 s
2018.02.06	1100	Checked lifetime		Checked lifetime after letting everything equilibrate over the weekend. Also took some loading curves to see how things are doing for 88. Picture on page "2018.02.05 - Characterizing 88 trapping" Still see a roughly 15s lifetime Pressure on the ion pumps is still good chamber one is bottomed out at 0.2uA and 0.1e-9. The source ion pump is varying a bit usually around 7e-9 but I've seen it go up to 2e-8

Heater and thermocouple setup

Wednesday, December 27, 2017 6:48 PM

Heater details

Heaters were grouped by approximately similar resistances. To see which thermocouples are closest refer to the hyperlink in the location column to jump to the pictures showing the thermocouple and heating band placements.

Cable Number	Description	Measured Resistance [Ohms]	Heater group	Location
9 & 10	Combined cable which connects to both the bottom and middle heater bands near the metal valve	72	H1	Figure 4 - Left view
21	Source chamber, right side connection to 6" tee	76	H1	Figure 3
27	4 connections in parallel to the heating wraps around the upper arms of the 2D collimator	51	H1	Figure 1 & Figure 2
28	3 connections in parallel to the heating wraps around the lower arms of the 2D collimator	70	H1	Figure 1 & Figure 2
29	Heating wrap around the bottom of the 6" tee to the right of the source chamber	54	H1	Figure 3
6	Chamber to tower connection	291	H2	Figure 4 - Right view
11	Top of metal valve	377	H2	Figure 4 - Left view
30	Laser input of 2D collimator	160	H2	Figure 1
31	2D collimator input connection to the 6-way cross of the 2D collimator	292	H2	Figure 1
33	90' elbow connection to tower	144	H2	Figure 4 - Left view
2	Top nipple connection of tower	56	H3	Figure 4
3	Band around upper mid part of tower	76	H3	Figure 4
4	Tower to ion pump connection	76	H3	Figure 4 - Left view
5	Self heater of chamber side ion pump	59	H3	Figure 4 - Left view
7	Band around bottom mid part of tower	59	H3	Figure 4
13	Bottom flange connection of tower	78	H3	Figure 4
16	Source side, large ion pump self heater	100	H4	Figure 3
20	Left viewport connection on source chamber	76	H4	Figure 3
22	Top connection of 2 3/4 tee above source to angle valve	300	H4	Figure 2 & Figure 3
23	Bottom connection of 2 3/4 tee above source to source chamber	145	H4	Figure 2 & Figure 3
25	Source side, small ion pump self heater	102	H4	Figure 2
24	Heater wire around source chamber body (thin white cable visible around oven flange)	11		Not used
				Not shown

Thermocouple details

Label	Description	Location
GB	2D collimator input viewport	Figure 1
GH	Source side of zeeman slower tube	Figure 2
GT	Nipple on top of tower	Figure 4
GP	Nipple connection to tower	Figure 4
GY	Upper part of tower body	Figure 4
GR	Connection to chamber side ion pump	Figure 4 - Left view
GQ	Connection between tower and chamber	Figure 4 - Right view
GW	Body of all metal valve	Figure 4 - Left view
GX	Middle body of elbow extension	Figure 4 - Left view
BA	2D collimator, upper right viewport	Figure 1
BB	2D collimator, upper left viewport	Figure 1 & Figure 2
BC	2D collimator, lower left viewport	Figure 1 & Figure 2
RA	Top of source side 6" tee	Figure 3
RB	Right side of source side 6" tee (fell off after a couple days)	
RC	Middle of the 2 3/4 tee on top of the source chamber	Figure 2 & Figure 3
RD	Source side, large ion pump, internal thermocouple	Figure 3
RE	Connection between 6" tee and source side large ion pump	Figure 3
RF	Left side of source side 6" tee	Figure 3
YA	Source side, small ion pump, internal thermocouple	Figure 1 & Figure 2

Heater and thermocouple positions

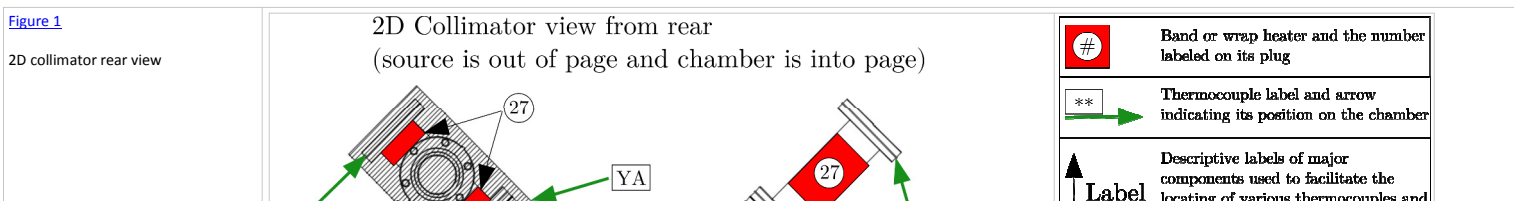
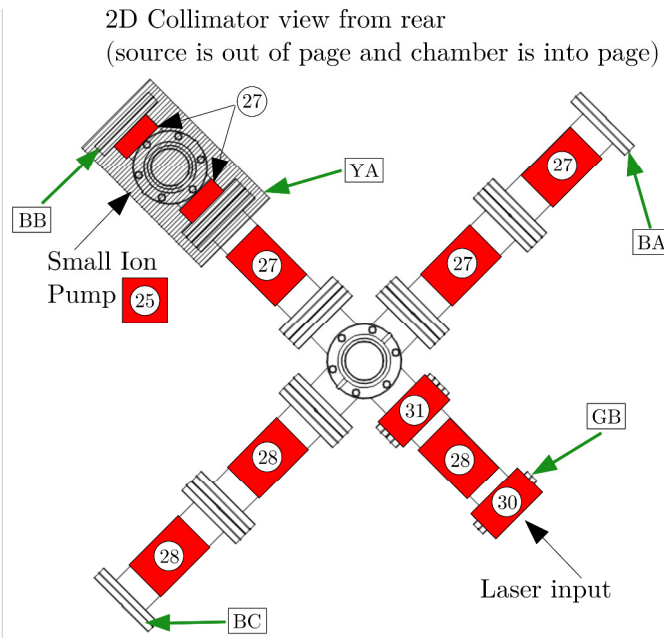


Figure 1

2D collimator rear view



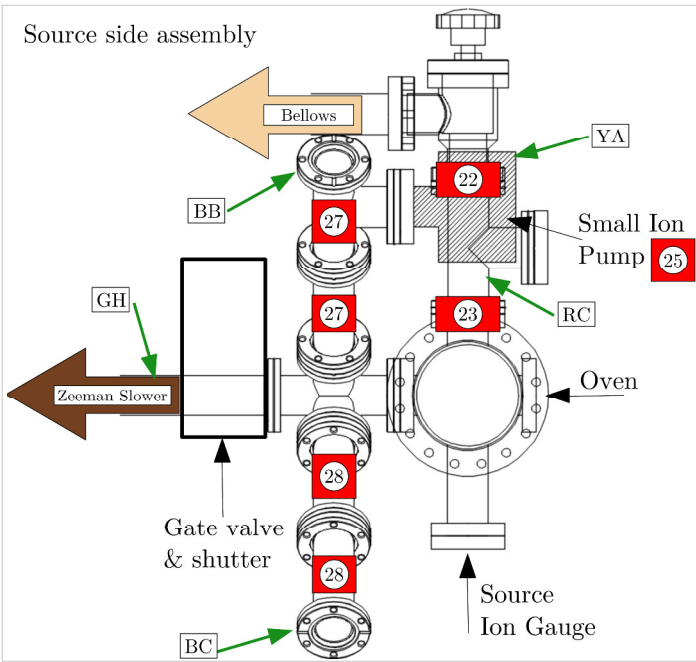
Band or wrap heater and the number labeled on its plug

** Thermocouple label and arrow indicating its position on the chamber

Label Descriptive labels of major components used to facilitate the locating of various thermocouples and heating elements

Figure 2

Source side assembly



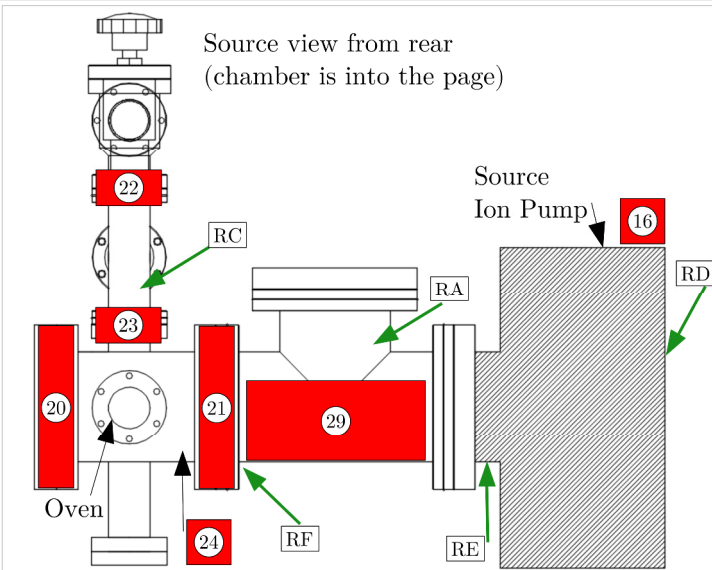
Band or wrap heater and the number labeled on its plug

** Thermocouple label and arrow indicating its position on the chamber

Label Descriptive labels of major components used to facilitate the locating of various thermocouples and heating elements

Figure 3

Source view from rear



Band or wrap heater and the number labeled on its plug

** Thermocouple label and arrow indicating its position on the chamber

Label Descriptive labels of major components used to facilitate the locating of various thermocouples and heating elements

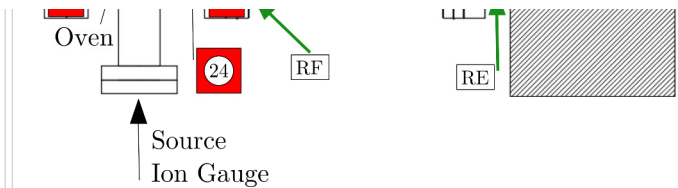
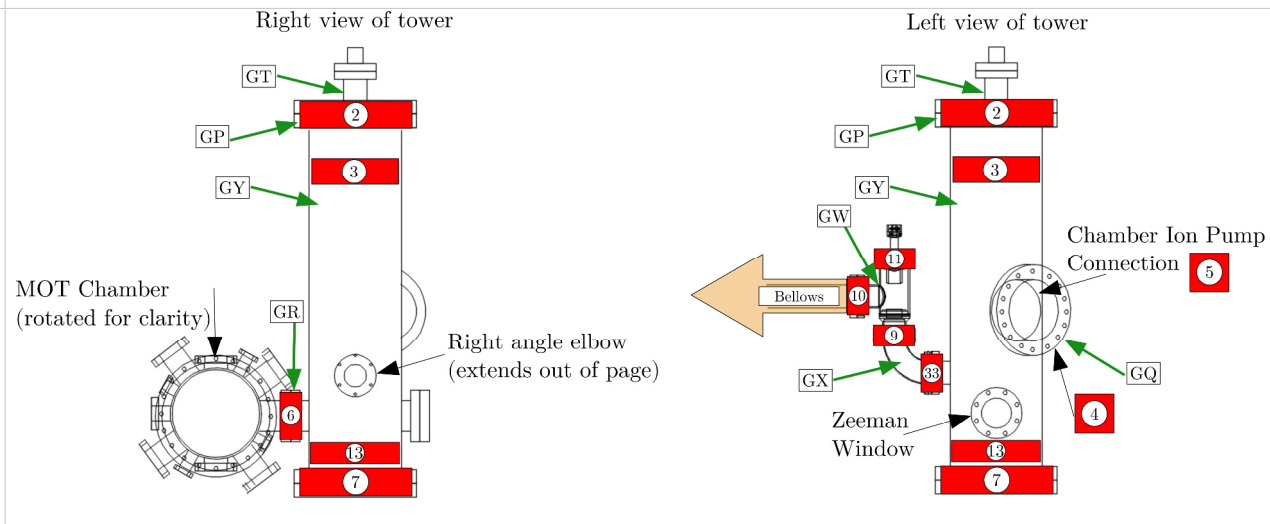


[Figure 4](#)

Cryo-pump and Ti Sub tower



Thermocouple readings

Wednesday, December 27, 2017 6:48 PM

All temperatures are given in **degrees Celsius**

Note: on 2017.12.27, the RB thermocouple fell off which might explain it's wildly different readings across days

Pressure readings

Friday, December 29, 2017 1:04 PM

Pressure history

Below is a reference for the pressure measurements made. It is the same data as in the reference table but gathered here to identify trends. The readings will likely jump up and down as we perform various activities (cycling Ti sub, ending the bake, etc.) but should provide a general trend of the pressure changes at each gauge.

Descriptions of positions of the ion gauges

- RGA ion gauge - the ion gauge on the cross that is connected to the turbo. This ion gauge travels with the pumping station and is not a permanent fixture of the Neutral apparatus
 - Chamber ion gauge - the ion gauge on arm B (the one pointing towards the computer) of the MOT chamber
 - Source ion gauge - the ion gauge directly beneath the oven on the source side of the apparatus

All pressures are given in **Torr** as read from the multi-gauge reader. Refer to the activity reference to see what action was taken when contextualizing the pressure readings.

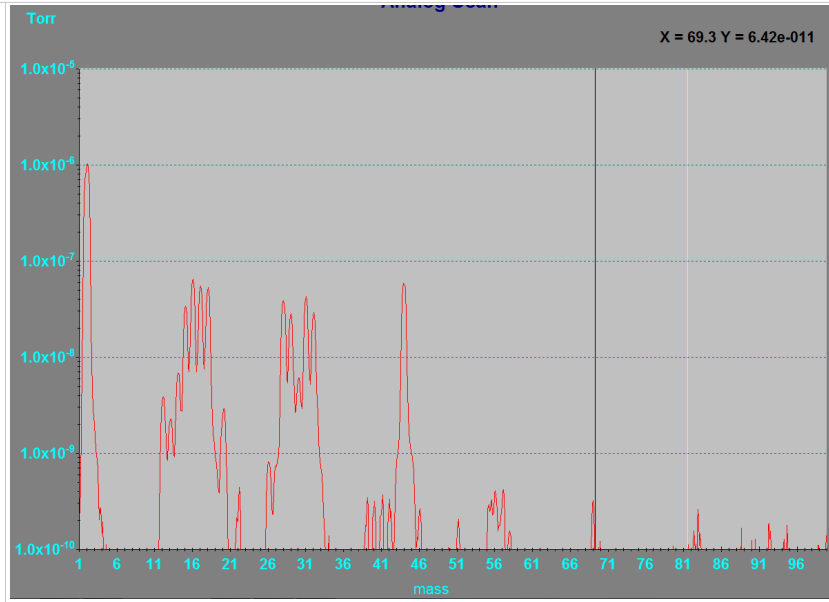
RGA spectra

Thursday, December 21, 2017 2:34 PM

Below I am going to save plots from the RGA and link the individual pictures on the primary vacuum table

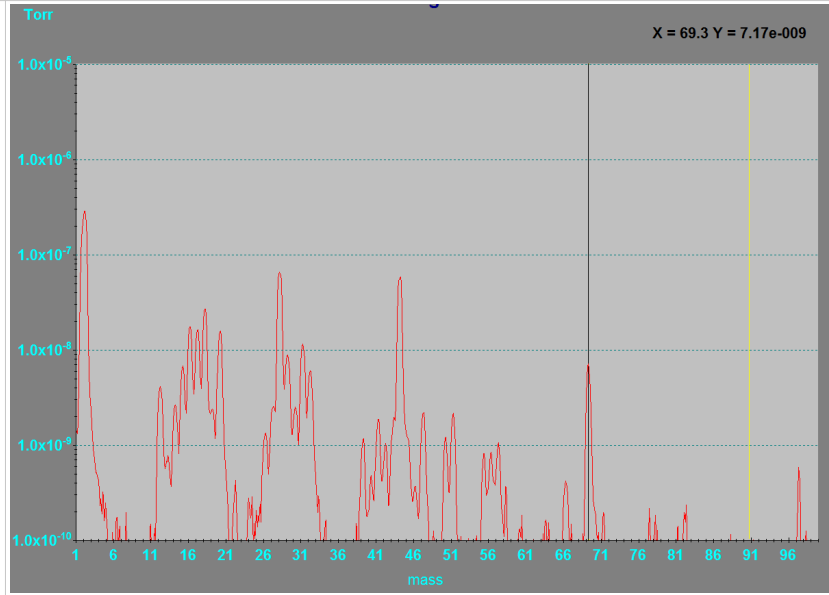
2017.12.22
1911

Day before the bake



2017.12.23
1341

Day 1 into the bake
Taken without electron multiplier



2017.12.24
NA

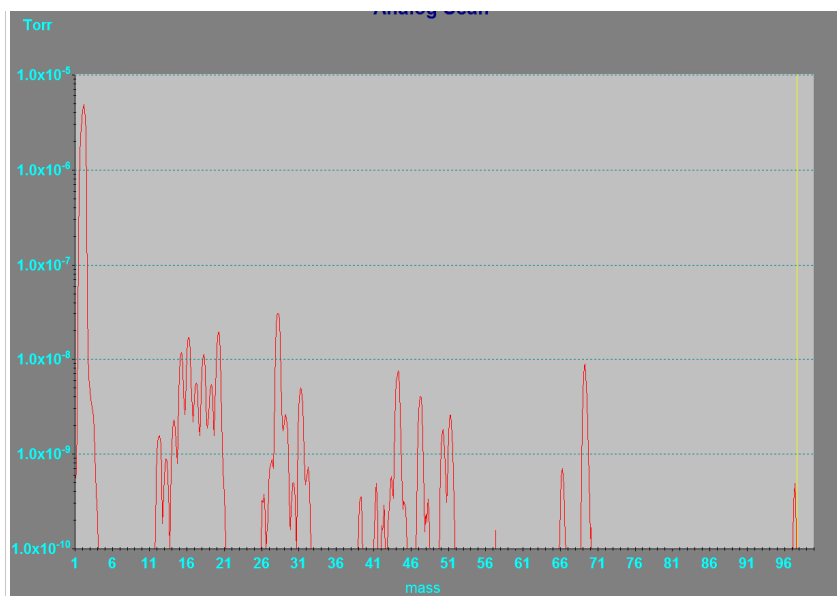
Scan unavailable

2017.12.25
NA

Scan unavailable

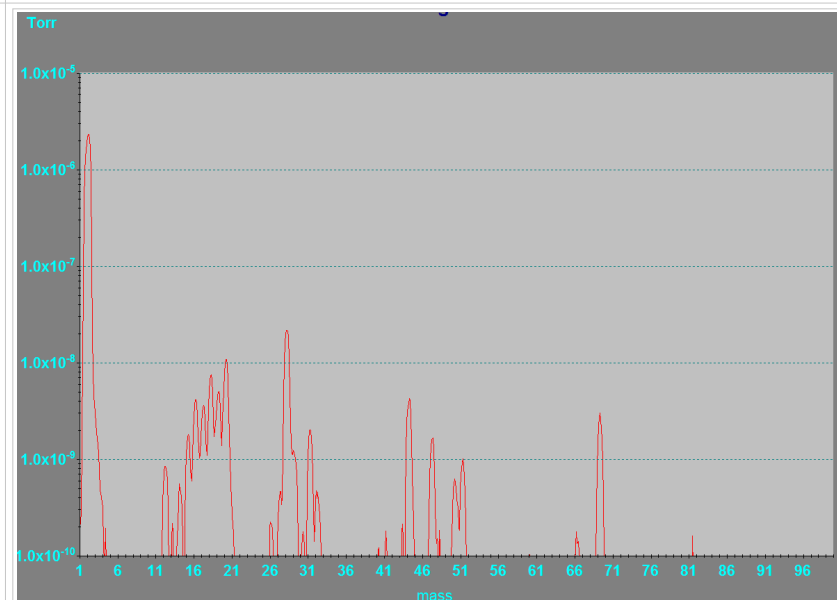
2017.12.26
1702

Day 4 into the bake
Taken without electron multiplier

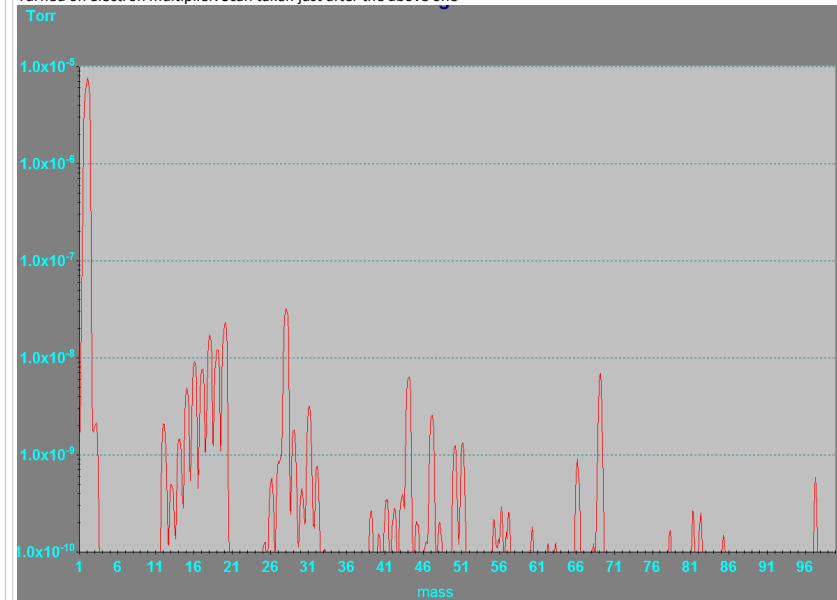


2017.12.27
1557

Day 5 into the bake
First scan taken without electron multiplier, second scan turn it on



Turned on electron multiplier. Scan taken just after the above one

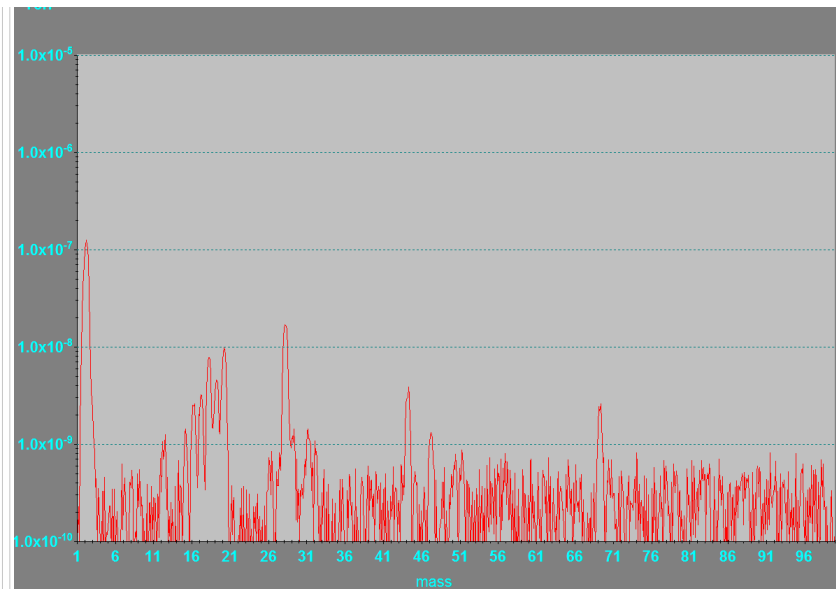


2017.12.28

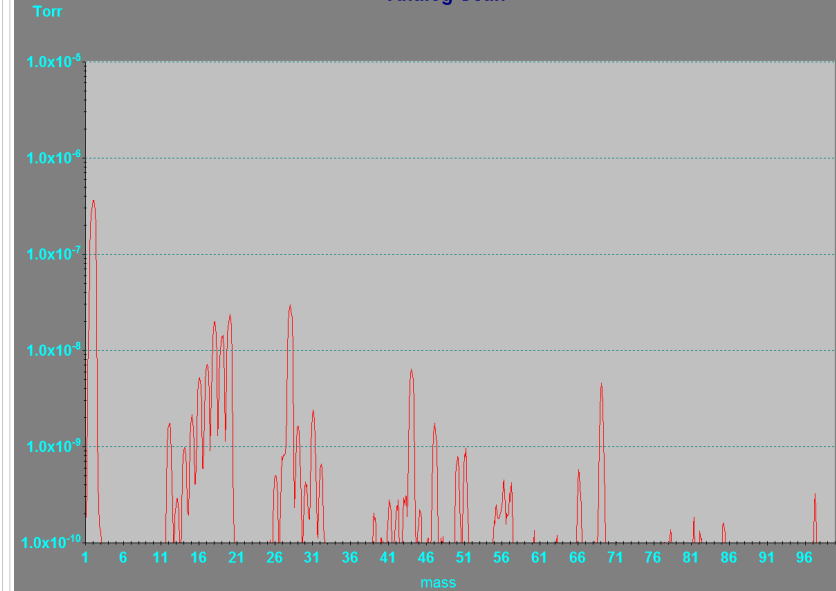
Day 6 into the bake

First scan taken without electron multiplier, second scan turn it on

Not sure why the first scan is so noisy but repeated scans consistently showed this noise. Could be because I had just started cycling the Ti Sub?



Turned on electron multiplier. Scan taken just after the above one



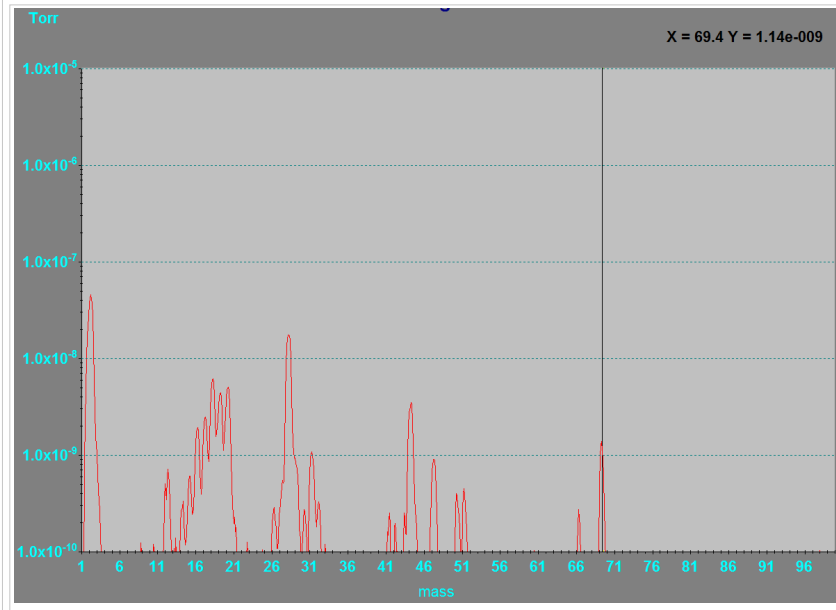
2017.12.29

1112

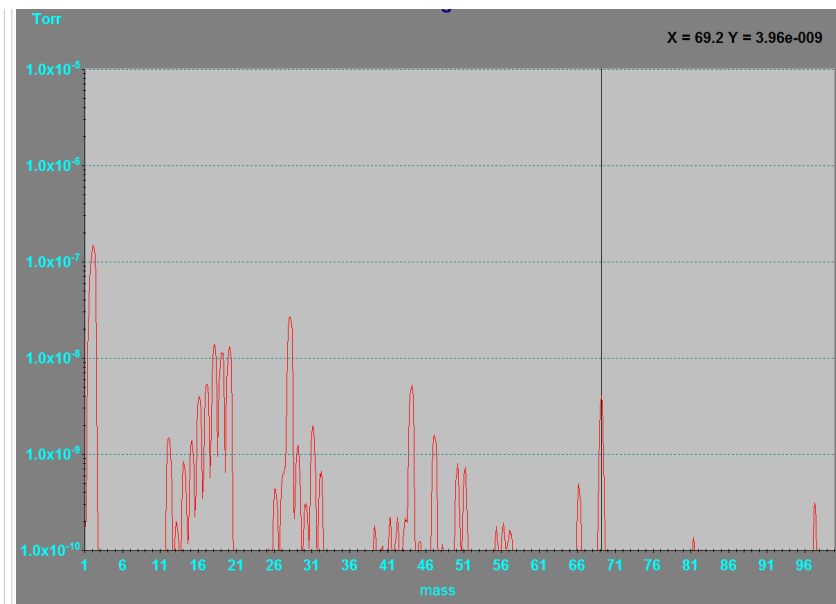
Day 7 into the bake

First scan taken without electron multiplier, second scan turn it on

I think I figured out why the first scan yesterday was so noisy. It seems that if you don't reapply the scan speed setting the scan happens very quickly and this causes a lot of noise with the baseline. I saw this when I took the first scan this morning and noticed the scan happening rapidly. After reapplying the scan parameters of 10 pnts per amu and and speed of 3, I was able to get a nice quiet baseline. So I do not think cycling the Ti Sub has a significant impact on the constituent gases measured in the chamber.

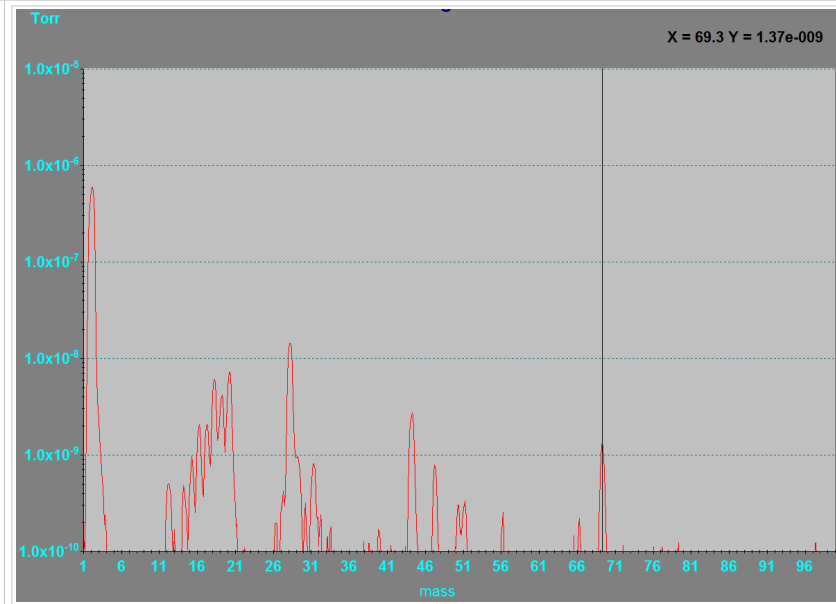


Turned on electron multiplier. Scan taken just after the above one

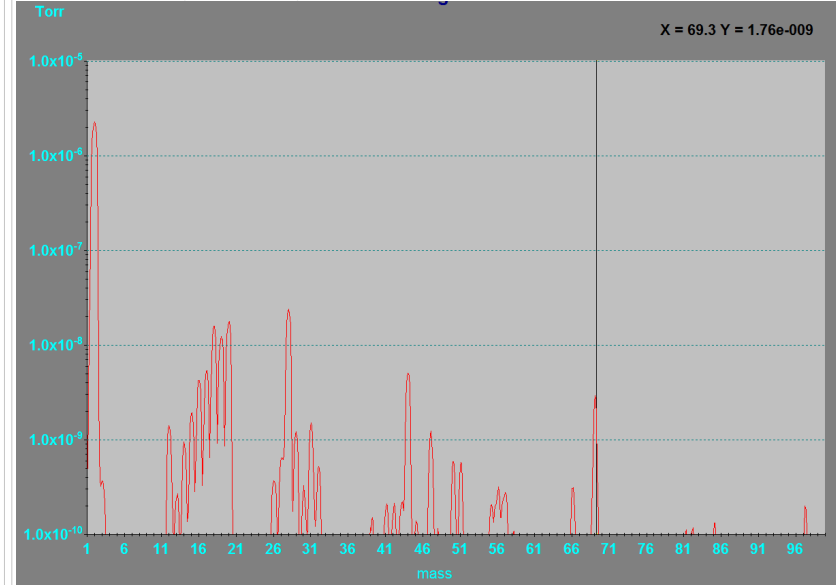


2017.12.29
1658

Day 7 into the bake with Heater settings #2
First scan taken without electron multiplier, second scan turn it on



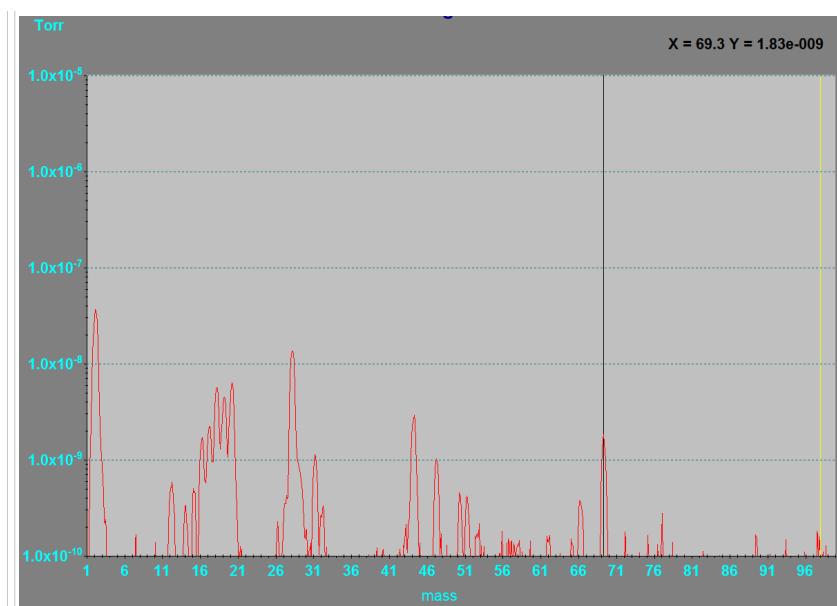
Turned on electron multiplier. Scan taken just after the above one



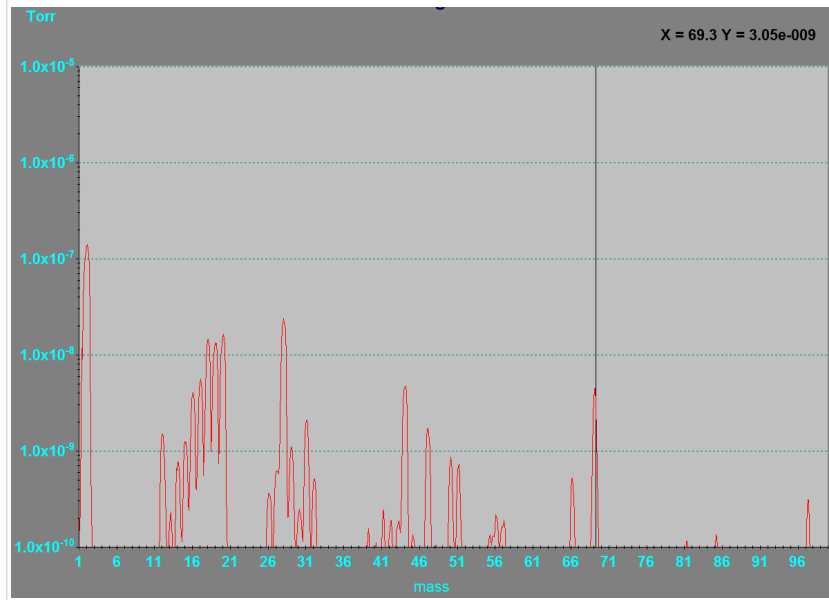
2017.12.30

1933

Day 8 into the bake with Heater settings #2
First scan taken without electron multiplier, second scan turn it on

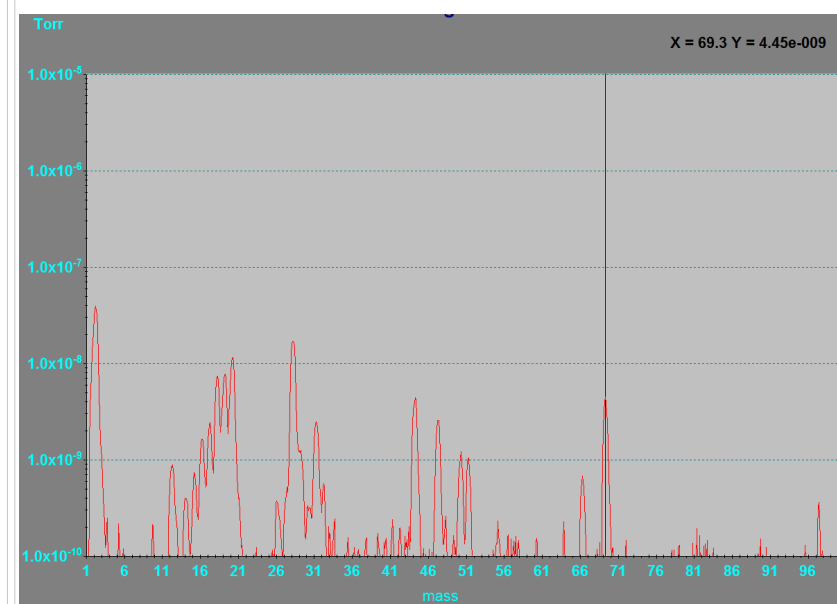


Turned on electron multiplier. Scan taken just after the above one

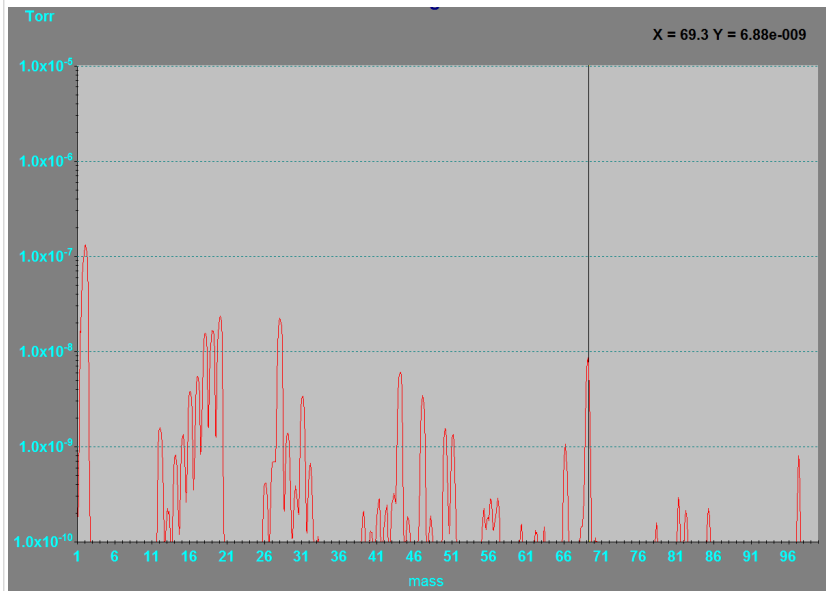


2018.01.02
0927

Day 11 into the bake with Heater settings #2
First scan taken without electron multiplier, second scan turn it on



Turned on electron multiplier. Scan taken just after the above one



2018.01.02
1746

5 hours after turning off the heaters on the chamber

With electron multiplier (did not take one without)

